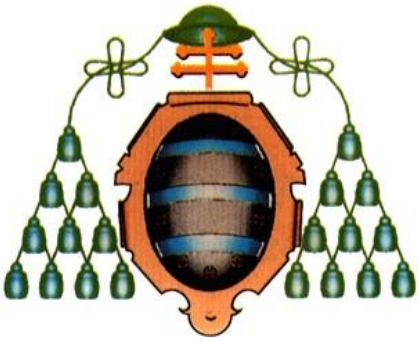

UNIVERSIDAD DE OVIEDO

Programa de Doctorado de Ciencia y Tecnología de Materiales

DISEÑO Y EVALUACIÓN DE MATERIALES COMPUESTOS CERÁMICA-METAL PARA APLICACIONES BIOMÉDICAS

TESIS DOCTORAL

Elisa Fernández García

Junio 2014

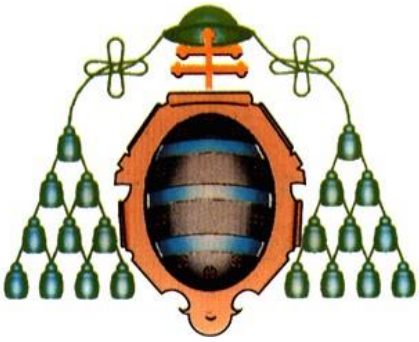

UNIVERSIDAD DE OVIEDO

Programa de Doctorado de Ciencia y Tecnología de Materiales

DISEÑO Y EVALUACIÓN DE MATERIALES COMPUESTOS CERÁMICA-METAL PARA APLICACIONES BIOMÉDICAS

TESIS DOCTORAL

Dra. Sonia López Esteban

Dr. Adolfo Fernández Valdés

Dr. Carlos F. Gutiérrez González

flexión que duplican los obtenidos antes de modificar el titanio.

El Capítulo 4, estudios *in vitro* demuestran que los métodos de fabricación no inducen citotoxicidad alguna. La compatibilidad de los materiales es evaluada a nivel celular mediante estudios de adhesión, proliferación y diferenciación. Estos estudios permiten correlacionar el comportamiento celular con las propiedades superficiales. Los sustratos de alúmina/titanio (más hidrófilos y con rugosidad sub-micrométrica formada por estructuras tipo valle) inducen mejor actividad osteoblástica que la alúmina pura, más hidrofóbica y con predominancia de picos en la topografía. En el sistema circona/titanio, la adhesión y la diferenciación a tiempos cortos se mejoran sobre la nano-estructura de la circona, permitiendo así verificar al SPS como una tecnología adecuada para fabricar nanomateriales bioactivos. Circona/75% vol. Titanio, el cermet más hidrofílico y polar, mejora la proliferación y diferenciación osteoblástica a tiempos largos.

En el Capítulo 5, se aborda la biofuncionalización de sustratos circona/titanio. Motivos biológicos (oligopéptidos con la secuencia RGDS) son inmovilizados covalentemente en las superficies inorgánicas, creando híbridos orgánicos/inorgánicos de actividad conocida. Así, este enfoque innovador, previamente optimizado para el titanio, es ahora extendido con éxito a materiales que contienen circona.

Por último, el Capítulo 6 recoge las técnicas experimentales más representativas, y el Capítulo 7 las conclusiones generales extraídas de esta tesis doctoral. Este trabajo de investigación contribuye a aumentar el conocimiento sobre el desarrollo de compuestos cerámica/metal, y sobre las interacciones biológicas con materiales de relevancia clínica, como son la alúmina, la circona, el titanio y sus compuestos. Determinar las causas últimas que dirigen el comportamiento celular es complicado debido a los efectos combinados de las propiedades superficiales. Sin embargo, biofuncionalizando los dispositivos inorgánicos con biomoléculas de actividad conocida, se puede inducir una respuesta biológica dirigida en el cuerpo.

RESUMEN (en Inglés)

The incidence of bone-related-diseases is increasing due to risk factors derived from the current lifestyle (smoking, obesity), chronic diseases, and the population aging. The replacement of hard tissues by synthetic devices is, in many times, the unique alternative. However, mechanical incompatibility between the implant and bone, and also the absence of bioactive interactions between the inert surface and the natural tissues lead frequently to implant failures. This phD thesis aims to develop new multifunctional materials that present both improved bio-mechanical features and biofunctionalized surfaces that are able of inducing bone healing, which constitutes a challenge in clinical of endoprosthesis.

The Introduction guides the reader through the main aspects related to the Biomaterials Science and the social impact of biomaterials. This section also presents cermets as a particular type of composites, which synergically combine dissimilar materials. Alumina, zirconia and titanium, by being widely-used structural biomaterials, are proposed to be combined in a composite form. Titanium has lower density and elastic modulus than other metals, a good strength and toughness, as well as excellent corrosion resistance. Oxide ceramics, such as alumina and zirconia, have been extensively used by their high wear resistance and outstanding compressive strength and hardness.

Alumina/titanium and zirconia/titanium cermets are manufactured and mechanically tested in Chapter 3. Traditionally, developing ceramic/titanium systems has been a challenge because the high reactivity among counterparts leads to form side compounds during sintering that weaken the microstructure. Using novel technologies that facilitate a fast conformation, such as Spark Plasma Sintering (SPS), Alumina/titanium (25 vol. %Ti) cermets with an effective resistance-curve toughening and noteworthy damage resistance were obtained. Zirconia/titanium composites had poor mechanical properties and accelerated aging due to the formation of α-Ti(O, Zr), Ti_2ZrO and/or TiO and $Y_2Ti_2O_7$ as a result of the higher zirconia reactivity with titanium than alumina. This problem is solved by an advanced two-step procedure consisting in attrition-milling of titanium powder and subsequent wet-deposition (sol-gel) of an yttria coating over the particles. Thereby, zirconia/titanium (25 vol. % Ti) composites without accelerated aging and with bending strength values that almost doubles the initial ones are achieved.

Chapter 4 includes *in vitro* studies that prove processing methods are safe in terms of cytotoxicity. Cytocompatibility is also assessed from adhesion, proliferation and differentiation studies using cell cultures and, by correlating cellular behaviour with the surface properties in cermets. More hydrophilic alumina/titanium substrates with sub-micrometric roughness mainly composed by valley-like structures induced better activity when compared with pure alumina, more hydrophobic and with peaks in its roughness. In the zirconia/titanium system, cell adhesion and early-differentiation were enhanced on nanostructured zirconia, whilst proliferation and late-differentiation were

improved on the most hydrophilic and polar cermet (75 vol. % Ti). Thus, SPS emerges a suitable technology for manufacturing nanomaterials with enhanced bioactivity.
Finally, Chapter 5 seeks to confer biofunctionality to the substrates, creating organic/inorganic hybrid materials, through the stable immobilization of biological motifs (RGDs containing oligopeptides) on the surface. This innovative approach based on the covalent immobilization of biological molecules on inorganic surfaces using silane chemistry, which has been optimized for titanium, is now successfully extended to zirconia/titanium composites and zirconia materials.

Finally, Chapter 6 collects the most representative experimental techniques, and Chapter 7 summarizes the general conclusions extracted from this phD thesis. This research work contributes to increase the knowledge on the development of ceramic/metal composites as well as on the biological interactions that occur on materials with clinical relevance, such as alumina, zirconia, titanium and their composites. Determining the ultimate causes that influence the cellular fate on synthetic biomaterials is a challenge due to the combined effects of the different surface properties. However, through the biofunctionalization of inorganic devices with organic molecules of known-activity, a positive biological response can be triggered in the body.

SR. PRESIDENTE DE LA COMISIÓN ACADÉMICA DEL PROGRAMA DE DOCTORADO EN CIENCIA Y TECNOLOGIA DE MATERIALES

A mis padres.

AGRADECIMIENTOS

Este trabajo ha sido realizado en el Departamento de Materiales Multifuncionales y Nanocomposites del Centro de Investigación en Nanomateriales y Nanotecnología (CINN); centro mixto del Consejo Superior de Investigaciones Científicas (CSIC), Principado de Asturias y Universidad de Oviedo (UNIOVI), bajo la dirección de los Dres. Sonia López Esteban, Adolfo Fernández Valdés y Carlos F. Gutiérrez González.

Quiera agradecer al Prof. Ramón Torrecillas San Millán tanto la posibilidad de desarrollar esta tesis doctoral en el Centro de Investigación en Nanomateriales y Nanotecnología (CINN), como sus valiosas aportaciones.

Quisiera también expresar mi más sincero agradecimiento a mis directores. A la Dra. Sonia López Esteban por haberme dado la oportunidad de realizar este trabajo, por infiltrarme desde la Biología en el mundo de los Materiales y permitirme comenzar esta aventura científica en un momento el que me hacía mucha ilusión. Mi agradecimiento a los Dres Carlos F. Gutiérrez-González y Adolfo Fernández Valdés es infinito. Gracias por estar a mi lado día a día, por todas las enseñanzas, las ideas y las soluciones. Las horas de laboratorio con Carlos no han podido ser más divertidas (que no negras) y didácticas. Gracias Adolfo por su visión siempre positiva, y por el esfuerzo, dedicación y apoyo en los momentos finales, más durillos.

También quisiera expresar mi más sincera gratitud a la prof. Maria Pau Ginebra por acogerme en el Departament de Ciència del Materials i Enginyeria Metal·lúrgica (Universitat Politècnica de Catalunya), por tratarme como uno más y poner a mi disposición todos los recursos del Grupo de Biomateriales, Biomecánica e Ingeniería de Tejidos (BIBITE). También al Dr. Jordi Guillém Martí, por su enseñanza rigurosa y metódica con los cultivos celulares. Gracia a vuestra supervisión y correcciones el estudio de biocompatibilidad ha llegado a buen puerto. También me gustaría agradecer a todos los chic@s del grupo, en especial, aquellos con los que compartí despacho ¡moltes gràcies, van ser tres mesos fantàstics!.

También me gustaría agradecer al Grupo de Ingeniería de Tejidos y Regeneración Ósea de la UCM, en especial, a Dres. López-Lacomba, Viviana Ramos y

Rodrigo Guzmán, por la colaboración en el estudio *in vitro* del sistema alumina/titanio.

Gracias a el trabajo realizado en el Minnesota Dental Research Center for Biomaterials and Biomechanics (MRCBB, University of Minnesota) esta Tesis ha adquirido un gran enfoque innovador. Mis seis meses en Mineápolis ha sido una experiencia increíble, a todos los niveles, y en ello ha tenido mucho que ver el Dr. Conrado Aparicio. Gracias por dirigirme durante la estancia y *a posteriori*, por enseñarme todo sobre biofuncionalización, por las conversaciones y los buenos consejos. Gracias Conrado, a ti y a Jane porque desde el minuto uno en la ciudad, me sentí en casa. Gracias también a todo el MRCBB, ha sido un gusto poder trabajar en ese ambiente. Gracias a Xi Chen por ayudarme en el laboratorio y, gracias a Carola Carrera por ser tan buena persona. A Jeno y Jon Geo, mil gracias por las risas de cada día.

Guardo tan buenos recuerdos de los momentos con la gente de mi grupo; en los laboratorios, en el café, en la comida y, sobre todo, en nuestro *pinchinquereis*. Gracias a todos, a los que aún estáis por aquí y a los que se han ido repartiendo por el mundo. Estos casi cuatro años se han pasado volando ¡gracias a vosotros!. Gracias en particular a Lucía y Lidia, que me han sufrido estoicamente estos meses de escritura acelerada.

También me gustaría agradecer a la Dra. Victoria García Rocha y al Dr. Laurent Gremillard la disposición para revisar y validar esta tesis dándome así la oportunidad de optar a la Mención Internacional.

También quiero dar las gracias al Consejo Superior de Investigaciones Científicas (CSIC) el haberme concedido una beca Jae-Pre y la posibilidad de realizar estancias de investigación.

Una tesis doctoral implica un trabajo intenso del que, al final, toma parte no sólo la gente con la que pasas tus horas de investigación. Los experimentos, la reactividad, las células, me han ido acompañando a casa. Por ello, quisiera agradecer todo el ánimo y el apoyo de mi familia y amigos.

A mis padres, Maximino y Esther, gracias por estar siempre incondicionalmente para todo. Gracias por vuestro esfuerzo para darme siempre de lo bueno lo mejor. Gracias también a mis tíos, a mis primos y a mis abuelos. En

especial, gracias a *Güelito* porque ¡*lo bien fecho, bien paez*!, y G*üelita* por su corazón enorme, te admiro tanto.

Gracias a mis amigas, a las de siempre, no hace falta que os nombre. A Marta, por las conversaciones interminables y la constante empatía. A Katia, por esa lección de fuerza. No puedo hacerme a la idea.

Y gracias a ti, Hugo, por la Química, a todos los niveles. Porque nunca dejarás de sorprenderme y porque siempre sabes sacarme una sonrisa. ¡Soy tan feliz!.

A todos los que directa e indirectamente habéis formado parte de este trabajo,

¡Muchas gracias!.

ABSTRACT

The incidence of bone-related-diseases is increasing due to risk factors derived from the current lifestyle (smoking, obesity), chronic diseases, and the population aging. The replacement of hard tissues by synthetic devices is, in many times, the unique alternative. However, mechanical incompatibility between the implant and bone, and also the absence of bioactive interactions between the inert surface and the natural tissues lead frequently to implant failures. This Ph. D. Thesis aims to develop new multifunctional materials that present both improved bio-mechanical features and biofunctionalized surfaces that are able of inducing bone healing, which nowadays constitutes a challenge in clinical of endoprosthesis.

The Introduction (Chapter 1) guides the reader through the main aspects related to the Biomaterials Science and the social impact of biomaterials. This section also presents cermets as a particular type of composites, which synergically combine dissimilar materials. Alumina, zirconia and titanium, by being widely-used structural biomaterials, are proposed to be combined in a composite form. Titanium has lower density and elastic modulus than other metals, a good strength and toughness, as well as excellent corrosion resistance. Oxide ceramics, such as alumina and zirconia, have been extensively used by their high wear resistance and outstanding compressive strength and hardness.

Chapter 2 establishes the overall objectives.

Alumina/titanium and zirconia/titanium cermets are manufactured and mechanically tested in Chapter 3. Traditionally, developing ceramic/titanium systems has been a challenge because the high reactivity among counterparts leads to form side compounds during sintering that weaken the microstructure. Using novel technologies that facilitate a fast conformation, such as Spark Plasma Sintering (SPS), alumina/titanium (25 vol. %Ti) cermets with an effective resistance-curve toughening and noteworthy damage resistance were obtained. Zirconia/titanium composites had poor mechanical properties and accelerated aging as a result of the formation of α-Ti(O, Zr), Ti_2ZrO and/or TiO and $Y_2Ti_2O_7$ due to the higher zirconia reactivity with titanium than alumina. This problem is solved by an advanced two-step procedure consisting in attrition-milling of titanium powder and subsequent wet-deposition (sol-gel) of an yttria coating over the particles. Thereby, zirconia/titanium (25 vol. % Ti) composites without accelerated aging and with bending strength values that almost doubles the initial ones are achieved.

Chapter 4 includes *in vitro* studies that prove processing methods are safe in terms of cytotoxicity. Cytocompatibility is also assessed from adhesion, proliferation and differentiation studies using cell cultures and, by correlating cellular behaviour with the surface properties in cermets. More hydrophilic alumina/titanium substrates with sub-micrometric roughness mainly composed by valley-like structures induced better activity when compared with pure alumina, more hydrophobic and with peaks in its roughness. In the zirconia/titanium system, cell adhesion and early-differentiation were enhanced on nanostructured zirconia, whilst proliferation and late-differentiation were improved on the most hydrophilic and polar cermet (75 vol. % Ti). Thus, SPS emerges a suitable technology for manufacturing nanomaterials with enhanced bioactivity.

Chapter 5 seeks to confer biofunctionality to the substrates, creating organic/inorganic hybrid materials, through the stable immobilization of biological motifs (RGDs containing oligopeptides) on the surface. This innovative approach based on the covalent immobilization of biological molecules on inorganic surfaces using silane chemistry, which has been optimized for titanium, is now successfully extended to zirconia/titanium composites and zirconia materials.

Chapter 6 summarizes the general conclusions extracted from this Ph. D. Thesis. In overall, this research contributes to increase the knowledge on the development of ceramic/metal composites as well as on the biological interactions that occur on materials with clinical relevance, such as alumina, zirconia, titanium and their composites. Determining the ultimate causes that influence the cellular fate on synthetic biomaterials is a challenge due to the combined effects of the different surface properties. However, through the biofunctionalization of inorganic devices with organic molecules of known-activity, a positive biological response can be triggered in the body.

Finally, Chapter 7 collects the most representative experimental techniques used to develop the research.

RESUMEN

La incidencia de enfermedades óseas aumenta en la población actual a consecuencia de factores de riesgo derivados del estilo de vida (tabaquismo, obesidad), enfermedades crónicas y al envejecimiento de la población. Frecuentemente, la única alternativa que se plantea es la sustitución de los tejidos afectados por dispositivos sintéticos pero, debido a la diferente biomecánica y/o a la ausencia de interacciones a nivel superficial con los tejidos óseos, los implantes actuales pueden fallar. Esta tesis doctoral tiene como objetivo desarrollar nuevos materiales multifuncionales con una biomecánica mejorada y superficies bio-funcionalizadas que induzcan mecanismos naturales de osteointegración, lo cual constituye un reto en clínica de las endoprótesis.

En la parte introductoria (Capítulo 1) se guía al lector a través de aspectos importantes en la Ciencia de los Biomateriales y su impacto social. También se presentan los cermets, materiales compuestos cerámica/metal que combinan sinérgicamente propiedades de los monolíticos. Como materiales de partida se utilizan alúmina, circona y titanio; *per se* biomateriales estructurales de uso extendido. El titanio tiene menor densidad y módulo elástico que otros metales, buena resistencia mecánica, y excelente resistencia a la corrosión. Alúmina y circona, presentan alta resistencia al desgaste, excelente resistencia a la compresión y dureza.

El Capítulo 2 estable los objetivos generales y el planteamiento de trabajo.

En el Capítulo 3, se fabrican y evalúan mecánicamente los nuevos sistemas alúmina/titanio y circona/titanio. Desarrollar materiales compuestos con una segunda fase de titanio ha sido tradicionalmente un reto ya que, dada la alta reactividad, durante la sinterización se forman compuestos secundarios que debilitan la microestructura. El uso de nuevas tecnologías que permiten la rápida conformación de los materiales, como es el *Spark Plasma Sintering* (SPS), ha facilitado el desarrollo de nuevos cermets alúmina/titanio (25% vol. Ti) con comportamiento de curva-R y notable tolerancia a los defectos. En el caso de los materiales circona/titanio, la mayor reactividad del titanio con la circona que con la alúmina, conduce a compuestos del tipo TiO, α-Ti(O, Zr), Ti_2ZrO y/o $Y_2Ti_2O_{7,}$ que inducen una pobre mecánica y el envejecimiento acelerado de los cermets. Mediante la molienda de atrición del polvo de titanio y su recubrimiento por sol-gel con una capa de itria se consiguen compuestos circona/titanio (25% vol. Ti) sin envejecimiento prematuro y con valores de resistencia a flexión que duplican los obtenidos antes de modificar el titanio.

El Capítulo 4, estudios *in vitro* demuestran que los métodos de fabricación no inducen citotoxicidad alguna. La compatibilidad de los materiales es evaluada a nivel celular mediante estudios de adhesión, proliferación y diferenciación. Estos estudios permiten correlacionar el comportamiento celular con las propiedades superficiales. Los sustratos de alúmina/titanio (más hidrófilos y con rugosidad sub-micrométrica formada por estructuras tipo valle) inducen mejor actividad osteoblástica que la alúmina pura, más hidrofóbica y con predominancia de picos en la topografía. En el sistema circona/titanio, la adhesión y la diferenciación a tiempos cortos se mejoran sobre la nano-estructura de la circona, permitiendo así verificar al SPS como una tecnología adecuada para fabricar nanomateriales bioactivos. Circona/75% vol. Titanio, el cermet más hidrofílico y polar, mejora la proliferación y diferenciación osteoblástica a tiempos largos.

En el Capítulo 5, se aborda la biofuncionalización de sustratos circona/titanio. Motivos biológicos (oligopéptidos con la secuencia RGDS) son inmovilizados covalentemente en las superficies inorgánicas, creando híbridos orgánicos/inorgánicos de actividad conocida. Así, este enfoque innovador, previamente optimizado para el titanio, es ahora extendido con éxito a materiales que contienen circona.

El Capítulo 7 recoge las conclusiones generales extraídas de esta tesis doctoral. Así, este trabajo de investigación contribuye a aumentar el conocimiento sobre el desarrollo de compuestos cerámica/metal, y sobre las interacciones biológicas con materiales de relevancia clínica, como son la alúmina, la circona, el titanio y sus compuestos. Determinar las causas últimas que dirigen el comportamiento celular es complicado debido a los efectos combinados de las propiedades superficiales. Sin embargo, biofuncionalizando los dispositivos inorgánicos con biomoléculas de actividad conocida, se puede inducir una respuesta biológica dirigida en el cuerpo.

Por último, el Capítulo 7 recoge las técnicas experimentales más representativas utilizadas para desarrollar esta investigación.

INDEX/ÍNDICE

CHAPTER 1: INTRODUCTION

CHAPTER 2: OBJETIVOS Y PLANTEAMIENTO DE TRABAJO

CHAPTER 3: CERAMIC/TITANIUM SYSTEMS: PROCESSING AND CHARACTERIZATION

CHAPTER 7: EXPERIMENTAL TECHNIQUES

Chapter 1

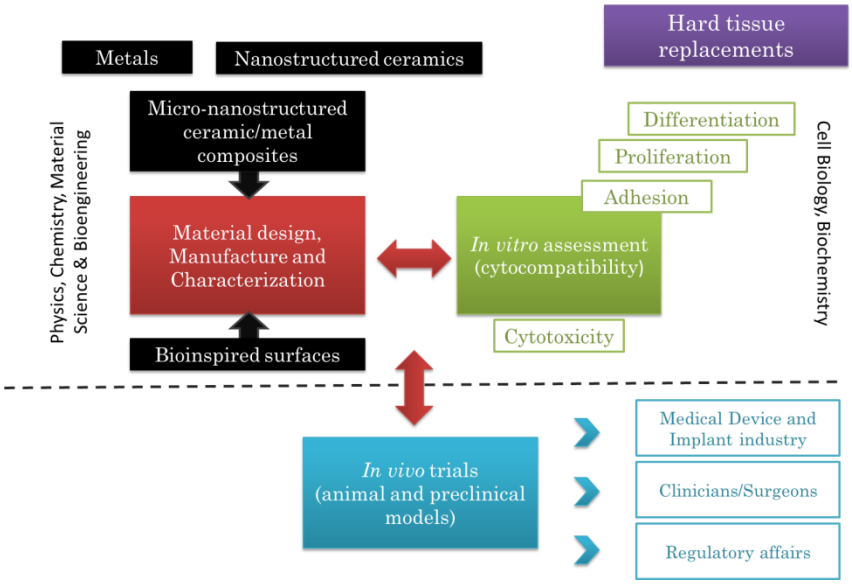

INTRODUCTION

Design and evaluation of ceramic/metal composites for biomedical purposes

1.1 BACKGROUND

Millions of lives have been saved by using devices fabricated from biomaterials, and life quality has been improved for millions more. The field of biomaterials has a significant impact on human health but also on the economy, and on many scientific fields [1, 2].

The incidence of bone-related-diseases and tooth loss is increasing exponentially due to risk factors derived from the current lifestyle (smoking, obesity), chronic diseases, and the population aging [3, 4]. The replacement of hard tissues by synthetic devices is in many cases the last and most costly solution to deal with the depletion of bone quality and/or the inability to preserve the natural hard tissues and structures.

Biomaterials used today to replace those tissues and structures, such as those used for making dental implants, are not fully compatible with the host bone, which in most cases results in second replacements after implantation [5, 6]. Lack of appropriate design of the replacing devices, periprosthetic fractures, micro-motions, wear debris, stress shielding, and infection are etiologies related to implant failure [7, 8]. Mechanical incompatibility between the implant and the surrounding bone, and no bioactive interactions between the inert biomaterial surface and the natural tissues are among the most significant causes for implant failures at mid and long term after implantation [9]. In this context, the development of new biomaterials with improved mechanical properties that furthermore have osseostimulative surfaces are of need for better addressing the clinical demands [10, 11].

The common thread in biomaterials is the physico-chemical interactions that take place between complex biological systems and synthetic or modified natural materials [12]. Thereby, Biomaterials Science can be defined as the physical and biological study of materials, and their interaction with the biological environment [13]. Traditionally, investigation has been focused on the synthesis, optimization, characterization or testing of materials, and also on the biology of host-material interactions. Nowadays, most biomaterials induce a non-specific biological reaction in the host body, so the today effort is addressed toward developing modified surfaces that can lead precise reactions with cells and proteins, tailored to a particular application [12, 13].

Biomaterials Science is an example of a new research model, in which the collaboration among multidisciplinary experts converges [14]. Indeed, this scientific discipline evolves from the knowledge of individual experts in biology, chemistry, physics, material science, and clinicians, that start to collaborate in order to solve the existing necessities in therapeutics and diagnostics.

In this line, a research work on biomaterials cannot be understood without a multidisciplinary approach. Thereby, we will design and evaluate materials for biomedical applications encompassing the knowledge of physics, chemistry and biology in order to develop new biocompatible materials with improved mechanically and with purposely-designed surfaces to integrate in the host tissues. Fig 1.1-1 discloses the bidirectional relationships between the diverse areas of knowledge involved in developing biomaterials. In order to advance in the path that links the basic science of biomaterials with the clinical framework, in which the material devices are applied, we will assess the newly developed biomaterials *in vitro*.

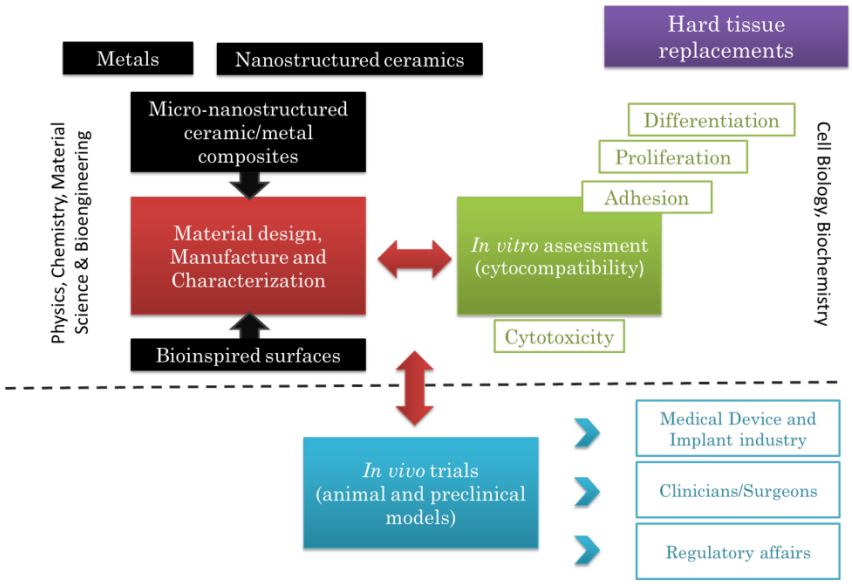

Fig 1.1-1. Interrelation between basic science of materials and the clinical application.

This chapter aims to establish an overview about the biomaterials in order to better understand the following experimental sections that form this Ph. D. Thesis. These sections will include the processing way of the new biomaterials, their mechanical and surface characterization, and also the assessment of their biocompatibility and the surface modification processes that are designed to facilitate

the device's osseointegration and avoiding the foreign-body response. First, definition, evolution, applications and uses of biomaterials will be presented. Then, the common types of materials used for biomedical applications will be briefly described. Ceramic/metal composites (cermets) will be presented as the particular types of composites that are studied in this research. Alumina, zirconia and titanium will be reviewed as the materials of choice to develop the cermets. Subsequently, the bone is presented as the structural material and biological system in which the inorganic devices are implanted. Finally, it is addressed an overall analysis about biological response to biomaterials once implanted and the biofunctionalization as innovative way to enhance that response.

1.2 BIOMATERIALS

1.2.1 DEFINITION

Biomaterials were firstly defined in 1987 as a *non-viable material used in a medical device, intended to interact with biological systems* [15]. The reference to *non-viability* was later deleted, preferring to define biomaterial as *a material intended to interface with biological systems to evaluate, treat, augment or replace any tissue, organ or function of the body* [16]. This definition, that emerges with classical Material Science, prevails until recently [17]. Nowadays, biomaterials are used in very different situations to those used a decade ago. Although implantable medical devices are hugely important, medical technologies also include drug and gene delivery systems, tissue engineering and cell therapies, organ printing and cell patterning; nanotechnology based imaging and diagnostic systems or microelectronic devices. Therefore, alongside the traditional structural biomaterials, other substances have been developed to control interactions with tissues. In this context, D.F. Williams has proposed that a *biomaterial is a substance that has been engineered to take a form which, alone or as part of a complex system, is used to direct, by control of interactions with components of living systems, the course of any therapeutic or diagnostic procedure, in human or veterinary medicine*[17].

1.2.2 EVOLUTION

Biomaterials research has been guided by advances in cell and molecular biology, chemistry, materials science, and engineering; thanks to the biomaterials community, the interactions among materials and physiological environment (*biointerface*) have been understood. The development of materials for medical

applications has evolved through generations with distinct objectives. The limits among such generations are not clear; they are temporally overlapping.

The first generation (1950s-1960s) involved available industrial materials, which had not been developed specifically for medical use. These were selected by a suitable combination of physical properties and by eliciting a minimal response in the host tissues (bioinert), which led to consider them as biocompatible.

The second generation (1980s) evolves from the earlier ones with the aim of inducing a determined therapeutic effect by means of controlling reactions within the tissues once implanted. Bioactive materials are used in orthopedic and dental surgeries, but also in localized drug release applications. Thus, this second generation of biomaterials also includes resorbable biomaterials that have specific degradation rates of soluble and non-toxic products.

Traditionally, the role of physicians has been palliative. However, with the advances in tissue engineering and regenerative medicine, healing using the living tissues may be possible. Tissue engineering uses a set of tools that involve living cells, or that seek attract endogenous cells in order to aid the tissue regeneration. Thanks to this new approach, damaged tissues like bladders, trachea, skin, corneal epithelium, and cartilage have already been replaced. In this context, the third generation includes biomaterials that are able to support and stimulate the regeneration of functional tissues.

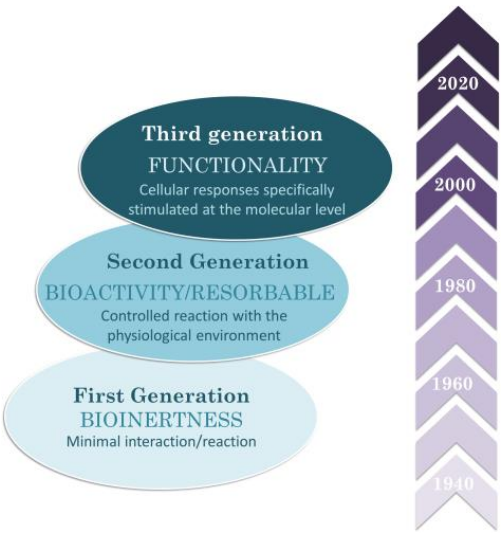

Fig 1.2-1. Evolution of biomaterials science and technology (adapted from [18] and [12]).

The ultimate goal of biomaterials research is to develop strategies that promote the individual self-healing but for this, further tissue-engineering research and more extensive understanding of the cellular basis of ageing are still needed. Today, there are a number of needs to be filled that require new multifunctional materials, which can be placed on the market relatively quickly. In this respect, by modifying the physicochemical properties of surfaces, the biological interaction of materials and tissues can be enhanced (biofunctionality), thus performing new structural and biofunctional biomaterials with diverse applications, such as biointegrative biomaterials for hard tissue replacements.

1.2.3 IMPACT OF USING BIOMATERIALS

Biomaterials are commonly used as prostheses in cardiovascular, orthopedic, dental, ophthalmological, and reconstructive surgery, and in other interventions such as surgical sutures, bioadhesives, and controlled drug release devices. Fig 1.2-2 shows examples of implantable biomaterials in the human body.

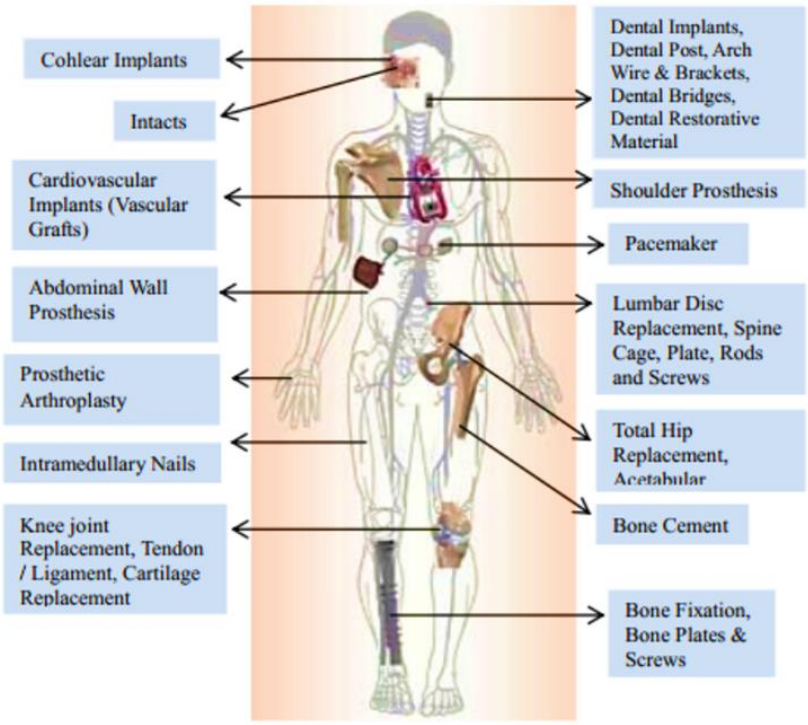

Fig 1.2-2. Implants for human anatomy [19].

In addition, Table 1.2-1 summarizes the main applications of biomaterials in the body, the most used materials for such applications and their impact in the market. These materials include metals, ceramics, polymers and composites are listed, which can be used as molded or machined parts, coatings, fibers, films, membranes, foams, fabrics, and nanoparticles. The number of medical devices implanted in humans each year, make us aware that the human impact, and the size of the commercial market for biomaterials and medical devices, is impressive.

Table 1.2-1: Key *applications of biomaterials [12].*

APPLICATION	BIOMATERIALS USED	NUMBER/YEAR – WORLD (WORLD MARKET IN US$)
SKELETAL SYSTEM		
Joint replacements (hip, knee, shoulder)	Titanium, stainless steel, PE	2,500,000
Bone fixation plates and screws	Metals, poly(lactic acid) (PLA)	1,500,000
Spine disks and fusion hardware		800,000
Bone cement	Poly(methyl methacrylate)	($600M)
Bone defect repair	Calcium phosphates	–
Artificial tendon or ligament	Polyester fibers	–
Dental implant-tooth fixation	Titanium	($4B)
CARDIOVASCULAR SYSTEM		
Blood vessel prosthesis	Dacron, expanded Teflon	200,000
Heart valve	Dacron, carbon, metal, treated natural tissue	400,000
Pacemaker	Titanium, polyurethane	600,000
Implantable defibrillator	Titanium, polyurethane	300,000
Stent	Stainless steel, other metals, PLA	1,500,000
Catheter	Teflon, silicone, polyurethane	1B ($20B)
ORGANS		
Heart assist device	Polyurethane, titanium, stainless steel	4000
Hemodialysis	Polysulfone, silicone	1,800,000 patients ($70B)
Blood oxygenator	silicone	1,000,000
Skin substitute	Collagen, cadaver skin, nylon, silicone	($1B)
OPHTHALMOLOGIC		
Contact lens	Acrylate/methacrylate/silicone polymers	150,000,000
Intraocular lens	Acrylate/methacrylate polymers	7,000,000
Corneal bandage lens	hydrogel	–
Glaucoma drain	Silicone, polypropylene	($200M)
OTHER		
Cochlear prosthesis	Platinum, platinum-iridium, silicone	250,000 total users
Breast implant	Silicone	700,000
Hernia mesh	Silicone, polypropylene, Teflon	200,000 ($4B)
Sutures	PLA, polydioxanone, polypropylene, stainless steel	($2B)
Blood bags	Poly(vinyl chloride)	–
Ear tubes (Tympanostomy)	Silicone, Teflon	1,500,000
Intrauterine device (IUD)	Silicone, copper	1,000,000

This Ph. D. Thesis has its scope in the skeletal system and aims to advance in the development of devices that can avoid current problems related to clinical of endoprosthesis, such as periprosthetic fractures, micro-motion, wear debris or stress shielding. All they are etiologies that lead to the early implant failure.

1.2.4 IMPLANTABLE MATERIALS: CLASSIFICATION ACCORDING TO CHEMICAL NATURE

As mentioned in the previous section, the most common materials used as biomedical materials are metals, polymers and ceramics. They are used alone or in combination to form most of the implant devices available today. Then, each of these groups is individually addressed to get an overview about its advantages and disadvantages.

1.2.4.1 Polymeric Biomaterials

Polymers are organic materials that form large chains made up of many repeating units [19]. The requirements of polymers as biomaterials are similar to other biomaterials: biocompatibility, sterilizability, adequate mechanical and physical properties, and manufacturability. Synthetic polymeric materials have been widely used in medical disposable supplies, prosthetic materials, implants, extracorporeal devices, encapsulants, polymeric drug delivery systems, tissue engineered products, etc. The main advantages compared to metal or ceramic materials are its easy manufacturability that allows to produce different shapes (latex, film, sheet, fibers, etc.), low coefficients of friction, reasonable cost, and wide range of mechanical and physical properties. However, polymeric materials easily adsorb water and biomolecules from the biological medium. They also may release degradation substances such as toxic monomers, catalysts or additives in the body. Furthermore, they have low mechanical properties that do not allow to use them in load-bearing applications.

1.2.4.2 Metallic biomaterials

Metals have been used almost exclusively for load-bearing implants, such as hip and knee prosthesis, dental implants and fracture fixation wires, pins, screws and plates [19]. Strength, stiffness, long fatigue cycle or fracture toughness are among the mechanical properties that make metals extremely useful as components of medical devices [19, 20]. Iron, cobalt, titanium, tantalum, niobium, molybdenum, and tungsten are often metals used for manufacturing implantable devices. They are

employed in their metallic form or also to make alloys, such as occurs with the widely-used Ti6Al4V [21]. The problem is that many metals can only be tolerated in tiny amounts because they can be naturally involved in physiological paths or because they can induce a cytotoxic effect *per se*. This is the case of the reactive oxygen species derived from Cr, Ni, Co and Ti that may cause damage to the nucleus, proteins and lipids, which would result in inhibition of DNA repair pathways, impaired nuclear signal transduction and defective gene expression [22, 23].

All metallic surfaces undergo an electrochemical corrosion in the physiological medium that reduces the structural integrity of the implant and lead to releasing potentially toxic degradation products [23]. Every metal has its own reactivity to oxidation and therefore, the biocompatibility of metallic implants will be related to its inherent capability of corrosion resistance in the biological environment [21]. In the particular case of nickel, chromium and cobalt, which are respectively released from SUS 316L or Co–Cr alloys, have been demonstrated that lead to hypersensitivity reactions and even to carcinogenesis [7, 24].

1.2.4.3 Ceramic biomaterials

Ceramics are generally defined as inorganic, non-metallic materials [25]. In clinical practice, the controlled implantation of bioceramics started late 18th century in dentistry with the use of porcelain for crowns and late 19th century in orthopaedics with the use of Plaster of Paris or gypsum (calcium sulfate dihydrate) for bone filling. With the advances in the ceramic technology, the 20th century had multiple *high-tech* ceramics available for medical purposes [26].

Ceramics used to manufacture implants are often classified as non-absorbable (relatively inert), bioactive or surface reactive (semi-inert), and biodegradable or resorbable (non-inert) [19, 21]. Alumina, zirconia, silicone nitrides, and carbons are inert bioceramics. Certain glass ceramics and dense hydroxyapatites are semi-inert (bioreactive), and calcium phosphates and calcium aluminates are resorbable ceramics [21].

Among the main features in structural ceramics are the high chemical stability that confers their characteristic resistance to corrosion and, also the outstanding response to wear. Other interesting characteristics are high hardness, good strength, and low density [19]. However, ceramics present important drawbacks that limit their use as biomaterials, such as the high brittleness and the low fracture toughness.

1.2.4.4 Composite biomaterials

As summarized in Table 1.2-2, all materials (polymers, metals and ceramics) in their monolithic form present valuable advantages but also important drawbacks (Table 1.2-3) that turn them into compromised biomaterials with a limited use. In this context, the composite forms of the materials arise to treat of solving at least some of the drawbacks derived from the inherent features at the monolithic materials.

Table 1.2-2: *Advantages of polymeric, metallic and ceramic monolithic biomaterials.*

	POLYMERS	METALS	CERAMICS
ADVANTAGES	Low coefficients of friction	Good ductility	High hardness - Resistance against burnishing from third-body wear like bone cement, particularly when articulates against PE
	Physical, chemical and mechanical properties tailorable to the specific needs thanks to the wide variety of copolymers, polymer blends and composites with other materials.	High strength for load-bearing parts of the body	
	Easy processing and workability	Good toughness	Inert wear debris
	Low risks of toxicity, immunogenicity and infections.	Low elastic modulus when compared to ceramics	No adverse effects
			High compressive strength

Table 1.2-3: *Disadvantages of polymeric, metallic and ceramic monolithic biomaterials.*

	POLYMERS	METALS	CERAMICS
DISADVANTAGES	Low mechanical properties Low chemical stability.	Inadequate corrosion resistance - Release of fine metallic ions results in adverse tissue effect	High elastic modulus - Stress shielding effect and bone loss
	Low thermal stability: - In some cases, difficult sterilization		High brittleness: - Unexpected fractures (particles might be embedded in the soft tissue and later become grinding media for future bearing surfaces) - Loss of options available to the surgeon and more bone resection
	Good biocompatibiliy	Inadequate wear resistance - Release of wear debris leads to inflammatory response and loosening	Limitation in component Fixation Loosening due to micro-movements
		Soft tissue interlayer	Soft tissue interlayer

A composite material is composed by two or more phases which are chemically distinct (metallic, ceramic, or polymeric) and which are separated by interface(s). In composites, materials are combined forming an extra material that if it is well designed may exhibit the best qualities of its components and often other qualities that neither constituent possesses [27, 28].

The classification of engineering composite materials is usually based on the matrix materials (metals, ceramics, and polymers) and/or on the reinforcement dimensions/shapes (particulates, whiskers/short fibers, and continuous fibers) [29]. Thus, reinforced plastics such as fiberglass or natural materials such as wood, dentin, bone, cartilage, and skin are considered composites, but alloys are not.

Today, a great effort is devoted to design new custom-made composites that meet mechanical expectations for top end biomedical applications [7, 8]. Polymer/polimer, polymer/ceramic, ceramic/ceramic and ceramic/metal are among the different types of composite materials developed for biomedical purposes. The research in this Ph. Thesis is focused on the development and evaluation ceramic/metal composites. By working with this type of composites opens the possibility of integrating the dissimilar properties of ceramics and metals in the composites, thus achieving properties that would never be achieved by using separately the components.

1.3 CERAMIC/METAL COMPOSITES (CERMETS)

The interest of ceramic/metal composites, also known as cermets, arises during the late 1980s and early 1990s. As it has been indicated in the preceding section, the properties in composites are substantially modified when compared with those of the counterparts. Thereby, cermets are excellent candidates to fabricate multifunctional devices with unique features. Indeed, a singular combination of mechanical, optical, electrical and/or magnetic properties has been accomplished in previous works by dispersing a network of metallic particles within an insulating matrix [30, 31].

As a consequence of the multiple combinations of materials that can be made working on cermets, this is a very innovative field that provides the opportunity to create an almost unlimited set of new composite materials with a large spectrum of properties [31]. Whole experimental part related with the development of new cermets will be extensively approached in Chapter 3 of this work.

1.3.5 CERMETS FOR HARD TISSUE REPLACEMENTS

It is well-known that many times the endosseous implants failure as a result of the mechanical incompatibility existing between the materials used to make the device and the surrounding bone. The implant failure is a complex and multi-etiology problem, in which the absence of an appropriate design in the replacing device, the periprosthetic fractures, micro-motion phenomena, wear debris and/or stress shielding are among the most important phenomena to avoid.

By incorporating a second phase of metal micro-particles in a nanostructured ceramic matrix, mechanically and tribologically improved materials in terms of toughness, flexural strength, hardness and also wear resistance can be accomplished [32, 33]. Indeed, one of the most effective methods to increase fracture toughness in monolithic ceramics is with a reinforcement of ductile particles that interacts with the cracks to slow down their propagation (Fig 1.3-1). Cermets with adherent ductile phases also exhibit generally stable crack-growth resistance behaviour (R-curve). The bridging ligaments exert closure stresses that reduce the stress intensity at the crack tip and offer resistance to further crack propagation. The magnitude of the crack closure is based on the stress–strain relation of the ligaments, which is influenced by the ligament yield stress, diameter, orientation, volume fraction and the nature of the ceramic/metal interface [31, 34].

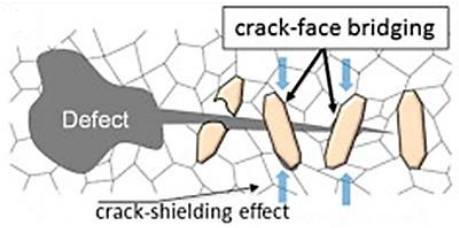

Fig 1.3-1. Schematics of the crack-face, which greatly increase the toughness of ceramic materials [34].

An essential issue to consider in the development of cermets for biomedical purposes (biocermets) is that every counterpart must be as biocompatible as possible with the human organism. This fact limits the number of materials that can be selected to form the composites. Zirconia, alumina, and titanium induce a good biological response in the host tissues, which has led to use them extensively as structural biomaterials. This is the reason why such materials have been chosen as starting materials for manufacturing the cermets.

1.3.6 STARTING MATERIALS

Due to *suitable* mechanical properties and *good* behaviour in the physiological medium, zirconia, alumina and titanium are widely used biomaterials in dental and orthopaedic fields. The noteworthy features presented by the individual forms leads to combine them into composites to create, in the framework of this Ph. D. Thesis, new alumina/titanium and zirconia/titanium cermets.

1.3.6.1 Alumina and Zirconia as biomaterials

Alumina and zirconia are most often considered as *bioinert* ceramics; although a material should never be considered as totally inert, since a soft tissue interlayer always shields the bone from the implant [25]. Bioceramics present, as main advantage, the reduced wear rates in bearing components and the negligible ion release [17]. More than 3.5 million alumina components and more than 600,000 zirconia femoral heads have been implanted worldwide since 1990. Although the fracture rate was initially quite high (up to 13% for some series) due to the intrinsic brittleness, the *in vivo* failure rate reported by the main producer of alumina is today below 0.01%. A similar failure rate was also reported by the main producer of zirconia heads, with the exception of the critical event that took place in 2001. Today, fracture rate of ceramics is negligible when compared to the overall failure rate of metallic implants, which is mainly due to aseptic loosening resulting from particles release [25]. Both alumina and zirconia materials are described below:

- Alumina

Alumina (Al_2O_3) was first investigated and used as a total hip arthroplasty (THA) bearing material by the surgeon Pierre Boutin (1970s). Among the mechanical properties that make it attractive include a Vickers hardness of more than 2000, compared to a value of less than 500 for other materials like cobalt–chrome and titanium. This high level of hardness protects alumina components from being scratched during surgery and furthermore, provides a wear solution in physiologic fluids, with very little deterioration of mechanical properties even after prolonged exposure to the *in vivo* environment [35].

As it can be observed in Table 1.3-1, modern alumina has superior features over previous generations of the same material. This progress is made by increasing purity and by achieving density close to the theoretical values. Thus, the compositions of the raw powders and the manufacturing methods have been refined to control

processing, minimizing inclusions and impurities and optimizing the material homogeneity. This, along with highly specialized sintering techniques, has resulted in an improvement in its physical properties; as a result of the smaller grain sizes, higher strength and much better fracture toughness properties have been achieved [26].

Table 1.3-1: *Improvements in Alumina over time (extracted from [35]).*

MECHANICAL PROPERTIES	1700S	1980S	1990S	BIOLOX®DELTA 2003
Strength (MPa)	≥400	≥500	≥580	≥1384
Hardness (H_V)	1800	1900	2000	2000
Bending strength (MPa)	>450	>500	>550	>550
Microstructure (µm)	≤4.5	≤3.2	≤2.0	≤2.0
Density (g/cm^3)	≥3.86	≥3.94	≥3.96	≥4.37
Young's Modulus (GPa)	≥380	≥380	≥380	≥380
Fracture toughness (MPa·m$^{1/2}$)	3.0	3.0	3.2	6.5
Hot isostatic pressing	No	No	Yes	Yes
100% quality control in manufacturing	Minimal	Moderate	Very high	Very high
Suitable for ceramic–ceramic articulations	Minimal	Moderate	Very high	Very high

Despite of all these improvements, alumina still presents as main disadvantage its high brittleness. Even so, the set of good mechanical properties that this material offers; its lower cost and ease of manufacturing, as well as absence of instability problems, make it a biomaterial that today is widely used.

- Zirconia

Zirconia is a crystalline dioxide of zirconium. According to thermodynamic conditions, zirconia crystals can be organized in three crystalline forms: monoclinic, cubic and tetragonal [36]. The cubic phase with fluorite-type structure is stable at 2370-2680 °C, the tetragonal phase presents distorted fluorite-type structure and stability between 1200 and 2370 °C and the monoclinic phase also has a distorted fluorite-type structure; it is stable below 1200 °C. In addition, there is an extra orthorhombic-polymorphism based on the composition of monoclinic form that takes place only in high-pressure experimental conditions (up to 60 GPa).

Zirconia was first proposed, in 1969, as a new material for hip head replacement instead of alumina or titanium [37]. Orthopaedic research focused on zirconia because of its mechanical behavior, wear resistance and biocompatibility within the live tissues [19, 37, 38]. In 1975, it was suggested a model to rationalize the mechanical properties of zirconia and, due to the similar features to those in stainless steel, this material was called as ceramic steel. In the 1990s, yttria-stabilised zirconia (Y-TZP) became a popular alternative as structural ceramic because of its higher fracture toughness and strength. Thus, tensile strength can be as high as 900-1200 MPa and its compressive strength is about 2000 MPa. Furthermore, zirconia tolerates well the cyclical stresses [37]. Moreover, zirconia meets the aesthetic requirements (colour, translucency) of dentistry [25].

Zirconia exhibits the best mechanical properties of single phase oxide ceramics as a result of the phase transformation toughening, which increases the crack propagation resistance (Fig 1.3-2). The stress-induced phase transformation involves the transformation of metastable tetragonal grains to the monoclinic phase at the crack tip, which is accompanied by a volume expansion that induces compressive stresses and hinders the crack propagation [25].

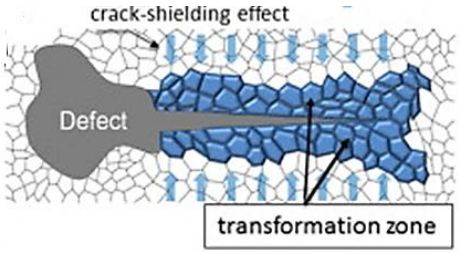

Fig 1.3-2. Schematics of the transformation-toughening mechanisms, which greatly increase the toughness of stabilized zirconia [34].

However, due to its metastability zirconia is prone to suffer hydrothermal aging in the physiological medium [39, 40]. Aging occurs by a progressive tetragonal to monoclinic transformation at the surface triggered by water or water vapor molecules, which results in surface roughening and micro-cracking. The transformation occurs by a nucleation and growth process. Transformation starts in isolated grains on the surface by a stress corrosion type mechanism. As schematically described in Fig 1.3-3, the transformation leads to a cascade of events occurring neighbor to neighbor. Thus, (a) nucleation on a particular grain at the surface leads to microcracking and stresses to the neighbors; (b, c) as a result of growth in the transformed zone, an extensive microcracking and the surface roughening is addressed [41].

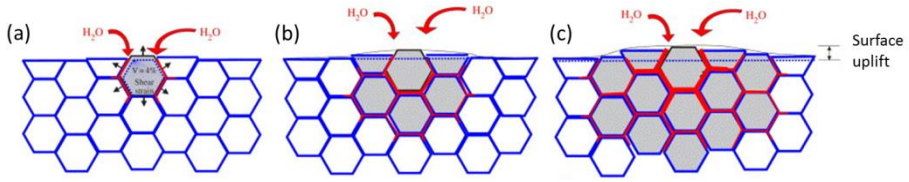

Fig 1.3-3. Scheme of the aging in a cross section (Transformed grains are gray ones. Red path represents the penetration of water due to microcracking around the transformed grains) [41].

Ageing has been widely studied because this process occured in vivo, giving isolated failures after some years of the device implantation or catastrophic events, such is the case of the fractures in hip joint heads in 2001. Nowadays, aging is a well-known phenomeno, many times related to unsuitable processing conditions. In fact, the failure in 2001 was due to sintering in a tunnel furnace that led to open porosities [42]. The main factors involved in aging are the type and content of stabilizer, the residual stress and the grain size. Environmental conditions, especially humidity together with temperature, are also involved [43]. Y_2O_3 is the most widely used stabilizer in high-tech application of zirconia; because of charge balance reasons, the introduction of Y_2O_3 in the ZrO_2 lattice gives origin to oxygen vacancies which are one of the mechanisms proposed for the stabilization effect [44].

Regarding zirconia biocompatibility, most of the *in vitro* and *in vivo* studies report good response within the host tissues and less bacterial adhesion/colonization on the surfaces [37, 38, 45, 46].

1.3.6.2 Titanium as biomaterial

Titanium is one of the transition elements. This group of metals has significant characteristics including high strength and an allotropic behaviour. The atom of titanium has intermediate diameter and is relatively light when compared with other elements. This results in a metal of intermediate density. This relative low density combined with the high resistance makes this material very useful for engineering.

At room temperature, titanium has a compact hexagonal crystal structure or α-phase. Above 882 °C, this stage is transformed into the allotrope cubic body centered; variety that is called β-phase. This new phase is stable up to the melting temperature of 1670 °C. The transformation temperature of α→β phase is known as *beta transus*. The presence of alloying elements alters the transformation temperatures. Aluminum, which is present in many titanium alloys, carbon, nitrogen and oxygen, enter in solid solution raising the temperature at which the alpha→beta

phase transforms. By contrast, other elements like molybdenum, vanadium, tantalum and niobium promote the stability of the β-phase, decreasing the transformation temperature even at room temperature when the content is high enough.

Titanium microstructure shows variations in the morphological development of the α-phase and the β-phase. This depends on the chemistry and processing; temperature from which cooled and the rate of cooling. Fig 1.3-4 shows the typical titanium microstructures. As observed, not only coarse and fine acicular structures can be produced, also equiaxed structures [47].

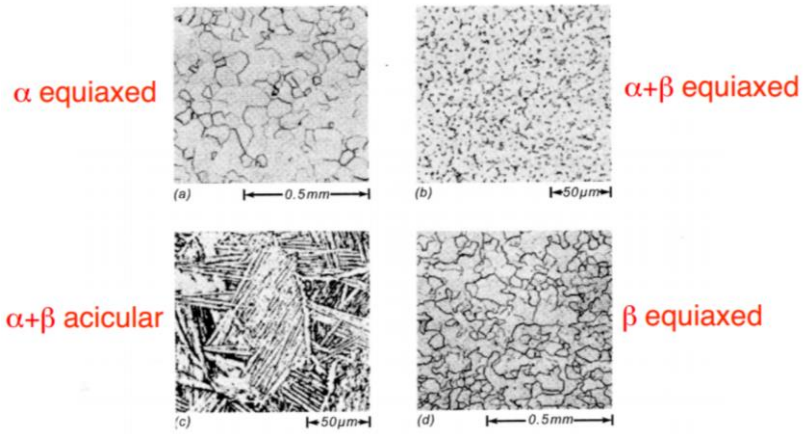

Fig 1.3-4. Typical microstructures of titanium from [47].

Titanium has been extensivaly used as biomaterial in bone surgery throughout recent decades particularly because of their good biocompatibility. This is maily attributed to two facts: the mechanical properties are better adapted at bone when compared with other metallic implant materials and the surface is always covered by a passive layer of titanium dioxide with few nanometeres of thickness, which reduces the material's corrosion and gives the bionert behaviour *in vivo*. However, titanium is also characterized by, especially in sliding situations, poor tribological properties, including high and unstable friction coefficients, severe adhesive wear, susceptibility to fretting wear, and a strong tendency to seize [48]. This may be related to the titanium electron configuration, crystal structure and lubrication characteristics and acts in every case accelerating the bone loss and implant loosening.

1.4 AN STRUCTURAL AND BIOLOGICAL FRAMEWORK

There is an overall tendency to classify the biomaterials into two wide groups: biomaterials for hard tissue replacements, typically represented by orthopaedic and dental materials, and biomaterials involved in soft tissue replacement, which are frequently associated with cardiovascular implants and general plastic surgery materials. As it was introduced in Section 1.2.3, this Ph. D. Thesis has its framework in the field of hard tissue replacement. Thereby, although studying materials from the structural point of view is important, we should not forget that the materials will be in a biological environment. Thus, to better understand this biological environment where the biomaterials are located, then the bone will be studied. This is the best example of material with dual structural and biological function.

Bone is involved in the protection, support and motion of the body. It is both highly stiff and elastic, supporting the mechanical action of soft tissues, as the contraction of muscles or expansion of lung. At the cellular level, bone is a production site for specialized tissues, such as bone marrow (the blood-forming system), and a mineral reservoir used by endocrine systems to regulate the calcium and phosphate homeostasis [49, 50].

1.4.1 BONE STRUCTURE

In overall, bone presents a basic dual structure: a smooth, continuous and dense (approximately 1.80 g/cm^3) external layer, or cortex, and the interior cancellous bone, with an average porosity of 75–95% and an average density of 0.2 g/cm^3. Cortical bone has tensile strength in the range of 78.8–151.0 MPa in longitudinal direction, and 51.0–56.0 MPa in transversal direction. Bone's elasticity is important in order to give the ability to the skeleton to withstand impacts; its modulus of elasticity is in the order of 17.0–20.0 GPa in longitudinal direction and of 6.0–13.0 GPa in the transversal direction. These remarkable mechanical properties are due to the microstructure of bone combining an organic matrix with apatite crystals, which are usually oriented in the longitudinal direction [51, 52].

By weight, bone mineral and dentin (inner part of the tooth) contains approximately 60% mineral (calcium phosphates), 10% water and about 30% organic matrix (90% type I collagen and 10% proteoglycans and non-collagenous proteins), while mature enamel is composed of more than 90% mineral and less than 10% organic matrix (mainly amelogenin). There are differences between the human

apatites as a consequence of their biological function. Thus, the collagen/nanohydroxiapatite composite structure of bone meets the mechanical requirements of the body. Furthermore, the high specific surface area and the numerous crystallographic vacancies are responsible of numerous ionic exchanges, acting as a calcium and phosphate reservoir for the entire body. Apatite content in enamel is higher and its crystalline structure is more cohesive and stable to resist to acid-etching and abrasion during mastication [20].

1.4.2 BONE AS A LIVING AND DYNAMIC SYSTEM

The previous section describes the bone as a purely structural material. However, the bone is also a living and dynamic system.

Skeletal tissues originate mostly from mesenchymal stem cells (MSCs) during embryonic development. In the adult stage, they can be isolated from bone marrow, adipose tissues, amniotic membrane or umbilical cord tissue. MSCs are multipotent cells with self-renewal capacity to repopulate the appropriate cell lineages (osteoblastic, myoblastic, adipogenic, chondrogenic, endothelial and neurogenic lineage). Regarding the osteogenic lineage, MSCs sustain a cascade of differentiation steps: MSCs → immature osteoprogenitor → mature osteoprogenitor → pre-osteoblast → mature osteoblast → osteocyte or lining cell. The later the differentiation stage, the lower the capacity for self-renewal and cell proliferation. Differentiating osteoprogenitor cells express several bone matrix proteins: alkaline phosphatase (ALP), collagen type I, bone sialoprotein (BSP), osteocalcin (OCN), osteopontin (OPN). Mature osteoblasts are non-migratory and can differ in properties depending on their development stage. Active osteoblasts have cuboidal shape and are rich in ALP activity, secrete collagen type I and glycoproteins (OCN, OPN), cytokines and growth factors into a region of unmineralized matrix (osteoid) between the cell body and the mineralized matrix. Osteocytes are mature osteoblasts that have become trapped within the bone matrix and are responsible for bone maintenance. Bone lining cells are placed along the bone surfaces that undergo neither de novo bone formation nor resorption, and inactive osteoblasts are elongated cells and undistinguishable morphologically from the bone lining cells.

On the other hand, osteoclasts are derived from hematopoietic stem cells (HSCs) that differentiate along the monocyte/macrophage lineage. Osteoclasts generate an acid medium, which acts dissolving to bone mineral. The demineralized extracellular bone matrix is enzymatically degraded.

In contrast with dental tissue, bone is a dynamic hard tissue that undergoes a remodelling process to maintain skeletal strength and integrity, with 10% of the skeleton being replaced annually. As shown in Fig 1.4-1 , bone is continuously under remodelation by a finely balanced, coupled and sequential process (indicated by the dashed arrows) implying that HSC-derived osteoclasts resorb bone (releasing growth factors and calcium) and MSC-derived osteoblasts replace the voids with new bone; process that depends on proliferation and differentiation of osteoblasts, coupled with production of type I collagen and its subsequent mineralization to form the calcified matrix of bone [53].

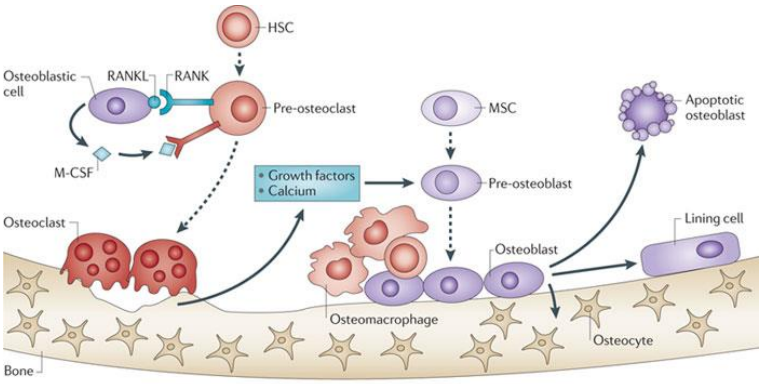

Fig 1.4-1. Bone remodeling [53].

When bone is injured cellular mechanisms are activated to reconstitute functional tissue. Fractures and defects can be self-repaired until a critical size; larger defects will require human interventions to completely restore the function [54].

1.5 BIOLOGICAL RESPONSE TO IMPLANTABLE MATERIALS

As aforementioned, the science of biomedical materials studies the composition and properties of biomaterials and the way that they interact with the environment where they are placed. Thus, the most important factor that distinguishes a biomaterial from any other material is its ability to exist in contact with human tissues without causing an unacceptable degree of harm.

There are very many different ways in which materials and tissues can interact; the search for biomaterials that provide the best performance has been based on understanding those interactions, which are discussed in the broad context of biocompatibility [55]. B*iocompatibility refers to the ability of a material to perform with an appropriate host response in a specific situation* [15]. This particular issue is studied for the newly-developed cermets in Chapter 4 of this Ph. D. Thesis.

As can be found in Experimental Techniques (Chapter 7, Section 7.5), the biocompatibility of the materials is studied from studies of osteoblastic adhesion, proliferation and differentiation. By studying these cellular phenomena, we will be able to establish differences in the osseoinduction capability associated with the variation in the nature of the investigated materials.

The biocompatibility of an artificial material in the body is an extremely complicated process that, as seen in Fig 1.5-1, involves several length scales [56]. Briefly, once the material interacts with the biological tissues, within a few milliseconds, a layer consisting of water and biomolecules from the physiological liquid covers the surface [56, 57]. Water molecules are the first ones that reach the surface (nanoseconds); their interaction and bonding with the substrates will take place differently depending on each surface's properties [58]. Then, the properties in the surface water-*shell* will influence the fundamental kinetic processes and the thermodynamics of the proteins and other biomolecules that will later arrive at the interface. For instance, it will determine that proteins denature or not, their orientation, coverage, etc., [58, 59]. Afterwards, bioproteins like cytokines and growth factors within the *biolayer* will stimulate the progenitor cells to migrate from the surrounding tissue to the material area [60].

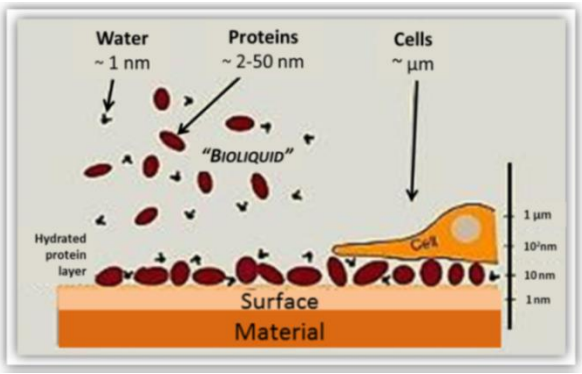

Fig 1.5-1. The diverse length scales that are involved in the biocompatibility of an inorganic device.

Once the cells get to the surface material, cellular phenomena like adhesion, proliferation, migration and differentiation may occur. These first interactions between cells and inorganic surfaces determine the quality in the tissue-device interface because they lead to transduction signals towards the nucleus that will induce cell adhesion followed by proliferation [61] and differentiation [62] if there are suitable conditions, or apoptosis [63] when adhesion is not facilitated.

As shown in Fig 1.5-2, the cell-surface contact starts with the specific cell recognition of serum proteins adsorbed at the material surface by means of receptor-like integrin [46, 64]. The integrins are transmembrane proteins that along with other intracellular proteins cluster into protein groups or *focal adhesions*, which physically connect the material surface with the nucleus through the cellular membrane by actin fibers constituting the cell's cytoskeleton. Fig 1.5-2 shows a detail of the structure of a plaque of focal adhesion, presenting the type of proteins involved in its formation.

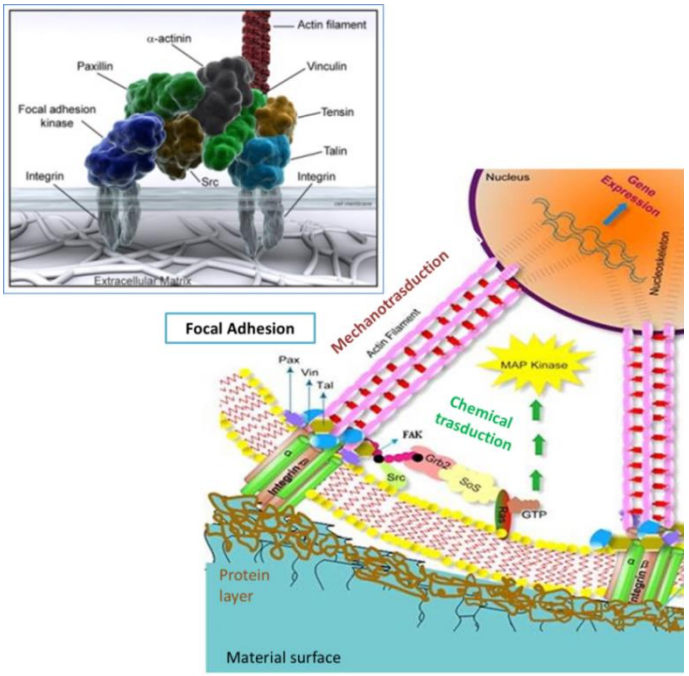

Fig 1.5-2. Diagram of cell adhesion at the material surface mediated by proteins, showing chemical and mechanotransduction events [65] (a focal adhesion is shown in detail).

As long as a suitable environment exists, cell attachment is accompanied by the rearrangement of cytoskeleton proteins, which triggers intracellular transduction pathways that ultimately promote cell proliferation and differentiation. As seen in Fig 1.5-2, mechanotransduction signals act directly at molecular level for regulating gene expression. In addition, indirect mechanisms involving biochemical signals are also transmitted to the nucleus to influence bone formation [65, 66]. Both mechanisms need adsorbed bioproteins on the surfaces in a physiological form, i.e. with the oligopeptidic ligands well-accessible to allow the cellular receptors cluster forming

focal adhesion plaques that can communicate with other focal adhesion proteins and with the actin cytoskeleton [59, 65].

Many times, in the presence of an implanted material, the normal process of wound healing begins to be prolonged and aberrant, triggering the foreign-body response (Fig 1.5-3). This response begins with adsorption of host proteins from biological fluids on the implant surface. Within hours, neutrophils infiltrate to the implant tissue site producing cytokines, chemokines, reactive oxygen species and other enzymes. During the next days, these products recruit undifferentiated monocytes and tissue-resident macrophages to the wound site. The phagocytic activities of macrophages are impeded by the inability to remove the foreign body so they respond producing a set of signaling molecules that attract fibroblasts, which produce matrix collagens. Besides, macrophages fuse with each other to form foreign-body giant cells (FBGCs) at the implant surface, whose role is poorly understood. With time, the dense collagenous fibrotic capsule isolates the implant physically and physiologically from the host tissue.

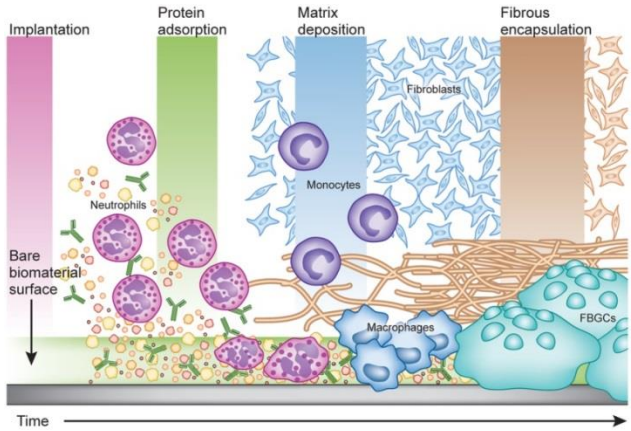

Fig 1.5-3. Stages involved in the foreign-body response [67].

To overcome the abovementioned foreign-body response different approaches have been followed. Among them, the effect of increasing surface roughness, alkaline or acid-etching, coating with calcium phosphates has been extensively tested both *in vitro* and in *vivo*. All these treatments are focused on the surface modification because this is the part in the implant material that interacts with the biological medium. Surface characteristics are specific for each type of material, so these properties would be assessed each time that a new material is developed.

Despite the large amount of work aimed at making materials more biocompatible, problems like severe immune responses or poor integration continue to seriously limit the performance of implantable biomedical devices and in many cases make revision surgery necessary. The functionalization of biomaterial surfaces with biological motifs, such as peptides, proteins or growth factors, which present a specific activity, has been currently opened as a promising avenue in the biomaterials field. In this research, Chapter 5 seeks to grant biofunctionality to the biomaterials through the stable immobilization of biological motifs that emulate nature. In fact, it is pretended to create organic/inorganic hybrid materials that mimic the biochemical composition of adhesion signals in the extracellular matrix. This innovative approach that has been successfully developed for metallic materials is now extended to cermets containing zirconia. The role of such bioinspired molecules is addressed to facilitate the integration of the implant within the local tissue. These biomolecules that elicit the appropriate cell adhesion and/or the differentiation will be covalently immobilized on the surface of the implant, because physically adsorbed or weakly attached molecules may be desorbed or displaced by other adsorbing proteins *in vivo* [68].

As can be extracted from this Introduction, ceramic/metal composites, consisting in a ceramic matrix (alumina or zirconia) and titanium as second phase has will be designed, manufactured and tested along this Ph. D. Thesis. Unlike the first-generation biomaterials, in which the use in engineering is extended to the medicine field, these materials will be purposely-designed to have a biological application as devices for hard tissue replacements. Thereby, their functionality will be assessed both mechanically and in terms of biological compatibility with osteoblastic cells. Furthermore, we will work to improve the osseointegration processes of the inorganic material by means of developing bioinspired surfaces that have covalently attached specific organic molecules, which may induce osteoinduction processes by acting at the molecular level.

1.6 REFERENCES

[1] Ratner BD, Bryant SJ. Biomaterials: where we have been and where we are going. Annu Rev Biomed Eng 2004;6:41-75.

[2] Ivanova EP, Bazaka K, Crawford RJ. New Functional Biomaterials for Medicine and Healthcare: Woodhead Publishing; 2014.

[3] Millennium WSGotBoMCatSotN. The Burden of Musculoskeletal Conditions at the Start of the New Millenium: Report of a WHO Scientific Group: Who; 2003.

[4] Bishop JA, Palanca AA, Bellino MJ, Lowenberg DW. Assessment of compromised fracture healing. Journal of the American Academy of Orthopaedic Surgeons 2012;20:273-82.

[5] Nasab MB, Hassan MR. Metallic Biomaterials of Knee and Hip-A Review. Trends in Biomaterials & Artificial Organs 2010;24:69-82.

[6] Brunski JB, Puleo DA, Nanci A. Biomaterials and biomechanics of oral and maxillofacial implants: current status and future developments. The International journal of oral & maxillofacial implants 2000;15:15-46.

[7] Bahraminasab M, Sahari BB, Edwards KL, Farahmand F, Arumugam M, Hong TS. Aseptic loosening of femoral components – A review of current and future trends in materials used. Materials & Design 2012;42:459-70.

[8] Darouiche RO. Treatment of Infections Associated with Surgical Implants. New England Journal of Medicine 2004;350:1422-9.

[9] Khan W, Muntimadugu E, Jaffe M, Domb A. Implantable Medical Devices. In: Domb AJ, Khan W, editors. Focal Controlled Drug Delivery: Springer US; 2014. p. 33-59.

[10] Chiara G, Letizia F, Lorenzo F, Edoardo S, Diego S, Stefano S, et al. Nanostructured biomaterials for tissue engineered bone tissue reconstruction. International Journal of Molecular Sciences 2012;13:737-57.

[11] George A, Ravindran S. Protein templates in hard tissue engineering. Nano Today 2010;5:254-66.

[12] Ratner B, Hoffman A, Schoen F, Lemons J. Biomaterials Science: An Evolving, Multidisciplinary Endeavor. Biomaterials Science: An Introduction to Materials in Medicine 2012;3.

[13] Ratner BD, Hoffman AS, Schoen FJ, Lemons J. Biomaterials science: a multidisciplinary endeavor. Biomaterials science: an introduction to materials in medicine 2004:1-9.

[14] Hunziker E, Spector M, Libera J, Gertzman A, Woo SL-Y, Ratcliffe A, et al. Translation from research to applications. Tissue engineering 2006;12:3341-64.

[15] Williams DF. Definitions in biomaterials: proceedings of a consensus conference of the European Society for Biomaterials, Chester, England, March 3-5, 1986: Elsevier Science Ltd; 1987.

[16] Williams DF. The Williams dictionary of biomaterials: Liverpool University Press; 1999.

[17] Williams DF. On the nature of biomaterials. Biomaterials 2009;30:5897-909.

[18] Rabkin E, Schoen FJ. Cardiovascular tissue engineering. Cardiovascular pathology 2002;11:305-17.

[19] Patel NR, Gohil PP. A Review on biomaterials: scope, applications & human anatomy significance. International Journal of Emerging Technology and Advanced Engineering 2012;2:91-101.

[20] Villani C, Calistri A. Material Implant. In: Albanese C, Faletti C, editors. Imaging of Prosthetic Joints: Springer Milan; 2014. p. 53-9.

[21] Behera A. Classification of Biomaterials used in Medicine. International Journal of Advances in Applied Sciences (IJAAS) 2012;1:31-5.

[22] Keegan G, Learmonth I, Case C. Orthopaedic metals and their potential toxicity in the arthroplasty patient A REVIEW OF CURRENT KNOWLEDGE AND FUTURE STRATEGIES. Journal of Bone & Joint Surgery, British Volume 2007;89:567-73.

[23] Sansone V, Pagani D, Melato M. The effects on bone cells of metal ions released from orthopaedic implants. A review. Clinical cases in mineral and bone metabolism 2013;10:34.

[24] Cancer IAfRo, Humans IWGotEoCRt. IARC monographs on the evaluation of carcinogenic risks to humans: International Agency for Research on Cancer; 2001.

[25] Chevalier J, Gremillard L. Ceramics for medical applications: A picture for the next 20 years. Journal of the European Ceramic Society 2009;29:1245-55.

[26] Rieger W. Ceramics in orthopedics–30 years of evolution and experience. World tribology forum in arthroplasty, C Rieker, S Oberholzer and U Wyss, eds Hans Huber Verlag, Bern, Suisse2001.

[27] Jones RM. Mechanics of composite materials: CRC Press; 1998.

[28] Strong AB. Fundamentals of composites manufacturing: materials, methods and applications: SMe; 2008.

[29] Chawla KK. Composite materials: science and engineering: Springer; 2012.

[30] Moya JS, Lopez-Esteban S, Pecharromán C. The challenge of ceramic/metal microcomposites and nanocomposites. Progress in Materials Science 2007;52:1017-90.

[31] Rodriguez-Suarez T, Bartolomé JF, Moya JS. Mechanical and tribological properties of ceramic/metal composites: A review of phenomena spanning from the

nanometer to the micrometer length scale. Journal of the European Ceramic Society 2012;32:3887-98.

[32] Pecharromán C, Esteban-Betegón F, Bartolomé JF, Richter G, Moya JS. Theoretical model of hardening in zirconia-nickel nanoparticle composites. Nano Letters 2004;4:747-51.

[33] Bartolomé JF, Gutiérrez-González CF, Pecharromán C, Moya JS. Synergistic toughening mechanism in 3Y-TZP/Nb composites. Acta Materialia 2007;55:5924-33.

[34] Pezzotti G, Yamamoto K. Artificial hip joints: The biomaterials challenge. Journal of the Mechanical Behavior of Biomedical Materials 2014;31:3-20.

[35] Garino JP. The reliability of modern alumina bearings in total hip arthroplasty—Update to a 2006 report. Seminars in Arthroplasty 2013;24:193-201.

[36] Basu B. Toughening of yttria-stabilised tetragonal zirconia ceramics. International Materials Reviews 2005;50:239-56.

[37] Manicone PF, Rossi Iommetti P, Raffaelli L. An overview of zirconia ceramics: Basic properties and clinical applications. Journal of Dentistry 2007;35:819-26.

[38] Hisbergues M, Vendeville S, Vendeville P. Review zirconia: Established facts and perspectives for a biomaterial in dental implantology. Journal of Biomedical Materials Research - Part B Applied Biomaterials 2009;88:519-29.

[39] Kohorst P, Borchers L, Strempel J, Stiesch M, Hassel T, Bach FW, et al. Low-temperature degradation of different zirconia ceramics for dental applications. Acta Biomaterialia 2012;8:1213-20.

[40] Mitov G, Gessner J, Lohbauer U, Woll K, Muecklich F, Pospiech P. Subcritical crack growth behavior and life data analysis of two types of dental Y-TZP ceramics. Dental Materials 2011;27:684-91.

[41] Chevalier J. What future for zirconia as a biomaterial? Biomaterials 2006;27:535-43.

[42] Sanon C, Chevalier J, Douillard T, Kohal RJ, Coelho PG, Hjerppe J, et al. Low temperature degradation and reliability of one-piece ceramic oral implants with a porous surface. Dental Materials 2013;29:389-97.

[43] Lughi V, Sergo V. Low temperature degradation -aging- of zirconia: A critical review of the relevant aspects in dentistry. Dental Materials 2010;26:807-20.

[44] Fabris S, Paxton AT, Finnis MW. A stabilization mechanism of zirconia based on oxygen vacancies only. Acta Materialia 2002;50:5171-8.

[45] Mai R, Kunert-Keil C, Grafe A, Gedrange T, Lauer G, Dominiak M, et al. Histological behaviour of zirconia implants: An experiment in rats. Annals of Anatomy - Anatomischer Anzeiger 2012;194:561-6.

[46] Salem NA, Taleb ALA, Aboushelib MN. Biomechanical and Histomorphometric Evaluation of Osseointegration of Fusion-Sputtered Zirconia Implants. Journal of Prosthodontics 2012:no-no.

[47] Donachie MJ. Titanium: a technical guide: ASM international; 2000.

[48] Dong H, Bell T. Enhanced wear resistance of titanium surfaces by a new thermal oxidation treatment. Wear 2000;238:131-7.

[49] Barrere F, Mahmood TA, De Groot K, Van Blitterswijk CA. Advanced biomaterials for skeletal tissue regeneration: Instructive and smart functions. Materials Science and Engineering: R: Reports 2008;59:38-71.

[50] Rogers K. Bone and Muscle: Structure, Force, and Motion: The Rosen Publishing Group; 2010.

[51] Weiner S, Wagner HD. The material bone: structure-mechanical function relations. Annual Review of Materials Science 1998;28:271-98.

[52] Yang Z, Jian W, Zhi-han L, Jun X, Liang Z, Ge Y, et al. The Geometry of the Bone Structure Associated with Total Hip Arthroplasty. PloS one 2014;9:e91058.

[53] Weilbaecher KN, Guise TA, McCauley LK. Cancer to bone: a fatal attraction. Nature Reviews Cancer 2011;11:411-25.

[54] Taylor D, Hazenberg JG, Lee TC. Living with cracks: damage and repair in human bone. Nature materials 2007;6:263-8.

[55] Williams DF. On the mechanisms of biocompatibility. Biomaterials 2008;29:2941-53.

[56] Hilborn J, Bjursten LM. A new and evolving paradigm for biocompatibility. Journal of tissue engineering and regenerative medicine 2007;1:110-9.

[57] Roach P, Eglin D, Rohde K, Perry CC. Modern biomaterials: a review—bulk properties and implications of surface modifications. Journal of Materials Science: Materials in Medicine 2007;18:1263-77.

[58] Richmond GL. Molecular Bonding and Interactions at Aqueous Surfaces as Probed by Vibrational Sum Frequency Spectroscopy. Chemical Reviews 2002;102:2693-724.

[59] Bacakova L, Filova E, Parizek M, Ruml T, Svorcik V. Modulation of cell adhesion, proliferation and differentiation on materials designed for body implants. Biotechnology Advances 2011;29:739-67.

[60] Lodish H. Molecular cell biology: Macmillan; 2008.

[61] Biggs M, Dalby M. Focal adhesions in osteoneogenesis. Proceedings of the Institution of Mechanical Engineers, Part H: Journal of Engineering in Medicine 2010;224:1441-53.

[62] Kalajzic I, Staal A, Yang WP, Wu Y, Johnson SE, Feyen JHM, et al. Expression profile of osteoblast lineage at defined stages of differentiation. Journal of Biological Chemistry 2005;280:24618-26.

[63] Wen L-P, Fahrni JA, Troie S, Guan J-L, Orth K, Rosen GD. Cleavage of focal adhesion kinase by caspases during apoptosis. Journal of Biological Chemistry 1997;272:26056-61.

[64] Planell JA, Navarro M, Altankov G, Aparicio C, Engel E, Gil J, et al. Materials surface effects on biological interactions.

. In: Advances in Regenerative Medicine: Role of Nanotechnology aEP, editor. NATO Science for Peace and Security Series A: Chemistry and Biology: Springer Verlag; 2010. p. 233-52.

[65] Divya Rani VV, Vinoth-Kumar L, Anitha VC, Manzoor K, Deepthy M, Shantikumar VN. Osteointegration of titanium implant is sensitive to specific nanostructure morphology. Acta Biomaterialia 2012;8:1976-89.

[66] Anselme K, Ponche A, Bigerelle M. Relative influence of surface topography and surface chemistry on cell response to bone implant materials. Part 2: Biological aspects. Proceedings of the Institution of Mechanical Engineers, Part H: Journal of Engineering in Medicine 2010;224:1487-507.

[67] Grainger DW. All charged up about implanted biomaterials. Nat Biotech 2013;31:1087-0156.

[68] Bilek MMM. Biofunctionalization of surfaces by energetic ion implantation: Review of progress on applications in implantable biomedical devices and antibody microarrays. Applied Surface Science.

Chapter 2

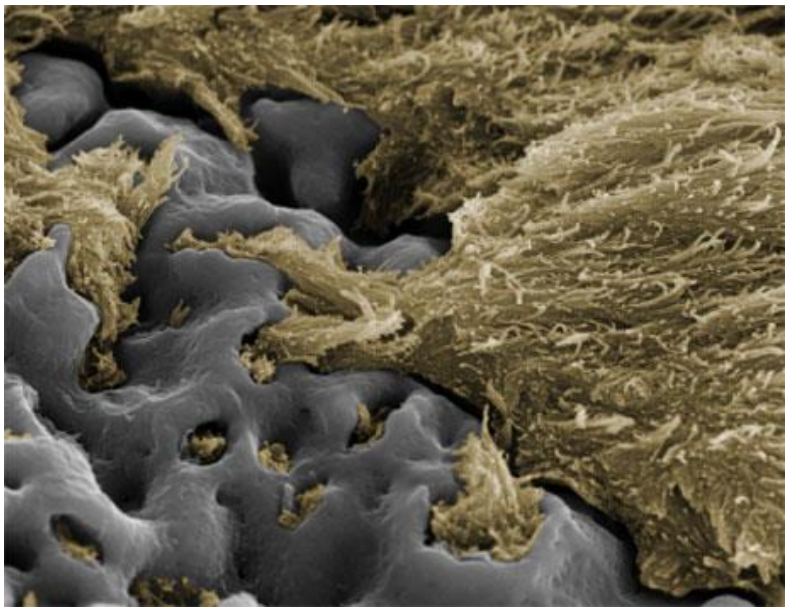

OBJETIVOS Y PLANTEAMIENTO DE TRABAJO

Design and evaluation of ceramic/metal composites for biomedical purposes

2.1 OBJETIVOS

El objetivo principal de esta tesis doctoral es crear una **nueva generación de biomateriales multifuncionales** con una combinación de propiedades que permitan solventar parte de la problemática que, a día de hoy, existe en el campo de la implantología estructural.

Dicha **multifuncionalidad** requiere la asociación de un conjunto de propiedades físicas (baja densidad, baja susceptibilidad magnética, conductividad etc.), mecánicas (tolerancia a los defectos, adecuada dureza, alta resistencia mecánica y tenacidad, etc.), químicas (estabilidad química, resistencia a la corrosión y a la degradación por desgaste) y biológicas (biocompatibilidad y capacidad de osteointegración).

Los materiales tradicionalmente utilizados en la fabricación de dispositivos implantables como son la alúmina, circona y el titanio presentan parte de esas propiedades, las cuales pueden ser combinadas **sinérgicamente** mediante el desarrollo de materiales compuestos cerámica/metal (cermets).

Para ello, se requiere:

- **Optimizar las técnicas de procesamiento y sinterización** con el fin de conseguir nuevos materiales compuestos de alúmina/titanio y circona/titanio.
- **Controlar la reactividad** entre los componentes de los cermets cerámica/titanio, para así obtener una mejora de las **propiedades mecánicas** y de sus **características microestructurales.**
- **Analizar las interacciones** que se establecen entre los materiales inorgánicos y el entorno biológico, teniendo en cuenta la influencia de las distintas **propiedades superficiales** en el comportamiento celular y, por lo tanto, en su **biocompatibilidad**.
- **Conferir actividad biológica** a los biomateriales mediante la inmovilización química de moléculas orgánicas en la superficies. En concreto, se trabajará con biopéptidos que actúen a nivel molecular promoviendo la osteointegración.

2.2 PLANTEAMIENTO DEL TRABAJO

Para alcanzar los objetivos anteriormente mencionandos se ha planteado la siguiente metodología de trabajo:

- Selección de composiciones para los compuestos cerámica/metal (cermets).
- Ajuste de los parámetros de procesamiento y sinterización en función de los requerimientos de cada sistema.
- Caracterización de la integridad y fiabilidad mecánica mediante ensayos de flexión e indentanción para determinar la resistencia mecánica, tenacidad, dureza, tolerancia a los defectos, etc.
- Caracterización físico-química de la superficie inicial.
    - Determinación de la rugosidad superficial mediante mediciones sobre el perfil 2D y 3D.
    - Análisis de la composición química superficial por espectroscopía de fotoelectrones emitidos por rayos X (XPS).
    - Evaluación de la mojabilidad mediante la técnica de la gota sésil a partir de un goniómetro y líquidos de referencia estándar.
- Realización de ensayos de citotoxicidad/viabilidad celular seguiendo indicaciones de normas internacional.
- Evaluación del efecto de las propiedades superficiales del biomaterial en la respuesta de osteoblastos.
    - Estudio de la adhesión celular mediante el estudio de la morfología osteoblástica, la observación de la disposición del citoesqueleto de actina y la formación de placas de adhesión focal, así como mediante la cuantificación del número de células a tiempos cortos..
    - Estudio de la proliferación celular mediante la cuantificación de enzimas citoplasmáticos, como la lactato deshidrogenasa (LDH).
    - Analisis de la capacidad de osteointegración inducida por los diferentes materiales a través de la quantificación de marcadores específicos de diferenciación, como es la fosfatasa alcalina (ALP).
- Adsorción química superficial de proteínas promotoras de la osteointegración en materiales de fase cerámica usando una molécula linker adecuada a la química del sustrato.

Chapter 3

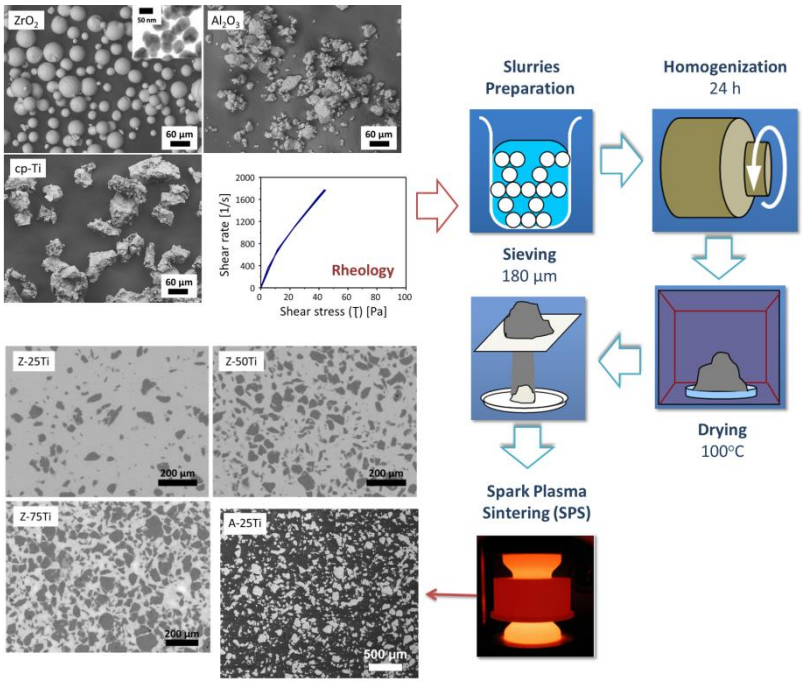

CERAMIC/TITANIUM SYSTEMS: PROCESSING AND CHARACTERIZATION

Design and evaluation of ceramic/metal composites for biomedical purposes

3.1 INTRODUCTION

As it has previously been explained in Chapter 1 (Section 1.3), the combination of dissimilar materials to form composites can lead to superior properties than the pure counterparts [1]. One of the most successful examples of composites is the group of ceramic/metal (cermet), which favorably combines the different properties of ceramic (as matrix) and metal (as the second phase) components in one material, opening up a whole world of emerging applications. In this framework, ceramic/metal nanocomposites with biocidal properties have been developed for bone-related applications [2]. C. Pecharroman et al. [3] have achieved ZrO_2/Ni composites with a notably increased hardness properties. F. Bartolome et al. [4] have performed ZrO_2/Nb composites synergistically toughened due to anticipated interactions between crack bridging and stress-induced phase transformation. In addition, C.F. Gutierrez-Gonzalez et al. [5] have demonstrated an optimal combination of *aging-free* and crack growth resistance in 3Y-TZP/Nb composites, with hardness properties never attained before, and also with a fatigue behavior similar to that in monolithic zirconia [6].

With the goal in mind of favorably combining the mechanical properties of ceramic (alumina or zirconia) and metal (titanium) counterparts, a new type of system with titanium as metallic phase (ceramic/titanium) is developed. Titanium is selected because of being one of the most used material for bone replacements due to its superior mechanical properties, especially high toughness and strength [7], its corrosion resistance and its outstanding biocompatibility and osseointegration capability [8, 9]. Regarding the ceramic matrix, alumina and zirconia are selected by being two oxide ceramics extensively used in prosthetic devices because of their high wear resistance and outstanding strength and hardness [10, 11]. Considering the type of ceramic that forms the matrix in the new ceramic/titanium system, two independent subsystems, alumina/titanium and zirconia/titanium, are designed and evaluated along this and the subsequent chapters in the Ph. D. Thesis. In particular, this chapter aims to approach the processing, conformation and mechanical characterization of alumina/titanium and zirconia/titanium subsystems.

In overall, processing cermets is more complex than processing monolithic materials. The mixture of powders of different nature may lead to the formation of aggregates in any phase. Furthermore, because of the differences in densities and particle sizes, the ceramic and metal particles in suspension could segregate, producing heterogeneous microstructures. Among the different preparation processes of ceramic-metal composites that can be found in the literature [12-14], a

wet processing route of powders has been selected. The experience of controlling the solid contend, the type of organic deflocculant as well as the liquid medium to obtain non-segregated ceramic-metal suspensions have been acquired in the group in previous works [15-17]. Nevertheless, the particular rheological behavior of each ceramic/titanium suspension must be studied in order to find the adequate parameters that provide the steric and electrostatic stabilization to perform homogeneous sintered blanks. Moreover, an exhaustive analysis of the raw materials before the rheological study is mandatory.

As sintering technique, spark plasma sintering (SPS) has been used because of the benefits that it presents when is compared to conventional technologies. Due to its elevated heating rates, high relative densities can be reached in very short time and nano-sized powders can be sintered without considerable grain growth. SPS consolidation is therefore a way of *freezing* nanostructured features of the starting powders in the final material microstructures [18]. Moreover, because SPS combines temperature and pressure, sintering times can be enormously reduced compared with the conventional techniques and the reactivity between the phases in the composites may also be controlled. This is particularly interesting in the case of titanium that have a strong reductor activity, which constitutes a significant handicap when one wants to combine it with other materials, especially ceramic oxides.

During recent years, a wide variety of materials, e.g., ceramics, composites, cermets, metals and alloys, have been successfully compacted by the SPS process [19, 20]. However, there are not too many references in the literature regarding SPSed Al_2O_3/Ti cermets [21, 22] and relative references to SPSed ZrO_2/Ti cermets have not been found. This fact promotes the interest in addressing their study.

In order to reach full densification, reactivity reduction and avoid grain growth, SPS parameters need to be adjusted in particular for each new system [20, 23, 24]. An additional item to consider when working with SPS, is the gradient of temperature that would be creating in non-conductive samples like ceramic ones. In this sense, by adding a content of metallic particles above 20% in the cermets, the conductivity would be increased substantially and the heterogeneity in temperature would be reduced [25]. That content in particles of metal is established according to the percolation theory, which marks the threshold from which an interconnected network of dispersed-phase is created within the ceramic matrix Moreover, this also confer conductivity properties, allowing to obtain electro-machinable cermets that avoid the important problem of machinability of ceramic materials.

After performing dense ceramic/titanium materials including either zirconia (75 vol. %, 50 vol. % and 25 vol. %) or alumina (75 vol. %) as ceramic phase, diverse microstructural and mechanical analyses will be performed to corroborate an uniform distribution of phases in the microstructure that ensures the appropriate mechanical behavior. This characterization includes X-ray diffraction (XRD), scanning electron microscopy (SEM) and energy-dispersive X-ray Spectroscopy (EDS) as well as tests for assessing the mechanical properties such as bending strength, fracture toughness, microhardness, damage tolerance and R-curve behavior.

3.2 OBJECTIVES

The overall goal in this chapter is to develope mechanically suitable ceramic/titanium composites using zirconia or alumina as ceramic matrix phase.

In order to achieve this main objective, it has been established the following specific purposes:

- Characterizing the titanium, zirconia and alumina raw powders from a physical-chemical standpoint.
- Studying the two new zirconia/titanium and alumina/titanium particulate suspensions in order to adjust the rheological parameters and thus avoiding the segregation of the components.
- Processing solid compacts with homogeneous microstructure by means of Spark Plasma Sintering (SPS) technology.
- Evaluating the mechanical response of this novel generation of ceramic/titanium materials.

3.3 RAW MATERIALS

The following commercially available powders were used as raw materials:

(1) High-purity α-alumina (99.99%) (Al_2O_3; TM-DAR, Taimei Chemicals Co., Ltd., Japan) with ultra-fine and agglomerate-free powders, which can densify near the theoretical density value at <1300 ˚C. The sintered bodies have fine and homogeneous microstructure, and shows good performance in many properties as strength, hardness, wear resistance, corrosion resistance, etc. [28].

(2) Partially-stabilized zirconia powder with 3 mol% yttria (ZrO_2; TZ-3Y-E, Tosoh Corp., Japan). With this type of zirconia, mostly used for biomedical applications, superior mechanical properties and higher aging resistance can be achieved at a lower sintering temperature. Hence, the sintered bodies obtained from TZ-3Y-E powders show a fine crystal grain structure that results in a great improvement in strength, fracture toughness, wear resistance and aging [27].

(3) Regarding the metallic phase, a commercially-pure-titanium powder (Ti, 99.5% purity) provided by Goodfellow (U.K) is employed because it guarantees a biomedical grade.

3.3.1 CHEMICAL COMPOSITION

Data about chemical composition of raw materials were collected from the manufacturer's analysis [27-29] and summarized in Table 3.3-1, Table 3.3-2 and Table 3.3-3. UNE-EN ISO 5832-2:2012 [30] and ASTM F67-00 [31] standards determine four different grades of commercially pure titanium (Cp-Ti) that could be used in biomedical applications. These grades are established as a function of the amount of minority interstitial elements in titanium (Table 3.3-4). As the grades increase from I to IV, the titanium strength also increases while its ductility and corrosion resistance decrease. Considering these characteristics, the type of titanium used in this work would fit with cp-Ti grade I; the one with the highest strength and the lowest ductility and corrosion resistance.

Table 3.3-1: *Chemical composition of alumina raw material (Al_2O_3).*

High-purity α-alumina (TM-DAR) (Taimei Chemicals Co, Ltd., Japan)										
COMPOSITION (ppm)										
Si	Fe	Na	K	Ca	Mg	Cu	Cr	Mn	U	Th
10	8	8	3	3	2	1	<1	<1	<0.004	0.005

Table 3.3-2: *Chemical composition of 3Y-TZP raw material (ZrO_2).*

Partially-stabilized ZrO_2 powder with uniform dispersion of 3 mol % Y_2O_3 (TZ-3Y-E) (Tosoh Corp., Japan)					
COMPOSITION (% Weight)					
ZrO_2	Y_2O_3	Al_2O_3	SiO_2	Na_2O	Fe_2O_3
95.00	4.98	0.005	0.002	0.003	0.004

Table 3.3-3: *Impurities in commercially pure titanium (Ti).*

Titanium with purity 99.5% (Goodfellow, UK)				
IMPURITIES (ppm)				
Chlorides	Fe	N	O	C
1700	200	100	100	< 100

Table 3.3-4: *ASTM indications for bars of c.p-Ti for biomedical applications.*

BIOMEDICAL GRADE TITANIUM	CHEMICAL COMPOSITION (Wt. %)					
	IMPURITIES					
Cp-Ti	N_{max}	C_{max}	H_{max}	Fe_{max}	O_{max}	Ti
I	0.03	0.01	0.0125	0.20	0.18	Balance
II	0.03	0.01	0.0125	0.30	0.25	Balance
III	0.05	0.01	0.0125	0.30	0.35	Balance
IV	0.05	0.01	0.0125	0.50	0.40	Balance

3.3.2 PARTICLE SIZE DISTRIBUTION

It can be observed in Table 3.3-5 that the raw powders involved in this work present very different average particle size. Whilst alumina and zirconia ceramics are in the nanometric range, titanium has micrometric size. This allows to process micro-nano ceramic/Ti powders which, once sintered, will lead to dense micro-nano-structured composites.

Table 3.3-5: *Average particle size of raw powders.*

MATERIAL	AVERAGE PARTICLE SIZE, d_{50} (μm)
Al_2O	0.1
ZrO_2	<0.2
Ti	150

3.3.3 X-RAY DIFFRACTION (XRD)

Diffractograms obtained by analyzing ZrO_2, Al_2O_3 and Ti powders are shown in Fig 3.3-1. According with the information provided by *the International Center of Diffraction Data (ICDD)*, the position and intensity of the peaks found in the tested materials corresponded with the characteristic peaks of zirconia (monoclinic, 24-1165, and tetragonal, 83-0113), alumina (hexagonal, 11-0661) and titanium (hexagonal, 44-1294), respectively.

3.3.4 SCANNING ELECTRON MICROSCOPY (SEM)

The morphology of all raw powders was studied by scanning electron microscopy at 15 eV and x300 magnification. On the left, Fig 3.3-2 shows the typical aggregates of spray-dried zirconia, with their spherical morphology and average size between 20-60 μm. Moreover, aggregates of alumina powder had irregular shape and variable particle sizes. Each one of the alumina and zirconia aggregates is formed by a set of nanoparticles that need to be dispersed during the processing. Details of nanoparticles forming the aggregates acquired by transmission electron microscopy (TEM) are also presented in Fig 3.3-2 (on the right). The metallic powder is constituted by large Ti particles with irregular morphology and sharp edges.

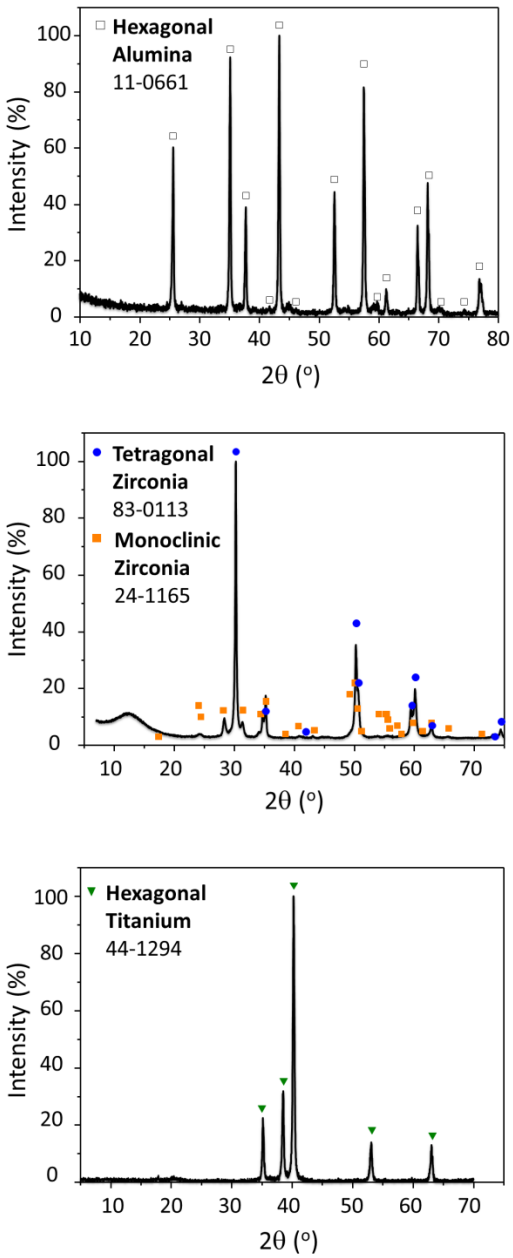

Fig 3.3-1. XRD patterns obtained from ZrO_2, Al_2O_3 and Ti powders.

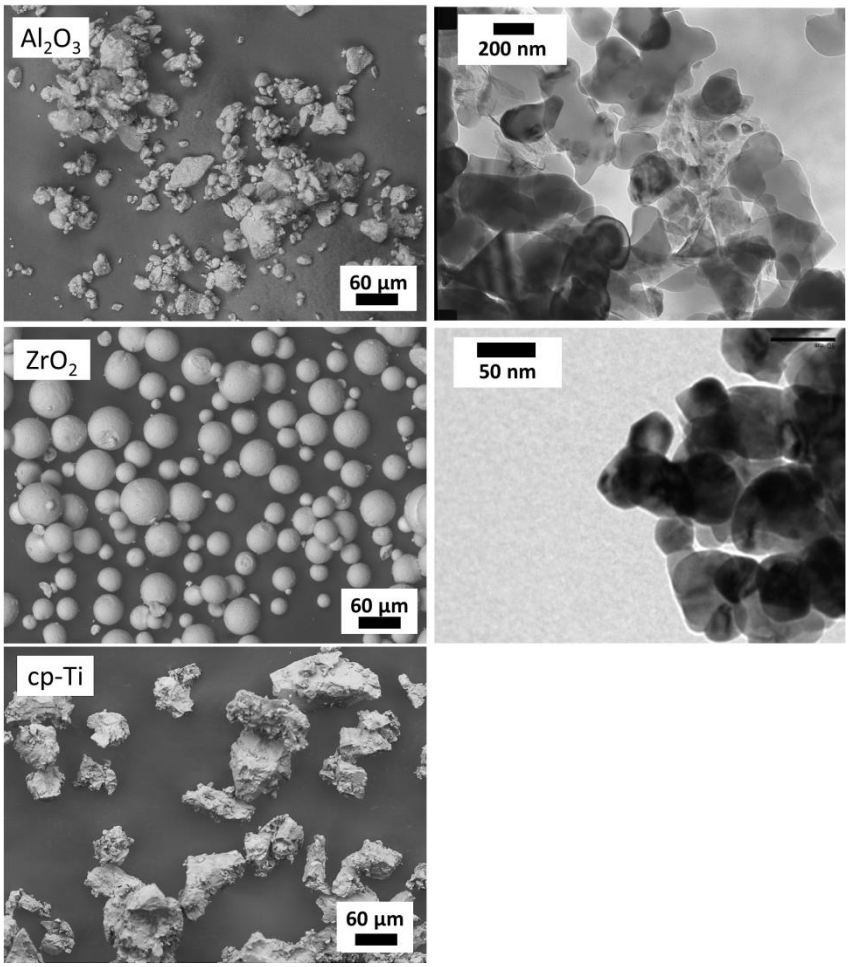

Fig 3.3-2. On the left: SEM-micrographs acquired from raw powders of Al_2O_3, spray-dried ZrO_2, and cp-Ti. On the right: TEM images disclosing details of Al_2O_3 and ZrO_2 nano-powders.

3.4 ALUMINA/TITANIUM SYSTEM

Alumina/titanium composites have been extensively studied in the last years, giving rise to the numerous works found in the literature. Some of them are focused on the characterization of the interfaces between the two components [32-34]. Other works are dedicated to the evaluation of the mechanical properties [21, 35, 36], although none of them evaluate the R-curve behavior. The most common techniques used to achieve a suitable conformation and densification of these composites are metal infiltration [37, 38], reactive metal penetration [39, 40], hot pressing [41, 42] or thermal spray processing [43]. Despite the benefits that Spark Plasma Sintering (SPS) could introduce compared with other methods of consolidation, SPS has got a very limited use as sintering technique in this kind of composites [21, 22].

On the other hand, a well-known problem of alumina is its inherent low toughness and absence of plastic deformation. Diverse methods have been investigated to overcome this drawback, and one of the most successful procedures involves the incorporation of toughening dispersed particles into the ceramic matrix in order to fabricate a composite material [1, 44-46]. When incorporating metallic particles, the composite is armored with extrinsic reinforcement mechanisms, such as crack bridging or crack deflection, that may lead to an increase of the fracture resistance with crack extension (R-curve)[47, 48]. The metallic particles interact with the crack to slow down its propagation because they act as ligaments between the crack faces, providing resistance to further crack opening or propagation. Such increase in fracture resistance provides damage tolerance characteristics to composite materials and narrows their strength distributions.

In this context, we aim to develop dense and homogeneous alumina/titanium composites by a wet-processing route and subsequent Spark Plasma Sintering, and evaluate their mechanical properties mainly in terms of the R-curve behavior and damage tolerance. The relative proportion of Ti used to prepare this new type of cermet was 25 vol. % (A-25Ti). This Ti ratio is selected in order to be over the percolation threshold, thus forming a network of metallic particles homogeneously dispersed throughout the alumina matrix that act improving the mechanical and electrical features. In addition, the influence of the titanium content in the consolidation of alumina/titanium cermets have been previously investigated, suggesting an appropriate continuity of metal across the interface with values among 10 <Ti< 25 (Ti wt. %) [36].

3.4.1 SEDIMENTATION AND RHEOLOGY STUDIES

Four different suspensions were prepared to study the influence of the processing parameters on the stability of the A-25Ti mixture of powder in order to find the processing conditions that may lead to homogeneous microstructures. The rheological behaviour of A-25Ti suspensions was studied as collected in Experimental Techniques (Chapter 7, Section 7.2.1). Table 3.4-1 summarizes the characteristics in the suspensions and the results obtained from this study.

Table 3.4-1: *Rheological behaviour of A-Ti (25 vol. %Ti) suspensions.*

SUSPENSION	SOLIDS (Wt. %)	DOLAPIX (Wt. %)	τ_0 (Pa)	dv/dx_{max} (s^{-1})	η (mPa·s)
A	70	1	< 1	1873	24
B	70	3	6	1594	31
C	80	1	< 1	1051	48
D	80	3	22	188	265

Although apparently there is no large difference between the density of the particles for Ti and Al_2O_3 (4.5 g·cm^{-3} and 3.9 g·cm^{-3}, respectively), in suspensions A and C the metallic particles settle. This behavior is probably due to the difference between grain sizes (0.1 and 150 µm for Al_2O_3 and Ti, respectively) that facilitates the sedimentation of Ti, but also by the low deflocculant amount that impedes the stabilization of these large particles. When the amount of deflocculant is raised up to 3 wt. %, no segregation is observed (slurries B and D) so this amount is enough to stabilize the particles in the suspensions. In addition, Fig 3.4-1 shows the flow curves of the four slurries prepared. As observed, suspensions A and C display a pseudoplastic behavior; the low amount of surfactant prevents the dispersion of the aggregates leading to the sedimentation of the larger particles. In slurry A, the solid content is lower than in C so the interaction between particles is also lower. This fact explains the observation of a faster sedimentation of the bigger particles in slurry A. Moreover, slurry B presents a slightly plastic behavior. In this case, the deflocculant content promotes the dispersion of the particles creating a net attractive interparticle force that gives rise to the formation of a three-dimensional network of particles. The formation of this network prevents the sedimentation of the particles and would facilitate homogeneously dispersed microstructures in the final materials.

One of the methods to quantify the strength of this network force is measuring yield stress (τ_0). As known, the higher yield stress, the stronger particle interaction and the higher strength of the particle network. In slurry B, τ_0 is approximately 6 Pa, which is a low value close to the pseudoplastic behaviour. No sedimentation is also observed but the formation of a supernatant shows a tendency

to eliminate water in order to increase the solid content and form a stable structure between particles and liquid media. This situation does not occur in slurry D, where the higher solid and deflocculant content led to the formation of a stable structure with a higher yield stress (22 Pa) that prevents sedimentation and the formation of a supernatant. Therefore, slurry D presents the rheological settings that would lead to Al_2O_3/Ti (25 vol. %Ti) homogenous mixtures.

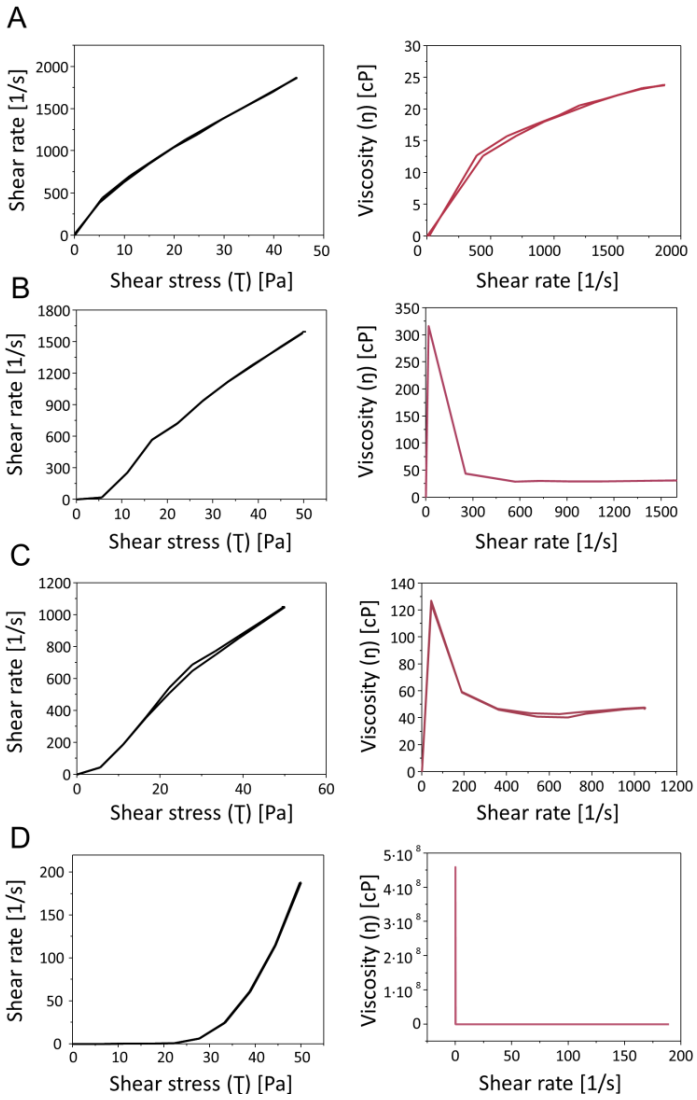

Fig 3.4-1. Flow curves for the different prepared A-25Ti suspensions.

3.4.2 A-25Ti POWDERS

3.4.2.1 Processing

From the positive results of the rheology and sedimentation tests exposed in the Section 3.4.1, stable A-25Ti suspensions were performed with an 80 wt. % of solids and 3 wt. % of Dolapix CE-64. In order to process the new mixture of Al_2O_3/Ti powders (A-25Ti), the general processing methodology exposed above in Fig 3.4-2 was followed. Firstly, slurries were prepared from the required quantities of Al_2O_3 and Ti powders. Then the mixtures of powder were milled with alumina balls in polyethylene containers at 150 rpm for 24 hours. The resulting powders were dried at 90 °C for 24 hours and sieved throughout 180 microns.

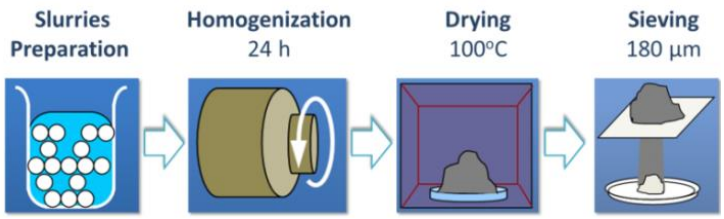

Fig 3.4-2. General scheme of processing ceramic/Ti composites.

The resulting A-25Ti powders were characterized by scanning microscopy, Energy-Dispersive X-Ray Spectroscopy and X-ray diffraction as explained below.

3.4.2.2 X-ray diffraction (XRD)

An X-ray diffractogram of the A-25Ti powders was obtained as explained in Experimental Techniques (Chapter 7, Section 7.2.3). The XRD pattern is presented in Fig 3.4-3. As expected, the found phases fitted with the crystallographic forms of hexagonal alumina and titanium, indicating the non-existence of further compounds as a result of external contamination or reaction during the wet processing.

3.4.2.3 Scanning electron microscopy (SEM)

Fig 3.4-4 presents a micrograph of A-Ti starting powders, which was acquired by SEM at 15 eV and a 600x magnification. In addition, a complementary chemical analysis by Energy-Dispersive X-Ray Spectroscopy (EDS) was performed to indentify Al_2O_3 and Ti phases. As it can be observed, nanometric alumina is disposed covering the big Ti particles in a ratio expected from the quantities used in the slurry preparation.

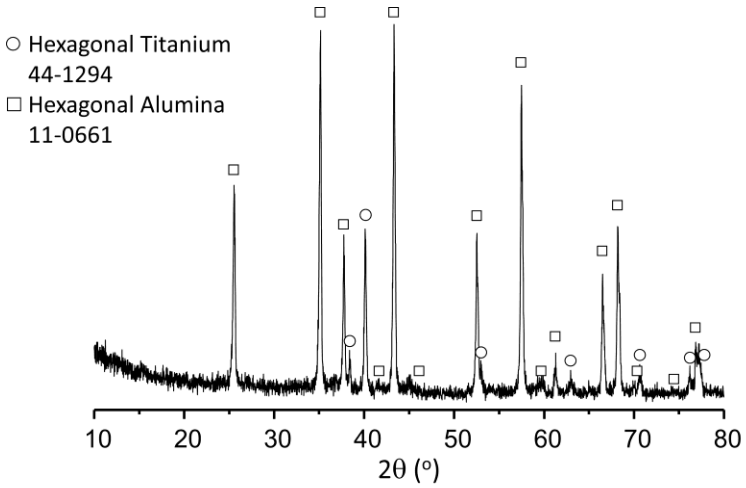

Fig 3.4-3. XRD pattern presented by A-25Ti starting powders (y-axis: arbitrary units of intensity).

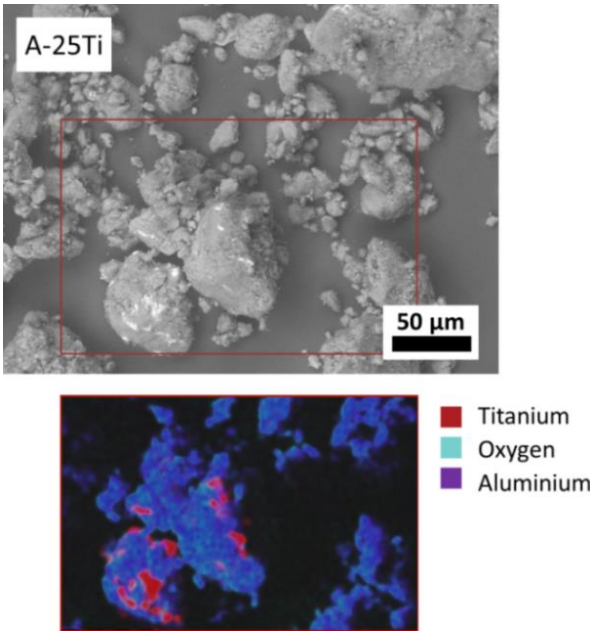

Fig 3.4-4. SEM image acquired from A-25Ti powders along with the EDS analysis.

3.4.3 DENSE COMPOSITES: CONSOLIDATION AND CHARACTERIZATION

3.4.3.1 Spark plasma sintering (SPS)

During sintering, the SPS equipment monitors diverse parameters. Among them, the relative movement of the piston (AV Speed) is particularly useful because provides information that is equivalent to that obtained through a dilatometer test. Fig 3.4-5 represents this relative movement of the piston along a SPS cycle of A-25Ti specimens, showing that the sintering process starts at around 1100°C and ends near 1200 °C. Therefore, using a sintering temperature of 1250°C, the densification of the compacts will be guaranteed.

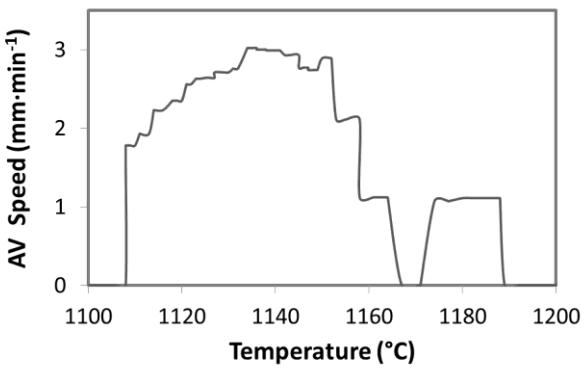

Fig 3.4-5. Relative movement of the piston (AV speed) in the SPS-cycle of A-25Ti cermets.

In addition, Table 3.4-2 summarizes the settings used for sintering for A-Ti powders in order to obtain dense specimens.

Table 3.4-2: *Spark Plasma Sintering (SPS) settings.*

SYSTEM		A-25TI
Composition (Vol. %)		75% Al_2O_3; 25% Ti
SETTING	Heating rate	100 °C/min
	Atmosphere	Vacuum
	Temperature	1250 °C
	Time	3 min
	Pressure	80 MPa
	Cooling rate	Free

3.4.3.2 Density

Bulk densities were measured as explained in Section 7.3.1 of Experimental Techniques and summarized in Table 3.4-3. The relative density of the sintered Al_2O_3/Ti composites was very close to the theoretical value, which was calculated according to the rule of mixtures, and also to the value of real density measured by helium pycnometry. Therefore, full densification was achieved after the sintering process designed in Section 3.4.3.1 for the A-25Ti system.

Table 3.4-3: *Densities of Al_2O_3 and Al_2O_3/Ti compacts.*

SYSTEM	MEASURED DENSITY ($g \cdot cm^{-3}$)	THEORETICAL DENSITY ($g \cdot cm^{-3}$)	REAL DENSITY ($g \cdot cm^{-3}$)	RATIO MEASURED-THEORETICAL DENSITY (%)
Al_2O_3	3.9 ± 0.1	3.9	3.9	>99
A-25Ti	4.1 ± 0.1	4.1	4.1	

3.4.3.3 X-ray Diffraction (XRD)

The A-25Ti fired specimens polished down to 1-µm were also analyzed by XRD as explained in Chapter 7, Section 7.2.3. The XRD-pattern of the sintered sample is shown in Fig 3.4-6. As it can be observed, Al_2O_3 and Ti are found as main phases. However, there is an evidence of the formation of a new product that is identified as Ti_3Al. The formation of this intermetallic product has already been reported in other works. These explain the facility of Ti for reducing Al_2O_3, precipitating Ti_3Al in the interface at temperatures ranging from 900 to 1700 °C [49-51].

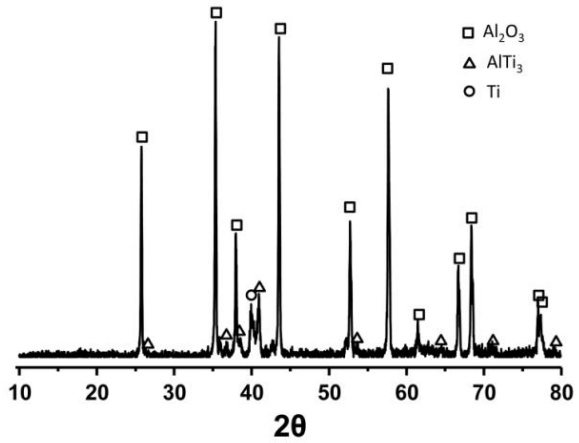

Fig 3.4-6. Representative diffractogram acquired from a A-25Ti fired sample (y-axis: intensity units).

3.4.3.4 Microstructure

Fig 3.4-7 presents the microstructure of the fired A-25Ti composites, which were processed and sintered as settings in Section 3.4.2.1 and Section 3.4.3.1, respectively. The darker phase is Al_3O_2 and the brighter one corresponds to Ti grains. The metallic particles are homogeneously dispersed throughout the ceramic matrix. Accordingly to the values of measured density (Fig 3.4-7), apparent porosity is not observed.

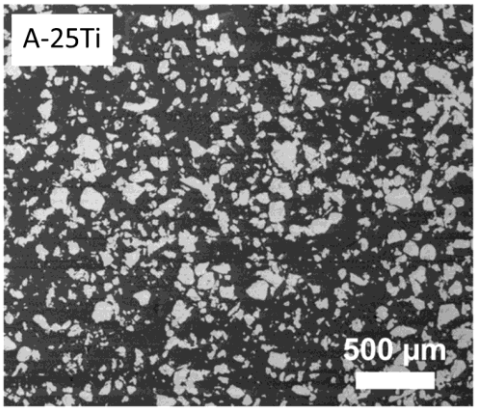

Fig 3.4-7. SEM image of an Al_2O_3-Ti (25 vol. % Ti) cermet.

In addition, the microstructure of pure Al_2O_3 was analyzed by FE-SEM on 1µm polished surfaces (Fig 3.4-8) after thermal etching at 1100°C in air atmosphere. The grain size calculated by the *Mean Lineal Intercept Method* [64, 65] was 735 ± 74 nm.

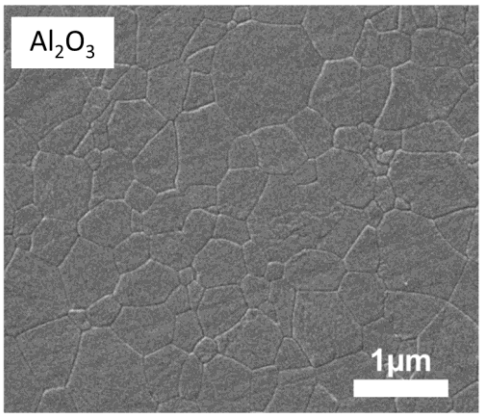

Fig 3.4-8. FE-SEM micrograph of alumina thermally etched.

It would be expected that alumina matrix in the composite has an equivalent microstructure of that disclosed in Fig 3.4-8 for pure alumina. Since cermets cannot be thermally etched, details on their microstructural characteristics will be analyzed in a subsequent analysis at higher magnification by means of fracture surfaces.

3.4.4 MECHANICAL PROPERTIES

3.4.4.1 Bending strength and hardness

Main ± SD values ($n \geq 10$) of bending strength, σ_f, are measured as indications in Section 7.3.3.1 of Experimental Techniques and presented in Table 3.4-4. The main σ_f values are 590 MPa and 350 MPa for Al_2O_3 and A-25Ti, respectively. Thus, the incorporation of the second phase into the alumina matrix resulted in a decrease of the flexural strength. This fact is probably due to the increment of the critical flaw value of the composite considering the high difference between the grain sizes in the two phases. On the other hand, a further mechanism that may be responsible of decreasing the bending strength is the high reactivity that leads to side compound in the system. Such reactivity was revealed by the XRD-assessment and discussed in the previous Section 3.4.3.3.

Hardness was assessed as indications in Section 7.3.3.3. Main ± SD values (n=90) of Vickers hardness, H_v, for the two systems, alumina and alumina/titanium, are also shown in Table 3.4-4 The hardness in the studied composite decreased, as expected considering that the hardness of titanium polycrystal is ≈ 1 GPa [52], much lower than that of alumina (20.7 GPa).

Table 3.4-4: *Bending strength and hardness properties of monolithic alumina and Al_2O_3/Ti (25 vol. %Ti) composites.*

SYSTEM	BENDING STRENGH, σ_f (MPa)	VICKERS HARDNESS, H_v (GPa)
Al_2O_3	590 ± 25	20.7 ± 0.6
A-25Ti	350 ± 15	15.0 ± 1.4

3.4.4.2 Damage tolerance and R-curve behavior

Damage tolerance and R-curve behavior test were performed under the specifications in Section 7.3.3.4 of Experimental Techniques. Fig 3.4-9 shows the mechanical resistance measurements in samples previously indented with different loads. Differences in mechanical strength losses were found, when results between the composite and the monolithic material are compared. Each point represents the mean and SD values of 20 indentation-flaw failure tests.

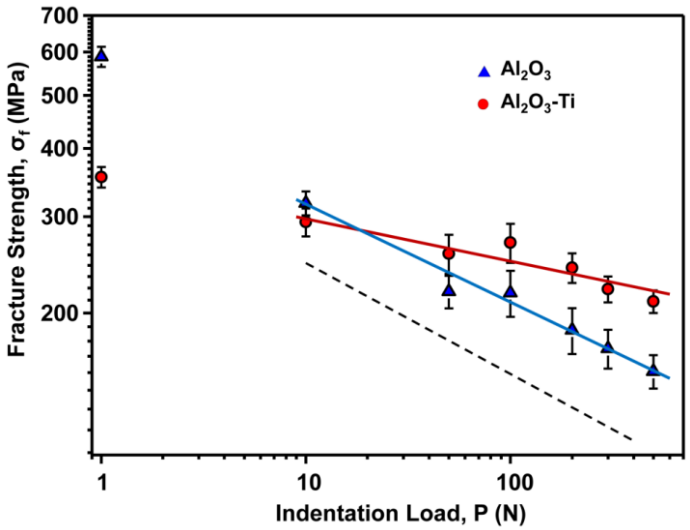

Fig 3.4-9. Indentation load vs. strength plots of monolithic Al_2O_3 and A-25Ti composite (dashed line represents the indentation-strength data to the $P^{-1/3}$ strength response)

In the specific case of brittle materials, the fracture strength can be related to the indentation load by means of Equation 3.4-1:

$$\sigma_f = A \cdot P^{-1/3} \qquad \text{Equation 3.4-1}$$

Where A is a constant depending on the toughness and P is the applied load at the time of breakage. This equation is only valid when the indentation induces cracks that are larger than the inherent flaws and it is assumed a constant value for the toughness. This function is represented by the dashed line in Fig 3.4-9.

However, whereas the toughness values increases with crack extension (i.e. R-curve behavior) the mechanical resistance values are less sensitive to increases in the indentation load and the experimental data do not fit to Equation 3.4-1. Linear regression was used to get the best fit for the data obtained for both studied

materials. The results found for the slopes values were 0.17 and 0.08 for Al_2O_3 and A-25Ti respectively. Comparing both responses, the composite material is more resistant to losses in strength with indentation loads greater than 20 N and it has a fracture strength of ≈ 210 MPa for an indentation load of 500 N; this is approximately a 25% higher than that of the monolithic alumina for the same indentation load. Thus, the fracture strength of this novel A-25Ti composite drops slower with the indentation load than the monolithic alumina, revealing the existence of an R-curve behaviour.

The data obtained in the damage tolerance test were further used to calculate the R-curve behaviour of both materials. For this purpose, it was used the indentation-strength K-field analysis of Braun et al. [53] that is described in Experimental Techniques (Section 7.3.3.4). The resulting R-curves obtained for Al_2O_3 and A-25Ti materials are shown in Fig 3.4-10.

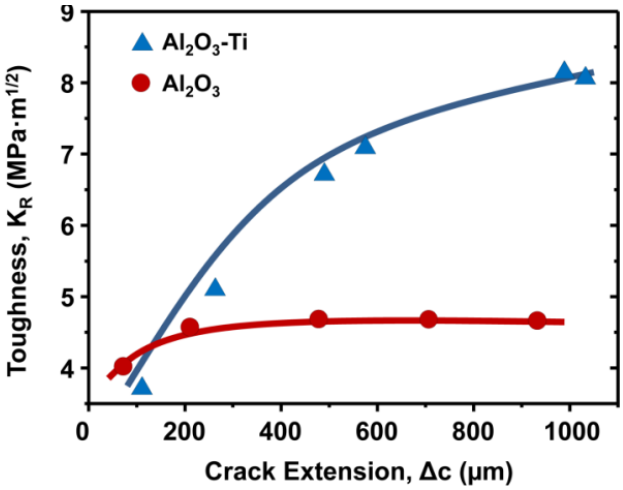

Fig 3.4-10. R-curves measured in Al_2O_3 monolithic and A-25Ti composite

Al_2O_3 has a very soft R-curve behaviour, which is probably due to the crack bridging between some large alumina grains. As observed, the initial and final toughness only changed from 4.0 to 4.5 MPa·$m^{1/2}$, and most of the increment is reached in the short crack region (up to 200 μm). In the case of the composite, the R-curve behavior is completely different.

The toughness values for the *short crack region* are similar in both materials, as the reinforcement-particles lying in the crack plane behind the tip are not present in the initial indentation flaw, because the indentation load needed to generate any initial crack is small, so that there is very limited bridging. Thus, crack growth initiation and propagation over the short crack region depends just on the applied *K*.

Beyond 200 µm (*long crack region*), R-curve for the composite material rises more quickly up to 1 mm, where it starts to reach a steady-state toughness value of 8.0 $MPa{\cdot}m^{1/2}$. This behavior evidences that the measured resistance curve is associated with the interactions between the crack and the titanium particles when the first one propagates.

In order to explain this behaviour, microstructure-crack interactions were investigated from cracks introduced on polished surfaces at 196 N of load with a Vickers indenter. Several mechanisms of reinforcement were evidenced through the observations by means of FE-SEM micrographs on the crack paths. In fact, Fig 3.4-11 shows four different cracks:

- Crack 1 propagates towards a small titanium grain. The crack bridges the metallic particle and continues propagating.
- Crack 2 penetrates into a titanium particle and deflects inside the metallic particle creating a more tortuous path to release stress, which helps also to increase the fracture toughness.
- Propagation of cracks 3 and 4 is completely stopped by the metallic particles improving the reinforcement of the composite. Moreover, in crack 4 it can also be noticed the crack blunting and renucleation in the ceramic phase. The non-evidence of debonding at the particle/matrix interface showing a strong adherence between phases.

Otherwise, the fracture mechanisms are disclosed in Fig 3.4-12 that shows a representative fracture surface of A-25Ti composites. The fracture of Ti particles occurred predominantly by cleavage, although some plastic deformation can also be observed (black arrows). Because of the thickness of the titanium particles, plastic deformation is more difficult to occur, so the metallic grains act as elastic bridges that fail during the crack propagation.

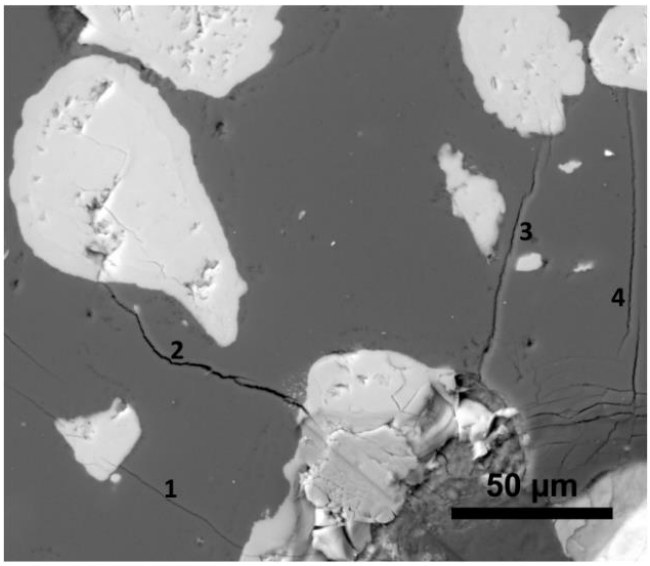

Fig 3.4-11. FE-SEM micrograph showing the diverse indentation cracks on the A-25Ti composite after indentation at 196 N.

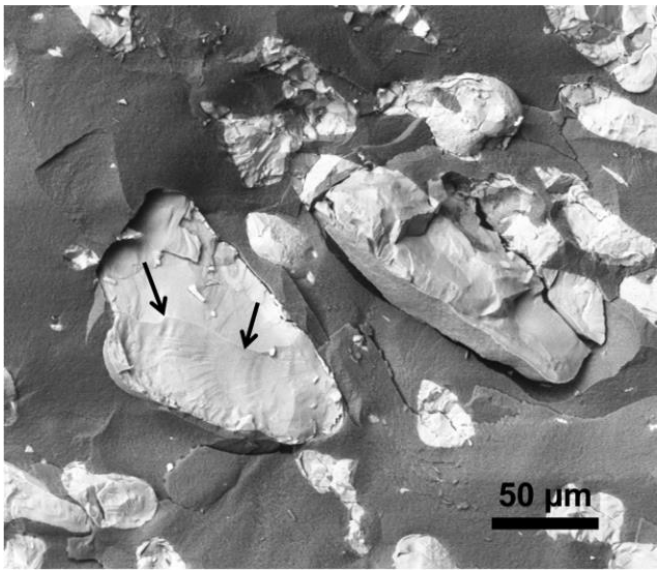

Fig 3.4-12. SEM micrograph acquired from a fracture surface of A-25Ti materials, indicating by arrows a plastic deformation in the metallic phase.

3.5 ZIRCONIA/TITANIUM SYSTEM

3Y-TZP or polycrystalline tetragonal zirconia partially stabilized with 3 mol% of Y_2O_3 is a biomaterial commonly used for manufacturing devices in load-bearing applications. Besides of its chemical stability in the biological environment and wear resistance, characteristics that are shared with other ceramics due to the covalent bindings in their structure, it also presents higher toughness values than, for instance, alumina. Unlike other types of zirconia-based materials, today aging problems are controlled in this kind of zirconia. These issues have already led to combine this ceramic with some metals in order to develop new *biocermets* (cermets with biological applications) with improved mechanical properties, such as those that include niobium as metallic phase [1, 4, 5, 54].

In the past decades, ZrO_2/Ti composites were considered as potential thermal barrier graded materials for applications in the aerospace industry [55]. The initial investigation on zirconia/titanium system dates back to the 1960s, when it was found that some properties, in particular thermal shock resistance and strength, may be enhanced in this ceramic by incorporating titanium [56-58]. Initially, this fact was attributed to the inhibition in the grain growth of zirconia due to the addition of titanium [57]. Posterior studies reported that those properties emerged because zirconia had been partially stabilized as cubic and tetragonal phases due to the dissolution of TiO [58]. However, these authors did not take into account the potential interfacial reactions between ZrO_2 and Ti. In fact, they were based on the Ellingham diagram to explain their results. This establishes that Ti does not reduce ZrO_2. That was a wrong conclusion, since the Ellingham diagram does not consider the reduction-dissolution mechanisms that really control the reactions between the phases in this ceramic-metal composite.

Posterior works focused in the knowledge of these interfacial reduction-dissolution reactions [51, 59, 60]. Some of them [60] have indicated that oxygen dissolves into Ti, producing blackened oxygen-deficient zirconia (ZrO_{2-x}). Experiments in Ti/ZrO_2 diffusion couples (1100-1550 °C) have related the existence of distinct layers in the reaction zone. Due to the importance of this on the development of ZrO_2/Ti composites, this topic will be extensively approached to better understand the new formed phases.

Thereby, Lin et al [61] have found, in the metal side of diffusion couples, five successive reaction layers: α-Ti(O), Ti_2ZrO+α-Ti(O, Zr), Ti_2ZrO+α-Ti(O, Zr)+β′-Ti (O, Zr), α-Ti (O, Zr)+β′-Ti (O, Zr), and β′-Ti (Zr, O). In the zirconia side, there were two reaction layers: near the original interface, β′-Ti coexisted with fine spherical c-ZrO_{2-x} and

acicular c-ZrO_{2-x}, which dissolved a significant amount of Y_2O_3 in solid solution; further away from the original interface, the coarsened intergranular α-Zr was excluded from metastable ZrO_{2-x}, resulting in the lenticular t-ZrO_{2-x} and ordered c-ZrO_{2-x}.

Moreover, Kun-Lin Lin and Chien-Cheng Ling [62] have later elucidated the reaction mechanism between the powders by sintering composites at 1500 °C with Ti contents up to 90 mol%. They conclude that Zr and O diffuse into Ti and simultaneously Ti diffuses into ZrO_2 during sintering. Furthermore, they found different reaction products depending on the ZrO_2/Ti ratio, although α-Ti(O, Zr), Ti_2ZrO and/or TiO was reported in all the cases. TiO was formed in those compacts with Ti ≤ 30 mol while Ti_2ZrO and α-Ti(O, Zr) appeared instead of it in specimens with Ti ≥ 50 mol%. Oxygen was supplied from ZrO_2 which appeared as deficient in oxygen. In samples with Ti ≤ 50 mol% monoclinic-ZrO_{2-x} and tetragonal-ZrO_{2-x} were disclosed, whilst cubic-ZrO_{2-x} appeared when Ti was higher than 70 mol%. In this case, high concentration of yttria was retained and there were many oxygen vacancies. Moreover, in samples of 90 mol% Ti, ceramic particles were almost dissolved in Ti, leading to precipitate $Y_2Ti_2O_7$.

Therefore, developing materials in the ZrO_2/Ti system is a challenge because the high reactivity hinders its processing and conformation. Indeed, most works have been focused on the reactivity, without assessing the mechanical properties derived of the bulk material. On the other hand, these ZrO_2/Ti cermets have been conventionally sintered during times up to one hour in vacuum [36, 56, 60]. It has hypothesized about the importance on the vacuum conditions on stabilizing ZrO_2 because within poor vacuum conditions zirconia was not stabilized [62]. Advanced technologies, such as Spark Plasma Sintering (SPS) where pressure and temperature are simultaneous applied in vacuum, allow to achieve shorter sintering times that could prevent the formation of further compounds. Thus, ZrO_2/Ti dense materials (labelled as Z-Ti from now on) will be developed by a wet powder processing route and Spark Plasma Sintering. The studied titanium concentration will be 25 vol. % Ti (Z-25Ti), 50 vol. % Ti (Z-50Ti) and 75 vol. % Ti (Z-75Ti) in order to cover the entire range of metal-content. For comparative purposes, pure ZrO_2 samples will be manufactured following an equivalent procedure. Mechanical characterization will also be carry out to ensure suitability in the new cermets.

3.5.1 SEDIMENTATION AND RHEOLOGY STUDIES

Such as it was mentioned in Section 3.4.1 for the Al_2O_3 system, sedimentation and rheology tests were developed for obtaining mixtures of ceramic/titanium powders with uniformly distributed phases. In order to find the appropriate solid content and the amount of dispersant that provides a stabilizing effect, different ZrO_2/Ti suspensions (Z-Ti) were prepared (Table 3.5-1). Regarding the different possible relative amounts of titanium in the suspension, the intermediate proportion of 50 vol. % Ti was used as representative metal ratio.

Table 3.5-1 Rheological conditions studied in Z-Ti (50 vol. % Ti) suspensions.

Z-50Ti SUSPENSION	SOLID CONTENT (Wt. %)	DOLAPIX (Wt. %)
A	80	1
B	80	3
C	70	1
D	70	3

Fig 3.5-1 shows the results after 24 hours of sedimentation in the tested suspensions. As observed in Fig 3.5-1(A) and Fig 3.5-1(C) the metallic phase segregated from the ceramic and, eventually, deposited on the bottom of the tube. Although the metal particles have a lower density comparing with those of zirconia (4.5 $g{\cdot}cm^{-3}$ and 6.1 $g{\cdot}cm^{-3}$ respectively), they settle faster due to the large difference between grain sizes. Therefore, it seems that 1 wt. % of deflocculant addition is not enough to stabilize the titanium particles. As corroborated in Fig 3.5-1 (B) and Fig 3.5-1(D), when deflocculant concentration rises up to 3 wt. %, no segregation is observed. However, in Fig 3.5-1 (D), part of the water is removed from the suspension due to a higher content. This effect is not observed in Fig 3.5-1 (B) where the water content is reduced, producing a higher deflocculant activity and reducing the distance between particles that leads to a higher particle interaction.

On the other hand, Table 3.5-2 summarizes the results obtained from the rheological study of Z-Ti (50 vol. % Ti) suspension. As it can be observed, only one parameter was changed in each case either the solids content or the surfactant content. In addition, the flow curves corresponding to the four studied suspensions are shown in Fig 3.5-2.

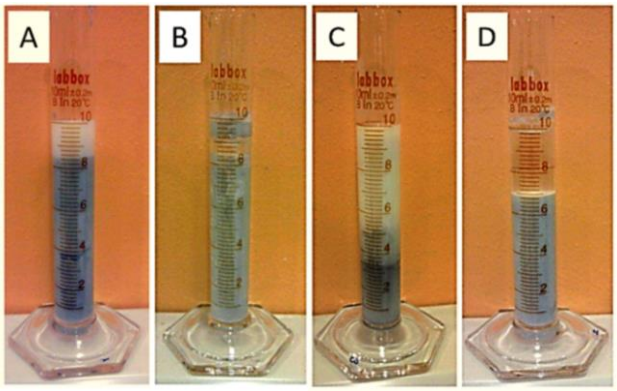

Fig 3.5-1. Sedimentation processes in Z-Ti suspensions (50 vol. % Ti).

Table 3.5-2: *Rheological study of Z-Ti (50 vol. % Ti) suspensions.*

Z-50Ti SUSPENSION	τ_0 (Pa)	dv/dx_{max} (s^{-1})	H (mPa·s)
A	4	1741	52
B	40	788	127
C	< 1	1725	23
D	4	1688	31

The suspensions A and C displayed a pseudoplastic behaviour, suffering an important segregation of powders. The low surfactant content prevents the dispersion of the aggregates leading to sedimentation of the particles. Moreover, in slurry C, with a 70 wt. % solid content, the interaction between particles is even lower than in slurry A. That explains the observation of a higher sedimentation of the bigger particles in this slurry. Slurry D presents a slightly plastic behavior. In this case, the deflocculant content promotes the particle dispersion creating a net attractive interparticle force that gives rise to the formation of a three-dimensional network of particles. The formation of this network prevents sedimentation of the differnt phases, which is the first requirement to produce homogeneously dispersed microstructures in the final materials. The yield stress (τ_0) can be taken as a representative value of the strength of the particle network; the higher yield stress, the stronger particle interaction and the higher strength of the particle network. In slurry D the yield stress is about 4 Pa, which is a low value close to the pseudoplastic behavior observed in slurries A and C. No sedimentation is observed in suspension D but the apparition of a supernatant shows the tendency of the slurry to eliminate

water in order to increase the solid content and form a stable structure between particles and liquid media. This situation does not occur in suspension B, where the higher solid and deflocculant content have led to the formation of a stable structure with a high yield stress (40 Pa) that prevents the slurry from sedimentation and the formation of supernatant. Thus, among the rheological conditions tested, the slurry B presents the settings that would lead to zirconia/titanium materials with a homogeneous microstructure.

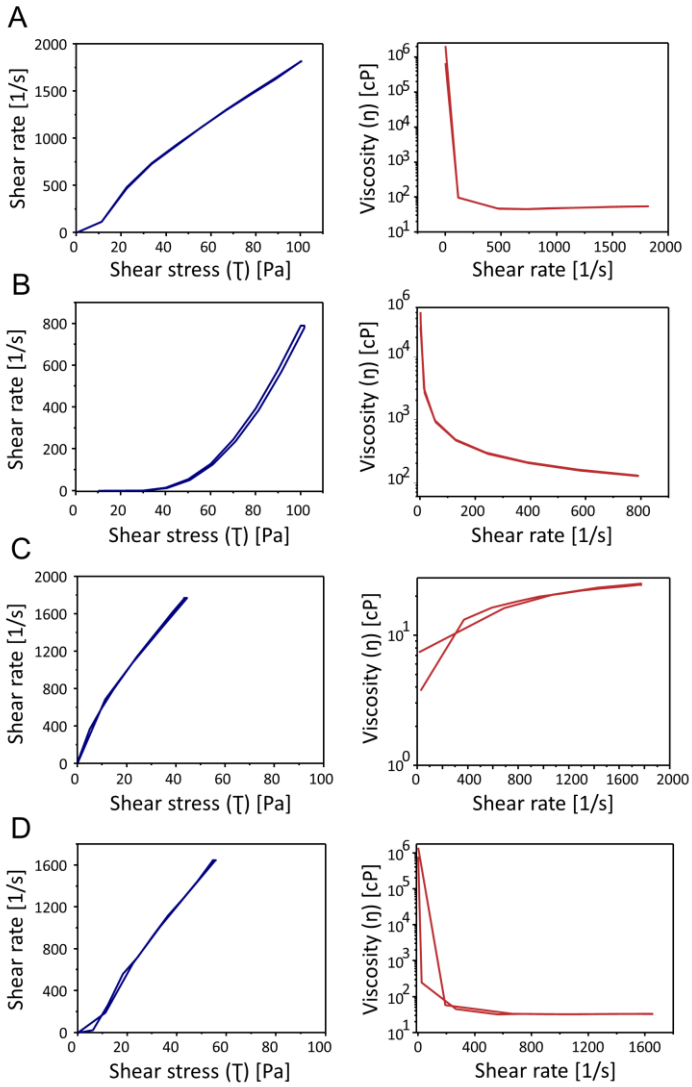

Fig 3.5-2. Flow curves for the different Z-Ti suspensions tested.

3.5.2 Z-Ti STARTING POWDERS

3.5.2.1 Processing

Based on the results of the sedimentation and rheological tests in Section 3.5.1, Z-Ti suspensions were prepared with an 80 wt. % of solid content and an amount of surfactant of 3 wt. %. Three different suspensions were studied by varying the relative proportion of titanium (25 vol. %, 50 vol. % and 75 vol. % of Ti). These new mixtures of ceramic/metal powders were denoted as Z-25Ti, Z-50Ti and Z-75Ti, respectively. They were processed following the general processing route for ceramic/titanium powder earlier schematized in Fig 3.4-2.

3.5.2.2 X-ray diffraction (XRD)

The diffractograms that resulted from analyzing the three types of Z-Ti powders are comparatively presented in Fig 3.5-3. The analyses were performed using a Bruker ASX D8 Advance diffractometer. Scans were obtained from 10° to 70°. The patterns obtained were compared with the data files in the ICDD for tetragonal zirconia (50-1089), monoclinic zirconia (37-1484) and hexagonal titanium (44-1294); as expected crystalline phases. The position and intensity of the peaks correspond to those anticipated for Ti and ZrO_2, rejecting additional contamination and/or the presence of side reactions along the wet processing of the powders. Moreover, the relative intensity of the ZrO_2-Ti peaks varies as a function of the ceramic-metal proportion in the suspensions.

3.5.2.3 Scanning electron microscopy (SEM)

Micrographs of the three types of Z-Ti staring powder were acquired with a scanning microscope working at 15 eV and 1200x magnification (Fig 3.5-4). As can be seen, the atomized zirconia was disaggregated during the wet processing to give isolated particles that are uniformly disposed over the micrometric particles of titanium. As such, the additional EDS analyses disclosed higher amount of ZrO_2 in Z-25Ti powders than in Z-50Ti starting powders. This study by energy-dispersive X-ray spectroscopy further suggested absence of contamination in the mixture of Z-Ti powders due to manufacturing.

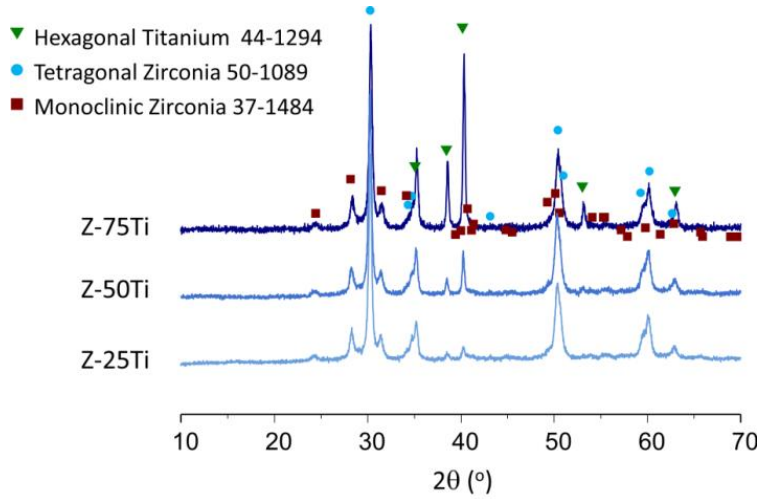

Fig 3.5-3. Diffractograms acquired from the diverse Z-Ti powders (y-axis: arbitrary units of intensity).

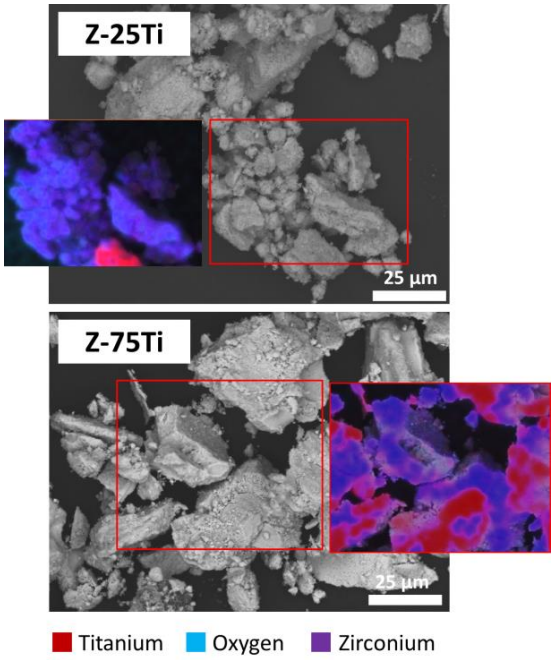

Fig 3.5-4. SEM-micrographs of Z-Ti powders together with their EDS analyses. EDS-images from Z-Ti starting powders with 25% vol. Ti (Z-25Ti) and 75% vol. Ti (Z-75Ti) allow contrasting the zirconia/titanium ratio.

3.5.3 DENSE COMPOSITES: CONSOLIDATION AND CHARACTERIZATION

3.5.3.1 Spark Plasma Sintering (SPS)

Z-Ti composites with 25 vol. % Ti (Z-25Ti), 50 vol. % Ti (Z-50Ti) and 75 vol. % Ti (Z-75Ti) as well as pure ZrO_2 and pure Ti were processed as explained in Fig 3.4-2 with the diverse slurries prepared such as the suspension B in Section 3.5.1.

As in A-25Ti composites, a preliminary analysis was also carried out in the Z-Ti cermets with the purpose of adjusting the suitable sintering conditions. Such analysis was performed on the different Z-Ti cermets with similar results. Fig 3.5-5 shows a representative depiction of the ΔV speed in the SPS cycle during the sintering process in a Z-50Ti sample. As it can be observed, densification starts approximately at 1000°C and finishes close to 1350 °C. Therefore using a temperature of 1350°C, we would assure that the full densification in the compacts would be reached.

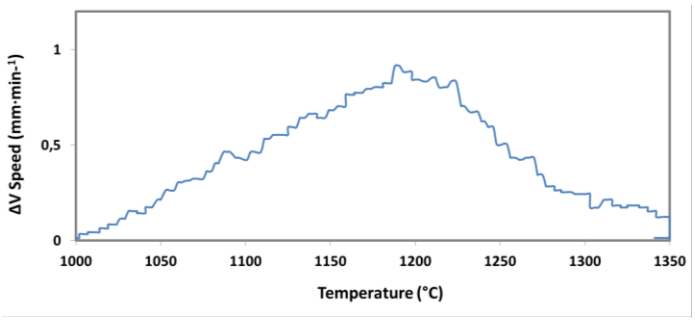

Fig 3.5-5. Relative movement of the piston during a SPS cycle of Z-50Ti composites.

In addition, Table 3.5-3 collects the conditions, in which the sintering took place for Z-Ti composites. Before sintering, the starting powders were placed in a graphite-mold (diameter, 20 mm) and pre-formed by uniaxial pressing (10 MPa) with a hydraulic press**.** A key difference between conventional sintering and spark plasma sintering is the sintering time. Heating by direct current pulses allows heating rates much higher than those achieved in a conventional furnace and in 20 minutes the complete cycle is finished. This is determinant for controlling the high reactivity among the zirconia and titanium phases. As the sintering times involved in the conventional procedure are longer, the side reactions that take place are more probable, giving side products like those described in the introduction part of this system (Section 3.5). Thus, a shorter sintering time together with a simultaneous pressing that are characteristics of spark plasma sintering could prevents an excessive

formation of side compounds, allowing a densification close to the theoretical in the 3Y-TZP/Ti system.

Table 3.5-3: *Spark Plasma Sintering (SPS) settings.*

SYSTEM		Z-25Ti	Z-50Ti	Z-75Ti
Composition (Vol. %)		75% ZrO_2 25% Ti	50% ZrO_2 50% Ti	25% ZrO_2 75% Ti
SETTING	Heating rate	100 °C/min		
	Atmosphere	Vacuum		
	Temperature	1350 °C		
	Time	5 min		
	Pressure	80 MPa		
	Cooling rate	Free		

3.5.3.2 Density

As explained in Experimental Techniques (Section 7.3.1), the bulk densities of the diverse Z-Ti systems were measured as per instructions in ASTM C 373-88 [63]. In addition, each measured value was divided by the theoretical density value, calculated according to the rule of mixtures, in order to evaluate the degree of densification. As shown in Table 3.5-4, the relative densities of all the sintered composites were very close to the theoretical values (>99 %th.) and thus, as expected, the selected SPS cycle (Table 3.5-3) was successful to obtain dense zirconia/titanium specimens covering the entire range of metal. Values of real density measured by helium pycnometry were slightly higher.

Table 3.5-4: *Densities of SPS-sintered ZrO_2/Ti compacts (theoretical density is calculated from the rule of mixtures).*

Z-Ti System	Measured Density ($g \cdot cm^{-3}$)	Theoretical Density ($g \cdot cm^{-3}$)	Real Density ($g \cdot cm^{-3}$)	Ratio Measured-Theoretical Density (%)
ZrO_2	6.0 ± 0.1	6.1	6.0	>99
Z-25Ti	5.6 ± 0.2	5.7	5.7	
Z-50Ti	5.4 ± 0.1	5.3	5.5	
Z-75Ti	4.8 ± 0.1	4.9	5.1	
Ti	4.4 ± 0.2	4.5		

3.5.3.3 X-ray diffraction (XRD)

In order to evaluate the possible side reactions between Ti and ZrO_2 during sintering, diverse X-ray diffraction analyses were carried out on sintered specimens after 1-µm polishing as per settings in Section 3.5.2.2. Fig 3.5-6 shows representative diffractograms of the different sintered composites. ZrO_2/Ti samples of lower Ti content (Z-25Ti) disclosed the presence of α-Ti (hexagonal, 44-1294) and t-ZrO_2 (tetragonal, 50-1089) as well as peaks fitting with TiO (cubic, 77-2170), such as occurred in previos works [62]. Unlike these earlier results, monoclinic-zirconia was qualitatively not detected; so higher stability may be achieved by using SPS as consolidation method. Moreover, the existence of Ti_2ZrO (orthorhombic, 72-1881) was disclosed in ZrO_2/Ti cermets, especially for those with high Ti content (Z-75Ti). This is not a surprising fact because previous works have revealed its presence in those sintered ZrO_2/Ti materials containing more than 50 mol% Ti. On the other hand, ZrO_2 transformation was not qualitativaly detected in the SPSed materials. Thereby, unlike the results in [62], neither monoclinic nor cubic peaks were found. In that work, cubic-zirconia increased as the Ti amount did, disappearing the tetragonal phase to favor the stabilization of cubic-ZrO_2 with Ti equal to 90 mol%.

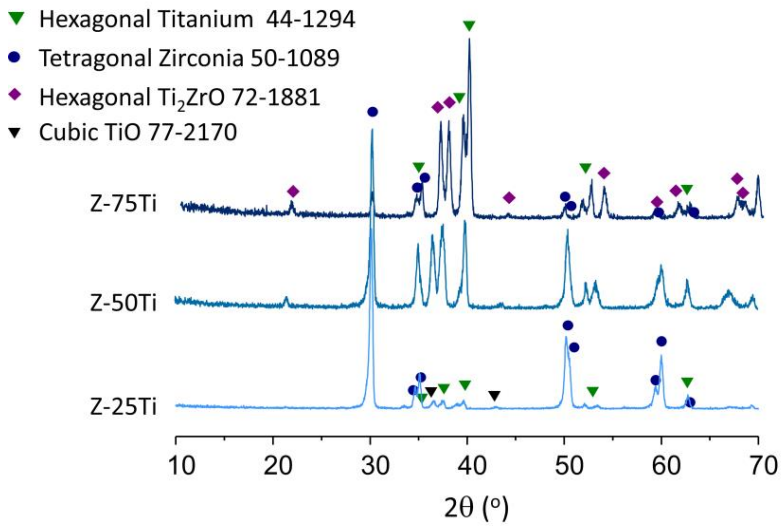

Fig 3.5-6. XRD-diffractograms of the different Z-Ti fired specimens (y-axis would be arbitrary units of intensity).

3.5.3.4 Microstructure

Zirconia microstructure was analyzed by FE-SEM onto a 1-µm polished surface thermally etched (1150°C) for 1 hour in air-atmosphere (Fig 3.5-7). The main ± SD grain size was 220 ± 27 nm measured by the *Mean Lineal Intercept Method* [64, 65].

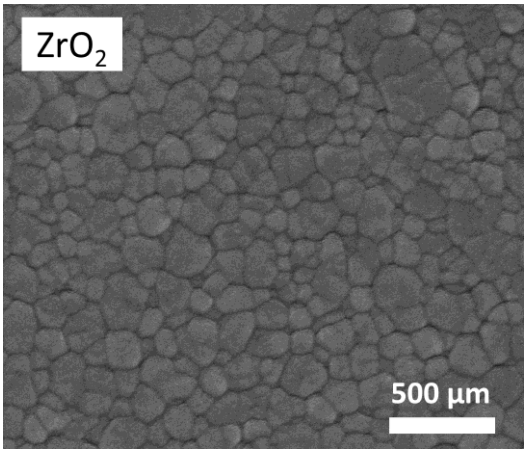

Fig 3.5-7. Microstructure of SPS-sintered pure zirconia visualized by FE-SEM after thermal etching.

The overall microstructure of dense Z-Ti cermets was studied by SEM on 1-µm polished surfaces, using the backscattered detector in order to achieve the maximum contrast between phases. In Fig 3.5-8, darker and brighter phases are Ti and ZrO_2 grains, respectively. All composites had metallic particles homogeneously dispersed throughout the ceramic matrix and no apparent porosity is observed in accordance with density measurements in Table 3.5-4.

At higher magnification (Fig 3.5-9), the formation of additional phases with platelet and globular shapes were disclosed in the interface of Z-75Ti composites. As was explained from the XRD-analysis in Section 3.5.3.3, during sintering of ZrO_2/Ti cermets with high Ti content, zirconium and oxygen enter into solid solution precipitating Ti_2ZrO [62]. L. Kun-Lin et al. [66] have specifically reported the dissolution of a large amount of zirconium and oxygen into Ti on heating, giving rise to a metastable supersaturated disordered α-Ti(Zr,O) solid solution where two different Ti_2ZrO phases, lamellar and spherical, subsequently precipitate. The spherical Ti_2ZrO is further described as an ordered hexagonal structure, with Zr and O occupying substitutional and interstitial sites, respectively. On the other side, considering morphological features, the globular shapes precipitated in the zirconia

phase may also be attributed to $Y_2Ti_2O_7$ (such as indicated in the Fig 3.5-9); this compound precipitates coarsened by the Ostwald ripening effect presenting a spherical shape.

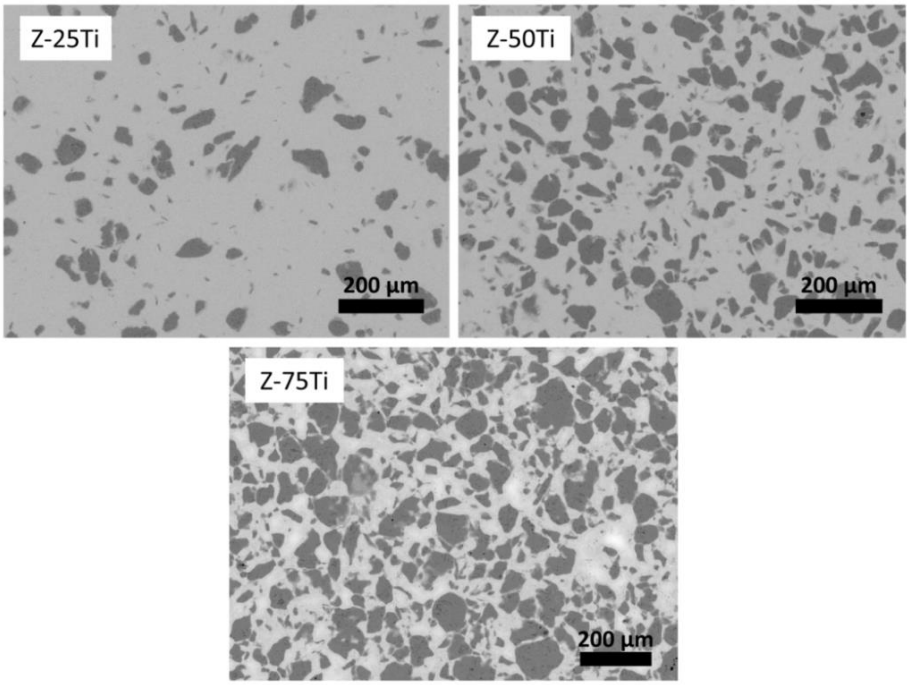

Fig 3.5-8. SEM-micrographs of fired ZrO_2/Ti specimens with 25 vol. % (Z-25Ti), 50 vol. % (Z-50Ti) and 75 vol. % (Z-75Ti) of Ti.

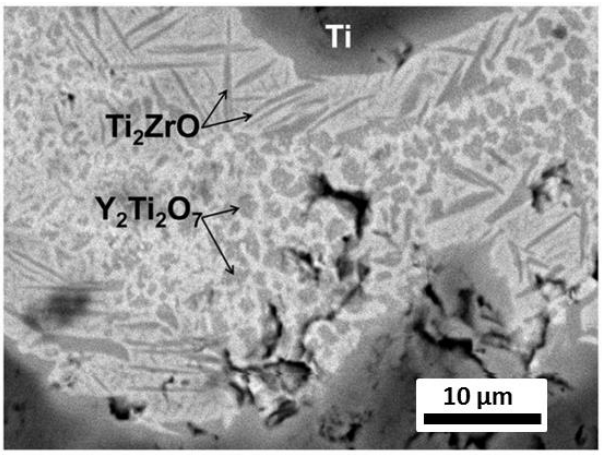

Fig 3.5-9. ZrO_2/Ti interface in Z-75Ti composites visualized by SEM (the reactions products are marked with arrows).

3.5.4 MECHANICAL PROPERTIES

Mechanical properties in Z-Ti composites were analyzed and compared to pure zirconia. The parameters evaluated were bending strength, toughness and hardness. The setup of each experiment is described in Section 7.3.3 (Experimental Techniques, Chapter 7).

3.5.4.1 Bending strength

The bending strength, σ_f, main ± SD values (*n=10*) of the Z-Ti composites are presented in Table 3.5-5. It was found that the average σ_f in all the Z-Ti composites was below the values expected from the rule of mixture. This may be a consequence of the difference in high size among ZrO_2 and Ti phases, which could increment the critical flaw value in the composites and/or it may be a result of the presence of the new phases at the ceramic-metal interface, which were previously disclosed by DRX (Fig 3.5-6) and SEM (Fig 3.5-9).

Table 3.5-5: *Mean and SD values of bending strength and toughness*

SYSTEM	BENDING STRENGTH, σ_f (MPa)	FRACTURE TOUGHNESS, K_{IC} (MPa·m$^{1/2}$)
ZrO_2	800 ± 112	6.0 ± 0.2
Z-25Ti	310 ± 35	5.1 ± 0.3
Z-50Ti	200 ± 50	3.3 ± 0.2
Z-75Ti	155 ± 25	2.0 ± 0.1

3.5.4.2 Toughness

The fracture toughness, K_{IC}, main ± SD values (*n=5*) of the different cermets are also presented in Table 3.5-5. Furthermore, Fig 3.5-10 presents a representative fracture surface of Z-75Ti composite, showing that the fracture of the Ti particles occurred predominantly by cleavage and there was no evidence of debonding at the metal-ceramic interface. This behaviour is typically associated with brittle fracture [4]. Due to this absence of ductile deformation of metal particles, no increase in the toughness is expected. On one hand, this brittle fracture may be explained as a consequence of the α-Ti(O) layer formed in the ceramic/metal interface, which has been described as very hard and brittle titanium due to oxygen interstitial effects [51, 67]. On the other hand, it is well-known that strength and toughness of composites are strongly affected by the particle/matrix adhesion, because strength depends on the effective stress transfer between filler and matrix and toughness/brittleness is controlled by adhesion [68]. Thus, not only the reactivity among components, also the

difference between their particle sizes can impair the particle/matrix adhesion, being responsible of these poor toughness properties.

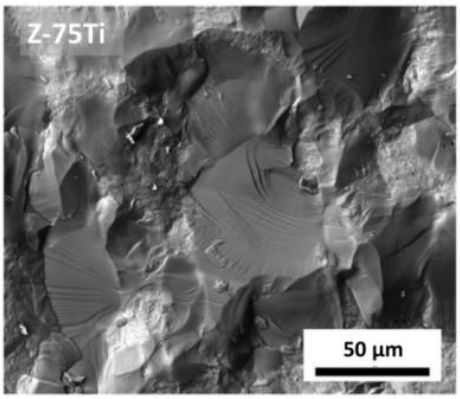

Fig 3.5-10. FE-SEM micrograph from a fracture surface of Z-75Ti composites.

3.5.4.3 Hardness

Fig 3.5-11 presents Vickers Hardness, H_v, main ± SD (*n=3; 30 indentations per sample)* values obtained for pure ZrO_2 and the Z-Ti cermets. The continuous line is outlined to represent the values of H_v predicted by the rule of mixtures in the diverse materials studied. Thus, the hardness of all three composites is higher than that predicted considering the Ti Vickers hardness (≈1 GPa) [69]. It can also be seen that the deviation from the rule is higher when the titanium content increases in such a way that the hardness measured for Z-75Ti (8.6 GPa) doubles the value predicted by the rule of mixtures (4.2 GPa). Therefore, as the formation of the reaction products increases with the titanium concentration, these reaction products seem to be responsible for the hardness improvement [70].

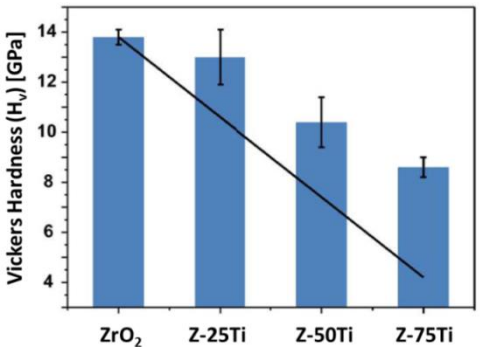

Fig 3.5-11. Hardness values for ZrO_2 and Z-Ti composites (the line represents the values predicted by the rule of mixtures).

3.5.5 AGING

Accelerated aging tests under hydrothermal environment in autoclave (Tuttnauer, model 2540 EL; US) were conducted for Z-Ti specimens according to ISO 13356:2008. This standard specifies the characteristics and the testing methods for ceramics based on yttria-stabilized tetragonal zirconia (Y-TZP) intended to be used in surgical implants. As requirement, the integrated intensity of monoclinic zirconia calculated as indicated in [71] by X-ray diffraction using Equation 3.5-1 must be below 25% after 5 hours of accelerated aging.

$$X_m = \frac{I_m(-111) + I_m(111)}{I_m(-111) + I_m(111) + I_t(101)} \qquad \text{Equation 3.5-1}$$

Where I_m (hkl) is the area of the peak associated to the plane (hkl) of the monoclinic phase and I_t (hkl) is the area of the peak associated to the plane (hkl) of the tetragonal phase.

The tetragonal-to-monoclinic transformation was evaluated up to 30 hours and the diverse XRD patterns were collected in Fig 3.5-12. In Z-25Ti specimens, an intense peak of monoclinic zirconia emerged after 10 hours of hydrothermal treatment, which was increased along the assay time. Z-50Ti and Z-75Ti composites had a less-intensity peak of tetragonal zirconia, as expected from a lower content of zirconia in the bulk material. When the values of fraction of monoclinic zirconia (X_m) calculated from Equation 3.5-1 are plotted along the time (Fig 3.5-13), it is found that Z-25Ti and Z-50Ti cermets met the requirement in the standard. However, Z-75Ti materials presented an X_m value around 35% before the hydrothermal treatment so this material did not meet the requirement in ISO 13356:2008. However, this value may be overestimated due to the low proportion of zirconia in the sample. Thus, in the Fig 3.5-12, the emergence of peaks related monoclinic-zirconia along the hydrothermal treatment is not evident for Z-75Ti composites. Moreover, the fraction of monoclinic zirconia in Z-25Ti and Z-50Ti composites increased with in the aging time as the content in titanium (the higher the Ti ratio in the bulk material, the higher monoclinic zirconia in the Z-Ti cermet).

Previous works have studied the effect of Ti on the martensitic tetragonal-to-monoclinic transformation of zirconia/titanium cermets, finding that the fraction of monoclinic-ZrO_2 increased while increasing the Ti content as long as it was higher than 12.5 vol. % [55]. The same authors suggested that to appropriately control the volume fraction of monoclinic phase, the content of Y_2O_3-stabilizing-agent should be increased as the Ti content increases in the preparation of ZrO_2/Ti composites [55].

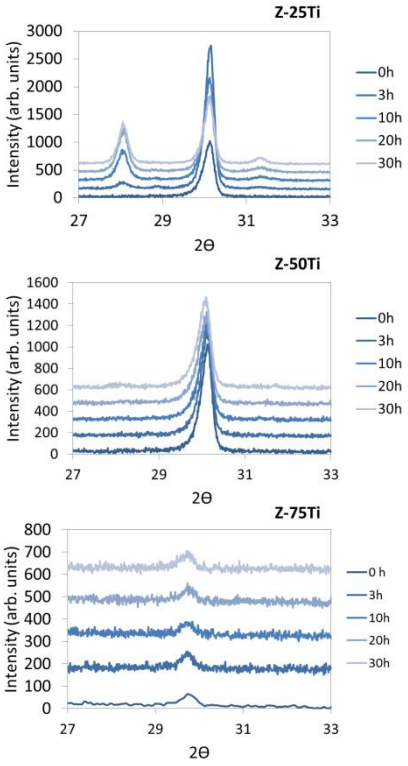

Fig 3.5-12. XRD pattern acquired from Z-Ti specimens before and after hydrothermal aging at 134 °C up to 30 hours (y-axis: arbitrary units of intensity).

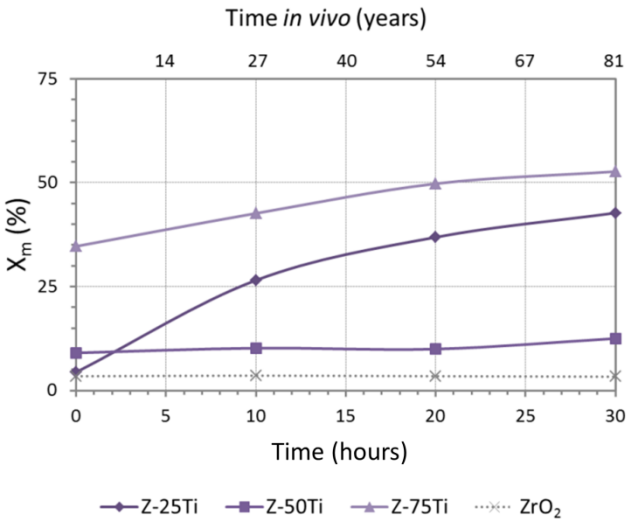

Fig 3.5-13. Fraction of monoclinic zirconia, Xm (%), in ZrO_2/Ti composites plotted as a function of the aging time.

3.6 MODIFICATION OF TITANIUM

Both studied ceramic/titanium composites showed a decrease in the main values of bending strength regarding those expected from the rule of mixtures (Table 3.5-5 and Table 3.4-4, respectively). This drop in mechanical properties is primarily attributed to redox reactions among the ceramic and metallic phases, which lead to undesirable intermetallic phases and side compounds [59]. Such reactivity is particularly revealed in ZrO_2/Ti cermets by XRD (Fig 3.5-6) and also in Z-75Ti specimens by SEM (Fig 3.5-9). In addition, fracture mechanisms in Z-Ti composites involved breakage of Ti particles mainly by cleavage, with absence of debonding (Fig 3.5-10). The fracture surface of Z-75Ti composites (Fig 3.5-10) also disclosed the characteristic marks in brittle fracture, pointing to the origin of breakage in the grain boundaries. Previous works [72] have suggested the grain refinement of metals as an effective method for reducing their susceptibility against their embrittlement. As the grain size becomes larger, more diffusive species can better penetrate into the metal. Furthermore, the grain refinement would also act reducing the critical flaw value in Z-Ti materials that result from the great difference among the grain sizes of Ti and ZrO_2.

Mechanical ball-milling is a straightforward method for reducing the powder particle size [3-75]. Thus, grinding of materials is a major component of ceramic processing and powder metallurgy industries. The objectives of milling include not only reducing the particle size, but also the mixing or blending and particle shape changes [76]. Mechanical attrition is a complex and dynamic milling process, in which the central event is the ball-powder-ball collision [77]. Although this process is less energetic than other milling operations and requires longer times, it allows to produce great sets of Ti with identical grain size to that derived of higher-energy techniques [74, 76, 78]. As Dabhade et al. explained [79], the properties of Ti-based materials could be improved by reducing the raw powder size. In addition, with a more reduced particle size, more cohesive ceramic/titanium interfaces would be created and, therefore, enhanced mechanical properties achieved; strength depends on the effective stress transfer between filler and matrix and toughness/brittleness is controlled by adhesion [68].

Another drawback that arises from the high reactivity is the interfacial formation of side products involving to zirconium, titanium and yttrium; in particular, when high Ti ratio forms the cermet (Z-75Ti) (Fig 3.5-9). Due to the precipitation of yttria compounds, the stabilizing effect in zirconia is lost and tetragonal-to-monoclinic transformation takes place in Z-Ti specimens (Fig 3.5-13). Therefore, as explained in

Section 3.5.5, the content of Y_2O_3-stabilizing-agent in ZrO_2 should be increased as the Ti content increases in the preparation of ZrO_2/Ti cermets [55].

Moreover, the development of a protective coatings on metal particles has been suggested as an interesting approach for reducing the reactivity among dissimilar materials [80]. One of the most practical solution–deposition methods to prepare oxide coatings is sol-gel. Chemical stability and oxidation control have been achieved in different metal substrates by creating inorganic oxide coatings of SiO_2, ZrO_2 and Al_2O_3 [81]. In this research, yttria was selected for coating titanium particles by being more stable with Ti when compared to Al_2O_3 or ZrO_2 [55, 59]. A protective yttria-coating on Ti particles could therefore reduce the reactivity between counterparts and also improve mechanical features as well as to protect against aging.

On the other hand, Ti element has a very negative standard redox potential of reduction [82]. However, it has high chemical stability due to the formation of a very resistant and protective oxide layer on its surface, which is not altered in very aggressive media like the oral medium or even in HCl or H_2SO_4 solutions [82, 83]. This thin passive oxide film (5-10 nm), that is formed in air at room temperature and acts protecting from subsequent oxidations, presents a three-layer structure: TiO adjacent to metallic titanium, intermediary Ti_2O_3 and anatase (TiO_2) in contact with the environment. TiO_2 is well-known due to its biocompatibility and chemical inertness. This chemical stability has led to successfully combine this ceramic oxide with other ceramics, developing improved composites for different applications [84-86]. This leads to think that by increasing the surface layer of titanium dioxide (titania) in Ti powder, higher stability among the phases in the Z-Ti system may be achieved. Thermal oxidation is proposed as a method to easily increase the thickness in the oxide film above 1 micron, besides of modifying its structure and morphology [87, 88] toward the presence of anatase and rutile. The presence of these crystalline forms together in the oxide film has been related with improvements in the osseointegration of titanium materials [89, 90].

The purpose of this next section is thus to approach mechanisms that allow to improve aging and mechanical features in ZrO_2/Ti cermets. On one hand, titanium powder will be modified by attrition milling in order to decrease the titanium particle size. Then, milled-titanium will be covered with an yttria-protective-coating by sol-gel. On the other hand, Ti powder will be subjected to a thermal treatment to get a thicker titania layer. Then, the different modified titanium powders (named in general as m/Ti) will be analyzed by SEM, XRD and XPS and then, used to develop new zirconia/titanium (25% vol. Ti) compact specimens. Sintered specimens will also be

physically/chemically characterized by SEM, DRX, and mechanically in terms of bending strength. In addition, aging tests will be carried out.

3.6.1 MODIFICATION PROCESSES

Titanium powder was characterized in Section 3.3 and then used to manufacture Z-Ti and A-Ti systems, as respectively indicated in Section 3.5 and 3.4. Now, titanium is modified in order to improve the mechanical features in the dense specimens. The following two routes of powder modification were performed:

- Treatment (a): Titanium powder acquired from the manufacturer was subjected to thermal treatment in air atmosphere (o/Ti) to get a consistent titania layer.

- Treatment (b): Titanium powder acquired from the manufacturer was grounded by attrition milling (a/Ti) and the milled titanium was then coated with an yttria layer (Y_2O_3/a/Ti) by sol-gel.

Each modification process is analyzed below in detail.

3.6.1.1 Thermal treatment: titanium passivation

Heating up to 425°C in air may result in a heavy oxide layer because of increased diffusion of oxygen through the titanium lattice. However, above 649°C, titanium oxidizes and becomes brittle. Thus, cp-Ti powder was thermally treated at 350°C (heating up 5°C/min) for 1 hour in air-atmosphere (Termolab 1200°C furnace - Fornos Eléctricos, Lda; Portugal) to create a thicker TiO_2 layer than the existing due to atmospheric passivation.

3.6.1.2 Attrition milling and sol-gel coating

On one side, the milling was performed in lots of 75 grams of Ti powder, 300 grams of zirconia balls and 63 grams of isopropanol in an attritor-mill (Telemecanique). Several variables can influence the minimum grain size attained; milling time is one of the most important. Thereby, in order to optimize the procedure, obtaining a grain size as small as possible, two different times were tested: 4 hours and 8 hours. The titanium powder obtained from 4 hours of milling was named as 4a/Ti and the titanium power obtained from 8 hours of milling was named as 8a/Ti.

On the other side, the basis of the sol-gel coating consisted in covering the substrate with a precursor solution containing the requisite components in the required proportion that, by solvent evaporation and/or chemical reactions, transforms into a gel layer. Organic components in the gel were then eliminated by heat treatment. The desired crystalline coat is also thermally formed. Fig 3.6-1 schematizes the sol–gel procedure used to perform the nanocrystalline-yttria-coating on Ti powder. The quantities were calculated to get an Y_2O_3 increase of 0.3 mol% in the Z-25Ti composite. The precursor solution was prepared with 0.4 grams of yttrium chloride hexahydrate ($YCl_3 \cdot 6H_2O$) (99.99%) (Aldrich Chemical Company, Inc; Milwaukee, US) using de-ionized water as solvent. A NH_4OH solution (Aldrich Chemical Company, Inc; Milwaukee, US) was secondly prepared. Then, 10 grams of milled titanium were added to the precursor solution. This mixture was dropwise added to the NH_4OH solution. The final solution was stirred at 60 °C until full water evaporation. The resulted powder, named as Y_2O_3/8a/Ti, was totally dried at 180°, disaggregated by milling in alumina mortar and finally thermally treated.

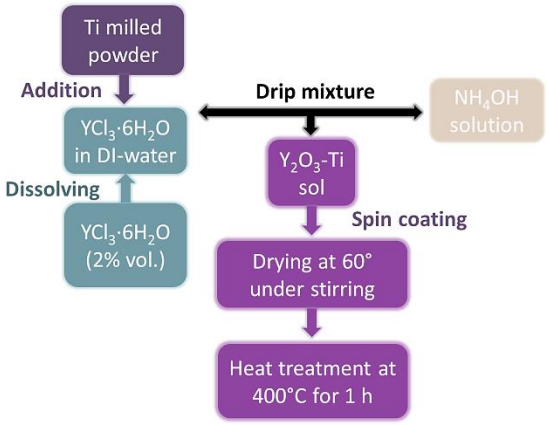

Fig 3.6-1. Preparation scheme of sol-gel coating of Y_2O_3/8a/Ti powder.

In order to find the suitable thermal conditions to eliminate chlorine compounds and other sol-gel side products without altering titanium, Y_2O_3/8a/Ti powder was subjected to a thermogravimetric analysis (TGA) up to 800 °C. A controlled-atmosphere was selected in order to avoid secondary reactions from titanium. Fig 3.6-2 presents the graphics derived of thermogravimetric analyses carried out in nitrogen and argon atmospheres. In both cases, a decrease in weight (%) is observed close to 400 °C that indicated the elimination of chlorides and other reaction products. Among 400 and 500 °C, there is a change in the slope difficult to substantiate. The increase in weight (%) near 500 °C suggests a reaction between Ti

powder and gas within the chamber, to a greater extent within nitrogen than in argon. Titanium has great avidity by nitrogen so, under nitrogen atmosphere, they may react to form titanium nitride. Thus, powders were thermally treated at 400 °C for 1 hour within argon atmosphere. The heating ratio was 5 °C/min.

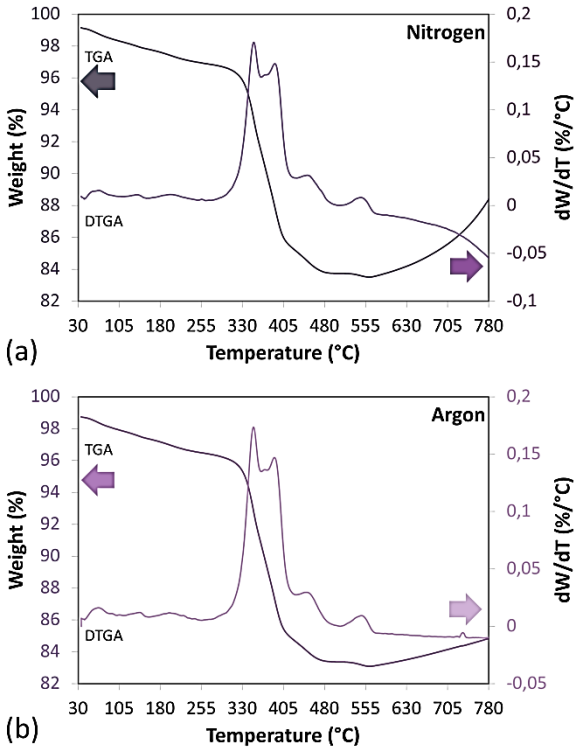

Fig 3.6-2. Thermogravimetric analysis (TGA) of milled-powder modified by sol-gel (Y_2O_3/8a/Ti) method in nitrogen (a) or argon (b) atmosphere.

3.6.1.3 Characterization of m/Ti powders

3.6.1.3.1 *Particle size of milled titanium*

A Beckman Coulter Particle Size Analyzer (LS 13 320 series; Beckman Coulter, Inc, Spain) was used to test the grain size of both 4a/Ti and 8a/Ti powders after sol-gel coating. As shown in Table 3.6-1, Ti powders had smaller size after attrition milling, so this process was effective for reducing the titanium particles. Along this mechanical process, Ti particles are trapped between the colliding balls, so that the powder undergoes deformation and/or fracture processes that refine its ultimate structure [77]. A longer time of milling (8 hours) was more effective for reducing the

titanium grain size. The average particle size decreased in fact 5-fold regarding the initial size (d_{50}=150 µm). Longer milling times were not tested because the difference in size particle among 4 and 8 hours was not very significant.

Table 3.6-1: *Average particle size of Ti powders after attrition milling.*

MILLED TI-POWDER	Average Particle Size, d_{50} (µm)
Ti (GoodFellow, UK)	150
4a/Ti	33.42
8a/Ti	28.86

3.6.1.3.2 *Morphology of milled titanium*

The morphology of 8a/Ti powder was further studied by scanning electron microscopy. Fig 3.6-3 shows a representative SEM-picture acquired from the milled powder. As it can be observed, titanium particles had a lamellar shape as a result of deformation processes during grinding. This can be explained because the kinetic energy of the balls is converted into deformation energy during the approach of their centers in collisions, and this acts modifying the morphology of titanium powder.

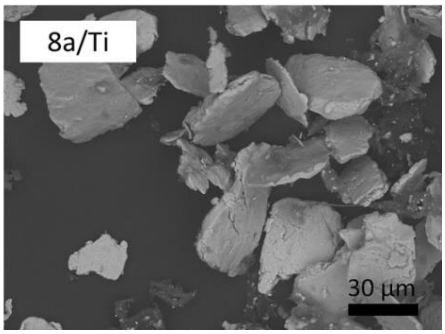

Fig 3.6-3. SEM-micrographs acquired from Ti powder milled for 8h (8a/Ti).

3.6.1.3.3 *X-ray diffraction (XRD)*

Modified Ti powders (m/Ti) were XRD-analyzed with the same setting that the previous XRD-analyses.

These powders were coded as:

On one hand, for Treatment (a):

(1) Ti powder acquired from the manufacturer thermally treated (o/Ti).

On the other hand, for Treatment (b):

(2) Ti powder acquired from the manufacture milled for 8 hours (8a/Ti).

(3) Ti powder acquired from the manufacture milled for 8 hours and Y_2O_3-coated by sol-gel before the calcination treatment (Y_2O_3/8a/Ti).

(4) Ti powder acquired from the manufacture milled for 8 hours Y_2O_3-coated by sol-gel and thermally treated following conditions selected in Section 3.6.1.2 (Ar-Y_2O_3/8a/Ti).

Their respective diffractograms are shown in Fig 3.6-4. According with the data in the ICDD, the position and intensity of the peaks corresponded in all the tested powders with the characteristic ones described for titanium metal (hexagonal, 44-1294). Contamination associated to the different modification processes may also be rejected because none additional crystalline phase is detected in Fig 3.6-4. Contamination is often a serious problem associated to attrition milling [75]. This contamination usually comes from the milling media [79] and may be a reason to discard this technique. This is the reason why zirconia balls were used for milling.

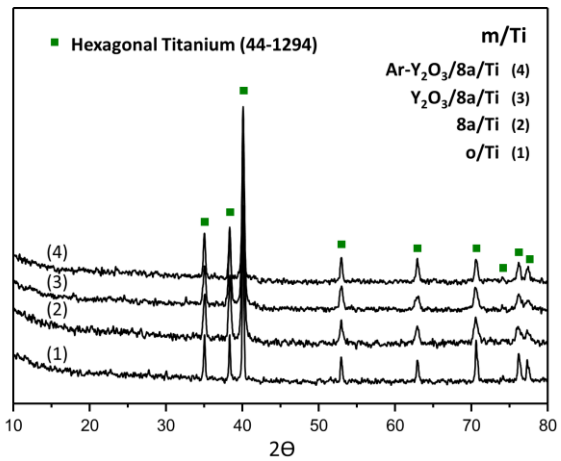

Fig 3.6-4. XRD patterns acquired from the diverse modified Ti powders (m/Ti) (y-axis: arbitrary units of intensity).

As expected from the low percentage introduced (0.3 mol%), the yttrium oxide surface layer created by sol-gel technology covering the titanium surfaces is not detected on sample (4) corresponding to Ar-Y_2O_3/8a/Ti powder.

Moreover, the XRD-pattern of the samples (2), (3) and (4), which involved milled titanium (8a/Ti), had a light increase in the width of the peaks when compared to the sample (1), which comes from oxidized but non-milled titanium powder (o/Ti).

This little difference may be due to microtensions that are introduced in the network as a result of attrition grinding and/or also by changes in the size of the powders.

As opposed to that expected, the diffractogram for the sample (1) that comes from oxidized powder (o/Ti) did not disclosed any peak associated to crystalline forms of rutile or anatase. Gemelli et al. [87] have previously studied the oxidation kinetics in cast titanium, finding that the crystallization of the passive oxide film into anatase occurs between 276 and 457 °C, and into anatase and rutile sublayers between 457 and 718 °C. However, from the XRD-analysis, the treatment at 400 °C seems neither suitable nor sufficient to modify the surface passivation layer of titanium powders.

3.6.1.3.4 *X-ray photoelectron spectroscopy (XPS)*

As the presence of yttria peaks was not detected by XRD over Ti particles, an additional XPS analysis is carried out to disclose the presence of the Y_2O_3-layer. Because this technique analyzes the outermost layer of Ti powders results more suitable for confirming the presence of a surface coating. The analysis was performed on milled-titanium powder after sol-gel coating both in non-thermally treated powder (Y_2O_3/8a/Ti) and in thermally treated powder (Ar-Y_2O_3/8a/Ti). Fig 3.6-5 shows the XPS survey-scans acquired as per setting in Section 7.4.3 (Experimental Techniques, Chapter 5). Table 3.6-2 collects the elementary quantification (%) calculated from the emerged peaks.

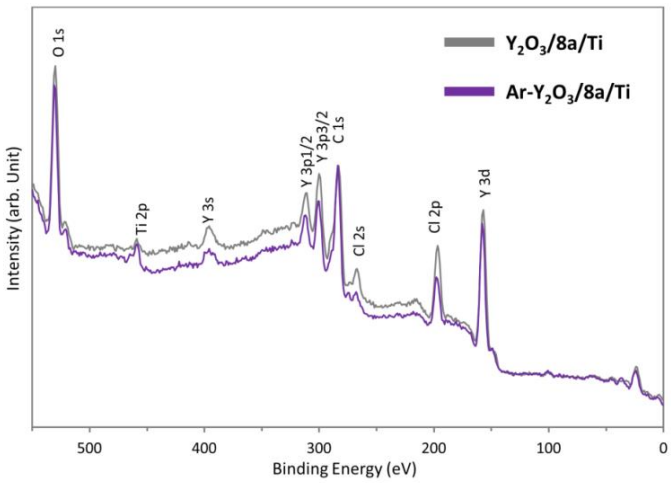

Fig 3.6-5. XPS survey scan acquired from the sol-gel modified powders.

Table 3.6-2: *Elementary quantification (atom %) from XPS-survey scans in* Fig 3.6-5.

SURFACE	ATOM (%)						
	O 1s	C 1s	Ti 2p	Cl 2p	Y 3d	Cl/Y	Y/O
Y_2O_3/8a/Ti	59.1	19.00	0.4	10.9	10.6	**1**	**0.2**
Ar-Y_2O_3/8a/Ti	35.1	37.9	2.8	7.5	16.7	**0.5**	**0.5**

The Y 3d peak emerged with highly-intensity confirming the presence of an yttrium-based coating over Ti particles. This was further supported by the presence of a Ti 2p peak of very low-intensity, suggesting that Ti would be below the coating (Fig 3.6-5). A lower % atomic of Cl 2p in Ar-Y_2O_3/8a/Ti revealed that chlorine products from sol-gel are thermally removed (Table 3.6-2). The Cl/Y ratio is halved in Ar-Y_2O_3/8a/Ti samples so chlorine is not totally eliminated. An increase after the thermal treatment in the Y/O ratio demonstrated that yttrium hydroxides formed as a result of sol-gel were oxidized through yttrium oxides.

In order to further study the chemical composition in the surface layer of Ar-Y_2O_3/8a/Ti powders, a high resolution analysis was carried out for Ti 2p, Y 3d and O 1s core electrons (Fig 3.6-6)

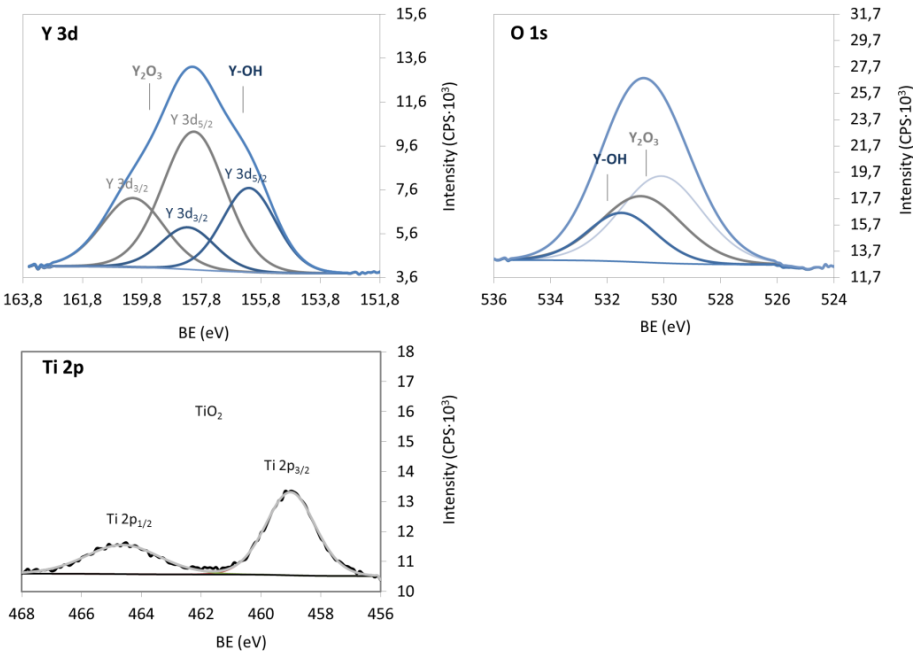

Fig 3.6-7. Y 3d, C1s, and O 1s high-resolution XPS spectra for yttrium oxide deposited on Ti powder.

The Y 3d peak was deconvoluted into two doublets using Gaussian functions. For each doublet a spin orbit splitting of 2.1 eV and peak area ratios of $I_{5/2}/I_{3/2}$= 1.5 is assumed and the Full Width at Half Maximum *w* of each doublet is permitted to vary but set equal for the 5/2 and 3/2 components ($w_{5/2}=w_{3/2}$). The Y $3d_{5/2}$ and $3d_{3/2}$ peaks for the sol-gel coating appeared at 158 eV and 160.1 eV, fitting with the nominal value for the Y $3d_{5/2–3/2}$ doublet in Y_2O_3. A good fit is also obtained for yttrium hydroxides, with values at 156.2 eV and 158.3 eV for the Y $3d_{5/2–3/2}$ doublet. The O1s peak is broad and shifted by 1.9 eV from the nominal position for the O1s peak in Y_2O_3 at 530 eV. The location of this peak is also compatible with the presence of hydroxylated sites at 530.8 eV (Y–OH). There is an extra peak at 531.5 eV that may come from other oxidized species. The Ti 2p peak was deconvoluted into the Ti $3d_{1/2-3/2}$ doublet for TiO_2.

3.6.2 MATERIAL PROCESSING AND SINTERING

Two new types of ZrO_2/Ti (25 vol. % Ti) materials were manufactured using the two types of modified-Ti powders (m/Ti). Processing of powders was performed as described in Section 3.5.2.1. The new mixtures of ZrO_2 and m/Ti powders were named as o/Z-mTi and Ar-Y_3O_2/8a/Z-mTi. From these starting powders, compact specimens were performed with the settings in Table 3.5-3. The new dense ZrO_2/Ti composites were denoted as o/Z-25Ti and Ar-Y_3O_2/8a/Z-25Ti considering each Ti modification. The code Z-25m/Ti was used to name together o/Z-25Ti and Ar-Y_3O_2/8a/Z-25Ti composites. Al these experimental groups are collected in Table 3.6-3.

Table 3.6-3: *Code and description of specimens related to Ti-modification.*

SAMPLE CODE		DESCRIPTION
Modified titanium powder (m/Ti)	o/Ti	Treatment (a): Ti powder acquired from the manufactured and thermally treated in air atmosphere.
	Y_3O_2/8a/Ti	Treatment (b): Ti powder acquired from the manufactured milled for 8 hours and Y_2O_3 coated by sol-gel.
ZrO_2/Ti (25 vol. %Ti) starting powders	o/Z-mTi	Treatment (a): Starting powder made with 75 vol. % zirconia and 25 vol. % of oxidized-titanium (o/Ti).
	Ar-Y_3O_2/8a/Z-mTi	Treatment (b): Starting powder made with 75 vol. % zirconia and 25 vol. % of milled and coated titanium powder (Y_3O_2/8a /Ti).
ZrO_2/Ti (25 vol. %Ti) fired samples (Z-25m/Ti)	o/Z-25Ti	Treatment (a): Compact specimens of ZrO_2/Ti (25 vol. %Ti) composites sintered from o/Z-mTi starting powder.
	Ar-Y_3O_2/8a/Z-25Ti	Treatment (b): Compact specimens of ZrO_2/Ti (25 vol. %Ti) composites sintered from Ar-Y_3O_2/8a/Z-mTi

3.6.3 CHARACTERIZATION OF Z-mTi: X-RAY DIFFRACTION (XRD)

A XRD study was also developed in the mixtures of Z-mTi starting powders in order to reject side reactions within the processing medium. The experimental setup was the same that the used in Section 3.5.2.2. As shown in Fig 3.6-8, additional crystalline phases different to zirconia (tetragonal or monoclinic) and titanium were not revealed, thus discarding the presence of additional compounds or contamination due to processing. Furthermore, no apparent differences in the XRD-pattern were found regarding the starting powders developed with non-modified Ti powder (Z-25Ti; Fig 3.5-3).

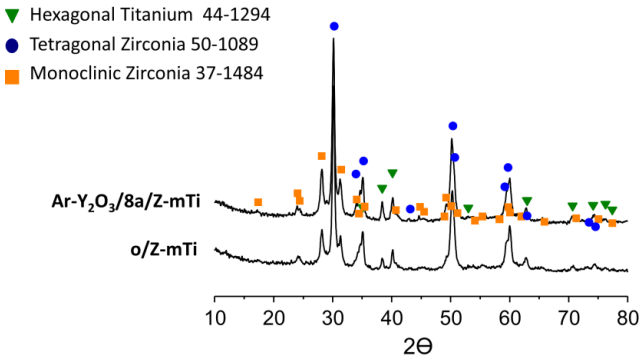

Fig 3.6-8. Diffractograms acquired from the diverse Z-mTi powders (the ordinate that presents arbitrary units of intensity is not shown).

3.6.4 CHARACTERIZATION OF COMPACT Z-mTi SPECIMENS

3.6.4.1 Density

Bulk densities are summarized in Table 3.6-4. The relative density of each sintered Z-mTi composite was very close to the theoretical value, so the used SPS program allowed to reach full densification.

Table 3.6-4: *Densities of SPS-sintered ZrO_2/Ti compacts (Z-mTi) performed with modified Ti (m/Ti).*

Z-mTi System	Measured Density ($g \cdot cm^{-3}$)	Theoretical Density ($g \cdot cm^{-3}$)	Ratio Measured-Theoretical Density (%)
o/Z-25Ti	5.6 ± 0.1	5.7	> 99
8a/Z-25Ti	5.7 ± 0.1		
Ar-Y_2O_3/8a/Z-25Ti	5.6 ± 0.1		

3.6.4.2 X-rays diffraction (XRD)

The new types of Z-mTi sintered specimens were XRD-analyzed with the same parameters that in Section 3.5.2.2. Representative diffractograms acquired from the two types of fired, o/Z-25Ti and Ar-Y_3O_2/8a/Z-25Ti, composites are presented in Fig 3.6-9.

In the case of o/Z-25Ti samples, instead of hexagonal-Ti appeared an oxidized form of titanium. According with the ICDD database, these emerged peaks matched with those specified for Ti_3O (73-1583). As a consequence of the high solubility of oxygen in Ti, titanium oxides can be formed in a wide O/Ti ratio. In an initial oxidation stage, titanium can incorporate low amounts of oxygen in its structure, forming a solid solution. All the phases of TiO_x ($x<0.7$) belong to this structure, highlighting Ti_6O, Ti_3O, Ti_2O and Ti_3O_2 [91]. Therefore, the oxidation treatment (400 °C) in air-atmosphere may favors oxygen entering into solid solution giving rise to Ti_3O. As in composites made with conventional Ti powder (non-thermally treated) (Fig 3.5-6), Ti_2ZrO is revealed, so again α-Ti dissolved a large amount of zirconium and oxygen forming a supersaturated and disordered α-Ti(Zr, O) solid solution at high temperature that results in interfacial Ti_2ZrO during cooling [66].

Ar-Y_2O_3/8a/Z-25Ti samples also disclosed Ti_2ZrO, although in a relatively lower quantity as indicated by lower-intense peaks. In this composite, Ti had face-centered-cubic (FCC) crystalline structure. Previous works have reported a metastable HCP→FCC polymorphic transformation in elemental titanium that is induced by high-energetic mechanical milling [92, 93]. This polymorphic change is associated with significant grain refinement, lattice expansion and increase in volume per atom [94]. Thereby, the thermodynamic and structural instability due to grain size reduction (capillary effect), high strain/strain rate, deformation and elastic strain energy (product of lattice expansion and negative hydrostatic pressure from grain–core to surface/boundary) led to this polymorphism, which is also reported in zirconium [95] and niobium (BCC→FCC)[96]. The FCC crystalline form of Ti was also found in samples after irradiation with 2.2x1015 ions/cm^2 [97] or in specimens submitted to external pressure [94]. Thus, the polymorphic transformation in Ar-Y_2O_3/8a/Z-25Ti materials would be favored within the pressure conditions in SPS.

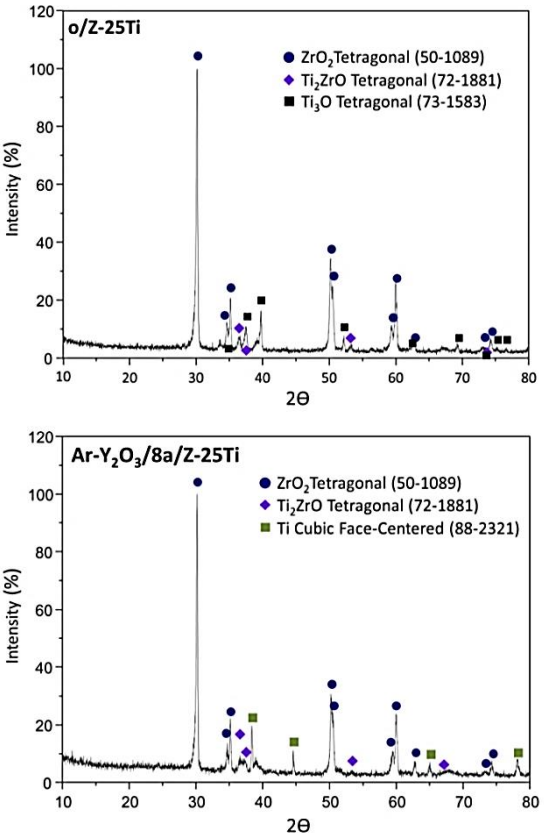

Fig 3.6-9. XRD-diffractograms of the different fired Z-mTi specimens.

3.6.4.3 Scanning electron microscopy (SEM)

A SEM study at low (50x) magnification was performed in order to analyze the overall microstructure in the two types of Z-mTi dense composites. The evaluation was carried out on 1-µm polished specimens using the adequate SEM parameters to reach the maximum contrast between phases. As seen in Fig 3.6-10, darker and brighter phases are Ti and ZrO_2 grains, respectively. All composites had metallic particles homogeneously dispersed throughout the ceramic matrix. In accordance with the density measurements in Table 3.6-4, there is no evidence of porosity. As expected, o/Z-25Ti samples presented bigger titanium particles in the ceramic matrix because they were manufactured from thermally treated Ti powder, which had not been previously milled.

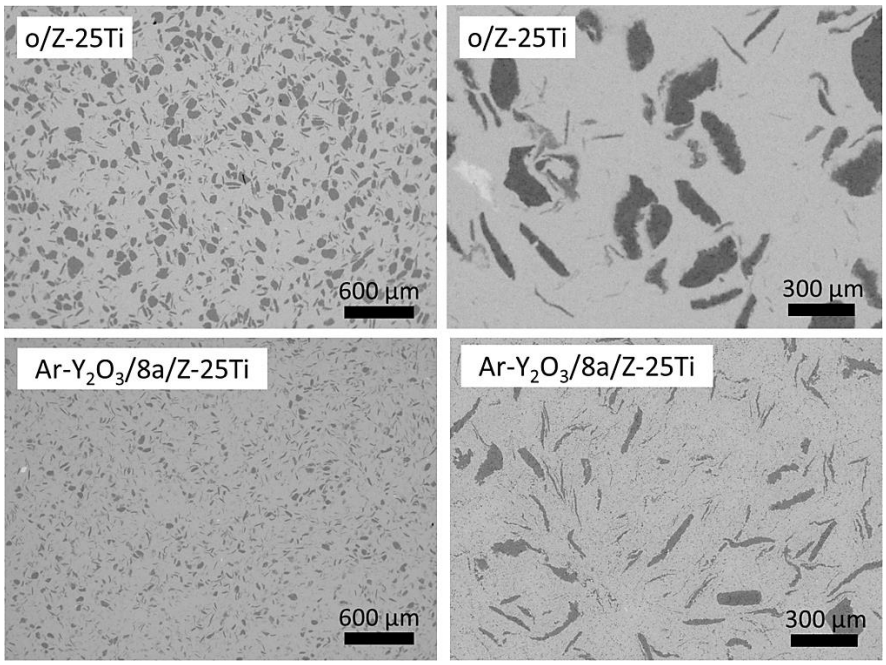

Fig 3.6-10. Microstructure of Z-Ti (25 vol. % Ti) composites manufacture from the diverse m/Ti powders.

3.6.4.4 Hydrothermal treatment

Accelerated aging tests were developed with the same settings that those in Section 3.5.5. The tetragonal-to-monoclinic zirconia transformation was evaluated up to 30 hours through XRD analyses following ISO 13356:2008 instructions. The obtained diffractograms are presented in Fig 3.6-11. Pure zirconia (3Y-TZPE) was also tested as experimental control. In cermets manufactured with thermally-treated Ti powder (o/Z-25Ti), zirconia was destabilized as much as in the Z-25Ti samples (Fig 3.5-12) or even more. However, Ar-Y_2O_3/8a/Z-25Ti specimens do not present apparent destabilization of tetragonal zirconia, even at the longer times; only a low intensity peak of monoclinic phase emerged after 30 hours of hydrothermal treatment. The X_m values (%) for the tested materials are furthermore plotted as a function of the aging time in Fig 3.6-12. In agreement with ISO 13356:2008, none of the studied specimens had X_m values above 25% after 5 hours of aging treatment. In addition, this study allowed to obtain a reasonable prediction of the *in vivo* behaviour of 3Y-TZP based materials. Thereby, the monoclinic fraction increased in o/Z-25Ti specimens with the treatment; above 5 hours of accelerated aging, which would be equivalent to 14 years in the body, this material would lose its stability. However, in

Ar-Y_2O_3/8a/Z-25Ti materials, the monoclinic fraction would remain within the standard's specifications even for a period of 81 years in the human body. Therefore, yttria-coating on milled-titanium particles was effective in order to prevent the hydrothermal tetragonal-to-monoclinic transformation.

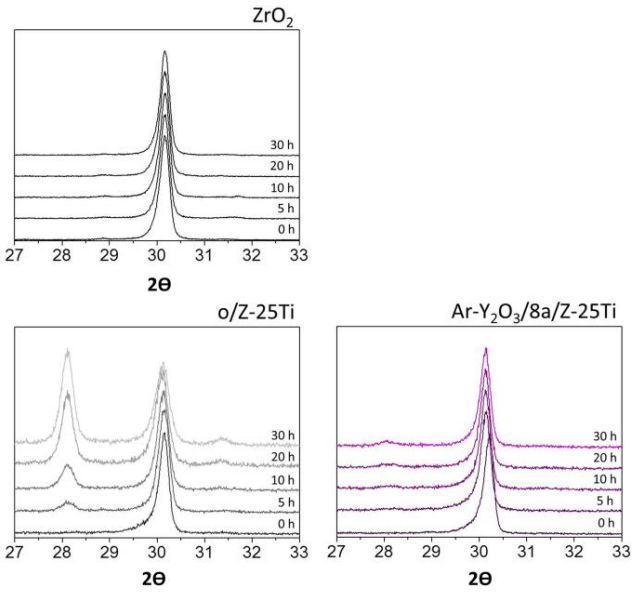

Fig 3.6-11. XRD pattern of Z-mTi samples before and after hydrothermal aging at 134 °C up to 30 hours (y-axis: arbitrary units of intensity).

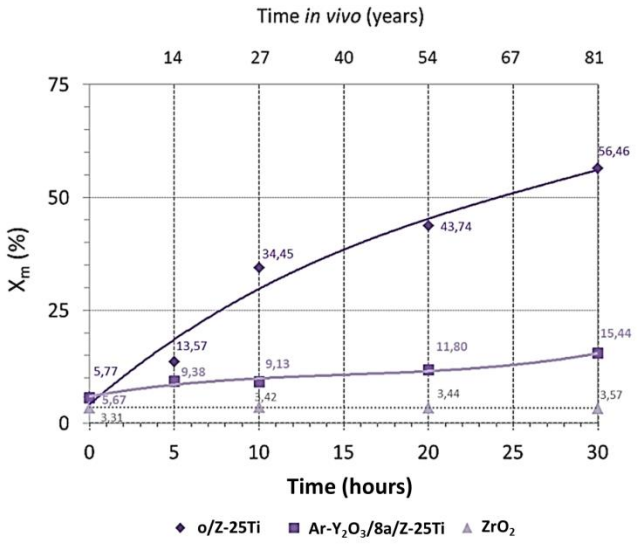

Fig 3.6-12. Monoclinic content in ZrO_2/Ti composites as a function of aging time.

3.6.4.5 Mechanical properties: Bending strength

Mechanical properties in the new ZrO_2/Ti (25 vol. % m/Ti) cermets were approached by bending strength test, which was carried out as explained in Experimental Techniques (Section 7.3.3.1). Table 3.6-5 summarizes the main ± SD (n=5) values of bending strength, σ_f. ZrO_2/Ti (25 vol. %Ti) samples made with milled titanium (named as 8a/Z-25Ti) are introduced to know the exclusive influence of the particle size on bending strength.

As observed, the introduction of a second phase of modified titanium into the zirconia matrix led to increase the flexural strength in all the materials, except for o/Z-25Ti composites. In these modified materials, the presence of Ti_3O (Fig 3.6-9) acted decreasing mechanical properties.

Moreover, cermets manufactured from milled-titanium (8a/Z-25Ti) exhibited enhanced mechanical properties as a result of its fine crystallite size and the larger number of atoms residing at the grain boundaries [79]. In fact, flexural strength in these composites made from milled-Ti was 20% increased regarding Z-25Ti. The bigger titanium grains acted therefore increasing the critical flaw value in the composites, which is also corroborated by the similar σ_f values of A-25Ti (Table 3.4-4) and Z-25Ti (Table 3.5-5).

The average σ_f was still 45% higher in Ar-Y_2O_3/8a/Z-25Ti composites than in 8a/Z-25Ti samples. Indeed, the average was 45% higher that σ_f values in Z-25Ti samples without any modification treatment. Thus, the Y_2O_3-coating on titanium powder, besides of preventing the monoclinic-to-tetragonal transformation in zirconia, synergizes the positive effect associated with the smaller titanium particles, resulting in improved mechanical properties.

Table 3.6-5: *Bending strength of Z-mTi (25 vol. %Ti) composites.*

SYSTEM	BENDING STRENGH, σ_f (MPa)
Z-25Ti	368 ± 47
o/Z-25Ti	119 ± 56
8a/Z-25Ti	440 ± 37
Ar-Y_3O_2/8a/Z-25Ti	637 ± 71

In addition, Fig 3.6-13 shows the fracture surfaces of Ar-Y_2O_3/8a/Z-25Ti cermets disclosing microstructural features. On the right, it can be observed that titanium particles are elongated in the longitudinal axis and disposed in parallel throughout the microstructure due to the application of unidirectional pressure during sintering. These titanium platelets disposed perpendicularly at the direction of the applied load in the bending test opposed the advance of the crack, enhancing flexural strength values. These values were furthermore improved by controlling the reactivity among phases. This can be inferred from the EDX analysis in Fig 3.6-14, which does not evidence the existence of side products.

Moreover, fracture mechanisms can be studied by the picture at higher magnification (on the right) in Fig 3.6-13. Zirconia grains presented the typical appearance of brittle fracture while titanium breakage was also by cleavage.

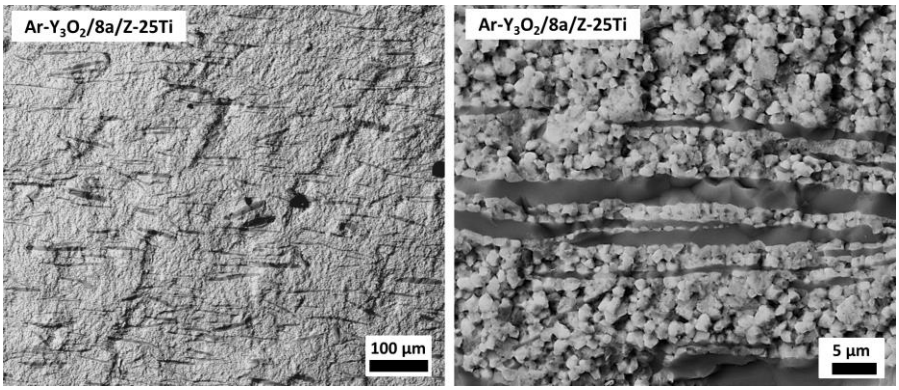

Fig 3.6-13. Fracture surface of Ar-Y_2O_3/8a/Z-25Ti cermets acquired by FE-SEM at low (left) and high (right) magnification.

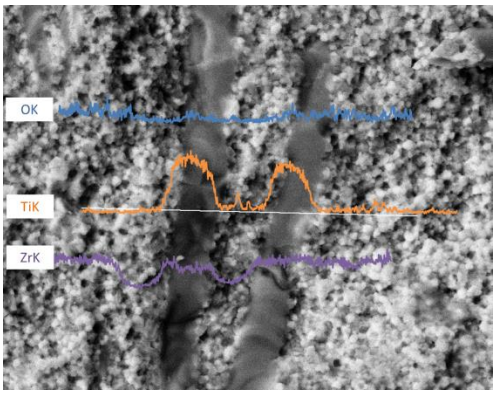

Fig 3.6-14. EDX analysis in fracture surface of Ar-Y_2O_3/8a/Z-25Ti samples disclosing absence of reactivity between zirconia and titanium phases as a result of an yttria coating covering Ti particles.

3.7 DISCUSSION

The application of composites for biomedical applications arises from the idea of improving several mechanical features to a greater extent than using the single components. New ceramic/metal materials (cermets) have been developed with the aim of favourably combining the dissimilar mechanical properties of ceramic and metal counterparts in order to develop better materials mechanically [1, 4, 5, 54]. In this work, the pure components selected were zirconia, alumina and titanium; three suited and widely used biomaterials in dental and orthopaedic fields [10, 11, 98-101].

Other groups had explored successfully the idea of sinergically combining alumina and titanium in a composite form. In this work the system is manufactured in a novel way using the Spark Plasma Sintering technology with the advantage of manufacturing large sets of fully dense specimens (Table 3.5-3) in a short time, besides of controlling the microstructural features and the reactivity among phases. In addition, the Al_2O_3/Ti (25% vol. Ti) system has been characterized in terms of curve-R behaviour and damage tolerance for the first time. It is a remarkable finding that materials with a alumina-matrix reinforced with only 25 vol. % of titanium presented an effective resistance-curve toughening, in such a way that the toughness in the composite was doubled (Fig 3.4-10). This fracture resistance was also accompanied by an exceptional damage resistance, in the form of a significant retention of fracture strengths after indentation on the tensile surfaces (Fig 3.4-9). Thereby, the strength loss in the A-25Ti cermets is much less sensitive to increases of the indentation load than in pure alumina.

ZrO_2 and Ti materials had never been conformed in a composite using spark plasma technology so far. This is a complicated system because during sintering both phases react with each other, forming side compounds that weaken the structure [62, 102]. The SPS technology allows to apply electrical pulses and uniaxial pressure simultaneously within a vacuum; this along with the high heating rates (100 °C/min) facilitates a fast material consolidation, reducing reactivity and maintaining a grain size similar to the starting powders. Micro-nanostructued specimens with 25 vol. %, 50 vol. % and 75 % vol. of Ti had metallic and ceramic constituents homogenously distributed throughout the microstructure (Fig 3.5-8) and density values close to the theoretical ones (Table 3.5-4). Mechanically, Z-Ti composites presented increased hardness values regarding to that expected by the rule of mixtures (Fig 3.5-11) due to the presence of intermetallic compounds.

Although reactivity was more controlled that in previous works, side compounds were formed during sintering of ZrO_2/Ti cerments. It is known that oxygen from the zirconium oxide has a stabilizer effect on α-Ti [51], from which is energetically favorable dissolving up to 34% at. oxygen [67]. Moreover, as a consequence of the high reactivity in the ceramic and metallic phases, yttria reacts with titanium and zirconium forming side compounds, such as $Y_2Ti_2O_7$ (Fig 3.5-9). This leads to drop the characteristic stabilization of 3Y-TZP against aging (Fig 3.6-11). Furthermore, the high difference in grain sizes between ceramic and the metallic particles depletes the adhesion in the ceramic/metal interface, decreasing the mechanical features. By a two-step modification process, which involved attrition milling for 8 hours and posterior yttria sol-gel coating of titanium powder, ZrO_2/Ti (25 vol. % Ti) composites with enhanced mechanical features were achieved. They double the initial bending strength values and did not experiment accelerated aging. Therefore, this line of investigation emerges as a promising way to develop new zirconia/titanium composites with better mechanical response.

3.8 CONCLUSIONS

As overall conclusion:

Two new types of ceramic/metal systems with interesting mechanical properties have been developed by combining three of the most used materials in the biomedical field: zirconia, alumina and titanium.

Particularly,

- A complete study of the rheological behaviour of the ceramic/Ti system has been performed. Powders homogeneously dispersed have been performed using 80 wt. % of solids and 3 wt. % of deflocculant including both alumina and zirconia as ceramic phase so the grain size of titanium conditioned the rheological behaviour of the diverse suspensions.
- The use of the Spark Plasma Sintering (SPS) technique was adequate to perform ceramic-Ti compacts of high density, which had not been achieved yet.
- An effective resistance-curve toughening has been achieved in the Al_2O_3/Ti (25 vol. % Ti) composite, with toughness values that double (from 4 to 8 $MPa{\cdot}m^{1/2}$) those presented by pure alumina.
- The fracture resistance in A-25Ti composites is accompanied by an outstanding damage resistance in terms of significant retention of fracture strengths after indentation on tensile surfaces. Thus, the strength loss in these composites is much less sensitive to increases of indentation load than in pure alumina.
- The processed Z-Ti materials presented were mechanically characterized mechanical in terms of bending strength, Vickers hardness and fracture toughness, with hardness values higher than expected.
- Bending strength was almost doubled in ZrO_2/Ti (25% vol. Ti) composites performed from mixtures of powders with milled and yttria-coated titanium. In addition, these new composites showed an excellent behavior under hydrothermal treatment up 30 hours, showing very close values to those in the samples before the treatment.

3.9 REFERENCES

[1] Moya JS, Lopez-Esteban S, Pecharromán C. The challenge of ceramic/metal microcomposites and nanocomposites. Progress in Materials Science 2007;52:1017-90.

[2] Miranda M, Fernández A, Lopez-Esteban S, Malpartida F, Moya JS, Torrecillas R. Ceramic/metal biocidal nanocomposites for bone-related applications. Journal of Materials Science: Materials in Medicine 2012;23:1655-62.

[3] Pecharromán C, Esteban-Betegón F, Bartolomé JF, Richter G, Moya JS. Theoretical model of hardening in zirconia-nickel nanoparticle composites. Nano Letters 2004;4:747-51.

[4] Bartolomé JF, Gutiérrez-González CF, Pecharromán C, Moya JS. Synergistic toughening mechanism in 3Y-TZP/Nb composites. Acta Materialia 2007;55:5924-33.

[5] Gutiérrez-González CF, Moya JS, Palomares FJ, Bartolomé JF. Low-temperature aging degradation-free 3Y-TZPNb composites. Journal of the American Ceramic Society 2010;93:1842-4.

[6] Smirnov A, Gutiérrez-González CF, Bartolomé JF. Cyclic Fatigue Life- and Crack-Growth Behavior of Zirconia–Niobium Composites. Journal of the American Ceramic Society 2013;96:1709-12.

[7] Katti KS. Biomaterials in total joint replacement. Colloids and Surfaces B: Biointerfaces 2004;39:133-42.

[8] Matsuno H, Yokoyama A, Watari F, Uo M, Kawasaki T. Biocompatibility and osteogenesis of refractory metal implants, titanium, hafnium, niobium, tantalum and rhenium. Biomaterials 2001;22:1253-62.

[9] Gil FJ, Manzanares N, Badet A, Aparicio C, Ginebra MP. Biomimetic treatment on dental implants for short-term bone regeneration. Clinical Oral Investigations 2013:1-8.

[10] Manicone PF, Rossi Iommetti P, Raffaelli L. An overview of zirconia ceramics: Basic properties and clinical applications. Journal of Dentistry 2007;35:819-26.

[11] Chevalier J, Gremillard L. Ceramics for medical applications: A picture for the next 20 years. Journal of the European Ceramic Society 2009;29:1245-55.

[12] Gutierrez-Gonzalez CF, Agouram S, Torrecillas R, Moya JS, Lopez-Esteban S. Ceramic/metal nanocomposites by lyophilization: Processing and HRTEM study. Materials Research Bulletin 2012;47:285-9.

[13] Luo L, Yao J, Li J, Yu J. Preparation and characterization of sol–gel Al2O3/Ni–P composite coatings on carbon steel. Ceramics International 2009;35:2741-5.

[14] Tuan WH, Liu SM, Ho CJ, Lin CS, Yang TJ, Zhang DM, et al. Preparation of Al2O3-ZrO2-Ni nanocomposite by pulse electric current and pressureless sintering. Journal of the European Ceramic Society 2005;25:3125-33.

[15] Diaz M. Procesamiento por vía húmeda de sistemas particulados disimilares Mullita-Molibdeno. Madrid: Universidad Autónoma de Madrid; 2001.

[16] Lopez-Esteban S. Procesamiento, caracterización eléctrica y mecánica de materiales compuestos 3Y-TZP/Ni. Madrid: Universidad Politécnica de Madrid; 2001.

[17] Lopez-Esteban S, Diaz M, Moya JS. Rheology of zirconia/nickel particulate system and microstructure of composites. Composites Science and Technology 2007;67:2303-10.

[18] Rodriguez-Suarez T, Bartolomé JF, Moya JS. Mechanical and tribological properties of ceramic/metal composites: A review of phenomena spanning from the nanometer to the micrometer length scale. Journal of the European Ceramic Society 2012;32:3887-98.

[19] Nygren M, Shen Z. On the preparation of bio-, nano- and structural ceramics and composites by spark plasma sintering. Solid State Sciences 2003;5:125-31.

[20] Tokita M. Development of large-size ceramic/metal bulk FGM fabricated by spark plasma sintering. Materials science forum: Trans Tech Publ; 1999. p. 83-8.

[21] Wang Z, Shi GP, Zhao J, Xing GH. Mechanism and Properties of Ti/Al2O3 Composites by Spark Plasma Sintering Technique. Rare Metal Materials and Engineering 2009;38:450-3.

[22] Zhi W, Kun X, Qiang S, Yingzi W, Lianmeng Z. Effect of Nb on the mechanical properties of Ti/Al2O3 composite. J Wuhan Univ Technol-Mat Sci Edit 2005;20:30-3.

[23] Chen K, Zhang X, Wang H, Zhang L, Zhu J, Yang F, et al. Making Nanostructured Ceramics from Micrometer-Sized Powders via Grain Refinement During SPS Sintering. Journal of the American Ceramic Society 2008;91:2475-80.

[24] Matsugi K, Kuramoto H, Yanagisawa O, Kiritani M. A case study for production of perfectly sintered complex compacts in rapid consolidation by spark sintering. Materials Science and Engineering: A 2003;354:234-42.

[25] Hussain S, Barbariol I, Roitti S, Sbaizero O. Electrical conductivity of an insulator matrix (alumina) and conductor particle (molybdenum) composites. Journal of the European Ceramic Society 2003;23:315-21.

[26] Pecharroman C, Bartolome JF, Requena J, Moya JS, Deville S, Chevalier J, et al. Percolative mechanism of aging in zirconia-containing ceramics for medical applications. Advanced Materials 2003;15:507-11.

[27] www.tosoh.com/Products/basic2_grades.htm.

[28] http://www.taimei-chem.co.jp/product/english/01.html.

[29] http://www.goodfellow.com/.

[30] AENOR. UNE-EN ISO 5832-2:2012 Implants for surgery - Metallic materials - Part 2: Unalloyed titanium (ISO 5832-2:1999)2012.

[31] International A. ASTM F67-00 Standard Specification for Unalloyed Titanium for Surgical Implant Applications (UNS R50250, UNS R50400, UNS R50550, UNS R50700).

[32] Peytour C, Barbier F, Berthet P, Revcolevschi A. Characterization of Al_2O_3/TA6V and ZrO_2/TA6V ceramic-metal interfaces. Journal de physique Colloque 1990;C1:897-902.

[33] Ji H, Jones S, Marquis PM. Characterization of the interaction between molten titanium alloy and Al2O3. Journal of Materials Science 1995;30:5617-20.

[34] Lu H, Bao CL, Shen DH, Zhang XJ, Cui YD, Lin ZD. Study of the Ti/Al_2O_3 interface. Journal of Materials Science 1995;30:339-46.

[35] Gunther R, Klassen T, Dickau B, Gartner F, Bartels A, Bormann R. Advanced alumina composites reinforced with titanium-based alloys. Journal of the American Ceramic Society 2001;84:1509-13.

[36] Braichotte G, Cizeron G. Sintering of (alumina + titanium) powder mixtures and elaboration of the corresponding cermets. Journal of Materials Science 1989;24:3123-36.

[37] Wu S, Gesing AJ, Travitzky NA, Claussen N. Fabrication and properties of Al-infiltrated RBAO-based composites. Journal of the European Ceramic Society 1991;7:277-81.

[38] Toy C, Scott WD. Ceramic-metal composite produced by melt infiltration. Journal of the American Ceramic Society 1990;73:97-101.

[39] Naga SM, El-Maghraby A, El-Rafei AM. Properties of ceramic-metal composites formed by reactive metal penetration. American Ceramic Society Bulletin 2007;86:9301-13.

[40] Loehman RE, Ewsuk K, Tomsia AP. Synthesis of Al_2O_3-Al composites by reactive metal penetration. Journal of the American Ceramic Society 1996;79:27-32.

[41] Claussen N, Knechtel M, Prielipp H, Rodel J. A strong variant of cermets. Berichte der Deutschen Keramischen Gesellschaft 1994:301-3.

[42] Ko SJ, Min KH, Kim YD, Moon IH. A study on the fabrication of Al_2O_3/Cu nanocomposite and its mechanical properties. Journal of Ceramic Processing Research 2002;3:192-4.

[43] Sampath S, Herman H, Shimoda N, Saito T. Thermal spray processing of FGM's. Materials Research Bulletin 1995;20:27-31.

[44] Gutierrez-Gonzalez CF, Bartolome JF. Damage tolerance and R-curve behavior of Al_2O_3-ZrO_2-Nb multiphase composites with synergistic toughening mechanism. Journal of Materials Research 2008;23:570-8.

[45] Rahaman MN, Huang T, Yao A, Bal BS, Li Y. SiC nanoparticle-reinforced Al_2O_3-Nb composite as a potential femoral head material in total hip arthroplasty. Materials Science and Engineering C 2010;30:1197-203.

[46] Fernandez-García E, Gutiérrez-González CF, Fernández A, Torrecillas R, López-Esteban S. Processing and spark plasma sintering of zirconia/titanium cermets. Ceramics International 2013;36:6931-6.

[47] Raddatz O, Schneider GA, Mackens W, Voss H, Claussen N. Bridging stresses and R-curves in ceramic/metal composites. Journal of the European Ceramic Society 2000;20:2261-73.

[48] Flinn BD, Ruhle M, Evans AG. Toughening in composites of Al_2O_3 reinforced with Al. Acta Metallurgica Et Materialia 1989;37:3001-6.

[49] Koyama M, Arai S, Suenaga S, Nakahashi M. Interfacial reactions between titanium film and single crystal α-Al2O3. Journal of Materials Science 1993;28:830-4.

[50] Mas-Guindal MJ, Benko E, Rodríguez MA. Nanostructured metastable cermets of Ti–Al2O3 through activated SHS reaction. Journal of Alloys and Compounds 2008;454:352-8.

[51] Lin K-F, Lin C-C. Interfacial reactions between Ti-6Al-4V alloy and zirconia mold during casting. Journal of materials science 1999;34:5899-906.

[52] Samsonov GV. Handbook of the physicochemical properties of the elements. New York: Plenum Press; 1968.

[53] Braun LM, Bennison SJ, Lawn BR. Objective Evaluation of Short-Crack Toughness Curves Using Indentation Flaws - Case-Study on Alumina-Based Ceramics. Journal of the American Ceramic Society 1992;75:3049-57.

[54] Gutiérrez-González CF, Smirnov A, Bartolomé JF. Aging effect on the tribological behavior of a novel 3Y-TZP/ nb biocomposite against ultra high molecular weight polyethylene. Journal of the American Ceramic Society 2012;95:851-4.

[55] Teng L, Li W, Wang F. Effect of Ti content on the martensitic transformation in zirconia for Ti–ZrO2 composites. Journal of Alloys and Compounds 2001;319:228-32.

[56] RUH R, TALLAN NM, LlPSITT HA. Effect of Metal Additions on the Microstructure of Zirconia. Journal of the American Ceramic Society 1964;47:632-5.

[57] Arias A. Mechanism by Which Metal Additions Improve the Thermal Shock Resistance of Zirconia. Journal of the American Ceramic Society 1966;49:339-41.

[58] Lin CL, Gan D, Shen P. Stabilization of Zirconia Sintered with Titanium. Journal of the American Ceramic Society 1988;71:624-9.

[59] ZHAO E-t, KONG F-t, CHEN Y-y, LI B-h. Interfacial reactions between Ti-1100 alloy and ceramic mould during investment casting. Transactions of Nonferrous Metals Society of China 2011;21:s348-s52.

[60] Ruh R. Reactions of Zirconia and Titanium at Elevated Temperatures. Journal of the American Ceramic Society 1963;46:301-7.

[61] Lin K-L, Lin C-C. Microstructural Evolution and Formation Mechanism of the Interface Between Titanium and Zirconia Annealed at 1550°C. Journal of the American Ceramic Society 2006;89:1400-8.

[62] Lin K-L, Lin C-C. Reaction Between Titanium and Zirconia Powders During Sintering at 1500°C. Journal of the American Ceramic Society 2007;90:2220-5.

[63] International A. C373 – 88. Standard Test Method for

Water Absorption, Bulk Density, Apparent Porosity, andApparent Specific Gravity of Fired Whiteware Products2006.

[64] Abrams H. Grain size measurement by the intercept method. Metallography 1971;4:59-78.

[65] Mendelson MI. Average grain size in polycrystalline ceramics. Journal of the American Ceramic Society 1969;52:443-6.

[66] Lin K-L, Lin C-C. Ti2ZrO Phases Formed in the Titanium and Zirconia Interface After Reaction at 1550°C. Journal of the American Ceramic Society 2005;88:1268-72.

[67] Pimenta J, Buschinelli A, Nascimento Rd, Martinelli A, Remmel J. Joining of zirconia mechanically metallized with titanium. Cerâmica 2010;56:212-21.

[68] Fu S-Y, Feng X-Q, Lauke B, Mai Y-W. Effects of particle size, particle/matrix interface adhesion and particle loading on mechanical properties of particulate–polymer composites. Composites Part B: Engineering 2008;39:933-61.

[69] Samsonov GV. Handbook of the physicochemical properties of the elements. Plenum Press 1968.

[70] Levashov EA, Kurbatkina VV, Zaitsev AA, Rupasov SI, Patsera EI, Chernyshev AA, et al. Structure and properties of precipitation-hardening ceramic Ti-Zr-C and Ti-Ta-C materials. Phys Metals Metallogr 2010;109:95-105.

[71] Garvie RC, Nicholson PS. Phase analysis in zirconia systems. Journal of the American Ceramic Society 1972;55:303-5.

[72] Takasawa K, Wada Y, Ishigaki R, Kayano R. Effects of grain size on hydrogen environment embrittlement of high strength low alloy steel in 45 MPa gaseous hydrogen. Strength, Fracture and Complexity 2011;7:87-98.

[73] Koch C. Structural nanocrystalline materials: an overview. Journal of Materials Science 2007;42:1403-14.

[74] Fang ZZ, Wang X, Ryu T, Hwang KS, Sohn HY. Synthesis, sintering, and mechanical properties of nanocrystalline cemented tungsten carbide – A review. International Journal of Refractory Metals and Hard Materials 2009;27:288-99.

[75] Koch C. Synthesis of nanostructured materials by mechanical milling: problems and opportunities. Nanostructured Materials 1997;9:13-22.

[76] Koch CC. The synthesis and structure of nanocrystalline materials produced by mechanical attrition: A review. Nanostructured Materials 1993;2:109-29.

[77] Yadav TP, Yadav RM, Singh DP. Mechanical Milling: a Top Down Approach for the Synthesis of Nanomaterials and Nanocomposites. Nanoscience and Nanotechnology 2012;2:22-48.

[78] Rawers J. Comparison of attrition milled, nanostructured, powder-compaction techniques. Nanostructured Materials 1999;11:513-22.

[79] Dabhade VV, Rama Mohan TR, Ramakrishnan P. Nanocrystalline titanium powders by high energy attrition milling. Powder Technology 2007;171:177-83.

[80] Liu W, Chen Y, Ye C, Zhang P. Preparation and characterization of doped sol–gel zirconia films. Ceramics international 2002;28:349-54.

[81] Wang D, Bierwagen GP. Sol–gel coatings on metals for corrosion protection. Progress in Organic Coatings 2009;64:327-38.

[82] Fovet Y, Gal J-Y, Toumelin-Chemla F. Influence of pH and fluoride concentration on titanium passivating layer: stability of titanium dioxide. Talanta 2001;53:1053-63.

[83] Lindholm-Sethson B, Ardlin B. Effects of pH and fluoride concentration on the corrosion of titanium. Journal of Biomedical Materials Research Part A 2008;86:149-59.

[84] Chen C-H, Shieh J, Liao H-Y, Shyue J-J. Construction of titania–ceria nanostructured composites with tailored heterojunction for photocurrent enhancement. Journal of the European Ceramic Society 2014;34:1523-35.

[85] Lin C-L, Chen Y-W, Chen E. Preparation and characterization of electrochromic tungsten oxide–titania composite thin films with different tungsten/titanium ratios. Thin Solid Films 2014;556:48-53.

[86] Sakka S, Bouaziz J, Ben Ayed F. Sintering and mechanical properties of the alumina-tricalcium phosphate-titania composites. Materials Science and Engineering: C.

[87] Gemelli E, Scariot A, Camargo NHA. Thermal characterization of commercially pure titanium for dental applications. Materials research 2007;10:241-6.

[88] Sul Y-T, Johansson C, Wennerberg A, Cho L-R, Chang B-S, Albrektsson T. Optimum surface properties of oxidized implants for reinforcement of osseointegration: surface chemistry, oxide thickness, porosity, roughness, and crystal structure. The International journal of oral & maxillofacial implants 2005;20:349.

[89] Rohanizadeh R, Al-Sadeq M, LeGeros R. Preparation of different forms of titanium oxide on titanium surface: effects on apatite deposition. Journal of Biomedical Materials Research Part A 2004;71:343-52.

[90] Oshida Y. Titanium material implants. Google Patents; 2001.

[91] Murray JL, Wriedt HA. The O–Ti (Oxygen-Titanium) system. JPE 1987;8:148-65.

[92] Manna I, Chattopadhyay PP, Nandi P, Banhart F, Fecht H-J. Formation of face-centered-cubic titanium by mechanical attrition. Journal of Applied Physics 2003;93:1520-4.

[93] Bera S, Manna I. Hexagonal close packed to face centered cubic polymorphic transformation in nanocrystalline titanium–zirconium system by mechanical alloying. Journal of alloys and compounds 2006;417:104-8.

[94] Chakraborty J, Kumar K, Ranjan R, Chowdhury SG, Singh S. Stress, Texture and Phase Transformation in Titanium Thin Films. Solid State Phenomena 2010;160:109-16.

[95] Dolgusheva EB, Trubitsin VY. Study of size effects in structural transformations of bcc Zr films by molecular-dynamics simulation. Computational Materials Science 2014;84:23-30.

[96] Seelam UMR, Barkhordarian G, Suryanarayana C. Is there a hexagonal-close-packed (hcp) → face-centered-cubic (fcc) allotropic transformation in mechanically milled Group IVB elements? Journal of Materials Research 2009;24:3454-61.

[97] Sadi S, Paulenova A, Loveland W, Watson P, Greene J, Zhu S, et al. Surface Morphology and Phase Stability of Titanium Foils Irradiated by 136 MeV 136Xe. arXiv preprint arXiv:13011371 2013.

[98] Li Z, Kawashita M. Current progress in inorganic artificial biomaterials. Journal of Artificial Organs 2011;14:163-70.

[99] Kohorst P, Borchers L, Strempel J, Stiesch M, Hassel T, Bach FW, et al. Low-temperature degradation of different zirconia ceramics for dental applications. Acta Biomaterialia 2012;8:1213-20.

[100] Hisbergues M, Vendeville S, Vendeville P. Review zirconia: Established facts and perspectives for a biomaterial in dental implantology. Journal of Biomedical Materials Research - Part B Applied Biomaterials 2009;88:519-29.

[101] Kolk A, Handschel J, Drescher W, Rothamel D, Kloss F, Blessmann M, et al. Current trends and future perspectives of bone substitute materials – From space holders to innovative biomaterials. Journal of Cranio-Maxillofacial Surgery 2012;40:706-18.

[102] Domagala R, Lyon S, RUH R. The Pseudobinary Ti-ZrO2. Journal of the American Ceramic Society 1973;56:584-7.

Chapter 4

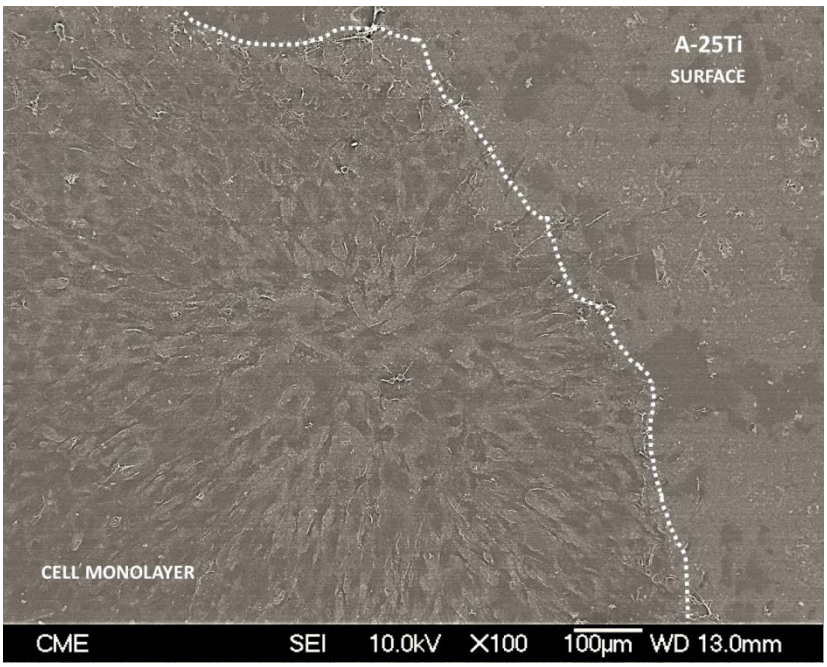

BIOCOMPATIBILITY OF CERAMIC/Ti COMPOSITES

Design and evaluation of ceramic/metal composites for biomedical purposes

4.1 INTRODUCTION

The chemical, physical and mechanical characterization of all materials intended to be used in biomedical applications is essential, but the evaluation of other different aspects such as their behaviour in the biological environment or biocompatibility is also crucial; the improvement of mechanical properties of an implantable device would be useless if it does not possess a suitable biocompatibility once implanted. Thereby, in the particular case of materials involved in the fabrication of bone replacement devices, the evaluation of their ability to osseointegrate is vital.

The key to evaluate biocompatibility of new materials is determining the mechanisms (physical, chemical, biochemical, physiological, etc.) that operate under the specific conditions associated with the contact between biomaterials and tissues, and the consequences of these interactions [1-3]. In this line, the inherent surface characteristics such as texture, roughness, chemical composition, charge, wettability, surface free energy, etc., have great importance because they strongly influence the properties of the *biolayer* (Fig1.5-1) that mediate the cellular interactions [4-7].

The primary material interaction zone with the biological tissues is the outermost atomic layer of the surface [5]. Physically, a surface may be defined as the sudden interruption of the atomic arrangement [8]. This sudden interruption results in different physic-chemical properties between the surface and the bulk regions. Theoretically, different methods utilized for material conforming will lead to different and unique surface properties that can potentially lead to changes in the host-to-implant response [9, 10].

Many studies have demonstrated different effects of material elementary composition on cell behavior [11-13]. L. Di Silvio et al. [14] have reported an enhanced cellular response in hydroxyapatite/polyethylene composites due to increasing the hydroxyapatite volume. Pure Ti and Ti alloys have also induced different cellular behaviour although it is not clear if this is due to the presence of elements of ions released to the cellular medium [15]. Other authors have suggested an improved osteoblastic activity on ZrO_2 materials compared with Ti substrates [13, 16, 17]

The surface energy measured indirectly by the liquid–solid contact angle (CA) is another surface characteristic that affects the biological response to implants. In overall, it is considered that hydrophilic surfaces are more desirable than hydrophobic ones from the biological standpoint [18]. Lim et al. [19] have reported that human

fetal osteoblasts adhered and proliferated better on hydrophilic substrates. R.A. Gittens et al. [20] have also established that hydrophobic surfaces can partially denature proteins, disturbing their tertiary structure and causing cell-binding sites less accessible, which diminish cell adhesion (Fig 4.1-1). However, the optimal degree of hydrophilicity remains unclear [20]. Bacakova et al. [13] have described an optimal cell adhesion in moderately hydrophilic and positively charged substrates, due to the adsorption of cell adhesion-mediating molecules in a geometrical conformation accessible to cell receptors. These authors further established that highly hydrophilic surfaces prevent from the protein adsorption, or lead a very weak bonding in biomolecules. Other authors [21] have nevertheless suggested the initial attachment of osteoblasts increased witht the surface hydrophilicity. Particularly, Wennerberg et al. [22] have demonstrated that on super-hydrophilic surfaces, the fibronectin adsorption would take place in a competitively mode, improving cell adhesion under physiological conditions. Indeed, new titanium systems favor superhydrophilicity. As schematized Fig 4.1-1, hydrophilic surfaces in contact with blood and biological fluids promote protein adsorption in a conformation that exposes adhesion motifs and enhances cell behavior.

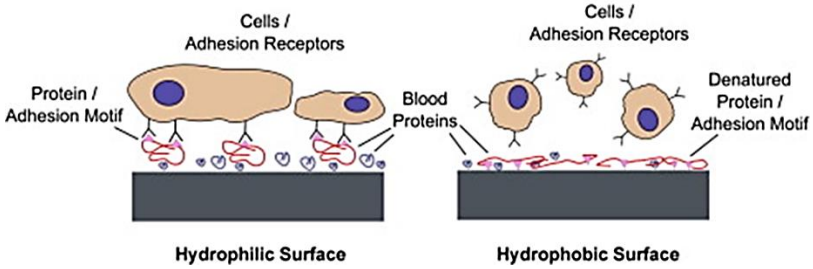

Fig 4.1-1. Schematic depicting the effects of hydrophilic and hydrophobic surfaces on protein adsorption and conformation [20].

Cells are also able to react at different macro/micro/nano-roughness levels [4, 5, 9, 23]. An appropriate macro roughness will enhance the mechanical interlocking between the implant surface and the surrounding bone [23]. Moreover, microroughness (ranging from 1 to 10 µm) has been described as the best to maximize interlocking between mineralized bone and the material surface [24]. Moreover, the effect of nano-roughness has nowadays great interest because of its influence on cellular behaviour at short times; for instance, osseinduction is conditioned by molecular interactions at this roughness level [5, 25]. Previous *in vitro* studies have corroborated an improved osteoblastic adhesion on micronic and

submicronic structures [26, 27]. In addition, cell spreading is increased on ordered and flat surfaces when compared with surfaces of random discontinuity [27].

Clearly, the surface properties determine and affect the biocompatibility of all biomedical devices, but they also influence indirectly on other inherent properties like corrosion resistance, stress shielding, wear debris or fatigue failure [28, 29], so their knowledge and understanding is a highlight in the material's development. Moreover, since the conformation of proteins adsorbed at the inorganic surfaces is determined by the surface properties, by selectively varying their features, materials may be tailored to maximize favorable cellular interactions in terms of increasing the tissue-forming functions [30].

The aim of this chapter is, on hand hand, to assess the *in vitro* biocompatibility of new-developed micro-nano-structured ceramic/titanium cermets, paying special attention to the effect of their surface properties (topography, roughness, surface chemical composition and wettability) on adhesion, proliferation and differentiation of osteoblast-like cells. The pure counterparts (ZrO_2, Al_2O_3 and Ti) were chosen as reference materials in order to better understand the role played by the individual constituents. On the other hand, there are many reports about the *in vitro* and *in vivo* biocompatibility of ZrO_2, Al_2O_3 and Ti in their monolithic form [16, 17, 25, 31-33] but the biological response to ZrO_2/Ti and Al_2O_3/Ti composites has never been studied yet. The new formulations and also the innovative manufacturing process could lead to new and unexpected biological responses that must be assessed.

4.2 OBJECTIVES

The main objective in this chapter is the surface characterization of novel ceramic/titanium composites and the pure counterparts (zirconia, alumina and titanium) in order to correlate these surface properties with the biological response that they induce on osteoblasts, and infer the biocompatibility.

In order to reach the main goal above, the following specific challenges have been established:

- Assessing the topography and roughness on the different composites and pure materials by scanning electron microscopy (SEM) and white light interferometry, respectively.
- Analyzing the different materials by X-ray photoelectron spectroscopy (XPS) for evaluating their surface chemical composition.
- Characterizing the surface wettability by means of an advanced contact angle (CA) goniometer.
- Evaluating a potential cytotoxic effect in the new materials associated to the manufacturing process.
- Studying the osteoblastic behavior induced on each surface both at short times, by evaluating the cell adhesion and cellular spreading, as well as at longer times by studies of cell proliferation and osteogenic differentiation.

With the goal of getting an easily interpretation of results, the two types of studied ceramic/titanium systems (alumina/titanium and zirconia/titanium) are presented in parallel through two independent sections.

4.3 ALUMINA/TITANIUM SYSTEM

As explained before, the final success of any biomedical device depends on both mechanical characteristics and biological aspects. Since the microstructural and mechanical features derived of this novel Al_2O_3/Ti system have already been assessed in the Chapter 3, now it will be come to evaluate the induced biological response.

New Al_2O_3/Ti cermets consist in Al_2O_3 reinforced with 25 vol. % Ti. Alumina has been widely studied in terms of cytocompatibility. In fact, initial works date back to 1990s [34, 35], when *in vitro* and *in vivo* standardized analyses demonstrated that alumina had good biocompatibility related to systemic toxicity, sensibilization, cytotoxicity, mutagenicity, hemolysis, and thrombogenicity [36]. More recent works have described the ability of human bone marrow-derived mesenchymal cells (BMMCs) to attach, proliferate and mineralize both on polycrystalline and single-phase alumina similarly to that on tissue culture polystyrene surfaces [37]. Moreover, enhanced mineralization was suggested on nanofiber alumina substrates [38], whilst nanostructured alumina presented the potential to improve osseointegration of implants by inducting differentiation via up-regulation of alkaline phosphatase, bone sialoprotein, osteopontin and Runx2 [39].

The biocompatibility study of other new alumina-based composites has already been approached; it is the case of alumina/hydroxyapatite [40], alumina/zirconia [41] or alumina/glass [42]. However, studies assessing the properties of alumina/metal composites in the biological environment have not been found in the literature. Thus, this section seeks to advance in the knowledge of the mechanisms induced particularly by Al_2O_3/Ti (25 vol. %Ti) materials in the biological framework and understand how the surface properties influence the behavior of osteoblasts-like cells to, finally infer if the use of this material as prosthetic device would be feasible.

Topography, roughness, surface chemical composition and wettability of Al_2O_3/Ti (25 vol. %Ti) materials were respectively assessed by scanning electron microscopy (SEM), white light interferometer microscopy, X-ray photoelectron spectroscopy (XPS) and contact angle (CA) goniometry. MC-3T3 osteoblasts were chosen to perform co-cultures with the inorganic materials. First, the potential cytotoxicity of these new materials, made by a wet route of powders and spark plasma sintering, was evaluated. Cell adhesion and spreading were tested by immunostaining the F-actin cytoskeleton and by analyzing by SEM the morphology of attached osteoblasts at the studied surfaces. Cell adhesion was also evaluated by measuring the cytoplasmic lactate dehydrogenase (LDH). Cell proliferation was

quantified by measuring the mitochondrial activity with the Alamar Blue assay. Finally, osteogenic differentiation was evaluated by means of measurements of alkaline phosphatase level along the assay time. Tissue culture polystyrene (TCPS) was used as positive control in these assays. Different cellular types can attach and proliferate on TCPS because is fabricated from crystal-grade polystyrene treated by a vacuum-gas plasma process, which introduces carboxyl and hydroxyl groups that give hydrophilic nature to their surfaces. Alumina as the majority phase in the cermet was used as reference material, which allows to get a more realistic approach than with TCPS.

4.3.1 SAMPLES PREPARATION

The alumina/titanium composite with 25 vol. % of Ti (named as A-25Ti) developed in Section 3.4 is now biologically assessed along with its counterpart α-alumina (Al_2O_3). Details about the raw materials, the powder processing and the sintering method have been already described in Section 3.3, Section 3.4.2 and Section 3.4.3, respectively.

SPS-fired samples of 40 mm in diameter were machined in order to obtain 10 mm side squared samples (3 mm of thickness) that fit within 48-well culture plates. Both Al_2O_3 and A-25Ti substrates were polished down to 15 microns in order to achieve a similar roughness pattern. All specimens used in the biological assays were sterilized before the experiments by dry-heating at 200 °C for 1 hour.

4.3.2 SURFACE CHARACTERIZATION

4.1.1.1 Topography/Roughness

The surface topography of Al_2O_3 and A-25Ti samples was evaluated before *in vitro* tests with the scanning electron microscope operating at 10 eV and 250x magnifications. The secondary electrons mode was adjusted in order to achieve the maximum contrast between alumina and titanium phases in the composite. Fig 4.3-1 shows representative SEM-micrographs acquired from the two studied materials. In the A-25Ti cermet, alumina is revealed as the darker component because of being more electron-dense. Ti particles with variable size were uniformly dispersed throughout the alumina matrix, such as was disclosed in the microstructural assessment in the previous Chapter 3. Both substrates had a smooth appearance, with certain degree of surface roughness due to polishing procedures, and there were none evidence of porosity.

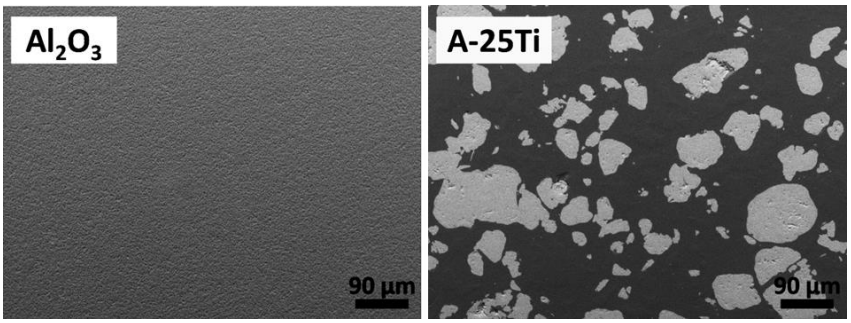

Fig 4.3-1. Topography of the Al_2O_3 and A-25Ti specimens involved in the biological assays (SEM-micrograph of A-25Ti showed the two well-dispersed phases, with Ti as the brighter component).

To exhaustively assess the roughness features of the investigated materials, the three-dimensional surface micro-roughness was studied with a white light interferometer microscopy. Fig 4.3-2 presents representative interferometric images acquired from A-25Ti composites and its counterpart alumina. Both materials had an isotropic roughness, with similar features on the diverse spatial directions, as expected from a uniform mechanical polishing. However, the overall roughness morphology was different depending on the type of material. While A-25Ti samples presented a smoother surface, pure Al_2O_3 had peaks of different heights arranged in a regular pattern. Thereby, materials of different nature (composite and monolithic ceramic) subjected to parallel protocols of polishing had dissimilar roughness characteristics.

Average roughness (S_a) and skewness (S_{sk}) were further quantified from the interferometry images to evaluate the differences in roughness that were found between the two surfaces. Table 4.4-1 summarizes the main ± SD values of these roughness parameters. Both surfaces had a sub-micrometer S_a roughness of approximately 200 microns. As explained in Experimental Techniques (Section 7.4.4), S_a measures the overall surface roughness resulting insensitive to differences in texture characteristics like peaks, valleys or their spacing. Thus, S_{sk} is also evaluated to know if the roughness pattern is mainly composed by valleys or peaks. A-25Ti samples presented negative main S_{sk} values. That means that there is a higher asymmetry related to the mean surface, and that the roughness of the surfaces is mainly due to valley-like structures in the topography. This would be associated with a differential behaviour related to polishing in the two phases forming the composite material. Thus, titanium is characterized to be a very soft material, whereas alumina presents high hardness. The average $S_{sk}>0$ in Al_2O_3 substrates revealed a predominance of

peaks. The posterior mathematical analysis confirmed that differences in average S_{sk} were statistically significant.

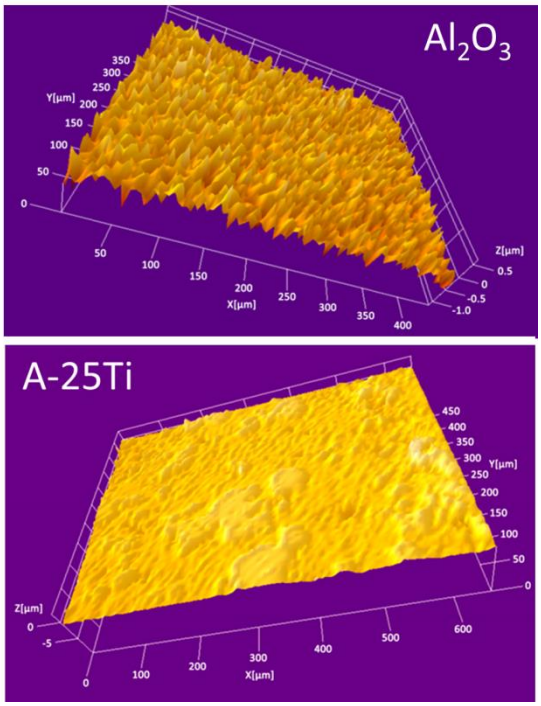

Fig 4.3-2. Roughness: 3D interferometer microscopy images of the Al_2O_3 and A-25Ti materials (some defects appeared due to polishing; in the A-25Ti sample, a burst of grain is revealed).

Table 4.3-1: *Mean ± SD values of roughness parameters S_a and S_{SK} for the A-Ti composite and alumina substrates;* (*a*) denotes statistic differences, p<0.01 (2 letters).

SAMPLE	S_a (nm)	S_{sk} (AU)
Al_2O_3	218.2 ± 9.1	12.82 ± 1.74
A-25Ti	232.3 ± 59.9	- 4.53 ± 1.24$^{(aa)}$

4.1.1.2 Surface chemical composition

The surface chemical composition in the two types of surfaces was analysed by X-ray photoelectron spectroscopy (XPS) as indicated in Experimental Techniques (Section 7.4.3). Fig 4.3-3 presents representative XPS survey-scans acquired from the studied substrates before being used as cell culture substrates. They did not show any

additional element on the surfaces to those derived from the chemical composition in the bulk material (Ti, A, O); with the exception of C, which proceeds from the atmospheric contamination. This analysis allows to discard any surface contamination due to handling or manufacturing operations, which may influence on the cellular response. In addition, elemental quantifications (atom %) from each survey are collected in Table 4.4-2. The DRX-pattern in Fig 3.4-3 informed about the presence of titanium in the bulk material whereas this XPS-analysis also detected Ti in the material surface, although in a low amount when compared with the quantities used in the manufacturing.

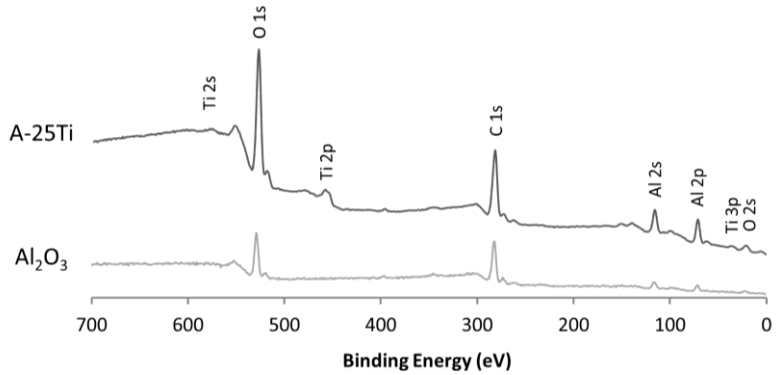

Fig 4.3-3. XPS surveys acquired from Al_2O_3 and A-25Ti substrates (y-axis: arb. units of intensity).

Table 4.3-2: *Elementary quantification (atom %) from XPS-survey scans in* Fig 4.3-3.

Surface	Atom (wt. %)			
	O 1s	C 1s	Al 2p	Ti 2p
Al_2O_3	20	61	19	-
A-25Ti	31	45	22	2

A second XPS study was further developed on A-25Ti and Al_2O_3 materials after *in vitro* experiments. Representative XPS survey scans acquired from these substrates are shown in Fig 4.3-4. This new evaluation makes known the presence of other elements besides of those found in the samples before the *in vitro* assays (Fig 4.3-3). In fact, peaks for nitrogen, chlorine, phosphorus and calcium emerged. In addition, the elementary quantification obtained from the survey-scans in Fig 4.3-4 is presented in Table 4.3-3. The amount of Al 2p (%) decreased compared with the contents in the samples before *in vitro* tests (Table 4.3-2), and Ti 2p (%) is not

detected. Moreover, the percentage of C 1s increased. This, together with the nitrogen peak, reveals the existence of an organic layer coating the inorganic materials. The presence of calcium and phosphorus are related to the formation of calcium phosphates along cell differentiation processes.

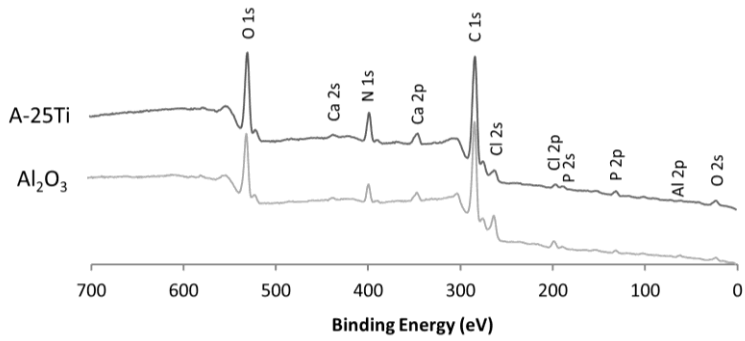

Fig 4.3-4. Surface chemical composition in Al_2O_3 and A-25Ti samples after *in vitro* tests disclosed by X-ray photoelectron spectroscopy (in the y axis, arbitrary units of intensity).

Table 4.3-3. *Elementary quantification (atom %) from XPS-survey scans in* Fig 4.3-4.

SURFACE	ATOM (wt. %)							
	O 1s	C 1s	Al 2p	Ti 2p	N 1s	Cl 2p	Ca 2p	P 2p
Al_2O_3	14.2	75.2	<1	-	6.0	1.7	1.3	1.6
A-25Ti	12.4	75.2	<1	-	7.1	1.5	1.3	1.7

4.1.1.3 Wettability

Wettability properties were assessed measuring the apparent contact angles (CA) of ultrapure distilled (DI) water on each type of material at room temperature as per the settings in Section 7.4.1 of Experimental Techniques Mean and SD values (*n=4*) are summarized in Table 4.4-3. Both Al_2O_3 and A-25Ti substrates presented high CA values. Considering that hydrophobic materials have water-CA values higher than 90° and hydrophilic substrates present values lower than 90° [20], A-25Ti specimens were hydrophilic while Al_2O_3 had hydrophobic character. It is not strange to find different wettability properties in these substrates because the solid-liquid surface interactions depends on the chemical composition, which determines polar (dipole-dipole and hydrogen bonding) and electrostatic (ion-dipole) interactions [43].

Furthermore, the solid-liquid interactions are also affected by the surface type (porosity, roughness and crystallinity) [44].

Table 4.3-4: *Main ± SD values of contact angle (CA) of distilled (DI) water on the Al_2O_3 and A-25Ti substrates.*

CA [°]	SURFACE	
	Al_2O_3	A-25Ti
DI-water	98.18 ± 3.39	80.64 ± 5.27

4.3.3 *IN VITRO* BIOLOGICAL ASSESSMENT

Co-cultures of Al_2O_3 and A-25Ti specimens with the MC-3T3 cell line (pre-osteoblast, mouse, CRL-2593) from the American Type Culture Collection (Manassas, Virginia) were performed. Routine passaging of the cells was carried out on flasks with Minimum Essential Medium (MEM) Alpha without ascorbic acid (Gibco, Life Technologies; Thermo Fisher Scientific Inc.), containing 10% fetal bovine serum (FBS) plus antibiotics (100 U/mL penicillin and 100 mg/mL streptomycin sulfate) and, maintained in an atmosphere with 5% CO_2 at 37 °C.

4.1.1.1 Cytotoxicity tests

The cytotoxicity tests were based on ISO 10993-5 [45]. After incubating the inorganic substrates (3 samples per type of material) for 72 hours in supplemented cell culture medium at 37 °C, the volume extractions and their serial dilutions up to 10^3 were used as culture media for osteoblasts grown during 24 hours. Quantifications of cell viability (%) and cytotoxicity (%) were carried out 24 hours later. Results of both assays are combined in Fig 4.3-5, which presents the main ± SD values of cell viability (%) and cytotoxicity (%).

On one hand, cell viability was assessed by measurements of the mitochondrial activity in osteoblasts. This was indirectly quantified with the colorimetric assay MTS (the basis are explained in Chapter 7, Section 7.5.2.1). According to ISO standard, values of cell viability above 70% confirm non-cytotoxicity for osteblast-like cells [45]. Cell viability was greater than 80% in both the presence of the extraction volume (Vol. Ext) and serial dilutions; thus, no dose-dependent effect related to the substances released from the material to the cell culture media was found to affect the metabolic activity of the cells.

On the other hand, the non-cytotoxic potential in the materials was corroborated by evaluating the LDH activity released from the cytosol of those potentially damaged cells to the culture medium. As explained in Experimental Techniques (Section 7.5.2.2), the higher concentration of LDH released toward the culture media, the higher damage in cellular membranes and higher potential cytotoxic in the materials. The cytotoxicity percentage related to Al_2O_3 and A-25Ti materials was found to be in all cases below 20%, confirming none alteration in the cellular membrane of metabolically active cells. Therefore, cytotoxic effects due to the materials or manufacturing processes are again rejected.

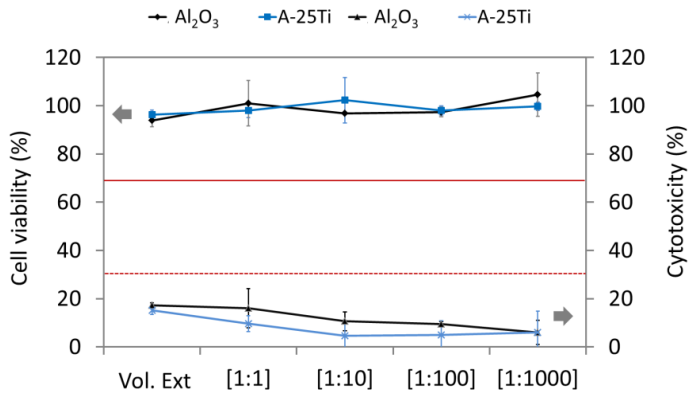

Fig 4.3-5. Cell viability (%) and cytotoxicity (%) tests (the red line indicates the threshold for cell viability, below which a material is considered cytotoxic; the red dashed line indicates the threshold, above which a material is considered cytotoxic).

4.1.1.2 Cell adhesion

The ability of MC3T3 osteoblasts (10^4 cells/ml) to attach at the studied substrates was assessed 24 and 72 hours after seeding. In order to establish possible differences between surfaces, cell adhesion was qualitatively analyzed both by studying the actin-cytoskeleton and the overall cell morphology. In addition, quantitative tests of cell adhesion were performed by measurements of the cytoplasmic lactate dehydrogenase (LDH) activity.

Fig 4.3-6 presents images of fluorescence microscopy that were acquired at 10x from the red-fluorescent actin-cytoskeleton of osteoblasts attached at the Al_2O_3 and A-25Ti substrates after 24 and 72 hours in cell culture. The protocol of immunostaining is collected in the following Chapter 7 (Section 7.5.4.4). The adhesion capability of osteoblasts at surfaces can be inferred by analyzing the organization of the actin-network. The flatter cell morphology of osteoblasts disclosed a better

spreading on A-25Ti surfaces 24 hours after seeding. These differences between substrates apparently disappeared when osteoblasts had been cultured for 72 hours.

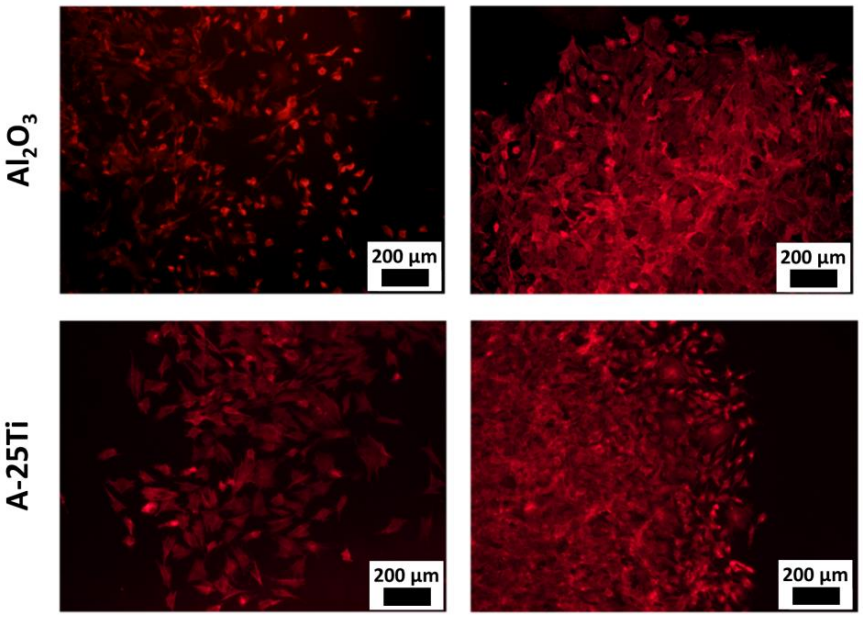

Fig 4.3-6. F-actine network in MC3T3 cells 24 and 72 hours after seeding.

Cell attachment at the surfaces was also analyzed by scanning electron microscopy (JSM-6400, JEOL Ltd., Japan). Before SEM examination, cells were dehydrated with an Et-OH gradient ranging from 30% to 100% and dried in a chamber with silica gel. Secondary electron images were taken operating at 700x and 20 keV. Representative micrographs are presented in Fig 4.3-7. A-25Ti surfaces induced an important dorsal activity in osteoblasts. Cells were well-adhered and presented a tendency to establish intercellular connections by long lamelipodia and filopodia, which allow easily colonizing the surfaces. Cells also spread on Al_2O_3 surfaces, although a lower number of less flattened cells suggested an earlier adhesion stage.

The capability of osteoblasts to adhere at the studied surfaces was further evaluated by measuring the LDH activity 1 and 3 days after plating. At each time, cells were lysed and the cellular extracts tested for 15 minutes at room temperature with the Cytotoxicity Detection Kit^{PLUS}, LDH (Chapter 7, Section 7.5.2.2). Results are shown in Fig 4.3-8 as relative fluorescence units (FAU) per area of sample (cm^2). Since the amount of fluorescence is proportional to the number of living cells, it can be inferred that the cell number increased on Al_2O_3 and A-25Ti substrates over time, to a greater extent on A-25Ti surfaces. Besides, the studied materials induced a statistically higher

cell number than TCPS, the gold-standard substratum for cell culture, at each time. Thereby, A-25Ti composites led to an enhanced osteoblastic adhesion regarding the Al_2O_3 materials, whose biocompatibility had already been proved extensively.

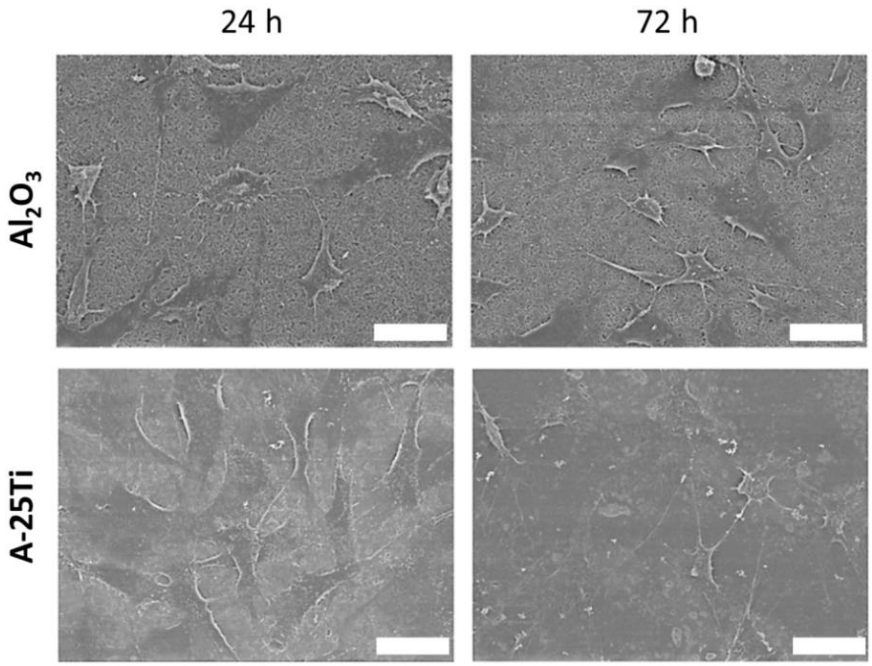

Fig 4.3-7. Cell-material interactions studied from SEM-micrographs of MC3T3 cells attached at the different materials, showing a flatter morphology of cells over the composite surface than on the control (scale bars are 10 µm).

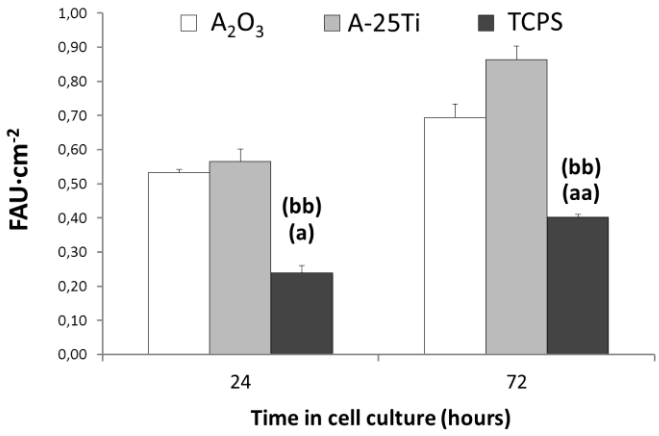

Fig 4.3-8. Time course study of osteoblastic adhesion at Al_2O_3 and A-25Ti surfaces. Data are mean ± SEM (*n=6*). (a) indicates statistically differences related to Al_2O_3 and (b) related to A-25Ti; 1 letter $p<0.05$ and 2 letters $p<0.01$.

4.1.1.3 Cell proliferation

Cells (10^4 cells/ml) were seeded at the center of the A-25Ti composite and, after 1 and 3 days in cell culture, they were prepared for SEM visualization as explained in Section 4.1.1.2. This test was carried out as a first approach to explore the proliferation ability of osteoblasts on the composite surface. Cells may present a preferential adhesion and/or proliferation in one of the constituent phases of the cermet. Fig 4.3-9 shows micrographs of proliferating cells taken at 100x and 10 eV after 24 (a) and 72 hours (b) of seeding. The cell monolayer advanced from the seeding point (marked with a blue dashed circle in Fig 4.3-9(a)) to cover the entire surface of the sample after 3 days in cell culture Fig 4.3-9(b), showing no preference for any specific phase.

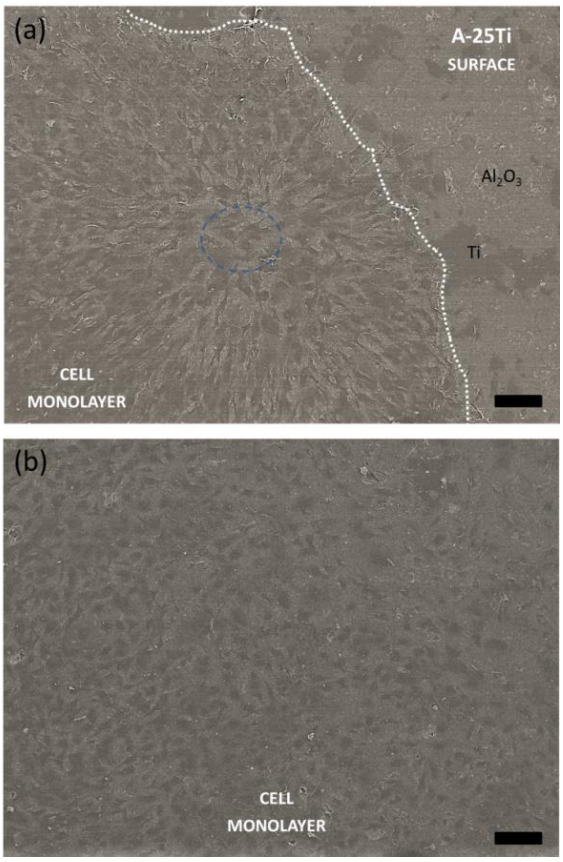

Fig 4.3-9. SEM image at 24 hours (a) and 72 hours (b) of proliferating cells on A-25Ti surfaces (Ti and Al_2O_3 phases are marked in the composite surface while the seeding point –blue dashed circle- is indicated in the cell monolayer) (scale bars=100 µm).

On the other hand, the health and division capability of osteoblasts cultured on the studied materials were monitored by testing their cellular metabolism with the alamarBlue assay kit (Chapter 7, Section 7.5.2.3). MC3T3 Cells (10^4 cells/ml) were seeded on the materials (*n=4*) and, the metabolic activity quantified after 1, 3, 7, 14 and 21 days in cell culture. Results are shown in Fig 4.3-10 (a) as relative fluorescence units (RFU) per cm^2. The amount of fluorescence is proportional to the number of living cells which are metabolically active. Osteoblasts proliferated on Al_2O_3 and A-25Ti substrates along the assay time, reaching the confluence at 21 days. At this time, a similar cell number was found on all materials. Cells reached confluence after 7 days in cell culture on reference TCPS. Thus, a different proliferation pattern is found on each material. When the trendline associated with average values is represented (Fig 4.3-10 (b)), it is found that A-25Ti substrates lead to a lineal osteoblastic growth, whilst Al_2O_3 adjusted better to an exponential proliferation rate and TCPS to a logarithmic growth.

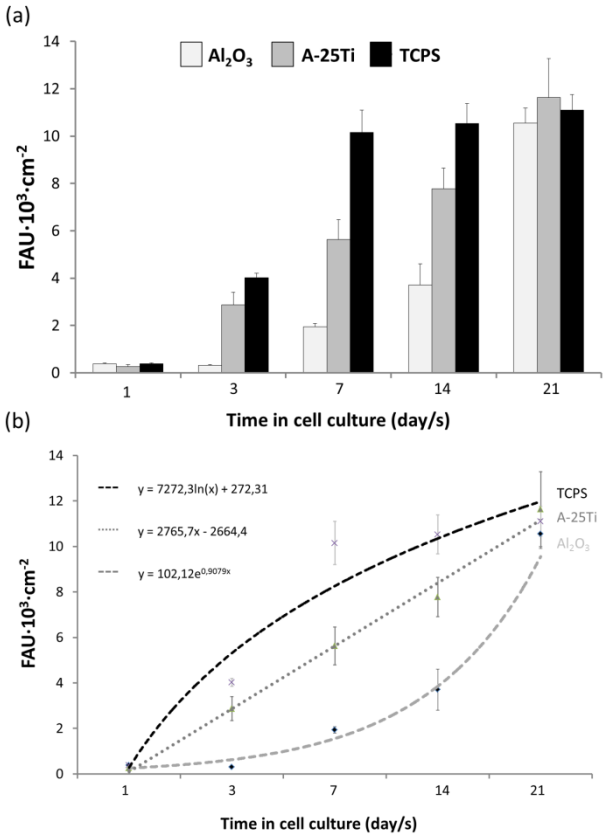

Fig 4.3-10. Osteoblastic proliferation up to 21 days. In (a) data are mean ± SD values (*n=4*); (b) shows the trendline associated to the growth rate of each material.

4.1.1.4 Cell differentiation

Osteoblastic differentiation follows the proliferation program and can be divided into matrix maturation and mineralization depending on the markers expressed [46]. Whilst the matrix maturation phase is characterized by maximal expression of alkaline phosphatase (ALP), mineralization requires induction of osteocalcin and other genes [47]. In order to evaluate the early-differentiation stage induced by the investigated materials, the ALP activity was quantified in cells cultured up to 21 days. Osteogenic factors (ascorbic acid, 50 μg/ml, β-glycerophosphate, 10 mM; dexamethasone, 100 mM) were added 3 days after seeding when osteoblasts reached confluence. The differentiation assay was performed with the SensoLyte pNPP Alkaline Phosphatese Assay Kit following the manufacturer's instructions (Chapter 7, Section 7.5.2.4). Osteoblasts (10^4 cells/ml) were seeded on the studied materials (*n=3*). At each assay time, the ALP activity was spectrophotometrically quantified after incubation the cell lysates with dye solution for 5 minutes. Optical density (λ=405 nm) values were extrapolated to a calibration curve of ALP standard. Results are shown in Fig 4.3-11 as main ± SEM values of ALP concentration (μg/ml) by minute. ALP increased along the assay time on the A-25Ti and Al_2O_3 substrates, which were as suitable as TCPS for supporting cell differentiation. Statistical differences were found between substrates after 7 days in cell culture, when A-25Ti composites induced higher ALP activity than pure Al_2O_3.

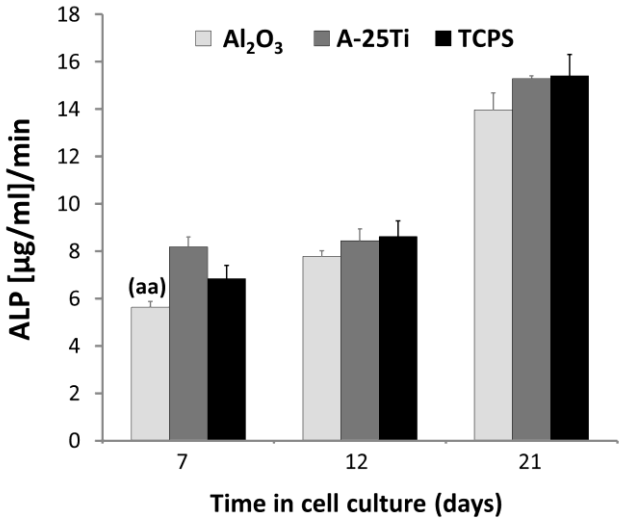

Fig 4.3-11. Time course study of osteoblastic differentiation through LDH quantification. Data are main ± SEM values (*n=6*). Statistical differences (p<0.05) related to A-25Ti are indicated by (aa).

4.3.4 DISCUSSION

Alumina has been studied for different applications. Among them, it has been used as material for orthopaedic devices along a number of years, due to its good biocompatibility, thin capsule formation and low coefficients of friction and wear rates [34, 35, 48]. However, important mechanical drawbacks like its low fracture toughness lead to seek alternative solutions. In this work, alumina-based composites with improved mechanically features have been manufactured by incorporating a uniformly dispersed titanium phase into the alumina matrix (Chapter 3, Section 3.4.4) [49].

Since the application of these novel Al_2O_3/Ti composites, for bone replacements, opens the possibility of improving several mechanical features compared to the monolithics, a study to approach their properties of biocompatibility is essential. Prior to clinical testing, relevant biochemical tests should be performed at the cellular and molecular level, to address biocompatibility issues and long term performance of the implantable devices [50].

On one hand, all new materials intended to be used in biomedical applications must be assessed in terms of *in vitro* cytotoxicity as per ISO 10993-5 [45]. Considering these indications, cell viability and cytotoxicity tests revealed that (Fig 4.3-5) SPSed A-25Ti composites and pure Al_2O_3 were non-cytotoxic.

On the other hand, it is well-known that the surface properties play a crucial role on the material-tissue interactions [4, 5, 10, 12, 13]. In this thesis, topography, wettability and chemical composition were studied.

SEM analyses (Fig 4.3-1) showed that Al_2O_3 and Ti phases were uniformly distributed into the composite's microstructure. Moreover, the surface chemical composition evaluated from XPS survey scans (Fig 4.3-3) fitted well with the relative amounts used for manufacturing the cermet (Table 4.3-2). From the XPS results, surface contamination due to manufacturing or handling on the specimens that may alter cellular phenomena is also discarded.

Surface wettability of Al_2O_3 and A-25Ti materials (Table 4.3-4) varied according the nature of the material. Whereas Al_2O_3 materials were hydrophilic (CA<90), A-25Ti specimens were hydrophobic (CA>90) [20]. Therefore, difference in surface chemical composition determined changes in other related surface characteristics such as wettability [5, 10]. Both chemical composition and wettability strongly influence the absorption of serum protein mediating cellular interactions with the inorganic surfaces [4, 5, 10]. These primary interactions between the surface

and the host tissues determine in first instance the ability of osseintegration and therefore the material biocompatibility [18].

Cell adhesion constitutes the first stage involving cellular interactions with the biomaterial and it affects the processes of proliferation and differentiation that take place later [13, 51, 52]. Cell adhesion involves successive events, which start with the physical-chemical fixation or *attachment* of cells by ionic forces, van der Waals bonds, etc., at the material surface [52]. *Cell adhesion itself* involves long-term events operated by biological molecules like extracellular matrix proteins, plasma proteins and proteins in the cellular membrane that interact with cytoskeleton, inducing the transcription factors that regulate gene expression [51, 52]. By the actin cytoskeleton, cell spreading is studied on the different materials (Fig 4.3-6). Cells cultured for 24 hours disclosed a strong signal for F-actin, indicating a well-organized cytoskeleton on all materials. However, osteoblasts had a more branched-shape on A-25Ti materials than on pure Al_2O_3. This more advanced cell adhesion stage was further confirmed from SEM images (Fig 4.3-7), which showed spreader and more flattened cells on the more hydrophilic A-25Ti surfaces. A larger cell number at 24 hours was also referred by means of quantifying the cytoplasmic LDH activity (Fig 4.3-8). This difference between Al_2O_3 and A-25Ti materials is not surprising because the primary interaction zone is the narrow atomic layer on the physical substrate. Thus, variations in the surface chemical composition [4] and also the wettability [18] influence on the interactions between cells and surfaces.

Interferometric microscopy disclosed an isotropic roughness pattern derived from the mechanical polishing of the studied materials (Fig 4.3-2). S_a values were in the sub-micrometric level, close to 0.2 µm (Table 4.3-1). Several studies have demonstrated the osteoblast adhesion is influenced by surface roughness when this ranges in the submicron to the micron scale [53]. Furthermore, values like those measured in the studied materials (Table 4.3-1) have been described as optimal [54, 55]. Unlike Al_2O_3 substrates, A-25Ti samples had predominantly valleys in its topography. Berry et al. [56] have reported that cells are sensitive to changes in the radius of curvature in the roughness presenting a preference to enter in the larger diameter pits.

A large cell number on the materials 72 hours after seeding (Fig 4.3-8; Fig 4.3-10) indicated that cell proliferation likely begins around this time. Cell number increased over the culture time on the two investigated materials, although with different rate, reaching similar values to TCPS after 21 day in cell culture (Fig 4.3-10). At 3, 7 and 14 days, statistically higher values of metabolic activity ($p<0.05$) were found in A-25Ti substrates suggesting improved proliferation.

As an essential element of ossification, ALP activity was quantified in order to evaluate the osteogenic tendency [17]. The enzymatic activity increased over the culture time on Al_2O_3 and A-25Ti substrates. However A-25Ti substrates led to higher ALP production, at 7 days, point around which the process of differentiation begins (Fig 4.4-11). This is further supported by more intense XPS-peaks of elemental calcium, phosphate, etc., on the surface of A-25Ti samples after cell culture (Fig 4.3-4); elements associated with the formation of calcium phosphates in the mineralization processes.

Therefore, the initial attachment is an important event that leads to produce extracellular matrix and cytoskeletal proteins preceding cell spreading. Thereby, only if the cells are well spread, they can begin to proliferate [23]. The combination of Al_2O_3 with 25% vol. of Ti in the cermet resulted in more hydrophilic surfaces, with submicrometic roughness composed preferentially by valleys, which induced an improved cell attachment (Fig 4.3-6; Fig 4.3-7). This furthermore led to improve the subsequent cellular responses, such as cell proliferation and differentiation. Thereby, in two independent experiments, A-25Ti surfaces were demonstrated better than pure Al_2O_3 to support cell proliferation and cell differentiation. Moreover, proliferating cells in the composite did not follow any preferential pattern associated with either alumina or titanium (Fig 4.3-8). This interesting biological response induced in vitro by the new alumina/titanium cermets opens a promising avenue to obtain new materials of improved mechanical features for biomedical applications and also encourages to continue with other deep biological analyses.

4.4 ZIRCONIA/TITANIUM SYSTEM

Whereas the new composite nature in the alumina/titanium system led to improved biological responses, this part of the work aims to analyze the osteoblastic behaviour associated with the novel zirconia/titanium composites also developed in Chapter 3 (Section 3.5). Thereby, ZrO_2/Ti composites (Z-Ti) with 25, 50 and 75 vol. % of Ti (named as Z-25Ti, Z-50Ti and Z-75Ti, respectively) are now biologically tested along with the pure materials: yttria-stabilized polycrystalline tetragonal zirconia (ZrO_2) and grade I commercially pure Titanium (Ti). The variation in the relative amount of Ti, comprising the entire range of metal, allows to study the effect of chemical composition on the surface properties and the cell behaviour. In addition, this study allows to obtain further information about *in vitro* activity of nanostructured ZrO_2, which is less known that the biological activity induced by conventional (micro-structured) ceramics.

Previous works have reported higher osteoblastic activity on nanosized materials, comparing to those of micrometric structures [16, 57-61]. As shown in Fig 4.1-1 , this is a consequence of the nanostructured surfaces, which possess unique properties that influence cell adhesion directly by affecting the cell–surface interactions and indirectly by influencing the protein–surface interactions [43]. In the latter case, the influence takes place by fostering a preferential adsorption of the proteins that act as an interface between the extracellular and intercellular compartments, thus improving cell behaviour [62, 63]. The specific effects as a result of nanotopography on cellular behaviour have been demonstrated using different cell types like epithelial cells, fibroblasts, myocytes and osteoblasts [62].

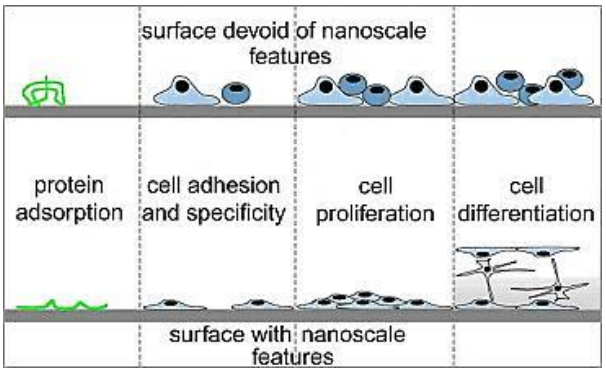

Fig 4.4-1.Depiction of broad-range of nanoscale topography effects observed in cellular protein adsorption due to the nanoscale modification of bulk material [62].

The biocompatibility of new ceramic/Ti cermets will be assessed *in vitro* by means of co-cultures with SaOS-2 osteoblast-like cells. In a first approach, the potential cytotoxicity of these new materials will be evaluated by quantification of the cell viability following instructions of the International Organization for Standardization (ISO). Surface properties under study will be topography, roughness, surface chemical composition and wettability, which will be respectively tested by scanning electron microscopy (SEM), white light interferometer microscopy, X-ray photoelectron spectroscopy (XPS) and contact angle (CA) goniometry. Cell adhesion and spreading will be quantified by using an image analysis system based on immunostaining the nuclei, F-actin and vinculin. Cell proliferation and osteogenic differentiation will also be examined by measuring respectively the LDH cytoplasmic activity and the ALP enzymatic activity along the time.

4.4.1 SAMPLES PREPARATION

Details on the starting powders, processing and sintering methods for all the Z-Ti materials are fully described in Section 3.3, Section 3.5.2 and Section 3.5.3, respectively. Fired samples of 40 mm in diameter were machined to 11.6x11.6x2 mm^3 specimens in order to fit in 24-well culture plates. All specimens were polished down to 1200 grit for achieving a similar surface roughness. The metallic matrix specimens were polished with silicon carbide grinding papers while the ceramic matrix samples with diamond grinding papers. Before *in vitro* experiments, samples were sterilized by ultrasonically cleaning up for 15 minutes in acetone, ethanol and demineralized water and dried at room temperature for 24 hours.

4.4.2 SURFACE ANALYSIS

4.1.1.1 Topography/Roughness

A study of scanning electron microscopy (SEM) was carried out in Z-Ti composites, pure ZrO_2 and pure Ti to qualitatively evaluate the surface topography of those samples that would be in contact with cells. Fig 4.4-2 presents images of representative microstructures of all the studied materials. As corroborated (Fig 3.5-8), the zirconia and titanium phases are well dispersed throughout the microstructure in the cermet. Regarding topography, Z-Ti surfaces had an overall smooth appearance that is interspersed with irregular valleys areas resulting from the mechanical polishing. Thus, ZrO_2 and Ti surfaces showed longitudinal parallel grooves, which are also visible, although in a less marked form, in Z-75Ti cermets. The soft surface of titanium can be inferred from the deeper polishing lines.

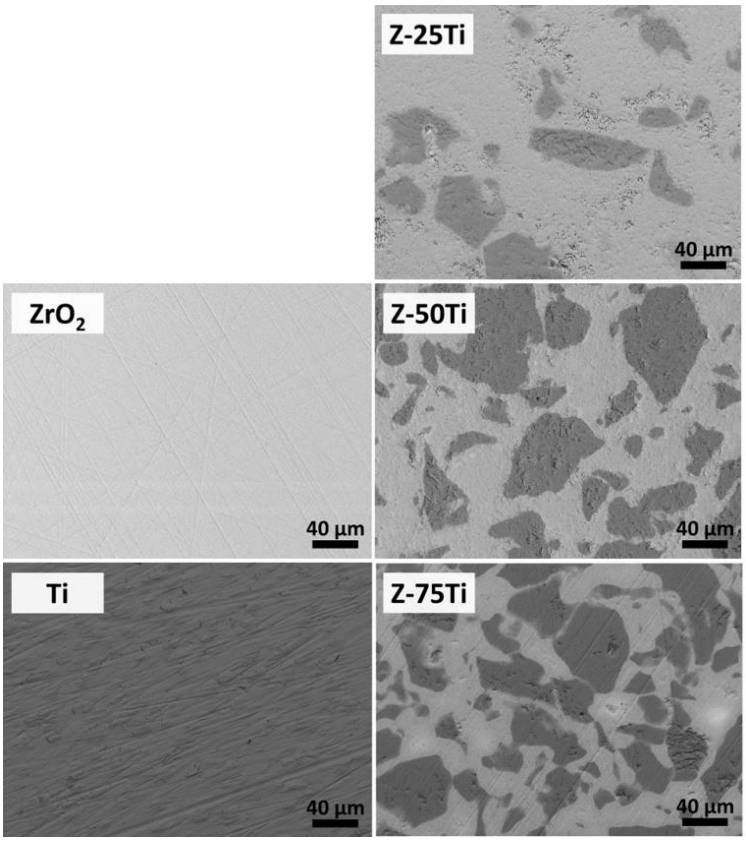

Fig 4.4-2. Topography: SEM-micrographs showing two well-dispersed phases on Z-Ti composites, with Ti as the darkest component.

Three-dimensional surface micro-roughness was examined using an optical laser interferometer with the settings collected in following chapter (Chapter 7, Section 7.4.2). Fig 4.4-3 presents interferometric 3-D images acquired from the diverse materials. All they had an isotropic topography, i.e. with a similar roughness pattern in all directions. The roughness morphology was nevertheless a bit different depending on the type of material, so the differences are associated to changes in composition.

The average roughness (R_a), mean roughness depth (R_z), index area (S_AI) and real surface area (RSA) were summarized in Table 4.4-1. These parameters were calculated by averaging the values of all individual profiles that were evenly distributed along the surface of analysis and were also used to reconstruct the 3-D images. Four measurements were randomly taken in each one of the three different samples of each group.

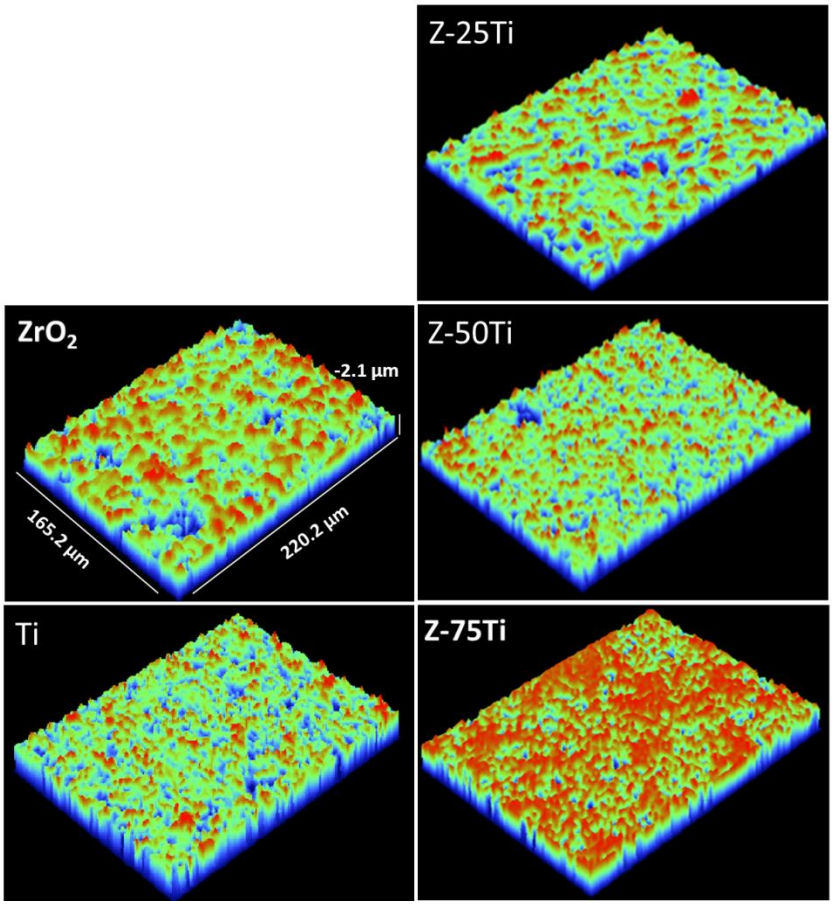

Fig 4.4-3. 3-D images of each surface roughness acquired by white light interferometer microscopy.

Table 4.4-1: *Main ± SD values of roughness parameters.*

SURFACE	R_a (µm)	R_z (µm)	S_AI	RSA (mm^2)
ZrO_2	0.46 ± 0.06	4.82 ± 1.54	1.09 ± 0.08	0.040 ± 0.003
Z-25Ti	0.31 ± 0.03	3.71 ± 0.17	1.05 ± 0.01	0.038 ± 0.003
Z-50Ti	0.53 ± 0.02	7.33 ± 0.31	1.36 ± 0.06	0.049 ± 0.002
Z-75Ti	0.20 ± 0.01	4.00 ± 0.77	1.07 ± 0.01	0.039 ± 0.002
Ti	0.48 ± 0.03	6.98 ± 0.45	1.23 ± 0.04	0.045 ± 0.001

Although all samples had a smooth and regular waved surface, differences in roughness values were found between materials. R_Z average values ranged from 7.3 to 3.7 µm. The higher R_z values were found for Z-50Ti and Ti surfaces. Z-25Ti and Z-75Ti specimens presented lower R_a values than the rest of the groups. Higher R_a values matched with higher RSA and S_Al values, as expected from rougher surfaces. As explained in Section 4.1, surface roughness affects osteoconduction and osseointegration at different scale levels. Indeed, cellular phenomena will be influenced by the measured length scale [5, 25] because molecular interactions with surfaces take place at sub-micrometric level.

4.1.1.2 Chemical composition

A chemical analysis in the different surfaces was conducted by X-ray photoelectron spectroscopy (XPS) such as explained in Experimental Techniques (Chapter 6, Section 6.4.3). As observed in Fig 4.4-4, XPS survey-scans did not show any additional element on the surfaces to those derived from the chemical composition of the bulk material: Ti, Zr, Y, O; except C that as usual appears from atmospheric contamination. The elementary quantification, in atomic percentages, calculated from the survey scans is also presented in Table 4.4-2. Besides of discarding the existence of surface contamination due to manufacturing, these XPS analyses also confirm that the amount of Ti (% atom) on the Z-Ti surfaces decreased in the same way that the ZrO_2 content is increased in the bulk material.

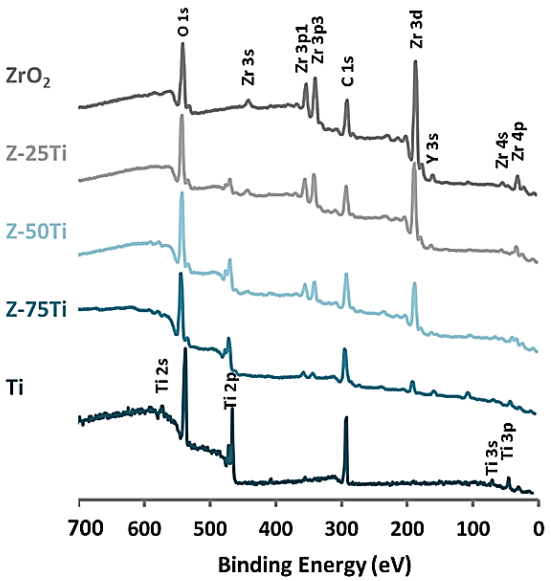

Fig 4.4-4. Surface chemical composition analyzed by X-ray photoelectron spectroscopy.

Table 4.4-2: *Elementary quantification (atom %) from XPS-survey scans. Data are mean ± SD (n=3).*

SURFACE	ATOM (% weight)				
	O 1s	Ti 2p	C 1s	Zr 3d	Y 3d
ZrO_2	28.9 ± 3.0	-	44.8 ± 6.2	24.5 ± 2.7	1.8 ± 0.5
Z-25Ti	28.5 ± 1.7	2.3 ± 1.3	51.6 ± 7.2	16.7 ± 4.2	0.9 ± 0.3
Z-50Ti	33.5 ± 3.1	5.5 ± 1.1	52.7 ± 1.5	7.9 ± 0.4	0.3 ± 0.1
Z-75Ti	36.1 ± 1.3	7.6 ± 0.7	52.0 ± 1.9	3.5 ± 0.2	-
Ti	36.9 ± 0.1	14.5 ± 3.2	52.2 ± 2.0	-	-

4.1.1.3 Wettability and Surface free energy (SFE)

Table 4.4-3 summarizes the mean and SD values of apparent static contact angle (CA) of DI-water on the different materials (n=12) measured with the sessile drop method through Young's equation as indicated in Experimental Techniques (Chapter 7, Section 7.4.1). The most hydrophilic surface was Z-75Ti, with a distilled-water CA of approximately 54°. The rest of the materials exhibited a hydrophobic behaviour, with CA values higher than 85°.

Table 4.4-3: *Main ± SD of contact angle (CA) of distilled (DI) water.*

CA [°]	SURFACE				
	ZrO_2	Z-25Ti	Z-50Ti	Z-75Ti	Ti
DI-water	85.58 ± 1.18	86.80 ± 3.26	88.10 ± 4.52	54.25 ± 1.31	86.59 ± 3.04

In addition the surface free energy (SFE) with its dispersive and polar components was studied from the diverse CA values of DI-water, formamide and diiodomethane by using the Owens-Wendt-Kaeble equation (Chapter 7, Section 7.4.1). Fig 4.4-5 presents the main ± SD values of SFE in the solid substrates (n=12). For each material, it is also indicated how the average dispersive component (light color) and the average polar component (dark color) contribute to the surface free energy. SFE ranged from 35 to 45 mJ/m^2. Z-75Ti surfaces, the most wettable studied surfaces, also presented the highest SFE and, in consequence, the highest surface polarity.

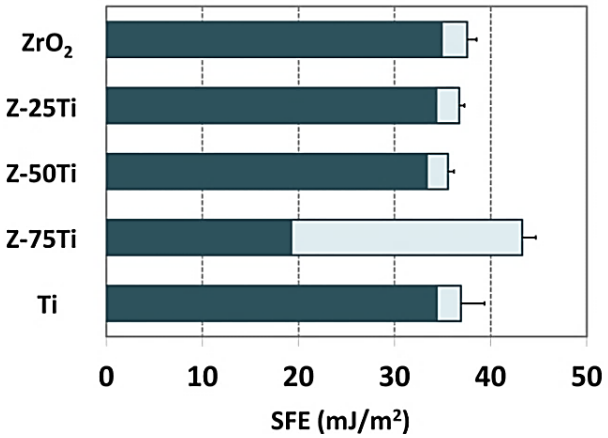

Fig 4.4-5. Average Surface Free Energy (SFE). The main dispersive component is represented as dark blue and the main polar component as light blue; error is the SD of the SFE.

The microstructural assessment developed in the previous Chapter 3 (Section 3.5.4.3), reported the presence of additional phases in the new Z-Ti composites, mainly in the interface of Z-75Ti specimens. Those compounds were identified as Ti_2ZrO and $Y_2Ti_2O_7$ from literature [64]. As known, differences in surface composition determine changes in the related surface characteristics such as wettability, CA or SFE [5, 10] so, these secondary compounds may act therefore modifying the wettability properties of Z-75Ti samples.

4.4.3 IN VITRO ASSESSMENT

The human osteoblast-like SaOS-2 cells (ATCC, Manassas, VA, US) were cultured in McCoy's 5A supplemented with 15% fetal bovine serum (FBS), L-glutamine (1.5 mM), sodium pyruvate (2 mM) and penicillin/streptomycin (50 U/ml and 50 µg/ml, respectively) at 37°C in a humidified incubator at 5% CO_2, changing the medium every 2 days. Subconfluent cells were trypsinized using a 0.05 % trypsin-EDTA solution, centrifuged and counted using a hemocytometer in order to ensure the required cell number for each *in vitro* assay.

4.1.1.1 Cytotoxicity test

As in the Alumina/Ti system, cytotoxicity tests were based on ISO 10993-5 [45]. Cell quantifications were performed at different exposure periods with the colorimetric assay WST-1 (Chapter 6, Section 6.5.2.1). In particular, cell viability was measured after 24 hours of cellular growing in presence of the extraction volumes

(Vol. Ext.) and the serial dilutions up to [1:1000], such as specified in the ISO standard and, complementarily, after getting in touch along 72 hours. Dehydrogenases in metabolically active cells cleaved the slightly yellow tetrazolium salt to dark yellow formazan salt, which was spectrophotometrically assessed at λ=440 nm. An increase in the absorbance of the dye solution directly correlated with an increase in cell number. Whilst the standard establishes that the cell viability ratio must be above 70% for the extraction volume and the dilutions, the found cell viability values were higher than 80% in all the tests; both for the zirconia/titanium cermets and for the ZrO_2 and Ti monolithic samples (Fig 4.4-6).

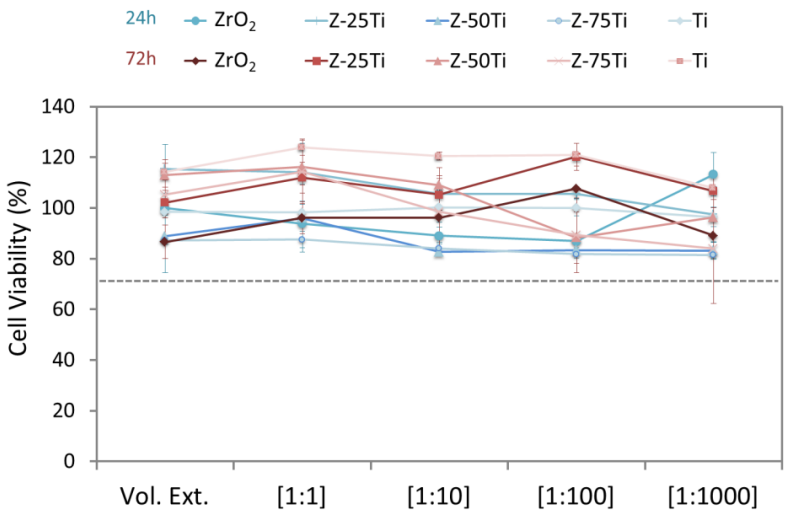

Fig 4.4-6. Cell viability (%) related to Z-Ti cermets and pure materials assessed as per ISO 10993-5 instructions after 24 (a) and 72 (b) hours; (the dashed line indicates the threshold below which a material is considered cytotoxic).

4.1.1.2 Cell adhesion

The capacity to adhere of SaOS-2 cells at the diverse substrates was assessed after 24 and 48 hours in cell culture. The cells ($20x10^3$ cells/ml) were seeded onto the samples, which had been previously sterilized within ethanol (70%, v/v), rinsed with PBS and incubated for 24 hours in FBS in order to ensure a uniform distribution of serum proteins onto the samples. In this case, agarose-coated 24-well plates were used, to prevent cell attachment on the well [38]. The triple immunostaining of cells was performed following indications in the *Actin Cytoskeleton and Focal Adhesion Staining Kit*, FAK 100 (Chapter 7, Section 7.5.3).

Fig 4.4-7 shows the morphology and spreading of attached SaOS-2 cells at the studied surfaces, which was studied by the rearrangement of the red-flourescence actin cytoskeleton.

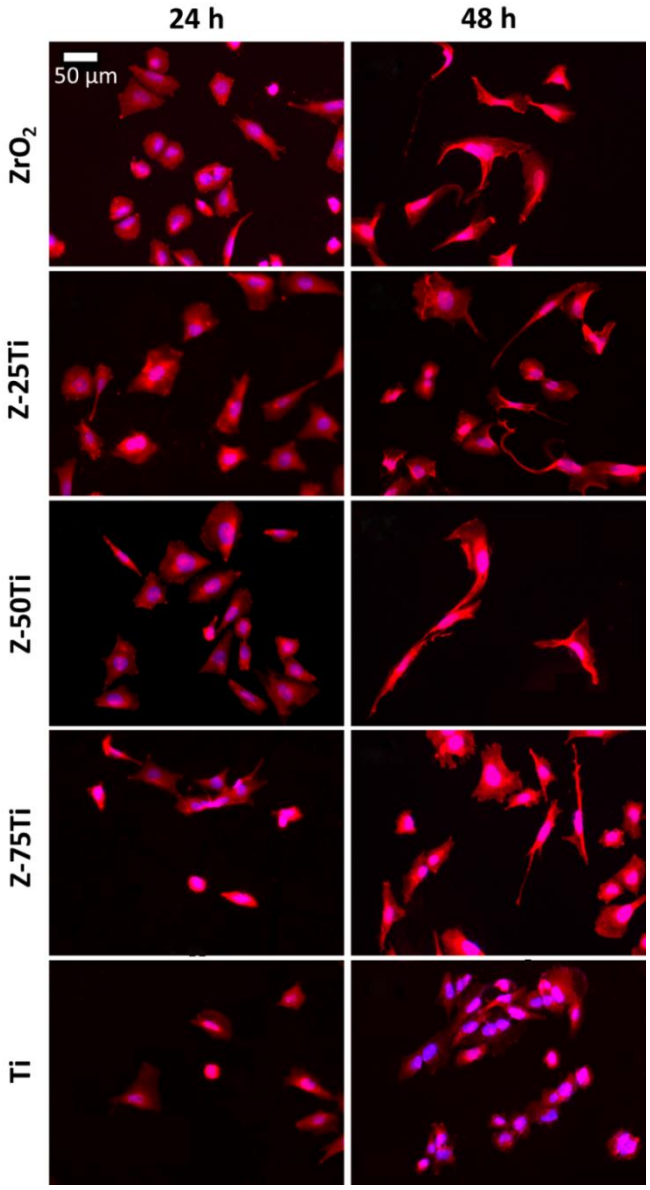

Fig 4.4-7. Morphology of adherent SaOS-2 cells disclosed by the rearrangement of immunolabeled F-acting in the cellular cytoskeleton. Images were taken by fluorescence microscopy at 20x. Cells were stained with DAPI for nuclei (blue) and FITC-phalloidine (red) for F-actin.

Osteoblasts presented spindle-shaped morphology and more complex morphologies at the longest culture time (48 hours). They also showed important dorsal activity and tendency to establish intercellular connections through filopodia after 48 hours of culture on the different substrates. In overall, ZrO_2 and Z-Ti cermets promoted a more elongated shape of osteoblasts than Ti. Indeed, the cytoskeletal reorganization was prominent in cells cultured on ZrO_2 containing materials, with actin fibers arranged throughout the cell body and the cellular extensions. Because cell attachment mechanisms influence signal transduction and regulation of gene expression [65], these early differential responses of osteoblasts may have functional implications on the subsequent extracellular matrix mineralization and bone ingrowth at the cell-biomaterial interface.

In addition, Fig 4.4-8 displays focal adhesion structures revealed by confocal microscopy from the green-fluorescence of immunolabeled vinculin. As previously presented in Fig 4.3-8, in order to form an anchoring junction, cells must first attach at the surfaces. Once they have been attached, a bulky cytoskeletal is assembled around the molecules that directly mediate cell adhesion and a well-defined adhesion structure, commonly referred as focal adhesion, is formed. The existence of large areas of focal adhesions distributed along the cell borderline is confirmed 48 hours after seeding in the different materials. Furthermore, it is noteworthy that Z-Ti surfaces enhanced the expression of vinculin.

Micrographs acquired by fluorescence microscopy at 20x magnification were additionally examined using the ImageJ software [66] to evaluate cell-shape parameters [13, 27]. Cell area was quantified to infer the cellular spreading. Circularity was calculated to assess the cellular morphology according Equation 4.4-1 so that, if values tend to one, cell shape is more circular than if they tend to zero.

$$\textbf{Circularity} = \left[\left(\frac{\boldsymbol{area}}{\boldsymbol{perimeter}^2}\right) \mathbf{4\pi}\right] \qquad \text{Equation 4.4-1}$$

Fig 4.4-9 shows how the area of the cells adhered at the tested substrates increased as the ZrO_2 vol. % in the bulk material, with values significantly enhanced on ZrO_2-containing materials, if compared to Ti specimens, at both 24 and 48 hours. Regarding morphology, cells had a 0.5 value of circularity onto every surface 24 hour after seeding. However, cellular circularity decreased on all substrates at 48 hours, to a higher extent in the samples containing ZrO_2.

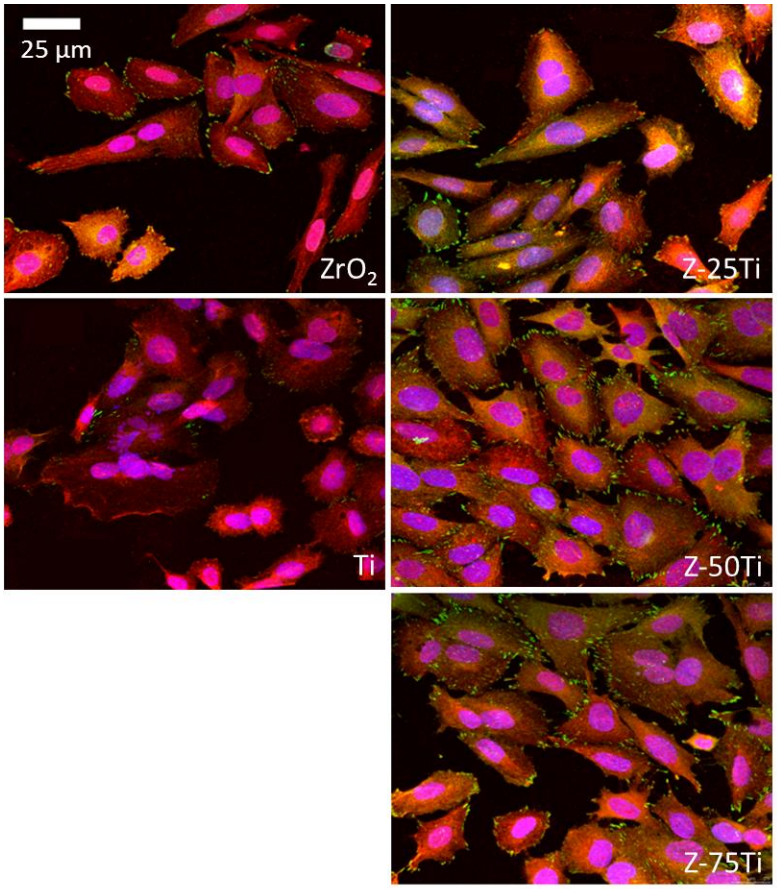

Fig 4.4-8. Focal adhesions visualized from immunostained vinculin by confocal microscopy in osteoblasts cultured for 48 hours. Cells were stained with DAPI for nuclei (blue), FITC-phalloidine (red) for F-actin and vinculin (green).

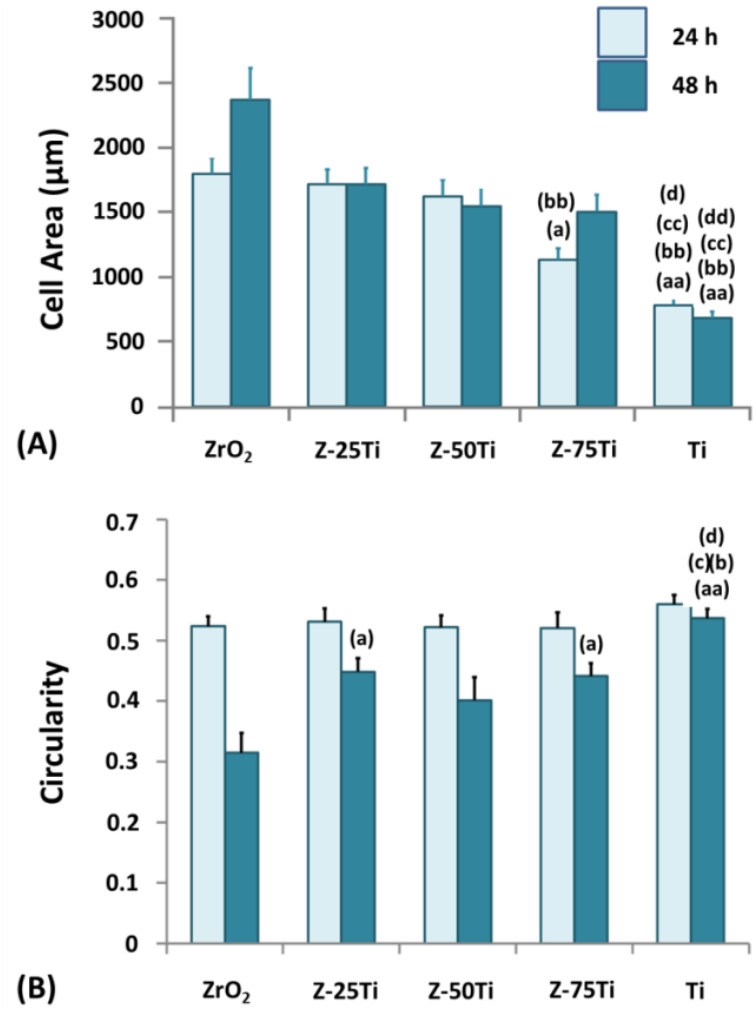

Fig 4.4-9. Cell area (a) and circularity (b) of osteoblasts cultured for 24 and 48 hours. Data are mean ± SD (*n=3 samples; 5 images per sample*). At each time, *(a)* compares to ZrO_2, *(b)* compares to Z-25Ti, *(c)* compares to Z-50Ti, *(d)* compares to Z-75Ti; p<0.01 (2 letters), p<0.05 (1 letter).

4.1.1.3 Cell proliferation

The proliferation capability of cells cultured on the materials was tested by evaluating cellular metabolism. With this goal in mind, the cytoplasmic lactate dehydrogenase (LDH) was quantified 1, 3, 7 and 14 day/s after cell seeding with the LDH Cytotoxicity Detection Kit (Chapter 7, Section 7.5.2.2). SaOS-2 cells (10^4 cells/ml) were plated onto each sample sterilized and pre-incubated in FBS, as described in Section 4.1.1.2 for the adhesion assays. The reduction of the tetrazolium salt into the formazan dye is a reaction coupled to the LDH activity and this can be measured spectrophotometrically at optical density of 492 nm. The cell number is obtained at each culture time from the extrapolated OD_{492} values in a calibration curve with cells ranging from 0 to $50x10^3$. Furthermore, the results are normalized through the corresponding S_AI index calculated by interferometric analyses (Table 4.4-1). Fig 4.4-10 shows the time course study of proliferation onto the different ZrO_2/Ti composites and the pure monolithics. In overall, the number of SaOS-2 cells increased during the culture time on the tested substrates so, all of them were sufficiently suitable to support cell proliferation. Cell number was enhanced on materials with high percentage of ZrO_2 at the beginning of the proliferation test (1 and 3 days). This trend was maintained at longer culture times (7 and 14 days), with the exception that statistically higher cell numbers were found on Z-75Ti surfaces at both time points.

4.1.1.4 Osteogenic differentiation

For this assay, osteoblasts (10^4 cells/ml) were seeded on the materials, supplementing the medium after 24 hours with osteogenic factors. Cells were lysed after 1, 3, 7 and 14 day/s and cellular extracts incubated for 15 minutes at room temperature with the substrate pNPP (Chapter 7, Section 7.5.2.4). The absorbance was measured (λ=405 nm) and optical density values were extrapolated to a calibration curve of ALP standard. Results were normalized with the number of cells obtained from LDH activity and with the incubation period. As shown in Fig 4.4-11, this enzymatic activity increased with time on all the studied series, which properly supported osteoblastic differentiation. Cytoplasmic ALP activity was higher on ZrO_2-containing surfaces at earlier culture times (1, 3 and 7 day/s). At 14 days, ALP activity was similar in all samples except for Z-75Ti, which showed the statistically significant highest value.

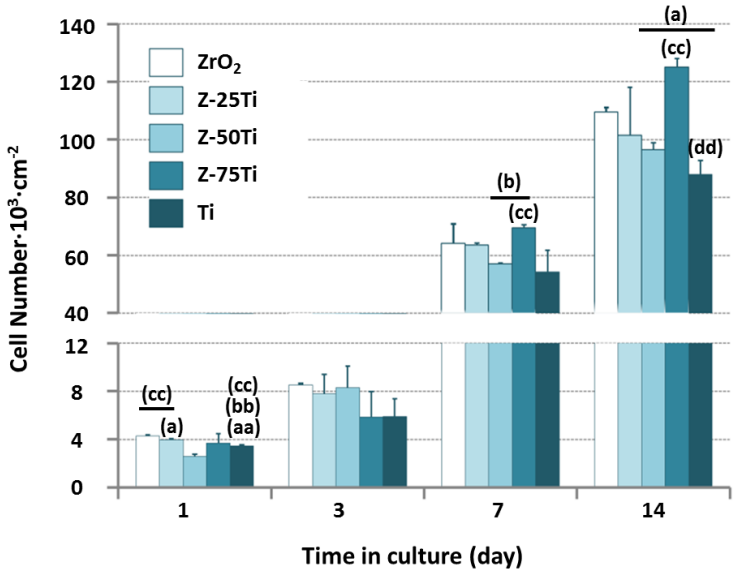

Fig 4.4-10. Time course study of osteoblast proliferation. Data are mean ± SD (n=3). At each incubation time, *(a)* compares to ZrO_2, *(b)* compares to Z-25Ti, *(c)* compares to Z-50Ti, *(d)* compares to Z-75Ti; p<0.01 (2 letters), p<0.05 (1 letter)

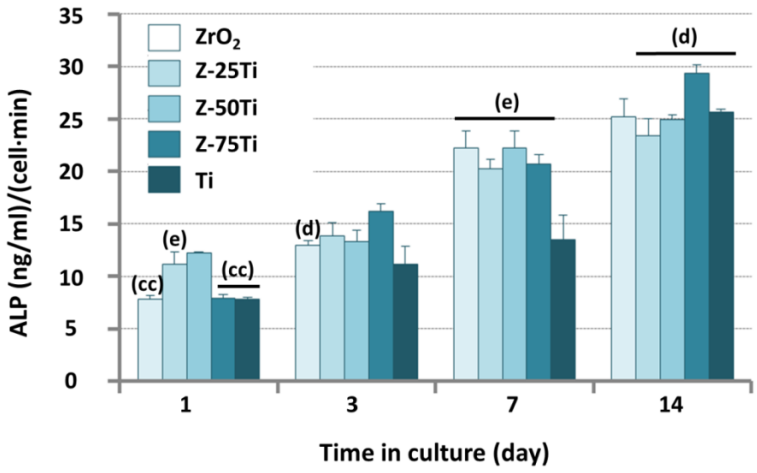

Fig 4.4-11. Time course study of osteogenic differentiation. Data are shown as mean ± SEM (*n=3*). At each incubation time, *(a)* compares to ZrO_2, *(b)* compares to Z-25Ti, *(c)* compares to Z-50Ti, *(d)* compares to Z-75Ti; p<0.01 (2 letters), p<0.05 (1 letter)

4.4.4 DISCUSSION

The biocompatibility of a material defines the suitability that this presents to integrate within biological environments, enabling the close contact of the inorganic material with living cells, tissues and biological fluids [1, 4, 5, 10, 67].

In overall, all new materials intended to be used in biomedical devices must be assessed in terms of *in vitro* cytotoxicity as per ISO 10993-5:2009 [45]. Regarding the new zirconia/titanium system, cytotoxicity rates were below 20% on all the materials when cells grew for 24 and 72 hours, either within the material extracts or their dilutions (Fig 4.4-6). Hence, a potential cytotoxic effect related to this new composite system or its pure compounds is dismissed.

Although *in vitro* tests can never substitute *in vivo* experiments, they provide relevant information on the biological performance of newly developed materials by using defined environments for cell-material interactions. They further allow elucidating how the different surface properties influence each one of the diverse aspects that constitute the osteoblastic behaviour.

The immunostaining of the actin cytoskeleton allowed studying the cell spreading on the different materials over the short-term adhesion stage (Fig 4.4-7). The cells cultured for 24 hours were spread and with a well-organized cytoskeleton on all materials. However, whilst osteoblasts were mostly branched on ZrO_2, Z-25Ti and Z-50Ti, they had more rounded shape on Z-75Ti and Ti substrates. Furthermore, the cytoplasm extension was significantly enhanced on ZrO_2 ($p<0.01$) and on materials containing ZrO_2 ($p<0.05$), either 24 or 48 hours after seeding (Fig 4.4-9).

The primary material interaction zone with the biological tissues is the outmost atomic layer, so variations in the chemical composition will lead to different interactions between cells and surfaces [4]. This fact has been also corroborated in the study related to alumina/titanium system. Other previous studies [22, 24] have demonstrated better osteoblast behaviour on zirconia than on titanium surfaces. In this study, cells also had a more advanced adhesion step disclosed by more complex spindle morphologies and long filopodia establishing intercellular contacts, mainly on ZrO_2 and Z-Ti cermets after 48 hours of culture. This agreed with a strong signal of vinculin, particularly on Z-Ti cermets (Fig 4.4-8). Moreover, cell circularity decreased on the set of materials along the culture time. This fact was more evident on ZrO_2 ($p<0.01$) and on Z-Ti cermets ($p<0.05$) than on Ti specimens (Fig 4.4-9). These results suggest that cell spreading on Z-Ti cermets was more influenced by surface chemical composition than by roughness and CA values.

A similar roughness pattern in the 3D-directions was found on all tested materials by interferometric microscopy (Fig 4.4-3). R_Z mean values ranged from 7.3 to 3.7 µm while R_a mean values ranged from 200 to 530 nm on the tested substrates (Table 4.4-1). Several studies have demonstrated that osteoblastic adhesion is influenced by surface roughness, particularly when it ranges in the submicron to the micron scale [53]. The small differences between our samples are in the sub-micrometric scale, and seem to be insufficient to affect cell adhesion. The values obtained are, in all cases, close to the previously reported as optimal values [54, 55].

All substrates, except Z-75Ti specimens, presented similar CA values (Table 4.4-3). The dissimilar behaviour of Z-75Ti may be related to the presence of intermediate compounds in the ZrO_2/Ti interface, like Ti_2ZrO and $Y_2Ti_2O_7$, as earlier reported [64]. None effect was found on cell adhesion as a consequence of the higher wettability and surface free energy (Fig 4.4-5) in Z-75Ti specimens. However, cell number increased over the culture time on each studied material (Fig 4.4-10), reaching proliferation values significantly higher on Z-75Ti substrates at 7 and particularly at 14 days.

Alkaline phosphatase (ALP), osteocalcin, osteopontin or type I collagen are often used to analyze osteoblastic differentiation [16, 68]. Among them, ALP activity is an early-marker of differentiation because it provides phosphate ions for the hydroxyapatite formation [17]. The ALP levels increased in all the tested surfaces (Fig 4.4-11), with a faster differentiation detected on ZrO_2-containing materials. Interestingly, proliferation and differentiation increased simultaneously on ZrO_2-containing materials at earlier culture times, in agreement with previous results [69]. Moreover, the specimens with the lower percentage of zirconia, Z-75Ti, promoted the highest proliferation and differentiation levels at longer culture times (14 days).

In general, higher values of adhesion, spreading, proliferation and earlier differentiation were found on pure zirconia and on the ZrO_2-containing materials as compared to plain titanium. A particular cellular behaviour was found on Z-75Ti specimens, with lower roughness and higher hydrophilicity and surface polarity. In fact, these substrates promoted the highest values of osteoblastic proliferation and differentiation at longer culture times. Moreover, this work revealed the Spark Plasma Sintering as a promising technique to obtain ZrO_2/Ti stable cermets and also nanostructured materials for biomedical applications, since no cytotoxic effects were found in osteoblasts cultured onto the different chemical compositions. Furthermore, these nanostructured materials enhanced cellular phenomena.

.

4.5 CONCLUSIONS

As overall conclusion, it can be established that:

Since no cytotoxicity has been related to the materials, Spark plasma sintering can be considered as a fast and reliable technology to manufacture new materials for biomedical purposes. Similar manufacturing methods led to different surface properties as a consequence of the different material nature. Moreover, by combining dissimilar properties of ceramic and titanium into cermets a better biological response was found comparing to the pure counterparts.

For the alumina/titanium system, it can be concluded that:

- A-25Ti composites had sub-micrometric roughness composed mostly of valley-like structure and hydrophilic surfaces. Otherwise, more hydrophobic Al_2O_3 substrates had a topography mainly composed by peaks.
- A-25Ti cermets showed an improved adhesion, proliferation and differentiation when compared to monolithic alumina.

For the zirconia/titanium system, it can be concluded that:

- Z-Ti composites had also sub-micrometric roughness. Z-75Ti specimens were the most hydrophilic substrates. They also had higher polar character.
- Z-Ti composites encouraged better adhesion, proliferation and differentiation than the pure counterparts.
- Improved cell attachment and early-differentiation were promoted on materials containing a nanostructured ZrO_2 phase.
- Best late-proliferation and advanced differentiation results were obtained on Z-75 cermets, revealing this material, from the osseintegration standpoint, as excellent to be used in bone replacements.

4.6 REFERENCES

[1] Williams DF. On the mechanisms of biocompatibility. Biomaterials 2008;29:2941-53.

[2] Hilborn J, Bjursten LM. A new and evolving paradigm for biocompatibility. Journal of tissue engineering and regenerative medicine 2007;1:110-9.

[3] Roach P, Eglin D, Rohde K, Perry CC. Modern biomaterials: a review—bulk properties and implications of surface modifications. Journal of Materials Science: Materials in Medicine 2007;18:1263-77.

[4] Fenoglio I, Fubini B, Ghibaudi EM, Turci F. Multiple aspects of the interaction of biomacromolecules with inorganic surfaces. Advanced Drug Delivery Reviews 2011;63:1186-209.

[5] Bauer S, Schmuki P, von der Mark K, Park J. Engineering biocompatible implant surfaces: Part I: Materials and surfaces. Progress in Materials Science 2013;58:261-326.

[6] Gindl M, Sinn G, Gindl W, Reiterer A, Tschegg S. A comparison of different methods to calculate the surface free energy of wood using contact angle measurements. Colloids and Surfaces A: Physicochemical and Engineering Aspects 2001;181:279-87.

[7] Chug A, Shukla S, Mahesh L, Jadwani S. Osseointegration—Molecular events at the bone–implant interface: A review. Journal of Oral and Maxillofacial Surgery, Medicine, and Pathology 2013;25:1-4.

[8] Kittel C, McEuen P. Introduction to solid state physics: Wiley New York; 1986.

[9] Coelho PG, Granjeiro JM, Romanos GE, Suzuki M, Silva NRF, Cardaropoli G, et al. Basic research methods and current trends of dental implant surfaces. Journal of Biomedical Materials Research Part B: Applied Biomaterials 2009;88B:579-96.

[10] Planell JA, Navarro M, Altankov G, Aparicio C, Engel E, Gil J, et al. Materials surface effects on biological interactions.

. In: Advances in Regenerative Medicine: Role of Nanotechnology aEP, editor. NATO Science for Peace and Security Series A: Chemistry and Biology: Springer Verlag; 2010. p. 233-52.

[11] Divya Rani VV, Vinoth-Kumar L, Anitha VC, Manzoor K, Deepthy M, Shantikumar VN. Osteointegration of titanium implant is sensitive to specific nanostructure morphology. Acta Biomaterialia 2012;8:1976-89.

[12] Anselme K, Ponche A, Bigerelle M. Relative influence of surface topography and surface chemistry on cell response to bone implant materials. Part 2: Biological aspects. Proceedings of the Institution of Mechanical Engineers, Part H: Journal of Engineering in Medicine 2010;224:1487-507.

[13] Bacakova L, Filova E, Parizek M, Ruml T, Svorcik V. Modulation of cell adhesion, proliferation and differentiation on materials designed for body implants. Biotechnology Advances 2011;29:739-67.

[14] Di Silvio L, Dalby MJ, Bonfield W. Osteoblast behaviour on HA/PE composite surfaces with different HA volumes. Biomaterials 2002;23:101-7.

[15] Lincks J, Boyan BD, Blanchard CR, Lohmann CH, Liu Y, Cochran DL, et al. Response of MG63 osteoblast-like cells to titanium and titanium alloy is dependent on surface roughness and composition. Biomaterials 1998;19:2219-32.

[16] Hempel U, Hefti T, Dieter P, Schlottig F. Response of human bone marrow stromal cells, MG-63, and SaOS-2 to titanium-based dental implant surfaces with different topography and surface energy. Clinical Oral Implants Research 2013;24:174-82.

[17] Hempel U, Hefti T, Kalbacova M, Wolf-Brandstetter C, Dieter P, Schlottig F. Response of osteoblast-like SAOS-2 cells to zirconia ceramics with different surface topographies. Clinical Oral Implants Research 2010;21:174-81.

[18] Anselme K, Ploux L, Ponche A. Cell/Material Interfaces: Influence of Surface Chemistry and Surface Topography on Cell Adhesion. Journal of Adhesion Science and Technology 2010;24:831-52.

[19] Lim JY, Liu X, Vogler EA, Donahue HJ. Systematic variation in osteoblast adhesion and phenotype with substratum surface characteristics. Journal of Biomedical Materials Research Part A 2004;68:504-12.

[20] Gittens RA, Scheideler L, Rupp F, Hyzy SL, Geis-Gerstorfer J, Schwartz Z, et al. A Review on the Wettability of Dental Implant Surfaces II: Biological and Clinical Aspects. Acta biomaterialia 2014.

[21] Jianhua W, Toshio I, Naoto O, Takayasu I, Takashi M, Baolin L, et al. Influence of surface wettability on competitive protein adsorption and initial attachment of osteoblasts. Biomedical Materials 2009;4:045002.

[22] Wennerberg A, Galli S, Albrektsson T. Current knowledge about the hydrophilic and nanostructured SLActive surface. Clinical, Cosmetic and Investigational Dentistry 2011;3:59-67.

[23] Anil S, Anand P, Alghamdi H, Jansen J. Dental implant surface enhancement and osseointegration. Implant Dentistry: A Rapidly Evolving Practice New York: InTech 2011:83-108.

[24] Wennerberg A, Albrektsson T. Effects of titanium surface topography on bone integration: a systematic review. Clinical Oral Implants Research 2009;20:172-84.

[25] Le Guéhennec L, Soueidan A, Layrolle P, Amouriq Y. Surface treatments of titanium dental implants for rapid osseointegration. Dental Materials 2007;23:844-54.

[26] Zhu X, Chen J, Scheideler L, Altebaeumer T, Geis-Gerstorfer J, Kern D. Cellular reactions of osteoblasts to micron- and submicron-scale porous structures of titanium surfaces. Cells Tissues Organs 2004;178:13-22.

[27] Ball M, Grant DM, Lo WJ, Scotchford CA. The effect of different surface morphology and roughness on osteoblast-like cells. Journal of Biomedical Materials Research - Part A 2008;86:637-47.

[28] Bahraminasab M, Sahari BB, Edwards KL, Farahmand F, Arumugam M. Aseptic loosening of femoral components – Materials engineering and design considerations. Materials & Design 2013;44:155-63.

[29] Bahraminasab M, Sahari BB, Edwards KL, Farahmand F, Arumugam M, Hong TS. Aseptic loosening of femoral components – A review of current and future trends in materials used. Materials & Design 2012;42:459-70.

[30] Khang D, Carpenter J, Chun YW, Pareta R, Webster TJ. Nanotechnology for regenerative medicine. Biomedical Microdevices 2010;12:575-87.

[31] Depprich R, Ommerborn M, Zipprich H, Naujoks C, Handschel J, Wiesmann HP, et al. Behavior of osteoblastic cells cultured on titanium and structured zirconia surfaces. Head and Face Medicine 2008;4.

[32] Mai R, Kunert-Keil C, Grafe A, Gedrange T, Lauer G, Dominiak M, et al. Histological behaviour of zirconia implants: An experiment in rats. Annals of Anatomy - Anatomischer Anzeiger 2012;194:561-6.

[33] Matsuno H, Yokoyama A, Watari F, Uo M, Kawasaki T. Biocompatibility and osteogenesis of refractory metal implants, titanium, hafnium, niobium, tantalum and rhenium. Biomaterials 2001;22:1253-62.

[34] Webster TJ, Siegel RW, Bizios R. Design and evaluation of nanophase alumina for orthopaedic/dental applications. Nanostructured Materials 1999;12:983-6.

[35] Boutin P, Christel P, Dorlot JM, Meunier A, de Roquancourt A, Blanquaert D, et al. The use of dense alumina–alumina ceramic combination in total hip replacement. Journal of Biomedical Materials Research 1988;22:1203-32.

[36] Takami Y, Nakazawa T, Makinouchi K, Glueck J, Nosé Y. Biocompatibility of alumina ceramic and polyethylene as materials for pivot bearings of a centrifugal blood pump. Journal of Biomedical Materials Research 1997;36:381-6.

[37] Kitamura S, Ohgushi H, Hirose M, Funaoka H, Takakura Y, Ito H. Osteogenic Differentiation of Human Bone Marrow-derived Mesenchymal Cells Cultured on Alumina Ceramics. Artificial Organs 2004;28:72-82.

[38] Price RL, Gutwein LG, Kaledin L, Tepper F, Webster TJ. Osteoblast function on nanophase alumina materials: Influence of chemistry, phase, and topography. Journal of Biomedical Materials Research Part A 2003;67A:1284-93.

[39] Metzger W, Schwab B, Miro MM, Grad S, Simpson A, Veith M, et al. Induction of Osteogenic Differentiation by Nanostructured Alumina Surfaces. Journal of Biomedical Nanotechnology 2014;10:831-45.

[40] Juang HY, Hon MH. Fabrication and mechanical properties of hydroxyapatite-alumina composites. Materials Science and Engineering: C 1994;2:77-81.

[41] Moraes MCCdS, Elias CN, Duailibi Filho J, Oliveira LGd. Mechanical properties of alumina-zirconia composites for ceramic abutments. Materials research 2004;7:643-9.

[42] Wolf WD, Vaidya KJ, Francis LF. Mechanical Properties and Failure Analysis of Alumina-Glass Dental Composites. Journal of the American Ceramic Society 1996;79:1769-76.

[43] Stumm W, Morgan JJ. Aquatic chemistry: chemical equilibria and rates in natural waters: John Wiley & Sons; 2012.

[44] Nel AE, Mädler L, Velegol D, Xia T, Hoek EM, Somasundaran P, et al. Understanding biophysicochemical interactions at the nano–bio interface. Nature materials 2009;8:543-57.

[45] 10993-5:2009 I. Biological evaluation of medical devices. . Part 5: Tests for in vitro citotoxicity2009.

[46] Stein GS, Lian JB, Van Wijnen AJ, Stein JL, Montecino M, Javed A, et al. Runx2 control of organization, assembly and activity of the regulatory machinery for skeletal gene expression. Oncogene 2004;23:4315-29.

[47] Lian JB, Stein GS, Javed A, Van Wijnen AJ, Stein JL, Montecino M, et al. Networks and hubs for the transcriptional control of osteoblastogenesis. Reviews in Endocrine and Metabolic Disorders 2006;7:1-16.

[48] Karlsson M, Pålsgård E, Wilshaw PR, Di Silvio L. Initial in vitro interaction of osteoblasts with nano-porous alumina. Biomaterials 2003;24:3039-46.

[49] Gutierrez-Gonzalez C, Fernandez-Garcia E, Fernandez A, Torrecillas R, Lopez-Esteban S. Processing, spark plasma sintering, and mechanical behavior of alumina/titanium composites. Journal of Materials Science 2014;49:3823-30.

[50] Thrivikraman G, Madras G, Basu B. In vitro/In vivo assessment and mechanisms of toxicity of bioceramic materials and its wear particulates. RSC Advances 2014;4:12763-81.

[51] Anselme K. Osteoblast adhesion on biomaterials. Biomaterials 2000;21:667-81.

[52] Sackmann E, Smith A-S. Physics of cell adhesion: Some lessons from cell-mimetic systems. Soft Matter 2014.

[53] Keller JC, Schneider GB, Stanford CM, Kellogg B. Effects of implant microtopography on osteoblast cell attachment. Implant dentistry 2003;12:175-81.

[54] Anselme K, Bigerelle M. Topography effects of pure titanium substrates on human osteoblast long-term adhesion. Acta Biomaterialia 2005;1:211-22.

[55] Rosa AL, Beloti MM. Effect of cpTi surface roughness on human bone marrow cell attachment, proliferation, and differentiation. Brazilian Dental Journal 2003;14:16-21.

[56] Berry CC, Campbell G, Spadiccino A, Robertson M, Curtis AS. The influence of microscale topography on fibroblast attachment and motility. Biomaterials 2004;25:5781-8.

[57] Wang G, Liu X, Zreiqat H, Ding C. Enhanced effects of nano-scale topography on the bioactivity and osteoblast behaviors of micron rough ZrO 2 coatings. Colloids and Surfaces B: Biointerfaces 2011;86:267-74.

[58] Ward BC, Webster TJ. Increased functions of osteoblasts on nanophase metals. Materials Science and Engineering: C 2007;27:575-8.

[59] Webster TJ, Ergun C, Doremus RH, Siegel RW, Bizios R. Enhanced functions of osteoblasts on nanophase ceramics. Biomaterials 2000;21:1803-10.

[60] Popat KC, Leoni L, Grimes CA, Desai TA. Influence of engineered titania nanotubular surfaces on bone cells. Biomaterials 2007;28:3188-97.

[61] Mendonça G, Mendonça DBS, Simões LGP, Araújo AL, Leite ER, Golin AL, et al. Nanostructured implant surface effect on osteoblast gene expression and bone-to-implant contact in vivo. Materials Science and Engineering: C 2011;31:1809-18.

[62] Mendonça G, Mendonça DBS, Aragão FJL, Cooper LF. Advancing dental implant surface technology – From micron- to nanotopography. Biomaterials 2008;29:3822-35.

[63] Skorb EV, Andreeva DV. Surface Nanoarchitecture for Bio-Applications: Self-Regulating Intelligent Interfaces. Advanced Functional Materials 2013.

[64] Fernandez-Garcia E, Gutierrez-Gonzalez CF, Fernandez A, Torrecillas R, Lopez-Esteban S. Processing and Spark Plasma Sintering of zirconia/titanium cermets. Ceramics International 2013;39:6931-6.

[65] Shah A, Sinha R, Hickok N, Tuan R. High-resolution morphometric analysis of human osteoblastic cell adhesion on clinically relevant orthopedic alloys. Bone 1999;24:499-506.

[66] http://rsbweb.nih.gov/ij/.

[67] Menzies KL, Jones L. The impact of contact angle on the biocompatibility of biomaterials. Optometry & Vision Science 2010;87:387-99.

[68] Owens DK, Wendt RC. Estimation of the surface free energy of polymers. Journal of Applied Polymer Science 1969;13:1741-7.

[69] Zhang S, Sun J, Xu Y, Qian S, Wang B, Liu F, et al. Adhesion, proliferation and differentiation of osteoblasts on zirconia films prepared by cathodic arc deposition. Bio-medical materials and engineering 2013;23:373-85.

Chapter 5

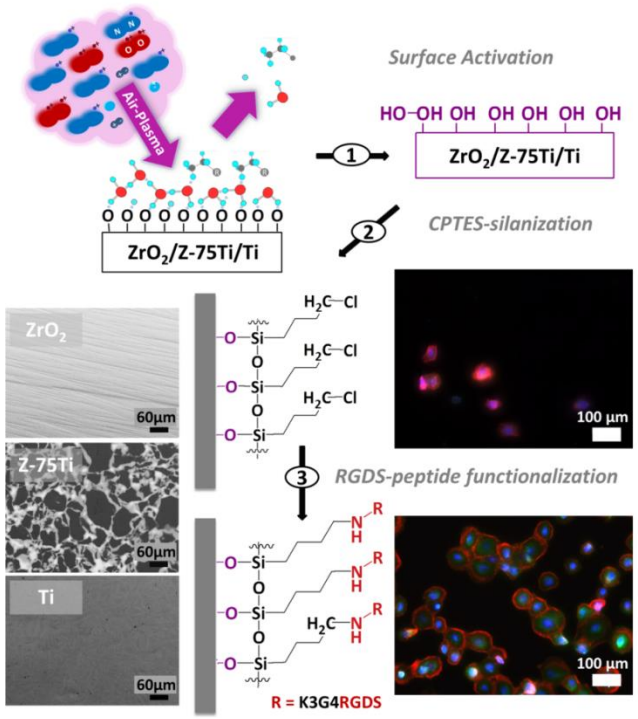

BIOFUNCTIONALIZATION OF ZIRCONIA/TI MATERIALS

Design and evaluation of ceramic/metal composites for biomedical purposes

5.1 INTRODUCTION

Lack of bioactive interactions between the inert biomaterial surface and the natural tissues are among the most significant causes for implant failures after implantation [1]. Thus, the development of new materials with improved biomechanics that furthermore have surfaces that are able of stimulate new bone formation are needed for better addressing the clinical demands [2, 3].

Surface functionalization with organic or inorganic coatings has become pivotal to induct bioactivity on metallic biomaterials [4-6]. The process changes surface composition, structure and/or morphology, without altering bulk properties and it is currently considered an effective and modern approach to design new multifunctional materials [7-10]. Physical (increased roughness [11-13]), chemical (acid-etching, alkaline treatment, deposition of calcium phosphate phases or incorporation of specific ionic species [13, 14]) and/or biological (coatings made of bioinspired molecules [3, 15-17]) approaches can be pursued to functionalize surfaces.

In overall, the immobilization of biomolecules on material surfaces, resulting in reduction or loss mobility, is referred as biofunctionalization [18]. C. Aparicio et al. [9, 19] have functionalized titanium surfaces with different bioactivities either to influence physiological paths involved in bone regeneration or to prevent bacterial colonization of the surface. Adsorption, encapsulation, covalent immobilization, self-assembled monolayers or electrochemical are methodologies used for this purpose [8, 18, 20, 21]. Specifically, covalent bonding of biomolecules at surfaces has been explored for assay technologies, biosensors, medical imaging devices, therapies, and biomaterials [18]

One of the approaches to covalently-immobilize biomolecules on inorganic materials that has been used in dentistry involves methodologies that are based on silane-chemistry [18, 22-24]. This same approach can be translated to develop biofunctional coatings on metallic implants that are mechanically and thermochemically stable to potentially withstand handling of the coated device during surgery as well as the aggressive oral and body environments derived from the contact with biofluids and cells [9, 19].

Diverse biomolecules with varied complexities (Arginine-Glycin-Aspartate (RGD) sequence [25-29], other oligopeptides [19, 30], proteins [26, 31], aptamers [32] recombinamers [17] or even multiple peptides with cooperative activities [9]) have been tethered to titanium and other metal surfaces using silanes as coupling agents

[8, 33]. Nevertheless, whereas the chemistry of silanes seems to be optimized to anchor biomolecules on microparticles in restorative materials or metallic substrates for dental implants, there is a lack of knowledge regarding the potential ability of biofunctionalizing other biomaterials of more recent interest, especially those that are based on zirconia [18].

The biofunctionalization of zirconia particles by protein chemisorption through a silane precursor has been reported [34, 35], but to date only physical methods (vapor-phase deposition of Si_xO_y) and tribological methods (silica coating) have been developed to competently functionalize dense ZrO_2 materials [36, 37]. Thus the stable immobilization of bioactive molecules on zirconia-based materials is a topic of notable technological interest [38, 39].

RGDs sequence oligopeptides were selected as a model biomolecule to validate the effectiveness of the biofunctionalization of ZrO_2-containing materials. Laminin, fibronectin or vitronentin are proteins in the bone extracellular matrix (ECM) that contain in their structure the Arg-Gly-Asp-Ser (RGDS) motif. As schematized in Fig 5.4-7, this specific sequence is recognized for the receptors like-integrin, which are involved in the attachment and growth of osteoblasts [27, 64]. Many *in vitro* and *in vivo* studies have demonstrated that with a RGDSs coating on the implant surface, the bone formation is improved [34-37].

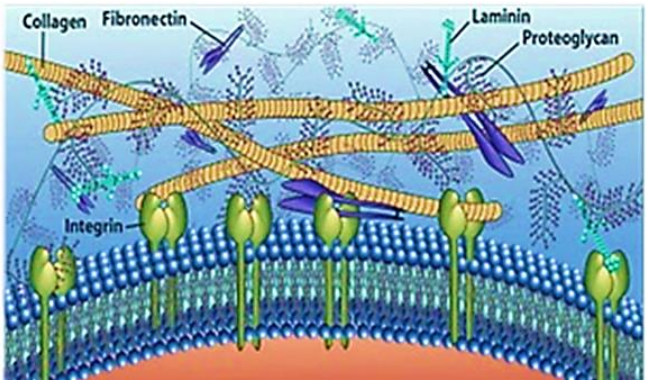

Fig 5.1-1. Specific recognition of the RGDs sequence in diverse extracellular matrix proteins by integrin receptors.

In Chapter 3, micro-nanostructured ZrO_2/Ti composites were developed. As was found in the biocompatibility study in Chapter 4, this novel system had a similar or superior biocompatibility to each pure counterpart, leading to interesting osteoblastic responses associated with the nanometric features in the microstructure. Moreover, in the particular case of ZrO_2/Ti (75 vol. %Ti) cermets, proliferation and

differentiation responses of osteoblasts were enhanced, so this system works better from the point of view of biocompatibility. Now, the goal is the covalent immobilization of bio-inspired molecules on ZrO_2 containing materials, particularly in zirconia/titanium (75% vol. Ti) composites (Z-75Ti) and monolithic zirconia (ZrO_2) by using a method based on silane chemistry. Thereby, the surfaces will be activated, silanized, and functionalized with coatings made of oligopeptides. Surface activation by plasma or etching will be studied. The surfaces will be coated by tethering a purposely-designed RGD-containing peptide. Successful treatments after each step of the process will be assessed by surface physical and chemical characterization with water contact angles and XPS, respectively. Stability of the coatings will be evaluated after 2 hours of sonication in water. MC3T3 pre-osteoblasts adhesion on the functionalized surfaces will also be studied.

5.2 OBJETIVES

The general objective in this chapter is the biofunctionalization of zirconia (TZ-3Y-E) and ZrO_2/Ti composites (75% vol. Ti), i.e. two materials with different nature by a three step mechanism based on silane-chemistry.

In order to achieve the main objective, the following challenges are purposed:

- Investigating different activation methodologies in order to optimize this crucial step in the biofunctionalization procedure.
- Facilitating a suitable surface silanization of activated surfaces using (3-Chloropropyl) triethoxysilane (CPTES) as covalent linker.
- Anchoring oligopeptides (KKKGGGGRGDS) containing the RGD-sequence, a vastly explored motif that induces cellular adhesion, to the silanized surfaces.
- Validating the bioactivity of the functionalized surfaces physical,chemical and biologically.

5.3 MATERIALS PROCESSING

Tetragonal zirconia stabilized with 3% mol. yttria (ZrO_2), zirconia/titanium (75% vol. of Ti) composites (Z-25Ti) and titanium (Ti) samples were performed as indicated in [40]. Fired specimens were machined to samples of 5x5 mm^2 (2 mm thick), grinded with SiC discs down to 1200 grit (25.5 µm) and polished with an alumina suspension (1 µm) on a velvet disc. Before the functionalization, samples were ultrasonically cleaned up 25 minutes in isopropanol, de-ionized (DI)-water and acetone and stored within a desiccator for 2 hours.

5.4 CHEMICAL BIOFUNCTIONALIZATION

A three-step-method based on surface activation, silanization and peptide-coating was performed to covalently functionalize the studied substrates. Each biofunctionalization step is then explained in detail.

5.4.1 SURFACE ACTIVATION

Increasing properly the surface free energy of chemically stable ceramics is crucial to enable the posterior silanization. Two alternative treatments were investigated in order to achieve the highest possible surface activation. On one side, etching in alkaline solution (NaOH) was studied because this allows to create a layer containing –OH and also to facilitate the precipitation of apatite crystals, which favors bone mineralization [41, 42]. On the other side, plasma cleaning was tested as a versatile solvent-free technology, efficient and appropriated to activate complex-shaped surfaces [43, 44]. As shown in Fig 5.4-1, plain samples were immersed in a 5M NaOH solution overnight at 60 °C. In addition, sets of samples were also submitted to diverse plasma treatments (PTs) using a PDC-32G (Harrick Plasma; NY) plasma cleaner (Fig 5.4-1). Samples were located on a glass tray and introduced in the plasma chamber under vacuum. A set of plasma cleaning conditions were investigated in order to optimize this treatment: O_2-plasma for 5 minutes (PT_1), O_2-plasma for 10 minutes (PT_2), air-plasma for 5 minutes (PT_3) and air-plasma for 10 minutes (PT_4).

The activated samples were named: ZrO_2/NaOH, Z-75Ti/NaOH and Ti/NaOH for alkaline etched-groups and ZrO_2/OH-PT_x, Z-75Ti/OH-PT_x and Ti/OH-PT_x for plasma-cleaned groups.

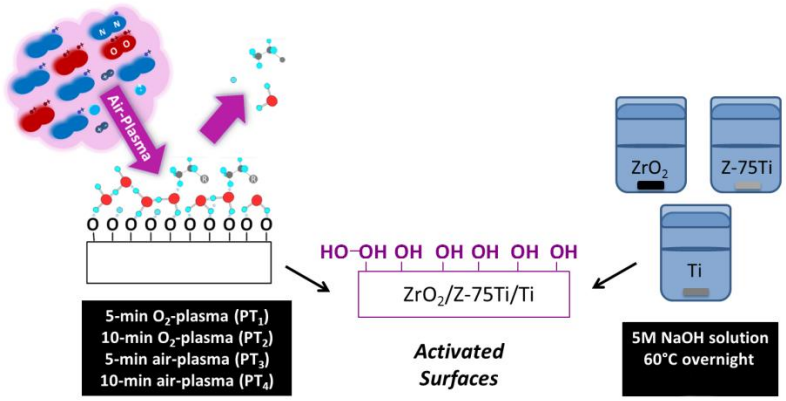

Fig 5.4-1. Surface activation by chemical etching and plasma treatments.

5.4.2 SILANIZATION

Among the different silanes availables for Chemistry applications [45], 3-aminopropyltriethoxysilane (APTES) was initially used as linker in biofunctionalization. Because it has an amino terminal group, coupling reactions to esterify carboxylic groups in the biomolecules are needed. This drawback is avoided with alternative silanes like (3- Glycidyloxypropyl)trimpethoxysilane (GPTES) or (3-Chloropropyl)triethoxysilane (CPTES). As displayed in Fig 5.4-5, GPTES has an epoxy functional group while CPTES has a chlorine-reactive motive. CPTES has demonstrated much higher coverage of biomolecules on inorganic surfaces [9, 46] and furthermore allows to avoid additional coupling agents (HBTU, EDC or glutaralhedido) and toxic solvents like toluene [28, 29, 32, 33, 42].

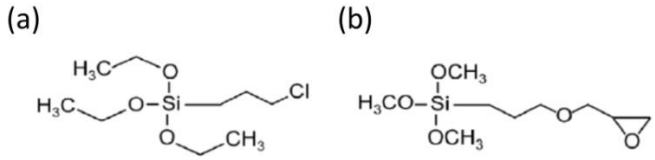

Fig 5.4-2. Chemical structure of useful silanes for biofunctionalization: (a) CPTES [(3-Chloropropyl)triethoxysilane] and (b) GPTES [(3-Glycidyloxypropyl)triethoxysilane].

Silanization depends on many surface factors, and the point of zero charge (PZC) is one of the most important ones. This determines the pH in which silanization is possible [20, 47]. As seen in Fig 5.4-3, at physiological pH, passivate titanium (TiO_2) surfaces are negatively-charged (PZC=4.5). This explains the corrosion resistance that

Ti has in physiological medium and the ability to osseointegrate, since the PZC is close to that of osteogenic proteins [48, 49]. In ZrO_2 powder, pH values ranging from 4 to 6 have been reported for the PZC [50, 51]. In particular, PZC at 4.5 has been described for nanocrystalline ZrO_2 [52]. This similar surface properties could explain why both TiO_2 and ZrO_2 would be used in catalysis procedures and as catalytic support [18]. Thereby, the strategies previously used to silanize titanium could be also applied to ZrO_2-containing materials.

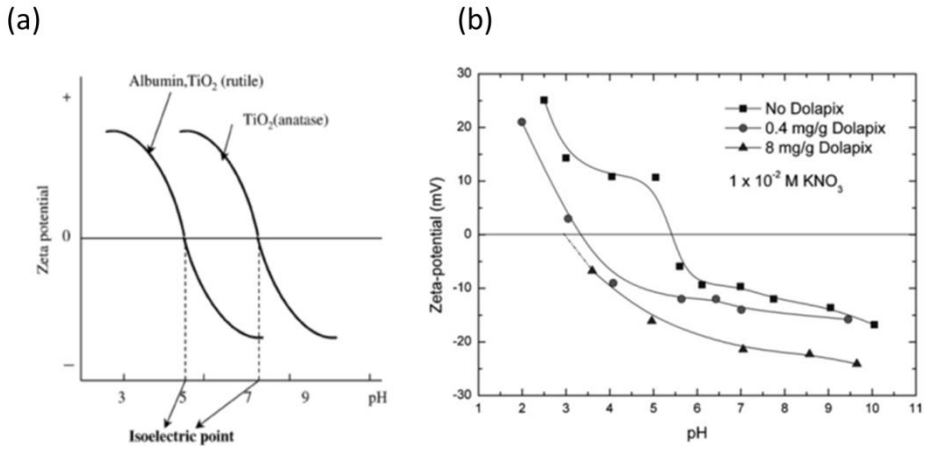

Fig 5.4-3. Z-potential of (a) TiO_2 and (b) ZrO_2 powders.

Fig 5.4-4 schematizes the main steps that take place in the silanization process: the hydrolysis of alkoxysilane molecules and the so-called curing. Humidity is a critical factor because it should let the initial hydrolysis of alkoxysilane but not further polymerizations. The first siloxane layer is formed by reaction of -OH groups in the surfaces with the monomers of hydroxysilane in the solution. This reaction releases water molecules, which hydrolyze preferably the unreacted alkoxysilanes rather than the fragments attached at the surface that remain like buried. The lateral cross-linking takes place then spontaneously on the wet surface, whilst it is being devoid of active -OH groups. Through the curing step, the inorganic surface is covered with a stable siloxane-grafted film, which bears the reactive chlorine groups available to react with the organic molecules [32].

Fig 5.4-5 schematizes the silanization methodology. The activated samples were placed in a fully-dried N_2-saturated glass chamber to hinder oligomerization of the organosilane molecules. Pentane, as non-polar dissolvent, 3-Chloropropyl)triethoxysilane (CPTES) and N,N-Diisopropiletilamina (DIEA), as base to create the alkaline medium for silanization, were sequentially added to the chamber.

Silanization reactions took place for 1 hour with application of ultrasonds for 2 minutes every 12 minutes to minimize nonspecific reactions. Then, the CPTES-silanized samples were rinsed within ethanol, isopropanol, DI-water, acetone and, finally, dried with a N_2-stream. Silanized groups are named CPTES.

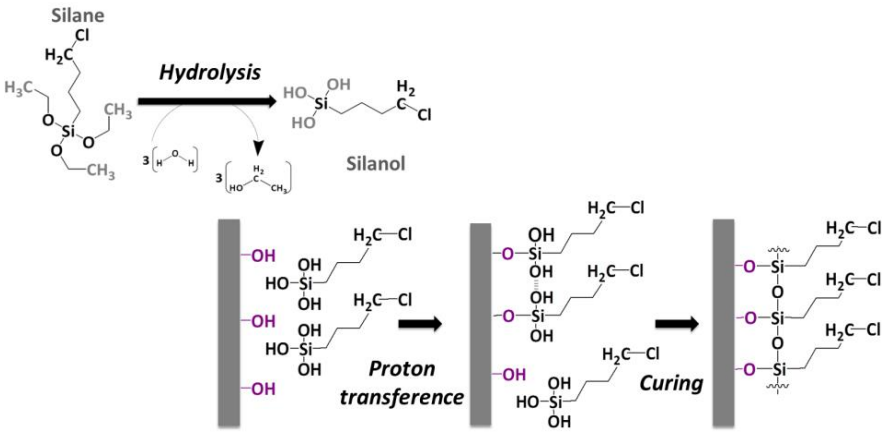

Fig 5.4-4. Steps involved in Silanization.

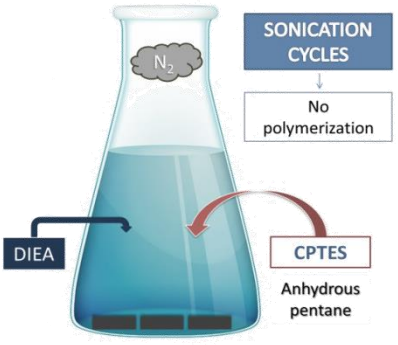

Fig 5.4-5. Silanization of the diverse substrates using the CPTES coupling agent.

5.4.3 COATING WITH BIO-INSPIRED MOLECULES

Oligopeptides containing the RGD-sequence were purposely-designed for biofunctionalization using silanes. They had the RGDS-active-sequence, four glycine (4G) acting as spacer and three lysine (3K) at the peptide N-terminus to enable the covalent anchoring at CPTES molecules (Fig 5.4-6).

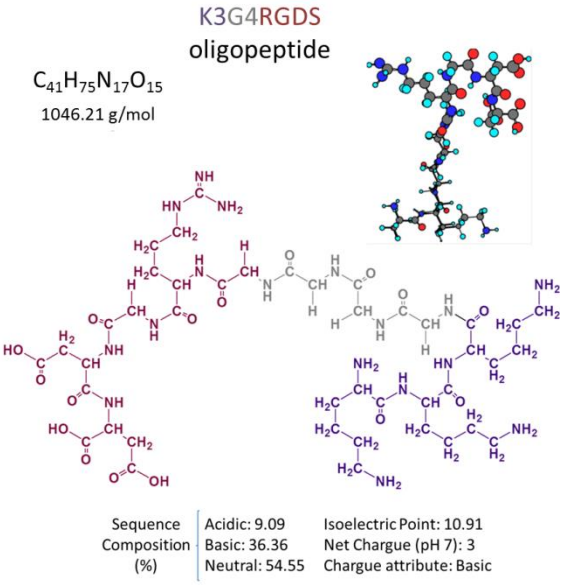

Fig 5.4-6. Physicochemical properties of RGDs oligopeptides.

Each N-terminal lysine provides an attachment point between the peptide and the CPTES-silane. Fig 5.4-7 (a) illustrates the nucleophilic substitution of the chloride end of the CPTES molecules by the free amines of each of the lysines at the N-terminus of the peptide. Thereby, the free amine in the lysine (nucleophile) yields its free electron pair to the carbon bonded to the chlorine group (electrophile) ($C^{\delta+} - Cl^{\delta-}$) in the organosilane joining covalently. In order to facilitate the substitution reaction, the oligopeptides are dissolved in Na_2CO_3 buffer solution at pH 9.5. The isoelectric point (IEP) of the KKKGGGGRGDS oligopeptides is 10.9 (calculated from [65]). By decreasing slightly the pH below the peptide IEP, the reaction follows the route (1) displayed in Fig 5.4-7 (b). Otherwise, at higher pH, hydroxyls in excess could react with chlorine forming alcohol groups that hardly would act as leaving group.

For enabling the covalent coating of peptides at silanized-surfaces, the oligopeptides (0.5 mg/ml, KKKGGGGRGDS) were dissolved in a 5mM Na_2CO_3 solution. The CPTES-silanized surfaces were immersed in the peptide solution overnight in an Ar-atmosphere. The different samples with the tethered peptides were rinsed in DI-water and stored in a vacuum chamber. The biofunctionalized surfaces with tethered peptides were named CPTES/RGD.

Control group samples with physisorbed RGD-containing peptides were also produced on the 3-types of substrates by direct immersion of activated samples in

the peptide solution under the same conditions previously described. These physically-coated surfaces were named RGD.

Mechanical-stability of the covalently-immobilized peptide coatings was assessed by applying ultrasonication to those surfaces in DI-water for 2 hours. These surfaces were named CPTES/RGD/S.

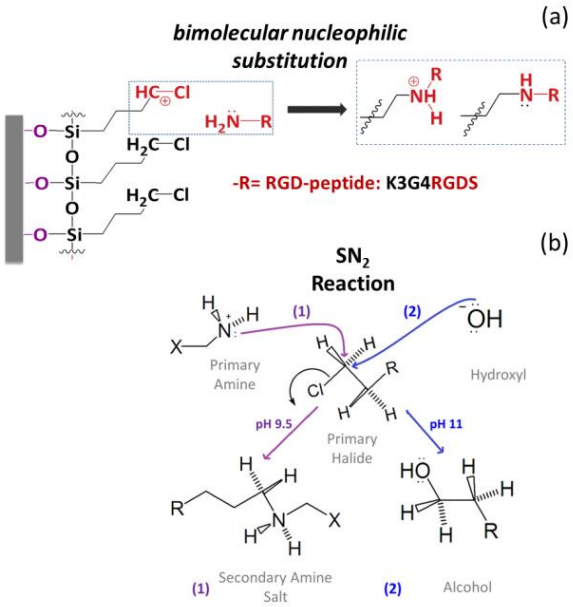

Fig 5.4-7 . Scheme detailing the covalently binding of peptides at surfaces, mediated by CPTES silanes.

5.5 ANALYSIS OF ACTIVATED SUBSTRATES

5.5.1 SURFACE TOPOGRAPHICAL INSPECTION

Any significant microstructural and topographical modification induced on the different materials after performing the activation treatments was assessed by SEM operating at 15 kV and 300x. Fig 5.5-1 displays SEM micrographs of untreated (plain), NaOH-etched and plasma-treated surfaces. PT_2 denotes surfaces that were treated with O_2-plasma for 10 minutes. Microstructures corresponding to PT_1 (O_2-plasma for 5 minutes), PT_3 (air-plasma for 5 minutes) and PT_4 (air-plasma for 10 minutes) are not displayed because they did not show any further difference with respect to the untreated ones.

After NaOH-etching all materials showed a notable alteration, in terms of roughness, in the original surface topography (ZrO_2/NaOH and Ti/NaOH) or microstructure (Z-75Ti/NaOH). This suggested potential activation of all those materials by effective reactivity with the strong base. Plasma treatments smoothed the topography of the substrates. Plasma treatments did not alter the topographies of the pure materials or the microstructures of the cermets, except in the case of the most aggressive treatment (O_2-plasma for 10-minutes).PT_2 preferentially oxidized the Ti-75Ti cermets at the interfaces of the two components. A close-up of the Z-75Ti/OH microstructure is inserted in Fig 5.5-1. This shows physical microstructural modifications associated to oxidative processes that take place during the PT_2 treatment (some of those alterations are marked with arrows).

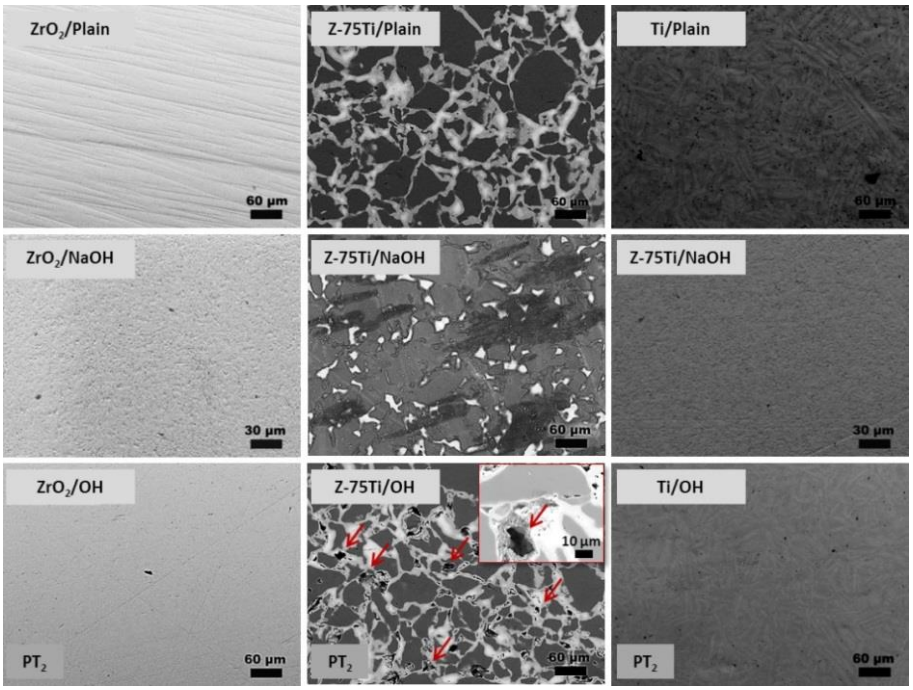

Fig 5.5-1. Comparison of the surface topography and microstructure of untreated (first row) substrates and surface-activated-NaOH-treated (second row) or plasma-treated (third row)-surfaces.

5.5.2 WETTABILITY

Wettability properties in the activated surfaces were assessed as indicated in Experimental Techniques (Chapter 7, Section 7.4.1). Table 5.5-1 presents values of contact angle of DI-water on original (plain) and all activated surfaces. All activated surfaces were more hydrophilic (lower CA values) than the non-treated surfaces as a result of an increasing amount of newly formed reactive polar groups, which is the main purpose of the activation process. The increased hydrophilicity was significantly higher for all plasma cleaning treatments than for the NaOH-etching treatment. Thus, it was decided to discard the alkaline etching treatment and select the best plasma cleaning process.

Table 5.5-1: *Mean ± SD of apparent contact angle (CA) values of DI-water on the studied surfaces after diverse activation treatments (n=3).*

ACTIVATION TREATMENT	APPARENT CONTACT ANGLE, CA [°]		
	ZrO_2	Z-75Ti	Ti
Plain	77.5 ± 6.1	70.3 ± 3.4	61.8 ± 3.0
Etching	22.5 ± 4.6	24.3 ± 4.7	31.6 ± 11.4
PT_1	7.5 ± 3.8	5.3 ± 2.4	2.3 ± 2.0
PT_2	3.6 ± 3.2	5.5 ± 3.0	2.9 ± 2.8
PT_3	7.6 ± 3.9	6.7 ± 2.9	3.7 ± 1.1
PT_4	2.1 ± 1.8	5.0 ± 2.2	4.0 ± 2.7

Plasma cleaning is a versatile and user-friendly technique that presents a main drawback: the effect is reversible, so it is lost as a consequence of the interaction with reactive species in air. Fig 5.5-2 discloses the ability of the activated surfaces to retain over 3 hours of storage under vacuum their activation/hydrophilic state depending on the conditions used for the plasma treatment. Conditions for PT_4 (air-plasma for 10 minutes) were optimal as this treatment produced surfaces with water contact angles below 15^{o} (high hydrophilicity) for at least 60 minutes of storage in all activated materials.

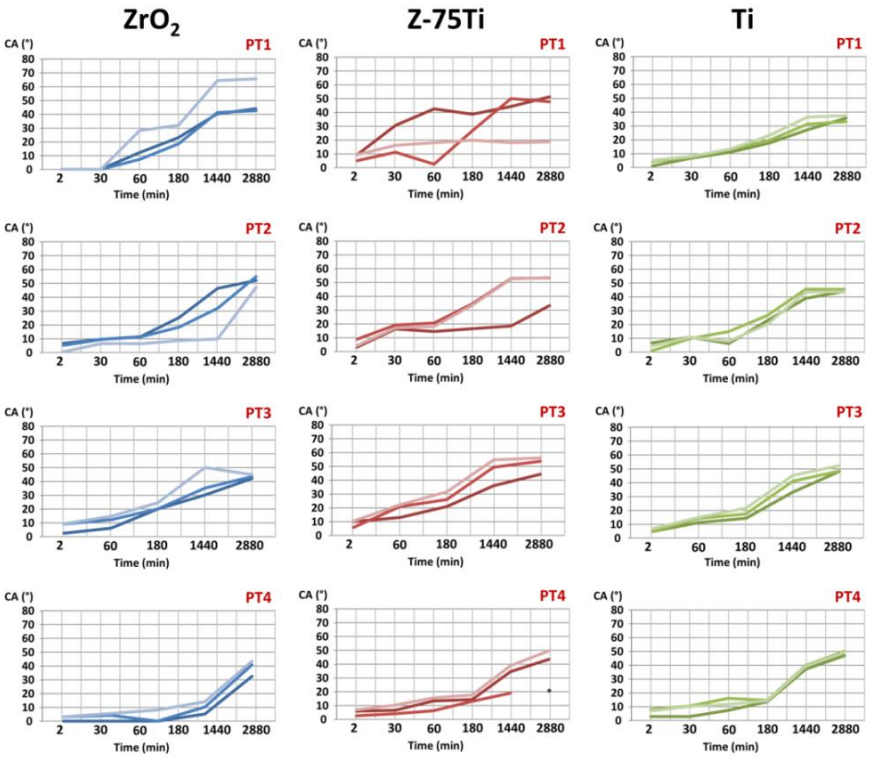

Fig 5.5-2. Time course of CA values of surfaces activated by different conditions of plasma treatment
Plasma-cleaning treatments: 5 minutes O_2-plasma (PT_1), 10 minutes O_2-plasma (PT_2), 5 minutes air-plasma (PT_3); and 10 minutes air-plasma (PT_4). Each curve shows the results for one of each of n= 3 samples per treatment.

5.5.3 SURFACE MICRO-HARDNESS

In order to investigate detrimental effects of the plasma treatments on the mechanical properties of the different materials, Vickers Hardness (H_v) of plain (PT_0) and plasma-activated substrates (PT_1-PT_4) was measured as indicated in Section 7.3.3.3 of Experimental Techniques (Chapter 7). Fig 5.5-3 shows the main ± SD values of H_v (*n=3* samples; 20 indentations per sample) that were found in the diverse substrates. O_2-Plasma treatments (PT_1 and PT_2) significantly affected the mechanical properties of the materials containing ZrO_2; i.e., ZrO_2 and Z-75Ti. Conversely, air-plasma (with aprox. 21% O_2-concentration) did not significantly affect the mechanical properties of any of the tested surfaces.

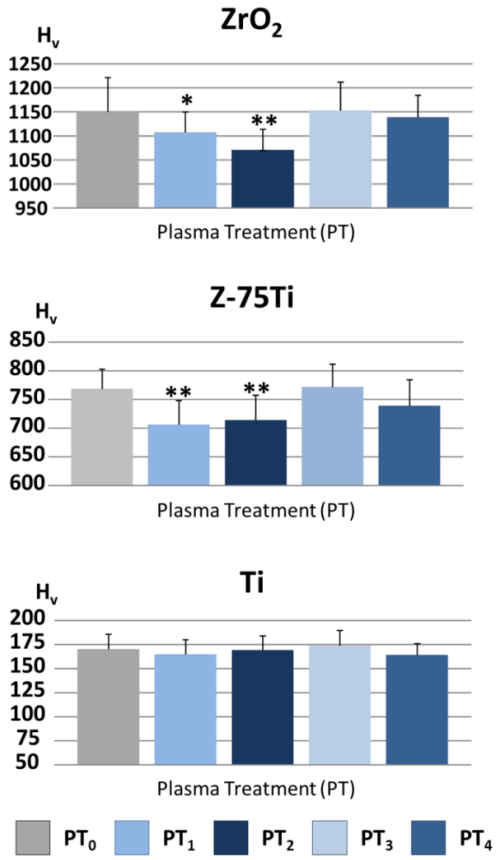

Fig 5.5-3. Microhardness of plasma-treated ZrO_2, Z-75Ti and Ti. Plasma-cleaning treatments: untreated (PT_0); 5 minutes O_2-plasma (PT_1), 10 minutes O_2-plasma (PT_2), 5 minutes air-plasma (PT_3); and 10 minutes air-plasma (PT_4) (n=60 indentations); error bars are SD; statistically significant differences with respect to untreated groups are ** $p<0.01$; and * $p<0.05$

5.6 PROPERTIES OF BIOFUNCTIONALIZED SURFACES

5.6.1 WATER CONTACT ANGLES

Wettability of the surfaces, evaluated as indicated in the next Chapter 7 (Section 7.4.1) changed due to modifications of the surface chemistry produced with the different steps of the biofunctionalization process (Fig 5.6-1). Untreated (plain) surfaces presented a moderate hydrophilic character (CA = 58.1°±8.0°, 64.7°±8.4° and 55.2°±7.3° for ZrO_2, Z-75Ti and Ti, respectively). The surfaces were highly hydrophilic after being plasma treated (PT_4) (Table 5.5-1), and silanization of the surfaces notably increased their CA values above the original values for all materials (CA = 63.9°±4.6°, 70.6°±3.1° and 73.0°±5.6° for ZrO_2/CPTES, Z-75Ti/CPTES and Ti/CPTES, respectively). CPTES has an alkyl chain that confers hydrophobic character to the molecule. When RGD-containing oligopeptides were immobilized on the silanized substrates (CPTES/RGD groups) the biofunctionalized surfaces were significantly more hydrophilic than the corresponding CPTES-silanized surfaces. The oligopeptides used here contained abundant aminoacids with charged side chains (lysines, arginine, and aspartate) and thus, they are notably hydrophilic. After ultrasonication the biofunctionalized surfaces of all materials (CPTES/RGD/S groups) retained their wettability state. When the RGD-containing oligopeptides were physisorbed on the different materials the surfaces were more hydrophilic than those with peptides immobilized on the silanized surfaces. This suggests that the silanized and biofunctionalized substrates showed a combination of the hydrophobic character of the silane molecules and the hydrophilic character of the oligopeptides.

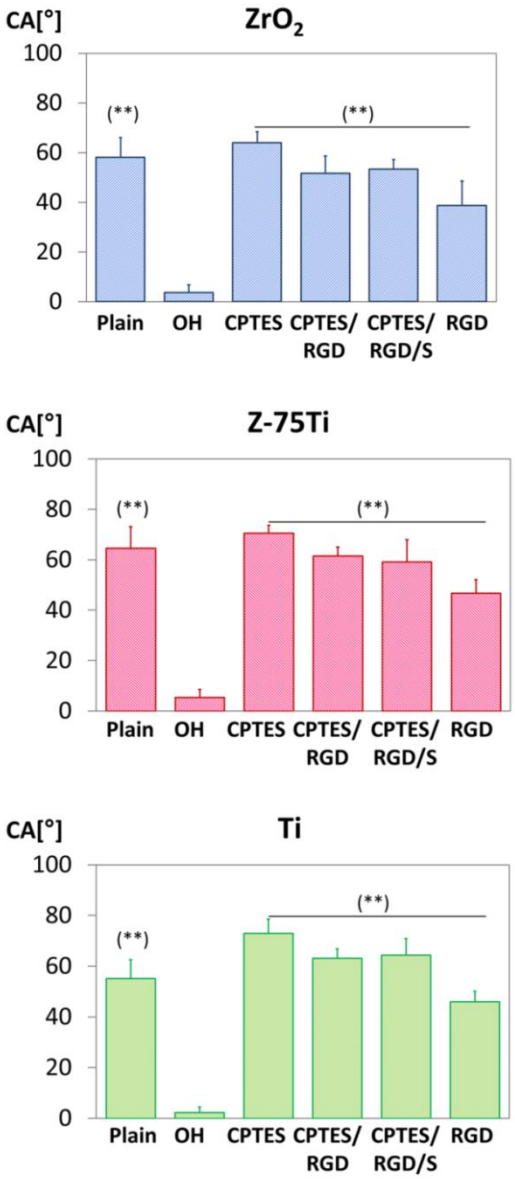

Fig 5.6-1. Apparent water contact angles (CA) on the modified surfaces after each step of the biofunctionalization process in ZrO_2, Z-75Ti, and Ti materials.

Plain: untreated surfaces of each material; *OH:* plasma-treated surfaces with PT_4 treatment, *CPTES:* silanized surfaces; *CPTES/RGD:* silanized and RGD-peptide coated surfaces; *CPTES/RGD/*S: CPTES/RGD *surfaces after* ultrasonication for 2 h; *RGD:* surfaces with physisorbed RGD-peptides. n=9; error bars are SD. Statistically significant differences are studied at $p<0.01$ (2 symbols) and $p<0.05$ (1 symbol); (*) compares with *OH* group.

5.6.2 SURFACE CHEMICAL COMPOSITION

The surface chemistry of all the investigated surfaces was characterized through XPS-analyses with the same settings as in Section 7.4.3 of Experimental Techniques (Chapter 7). Table 5.6-1 and Fig 5.6-2 show respectively elemental quantification and XPS-spectra of silanized (CPTES), RGD-peptide biofunctionalized (CPTES/RGD) and RGD-peptide biofunctionalized and sonicated for 2 hours (CPTES/RGD/S) surfaces. Si 2s and Cl 2s peaks were distinctive after silanization on CPTES-samples, which indicated that the silanes were successfully retained on the different materials. N 1s peaks appeared after immobilizing the RGD-containing peptides on the CPTES/RGD surfaces. N 1s peaks were also detected in spectra for biofunctionzalized surfaces after sonication for 2 hours. The later suggested that the peptides were strongly anchored to the surface and thus, the CPTES molecules successfully acted as covalent linkers between the inorganic substrates and the oligopeptides. The higher N% on the biofunctionalized surfaces after ultrasonication can be a consequence of the removal from the surfaces of loosely bound CPTES molecules. This is further confirmed by the decrease of the ratio of Cl and Si and/or increase of the ratio of N with respect to the base metal of the substrates on the sonicated surfaces (Table 5.6-1).

Table 5.6-1: *Surface chemical composition of modified surfaces.*
Elemental quantification (atom %) from XPS-survey scans shown in **Fig 5.6-2**.
CPTES*:* silanized surfaces; *CPTES/RGD:* silanized and RGD-peptide coated surfaces; *CPTES/RGD/*S: CPTES/RGD surfaces after ultra-sonication for 2 hours. Me: main metal component of each substrate: Zr for ZrO_2 and Ti for titanium (Ti); Zr plus Ti content for Z-75Ti.

SUBSTRATE		Elemental quantification (atom %)										
		O1s	Ti2p	N1s	C1s	Cl2p	Zr3d	Si2p	Si/ Me	Cl/ Me	N/ Me	Cl/ N
ZrO_2	CPTES	22.4	-	-	62.5	6.4	4.4	4.6	**1.0**	**1.5**	**-**	**-**
	CPTES/RGD	35.3	-	3.3	45.4	3.8	7.7	4.5	**0.6**	**0.5**	**0.4**	**1.2**
	CPTES/RGD/S	26.0	-	5.1	57.4	2.8	6.3	2.3	**0.4**	**0.4**	**0.8**	**0.6**
Z-75Ti	CPTES	28.8	3.2	-	52.8	7.3	1.0	7.0	**1.7**	**1.7**	**-**	**-**
	CPTES/RGD	23.6	3.0	2.8	63.4	2.5	1.1	3.7	**0.9**	**0.6**	**0.7**	**1.1**
	CPTES/RGD/S	36.3	3.4	5.3	53.4	0.0	1.6	0.0	**0.0**	**0.0**	**1.1**	**0.0**
Ti	CPTES	41.5	7.4	-	39.9	3.9	-	7.3	**1.0**	**0.5**	**-**	**-**
	CPTES/RGD	18.4	2.1	1.8	71.9	1.2	-	2.9	**1.4**	**0.6**	**0.9**	**0.7**
	CPTES/RGD/S	37.7	5.6	4.3	52.6	0.0	-	0.0	**0.0**	**0.0**	**0.8**	**0.0**

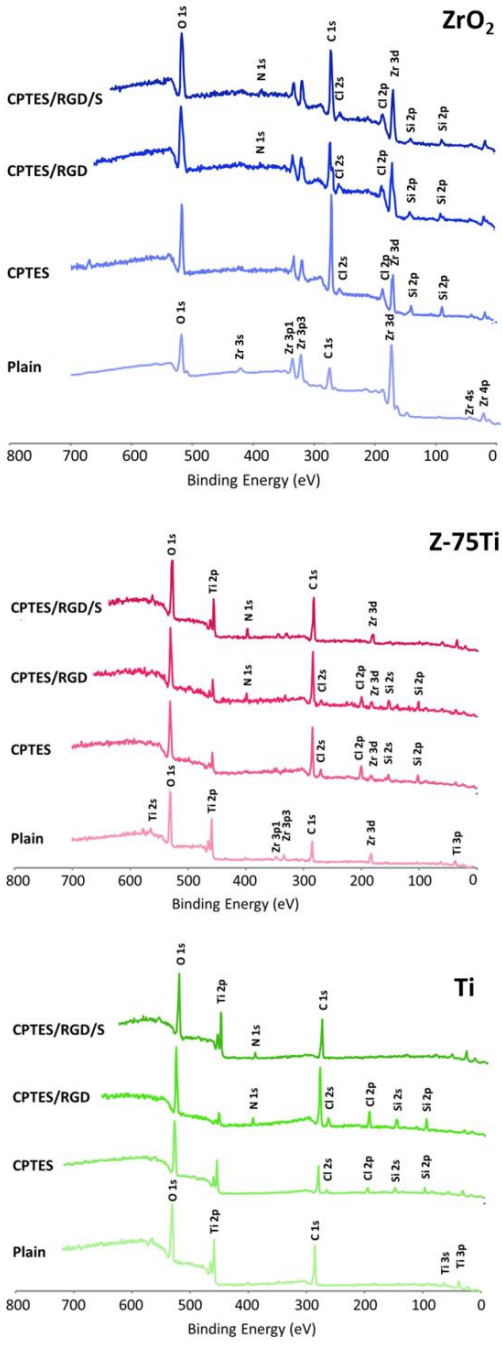

Fig 5.6-2 XPS-spectra of ZrO_2, Zr-75Ti and Ti modified surfaces.

CPTES: silanized surfaces; *CPTES/RGD:* silanized and RGD-peptide coated surfaces; *CPTES/RGD/*S: CPTES/RGD surfaces after ultrasonication for 2 hours. Characteristic peaks on untreated (*Plain*) samples: C 1s (285 eV), Ti 2p (460 eV), O 1s (530 eV) and Zr 3d (182 eV).

5.6.3 FLUORESCENT VISUALIZATION OF BIOFUNCTIONAL COATINGS

Fig 5.6-3 shows fluorescent images of green-labeled KKKGGGGRGDS oligopeptides that were physically (f-RGD) or covalently (CPTES/f-RGD) immobilized on ZrO_2, Z-75Ti and Ti surfaces. The fluorescent oligopeptides were immobilized on the studied surfaces following the procedure explained in Experimental Techniques (Chapter 7, Section 7.5.4.5). The images were taken before (f-RGD and CPTES/f-RGD) and after ultrasonication in DI-water for 2 hours (f-RGD/S and CPTES/f-RGD/S). Unlike f-RGD-surfaces, CPTES/f-RGD-surfaces showed strong green signal after peptide immobilization on all three materials. Only a small portion of the peptides on the biofunctionalized surfaces was lost after ultrasonication. This further suggested the oligopeptides were successfully and strongly bonded to the different substrates using a silanization process.

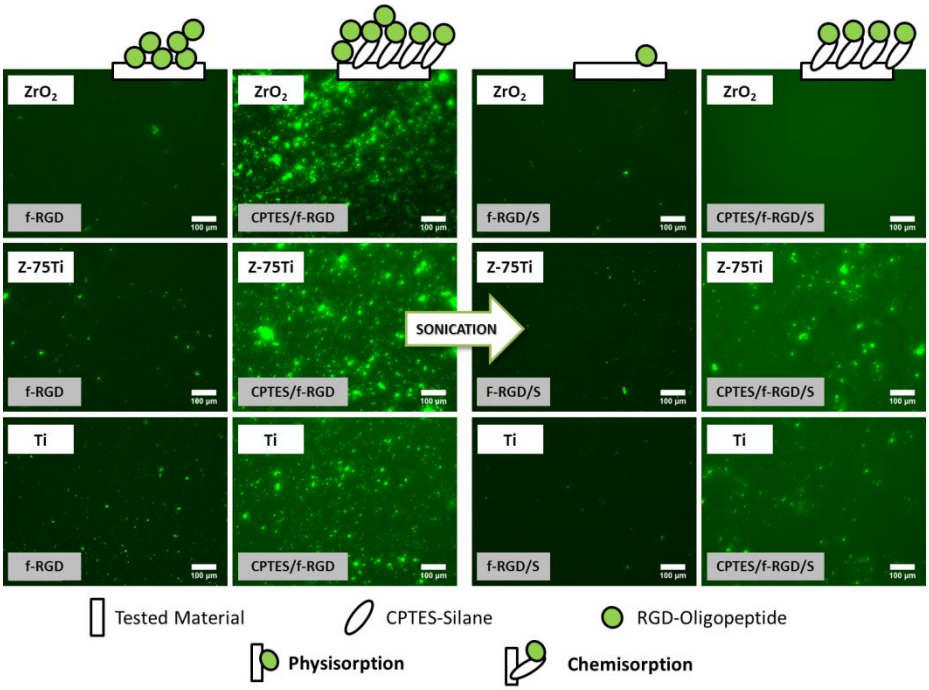

Fig 5.6-3. Visualization of the fluorescently-labeled RGD-coatings on ZrO_2, Z-75Ti and Ti surfaces. RGD-containing oligopeptides were labeled with 5-FAM cadaverine (green-fluorescence probe) before being immobilized on the surfaces. The labeled peptides were physisorbed (*f-RGD*) or chemisorbed using silane chemistry (*CPTES/f-RGD*). Fluorescent micrographs were taken before (*f-RGD and CPTES/f-RGD*) and after ultrasonication for 2 h (*f-RGD/S* and *CPTES/f-RGD/S*).

5.6.4 BIOLOGICAL *IN VITRO* ASSAYS

Cells of the murine pre-osteoblast MC3T3-E1 (ATCC, Manassas, VA, USA) line were cultured in α-MEM minimum essential medium supplemented with 10% FBS and 1% penicillin/streptomycin (P/S) at 37°C in a 5% CO_2 humidified incubator. Media was changed every 2-3 days. Sub-confluent cells were detached using a 0.05% trypsin-HBSS (Hanks Buffered Saline Solution, Sigma Chemicals) solution, centrifuged and seeded at a density of 10^4 cell/ml on the different samples. Samples were placed in 48-well microplates coated with agarose gel to prevent cell attachment at the bottom of the tissue-culture treated polystyrene (TCTP) wells. Samples were immersed in ethanol (70%, v/v), sterilized with UV light for 1 hour, and rinsed three times in PBS before cell assessment was performed.

5.6.4.1 Cell adhesion assays

In order to study how the diverse untreated (ZrO_2, Z-75Ti and Ti) and modified substrates (CPTES, CPTES/RGD, CPTES/RGD/S and RGD) influence cell adhesion, a triple-immunostaining was carried out following the protocol explained in (Chapter 7, Section 7.5.4.4). Fig 5.6-4 shows the number of adhered MC3T3 murine osteoblasts and Fig 5.6-5 present flurorescence images of the adhered cells on all modified surfaces after different times of cell culture. No significant differences were found between glass surfaces (positive control) and plain ZrO_2, Z-75Ti and Ti surfaces. Silanized surfaces (CPTES) significantly reduced cell attachment after 4, 6 and 18 hours in culture. Biofunctionalized surfaces (CPTES/RGD) significantly increased the number of adhered cells with respect to untreated surfaces and reached the highest numbers of cell adhesion after 6 hours of cell culture. Cellular spreading increased over time on untreated and, most notably, on biofunctionalized (CPTES/RGD) surfaces for all materials. The number of focal adhesion points developed by MC3T3 cells on the biofunctionalized surfaces was higher than on all other substrates at all periods of culture.

These results demonstrated that the biofunctionalized surfaces on all different materials displayed the expected bioactivity; that is, increasing cell adhesion, spreading, and development of focal adhesion points by cell recognition of the RGDS motif on the oligopeptide-coated surfaces.

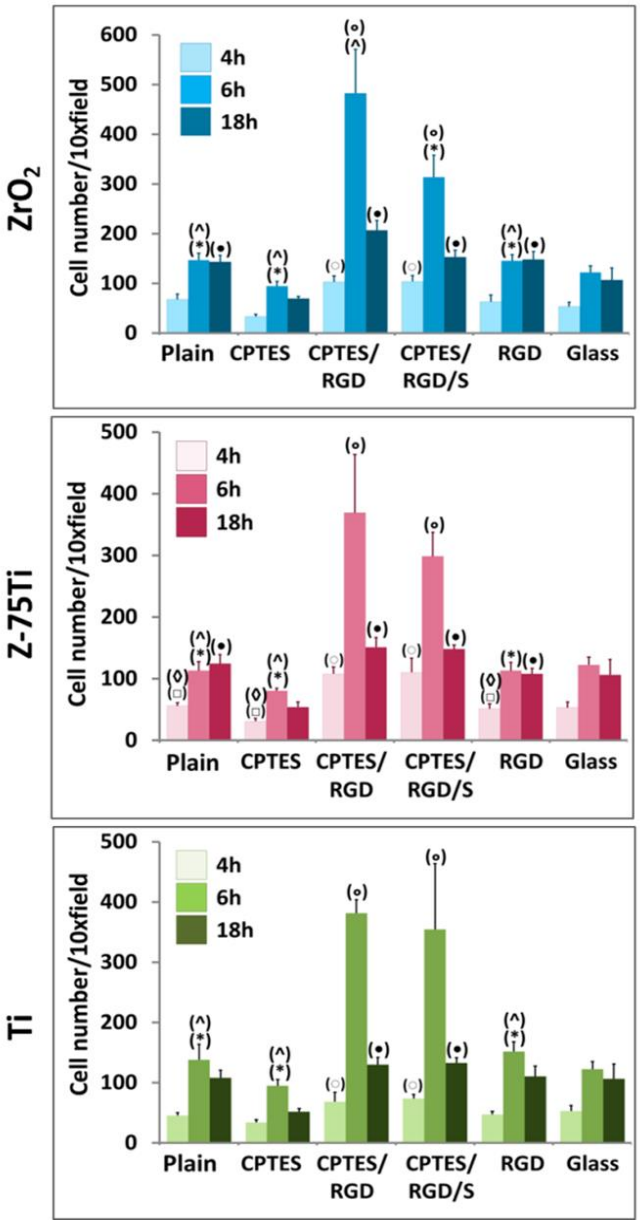

Fig 5.6-4.. Cell adhesion over time on the modified surfaces. 10^4 cells/ml of MC3T3-E1 osteoblasts were plated on the different surfaces for 4, 6 and 18 hours. Data are main number of adhered cells on the different modified surfaces (*n=5*); error bars are SEM. Symbols indicate significant differences: 1 symbol, $p<0.05$. ◌ compared to CPTES (4 hours), □ compared to CPTES/RGD (4 hours), ◊ compared to CPTES/RGD/S (4 h) * compared to CPTES/RGD (6 h), ^ compared to CPTES/RGD/S (6 hours), ◦ compared to CPTES (6 hours), • compared to CPTES (18 hours). Untreated surfaces: ZrO_2, Z-75Ti, T, and glass (positive control); CPTES*:* silanized surfaces; *CPTES/RGD:* silanized and RGD-peptide coated surfaces; *CPTES/RGD/*S: *CPTES/RGD surfaces after* ultra-sonication for 2 hours.

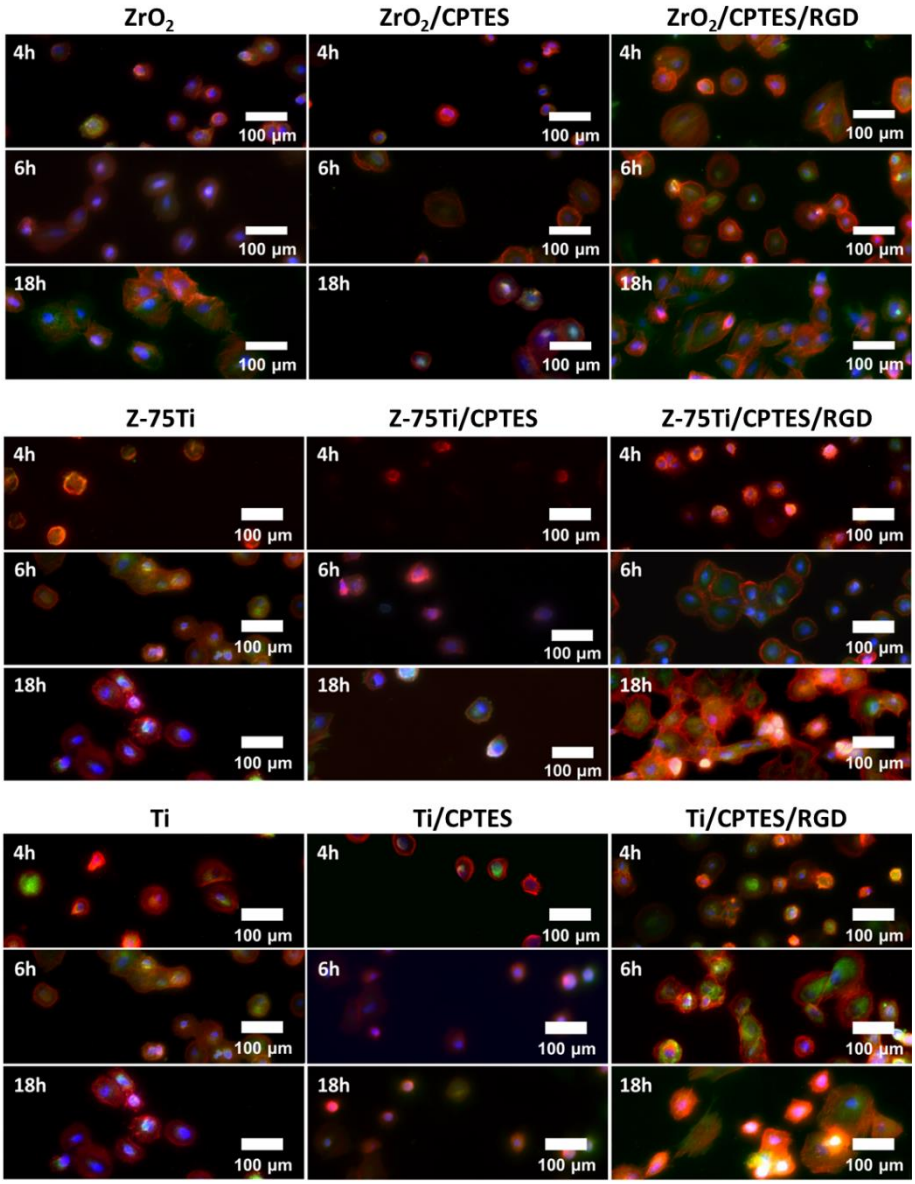

Fig 5.6-5. Fluorescent images of triple-stained cells adhered on the different modified surfaces after different periods in culture. Untreated surfaces: ZrO_2, Z-75Ti, Ti; CPTES*:* silanized surfaces; *CPTES/RGD:* silanized and RGD-peptide coated surfaces.

5.7 DISCUSSION

Implant loosening takes place in a significant proportion of patients due to the surface colonization by pathogenic bacteria or/and inflammatory mechanisms that lead to the fibrous encapsulation and bone resorption [1-4, 6, 21, 49, 50]. The biofunctionalization of biomechanically suitable biomaterials with organic molecules of specific-activity has been demonstrated as a high-effective method to control the adsorption of serum proteins, cells, platelets and bacteria in order to enhance osseointegration in short and last-term [18-21, 27, 51].

Stable biocoatings have been performed using silane-chemistry [28, 32, 42]. This technique was previously used in Ti implants with promising results [29, 30] and it is now extended to ZrO_2-containing materials. ZrO_2 is a widely used biomaterial in orthopedic and dental applications [9, 12, 52] that, to our knowledge, has not successfully been covalently biofunctionalized using silanes yet [28, 46-48, 53, 54]. In Chapter 4, Z-75Ti composites were disclosed as excellent biomaterials from the osseointegration point of view so this material together with pure zirconia was selected to be biofunctionalized. Ti samples were used as experimental control.

The biofunctionalization method implied surface activation, silanization and organic coating. NaOH-etching has allowed creating a hydrated metal oxide gel (1 µm) with alkaline ions on Ti metal, Ti alloys, tantalum or zirconium surfaces [55]. However, wettability tests (Table 5.5-1) suggested less reactivity on NaOH-etched surfaces, which is disclosed by their higher hydrophobicity. This method is thus rejected as an efficient procedure of surface activation, which was further supported by a microstructural destabilization and/or a non-controlled micro-roughness in the etched-surfaces (Fig 5.5-1). Other studies have also found the wet-chemical etching as a non-specific and non-reproducible procedure for activating substrates because of inducing topographical alteration and irregular etching [56-58].

Plasma treatments induced a high hydrophilicity so the surface free energy in the surfaces was increased (Table 5.5-1). Non-thermal plasma with high electron energy was used, which may produce physicochemical changes in the substrates [56, 57]. Indeed, ZrO_2 containing samples presented a microstructural alteration after 10-minutes in O_2-plasma (Fig 5.5-1). A significant decrease in Vickers hardness compared to untreated materials was also found both 5 and 10 minutes after oxygen-plasma (Fig 5.5-3). However, air-plasma led to suitable surface activation without any surface alteration (Fig 5.5-1). Conditions for PT_4 (air-plasma for 10 minutes) were optimal because this treatment produced surfaces with high hydrophilicity for at least 60 minutes in all the activated materials (Fig 5.5-2).

Successfully biofunctionalization was physically confirmed (Fig 5.6-1). Thus, high surface reactivity induced by the plasma treatment (PT_2) led to very low water-CA values on the activated (OH) samples. On silanizated (CPTES) materials, the main CA increased due to the siloxane nanolayer with alkyl chains provides a hydrophobic character to the surfaces. Substrates chemically-coated with RGDs-peptides (CPTES/RGD) had more hydrophilic character than silanized specimens. As expected, surfaces with directly-adsorbed RGDs-peptides (RGD) presented the highest hydrophilicity; K3G4RGDS peptides possess 15.3° of water CA in the Hopp and Woods scale for aminoacid hydrophilicity. No differences in the average water-CA on those chemically-coated specimens before (CPTES/RGD) and after (CPTES/RGD/S) mechanical challenge confirmed stability in the peptide anchorage.

The covalently immobilization of oligopeptides on the investigated substrates was chemically demonstrated through XPS analyses (Fig 5.6-2). Plain Ti presented characteristic C 1s, O 1s and Ti 2p peaks while plain zirconia showed C 1s, O 1s, Zr 3d and Y 3d peaks. Z-75Ti substrates had C 1s, O 1s, Ti 2p and Zr 3d peaks. Cl 2p and Si 2p peaks emerged on the CPTES-silanized samples, whilst the N 1s signal was revealed in the chemically-coated samples before and after sonication, demonstrating stability in the organic coating. In addition, Cl ratio decreased on all the RGD-coated samples due to the liberation of chlorine groups by the nucleophilic reaction (Table 5.6-1). Nitrogen (atom. %) increased after sonication and silicon decreasing because of releasing the non-linked silanes.

5-FAM cadaverine reacts with –COOH groups in the peptides leaving available $–NH_2$ groups for the subsequent attachment at surfaces. These green-fluorescent probes allowed to visualize the biocoatings physically (f-RGD) and chemically (CPTES/f-RGD) immobilized on the surfaces (Fig 5.6-3). Samples with peptides chemisorbed had a stronger green-signal than substrates with peptides physisorbed (f-RGD). Fluorescence was decreased by releasing the physisorbed peptides (f-RGD/S) after ultrasonication. The green fluorescence in the three investigated materials after mechanical challenge (CPTES/f-RGD), again demonstrated stability in the covalent attachment of oligopeptides.

In vitro assays (Fig 5.6-4; Fig 5.6-5) biologically corroborated the success in the biofunctionalization procedure. After 6 hours in cell culture, surfaces with chemisorbed RGDs-peptides inducted significantly higher cell number than untreated substrates. Moreover, CPTES-silanized samples supported statistically fewer cell number than plain and biocoated substrates. Surfaces with physisorbed RGDs-peptides had similar cell number than untreated ones because the weak forces in physical bindings (electrostatic, Van der Walls, hydrogen…) did not withstand

sterilization and cell culture procedures. Rather more cellular spreading on samples with peptides anchored covalently (Fig 5.6-5) was also disclosed. In particular, cells were well-stretched, and presented a well-defined F-actin cytoskeleton with large areas of focal adhesions anchoring at the inorganic surfaces 18 hours after seeding.

Therefore, the biofunctionalization of ZrO_2 and Z-75Ti substrates was as good, or even better, that for the reference material (Ti). It was noteworthy that the total number of cells varied according to the material nature (Fig 5.6-4). Wang et al. [67] have explained the higher reactivity in nanostructured materials by the presence of -OH groups in grain boundaries. More osteoblasts were recounted on ZrO_2 than on Z-75Ti and on Ti surfaces. Thus, nanofeatures in zirconia may favor the biochemical reactions.

5.8 CONCLUSIONS

As overall conclusion, it can be established that:

The 3-step method based on surface activation by plasma cleaning, CPTES-silanization and RGDs-coating allowed to successfully biofunctionalize zirconia/titanium (75 vol. %Ti) cermets as well as pure zirconia and titanium materials.

Particularly,

- Plasma treatment was disclosed as the most effective method to achieve uniform and suitable density of functional groups on all the surfaces. In fact, air-plasma treatment for 10-minutes increased properly the surface energy without causing any microstructural alteration or altering the inherent material properties, particularly microhardness.
- The technology based on silane-chemistry allowed the covalent immobilization of biomolecules with specific-known-activity on materials with different nature but with similar surface properties in terms of Z-potential.
- The three-step method of biofunctionalization purposed assured a successful bioactivation of zirconia-containing materials, which has been demonstrated through wettability studies, by means of XPS analyses, by direct visualization of the biocoatings labeled with fluorescent probes and by in vitro assays.
- Nano-topographic cues in the surfaces influenced the biofunctionalization process and the attachment of osteoblasts. Thereby, the osseconductive properties may be further improved by means of surfaces designed with submicrometric features
- The ability of functionalizing zirconia based materials with mechanically stable bio-coatings opens the possibility of their emerging applications for dental and orthopedic applications.

5.9 REFERENCES

[1] Khan W, Muntimadugu E, Jaffe M, Domb A. Implantable Medical Devices. In: Domb AJ, Khan W, editors. Focal Controlled Drug Delivery: Springer US; 2014. p. 33-59.

[2] Chiara G, Letizia F, Lorenzo F, Edoardo S, Diego S, Stefano S, et al. Nanostructured biomaterials for tissue engineered bone tissue reconstruction. International Journal of Molecular Sciences 2012;13:737-57.

[3] George A, Ravindran S. Protein templates in hard tissue engineering. Nano Today 2010;5:254-66.

[4] Mager MD, LaPointe V, Stevens MM. Exploring and exploiting chemistry at the cell surface. Nature Chemistry 2011;3:582-9.

[5] Goodman SB, Yao Z, Keeney M, Yang F. The future of biologic coatings for orthopaedic implants. Biomaterials 2013;34:3174-83.

[6] Chen X, Li Y, Aparicio C. Biofunctional Coatings for Dental Implants. In: Nazarpour S, editor. Thin Films and Coatings in Biology: Springer Netherlands; 2013. p. 105-43.

[7] Hanawa T. An overview of biofunctionalization of metals in Japan. Journal of the Royal Society Interface 2009;6:S361-S9.

[8] Beutner R, Michael J, Schwenzer B, Scharnweber D. Biological nano-functionalization of titanium-based biomaterial surfaces: A flexible toolbox. Journal of the Royal Society Interface 2010;7:S93-S105.

[9] Chen X, Sevilla P, Aparicio C. Surface biofunctionalization by covalent co-immobilization of oligopeptides. Colloids and Surfaces B: Biointerfaces 2013;107:189-97.

[10] Wang Z, Shen Y, Haapasalo M. Dental materials with antibiofilm properties. Dental Materials 2014;30:e1-e16.

[11] Ball M, Grant DM, Lo WJ, Scotchford CA. The effect of different surface morphology and roughness on osteoblast-like cells. Journal of Biomedical Materials Research - Part A 2008;86:637-47.

[12] Gil FJ, Manzanares N, Badet A, Aparicio C, Ginebra MP. Biomimetic treatment on dental implants for short-term bone regeneration. Clinical Oral Investigations 2013:1-8.

[13] Le Guéhennec L, Soueidan A, Layrolle P, Amouriq Y. Surface treatments of titanium dental implants for rapid osseointegration. Dental Materials 2007;23:844-54.

[14] Kim H-W, Georgiou G, Knowles JC, Koh Y-H, Kim H-E. Calcium phosphates and glass composite coatings on zirconia for enhanced biocompatibility. Biomaterials 2004;25:4203-13.

[15] Gomes S, Leonor IB, Mano JF, Reis RL, Kaplan DL. Natural and genetically engineered proteins for tissue engineering. Progress in Polymer Science 2012;37:1-17.

[16] Joddar B, Ito Y. Biological modifications of materials surfaces with proteins for regenerative medicine. Journal of Materials Chemistry 2011;21:13737-55.

[17] Salvagni E, Berguig G, Engel E, Rodriguez-Cabello JC, Coullerez G, Textor M, et al. A bioactive elastin-like recombinamer reduces unspecific protein adsorption and enhances cell response on titanium surfaces. Colloids and surfaces B, Biointerfaces 2014;114:225-33.

[18] Treccani L, Yvonne Klein T, Meder F, Pardun K, Rezwan K. Functionalized ceramics for biomedical, biotechnological and environmental applications. Acta Biomaterialia 2013;9:7115-50.

[19] Holmberg KV, Abdolhosseini M, Li Y, Chen X, Gorr SU, Aparicio C. Bio-inspired stable antimicrobial peptide coatings for dental applications. Acta Biomaterialia 2013;9:8224-31.

[20] Fenoglio I, Fubini B, Ghibaudi EM, Turci F. Multiple aspects of the interaction of biomacromolecules with inorganic surfaces. Advanced Drug Delivery Reviews 2011;63:1186-209.

[21] Khang D, Carpenter J, Chun YW, Pareta R, Webster TJ. Nanotechnology for regenerative medicine. Biomedical Microdevices 2010;12:575-87.

[22] Lung CYK, Matinlinna JP. Aspects of silane coupling agents and surface conditioning in dentistry: An overview. Dental Materials 2012;28:467-77.

[23] Rodríguez-Cano A, Cintas P, Fernández-Calderón M-C, Pacha-Olivenza M-A, Crespo L, Saldaña L, et al. Controlled Silanization-Amination Reactions on the Ti6Al4V Surface for Biomedical Applications. Colloids and Surfaces B: Biointerfaces 2013.

[24] Bauer S, Schmuki P, von der Mark K, Park J. Engineering biocompatible implant surfaces: Part I: Materials and surfaces. Progress in Materials Science 2013;58:261-326.

[25] Park J-W, Kurashima K, Tustusmi Y, An C-H, Suh J-Y, Doi H, et al. Bone healing of commercial oral implants with RGD immobilization through electrodeposited poly(ethylene glycol) in rabbit cancellous bone. Acta Biomaterialia 2011;7:3222-9.

[26] Rammelt S, Illert T, Bierbaum S, Scharnweber D, Zwipp H, Schneiders W. Coating of titanium implants with collagen, RGD peptide and chondroitin sulfate. Biomaterials 2006;27:5561-71.

[27] Schliephake H, Scharnweber D, Dard M, Sewing A, Aref A, Roessler S. Functionalization of dental implant surfaces using adhesion molecules. Journal of Biomedical Materials Research Part B: Applied Biomaterials 2005;73B:88-96.

[28] Elmengaard B, Bechtold JE, Søballe K. In vivo study of the effect of RGD treatment on bone ongrowth on press-fit titanium alloy implants. Biomaterials 2005;26:3521-6.

[29] Ferris DM, Moodie GD, Dimond PM, Giorani CWD, Ehrlich MG, Valentini RF. RGD-coated titanium implants stimulate increased bone formation in vivo. Biomaterials 1999;20:2323-31.

[30] Yazici H, Fong H, Wilson B, Oren EE, Amos FA, Zhang H, et al. Biological response on a titanium implant-grade surface functionalized with modular peptides. Acta Biomaterialia 2013;9:5341-52.

[31] Kim SE, Song S-H, Yun YP, Choi B-J, Kwon IK, Bae MS, et al. The effect of immobilization of heparin and bone morphogenic protein-2 (BMP-2) to titanium surfaces on inflammation and osteoblast function. Biomaterials 2011;32:366-73.

[32] Shiba K. Exploitation of peptide motif sequences and their use in nanobiotechnology. Current Opinion in Biotechnology 2010;21:412-25.

[33] Nayak S, Dey T, Naskar D, Kundu SC. The promotion of osseointegration of titanium surfaces by coating with silk protein sericin. Biomaterials 2013;34:2855-64.

[34] Huckel M, Wirth H-J, Hearn MTW. Porous zirconia: a new support material for enzyme immobilization. Journal of Biochemical and Biophysical Methods 1996;31:165-79.

[35] Reshmi R, Sanjay G, Sugunan S. Immobilization of α-amylase on zirconia: A heterogeneous biocatalyst for starch hydrolysis. Catalysis Communications 2007;8:393-9.

[36] Piascik J, Swift E, Thompson J, Grego S, Stoner B. Surface modification for enhanced silanation of zirconia ceramics. Dental Materials 2009;25:1116-21.

[37] Xible AA, De Jesus Tavarez RR, De Araujo CDRP, Bonachela WC. Effect of silica coating and silanization on flexural and composite-resin bond strengths of zirconia posts: An in vitro study. Journal of Prosthetic Dentistry 2006;95:224-9.

[38] Piascik JR, Wolter SD, Stoner BR. Development of a novel surface modification for improved bonding to zirconia. Dental Materials 2011;27:e99-e105.

[39] Thompson JY, Stoner BR, Piascik JR, Smith R. Adhesion/cementation to zirconia and other non-silicate ceramics: Where are we now? Dental Materials 2011;27:71-82.

[40] Fernandez-Garcia E, Gutierrez-Gonzalez CF, Fernandez A, Torrecillas R, Lopez-Esteban S. Processing and Spark Plasma Sintering of zirconia/titanium cermets. Ceramics International 2013;39:6931-6.

[41] Uchida M, Kim H-M, Miyaji F, Kokubo T, Nakamura T. Apatite formation on zirconium metal treated with aqueous NaOH. Biomaterials 2002;23:313-7.

[42] Kokubo T, Kim H-M, Kawashita M, Nakamura T. Process of calcification on artificial materials. Zeitschrift für Kardiologie 2001;90:86-91.

[43] Jacobs T, Morent R, Geyter N, Dubruel P, Leys C. Plasma Surface Modification of Biomedical Polymers: Influence on Cell-Material Interaction. Plasma Chem Plasma Process 2012;32:1039-73.

[44] Chu PK, Chen JY, Wang LP, Huang N. Plasma-surface modification of biomaterials. Materials Science and Engineering: R: Reports 2002;36:143-206.

[45] Matinlinna JP, Lassila LVJ, Özcan M, Yli-Urpo A, Vallittu PK. An introduction to silanes and their clinical applications in dentistry. International Journal of Prosthodontics 2004;17:155-64.

[46] Godoy Gallardo M. Biofuncionalización de superficies de titanio para la mejora del proceso de osteointegración.pdf. 2009.

[47] Witucki GL. A silane primer: chemistry and applications of alkoxy silanes. Journal of coatings technology 1993;65:57-.

[48] Yoshinari M, Matsuzaka K, Inoue T, Oda Y, Shimono M. Bio-functionalization of titanium surfaces for dental implants. Materials Transactions(Japan) 2002;43:2494-501.

[49] Liu X, Chu PK, Ding C. Surface modification of titanium, titanium alloys, and related materials for biomedical applications. Materials Science and Engineering: R: Reports 2004;47:49-121.

[50] Rao SP, Tripathy SS, Raichur AM. Dispersion studies of sub-micron zirconia using Dolapix CE 64. Colloids and Surfaces A: Physicochemical and Engineering Aspects 2007;302:553-8.

[51] Lopez-Esteban S, Diaz M, Moya J. Rheology of zirconia/nickel particulate system and microstructure of composites. Composites science and technology 2007;67:2303-10.

[52] Chakravarty R, Shukla R, Tyagi AK, Dash A, Venkatesh M. Nanocrystalline zirconia: A novel sorbent for the preparation of 188W/188Re generator. Applied Radiation and Isotopes 2010;68:229-38.

Chapter 6

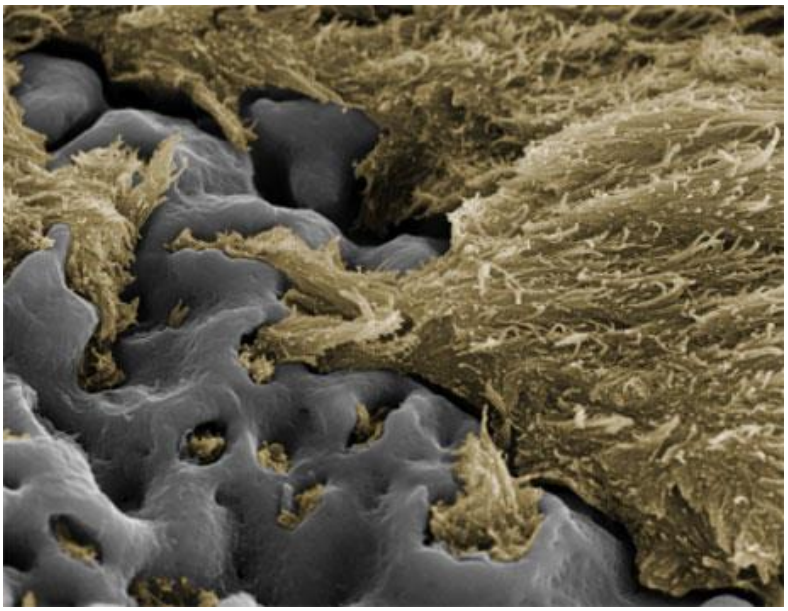

CONCLUSIONS/CONCLUSIONES

Design and evaluation of ceramic/metal composites for biomedical purposes

6.1 CONCLUSIONS

- Micro-nanostructured ceramic/titanium composites have been manufactured in a pioneer way using Spark Plasma Sintering (SPS) as sintering technique.
- Alumina/titanium composites with toughness twice higher than monolithic alumina and with and R-curve behaviour were achieved by uniform dispersion of metal particles (25 vol. % titanium) throughout the alumina matrix. This fracture toughness was accompanied by an excellent damage tolerance. Thus, these cermets were less sensitive to the loss of strength due to an increase in the indentation load.
- Fully dense zirconia/titanium cermets with 25 vol. %Ti, 50 vol. %Ti and 75 vol. %Ti were manufactured for first time as a result of shorter sintering times. Although the use of SPS allowed reducing the reactivity, side compounds such as α -Ti(O), Ti_2ZrO , α-Ti(Zr) and/or $Y_2Ti_2O_7$, are formed decreasing the flexural strength, toughness and inducing accelerated zirconia aging.
- The sol-gel coating of milled titanium particles with a layer of yttria was disclosed as a successful strategy to solve reactivity problems. Thus, this two-step method for modifying titanium powder led to twice σ_f values and absence of hydrothermal zirconia aging.
- Studies *in vitro* about cell viability demonstrated none alteration either in metabolic activity or in cellular membrane of osteoblasts. Thereby, the processing methodology used for manufacturing the biomaterials was revealed as safe in terms of cytotoxicity.
- *In vitro* studies revealed differences in the biocompatibility between materials, which were associated with the different chemical composition in the materials. Thus, the capability of osteoblasts to adhere, proliferate and differentiate was enhanced on the investigated ceramic/zirconia cermets when compared with the monolithic materials. Attachment of osteoblasts and their short-term differentiation were improved in the presence of the nanostructured zirconia. SPS emerges therefore as a suitable technique in order to manufacture dense materials with nanofeatures that trigger positive responses at molecular level.
- The purposed three-step method of biofunctionalization consisting in the surface activation within plasma treatment in air atmosphere for 10 minutes,

the subsequent silanization and (RGD) peptide coating assured a successful bioactivation of zirconia-containing materials. This was demonstrated through wettability studies, XPS analyses, as well as direct visualization of the labeled biocoatings with fluorescent probes and *in vitro* assays. This ability of functionalizing zirconia based materials with mechanically stable bio-coatings opens the possibility of their emerging applications for dental and orthopaedic applications.

6.2 CONCLUSIONES GENERALES

- Mediante la utilización de la técnica Spark Plasma Sintering (SPS) ha sido posible obtener materiales compuestos micro-nanostructurados en los sistemas alúmina/titanio y circona/titanio.
- En el caso del sistema alumina/titanio, la dispersión de una fase metálica (25 vol. % Ti) en la matriz de alúmina, ha permitido duplicar los valores de tenacidad y proporcionar un comportamiento de curva-R. Además, esta resistencia a la fractura ha sido acompañada de una excelente tolerancia a los defectos y, en consecuencia, estos cermets han resultado menos sensibles a la pérdida de resistencia como consecuencia del incremento en la carga de indentación.
- Gracias a los cortos tiempos de sinterización, se han podido obtener, por primera vez, cermets circona/titanio totalmente densos con un contenido en volumen de titanio del 25, 50 y 75%. Pese a que la utilización del SPS como técnica de sinterización ha permitido reducir la reactividad entre los componentes, aún han sido detectado compuestos secundarios (α-Ti(O), Ti_2ZrO, α-Ti(O, Zr) y/o $Y_2Ti_2O_7$) que inducen la caída de la resistencia mecánica a flexión, de la tenacidad y dan lugar al envejecimiento acelerado de la circona.
- Los problemas de reactividad en el sistema circona/titanio han sido reducidos modificando el polvo de titanio mediante una técnica en dos pasos consistente en la molienda de atrición del polvo y su posterior recubrimiento con una capa de itria por sol gel. Esta ha sido demostrada como una metodología eficaz ya que los valores medidos de σ_f se duplicaron respecto a los originales. Además, se ha verificado la resistencia a la degradación hidrotermal en la circona.
- Estudios *in vitro* de vialidad celular han demostrado la actividad metabólica de las células y su la membrana plasmática no resultan alterados como consecuencia de las metodologías de procesamiento y conformación

utilizadas para fabricar este tipo de biomateriales, las cuales son reveladas como seguras.

- Mediante estudios *in vitro* de adhesión, proliferación y diferenciación osteoblástica se ha demostrado que la biocompatiblidad en los sustratos investigados depende de su composición química superficial. Así, en ambos sistemas cerámica/titanio, la respuesta celular ha sido mejorada al utilizar los cermets como sustrato. En el caso particular del sistema circona/titanio, la adhesión y diferenciación a tiempos cortos han sido mejoradas en presencia de la fase cerámica nanoestructurada. En este sentido, el SPS surge como una técnica muy interesante para fabricar materiales capaces de desencadenar respuestas positivas a nivel celular, gracias a su potencial para obtener materiales densos nanostructurados,
- El método de biofuncionalización propuesto ha permitido inmovilizar con éxito moléculas orgánicas en la superficie de materiales compuestos que incluyen circona como matriz cerámica. Dicho método ha consistido en el tratamiento con plasma de las superficies en atmosfera de aire durante 10 minutos y un posterior proceso de silanización que permite el subsequente anclaje covalente de péptidos que, en este estudio, incluyen secuencias activas RGD. El éxito en el método de funcionalización ha sido comprobado mediante estudios de mojabilidad, análisis de XPS, por visualización directa de los recubrimientos biológicos marcados con sondas fluorescentes y mediante ensayos *in vitro*. Esta habilidad para funcionalizar materiales basados en circona con recubrimientos biológicos estables presenta un gran interés para multitud de aplicaciones en el campo dental y ortopédico.

Chapter 7

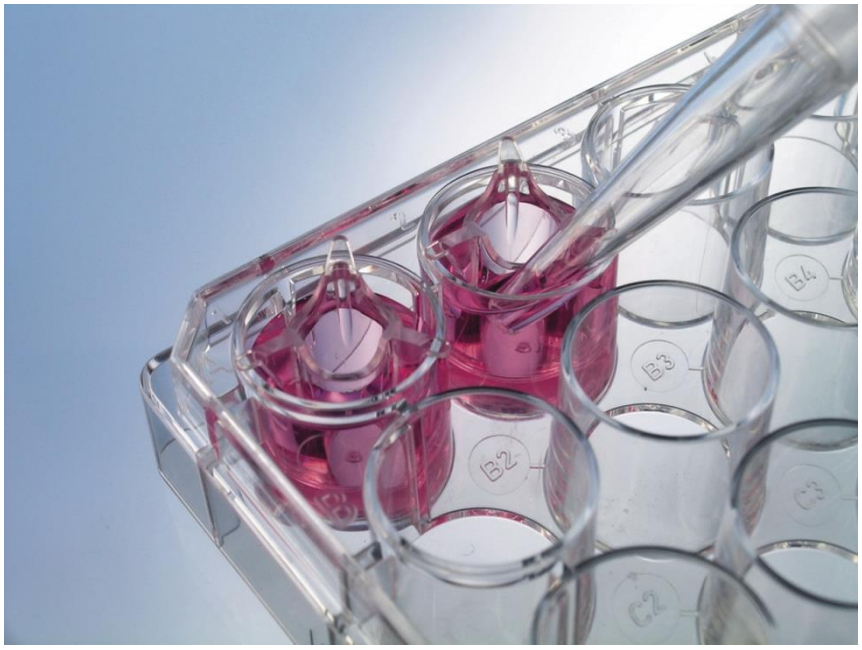

EXPERIMENTAL TECHNIQUES

Design and evaluation of ceramic/metal composites for biomedical purposes

7.1 INTRODUCTION

This chapter includes the description of the main techniques and procedures involved in the development of the experimental part of this thesis. These experimental techniques have been grouped into four wide-groups depending on their scope. First, the methodologies used for processing cermets. Then, the tecniques employed for assessing the developed materials from a physic/chemical standpoint will be described. The more representative technologies used for the characterization of surfaces that interact with the biological systems will also been approached. Finally, *in vitro* biological assays based on co-cultures of the inorganic materials with cell lines will be summarized.

7.2 PROCESSING CERMETS

Cermets are manufactured by a wet-processing of dissimilar powders followed by the appropriate sintering program to obtain compact materials with the highest density. On one hand, rheology and sedimentation studies are carried out to develop reliable suspensions that lead to mixtures of ceramic/metal powders distributed uniformly. On the other hand, spark plasma sintering will lead to fired specimens designed up to the nanolevel.

7.2.1 RHEOLOGY

In order to develop an homogeneous mixture of ceramic/metal powders, a wet route of powder processing was selected. An organic deflocculant that provides mainly steric stabilization has been chosen to obtain stable and fluid suspensions. Fig 7.2-1(a) shows an hypothetical diagram of a stable suspension, as well as a detail of a ceramic particle with deflocculant molecules adsorbed on its surface. The stabilizing effect of the deffloculant is mostly based on the electrostatic repulsion due to the negative charge in the anions that are adsorbed on the particle surface. Furthermore, there are steric effects as a consequence of the presence of $-CH_3$ groups. Considering both Van-der-Waals attractive forces and the repulsive -electrostatic and steric- interactions, there is an interparticle distance that will act as a barrier preventing the particles from collapsing. Thus, achieving that balance of energies is necessary to get stable ceramic/titanium suspensions.

Based on the experience in the group [1-3], a organic deflocculant was used for obtaining stable and fluid ceramic/metal suspensions [4]. In particular, the cationic polyelectrolyte Dolapix CE-64 (Zschimmer & Schwarz; Lahnstein, Germany) was

chosen as deflocculant. As it can be seen in Fig 7.2-1(b), this surfactant is based on an ammonium salt of a polycarboxylic acid and has NH_4^+ instead of Na^+, which is easier to remove with an appropiate thermal treatment. Besides, NH_4^+ ions because of their small charge density exert a relatively weak effect on the electrical double layer.

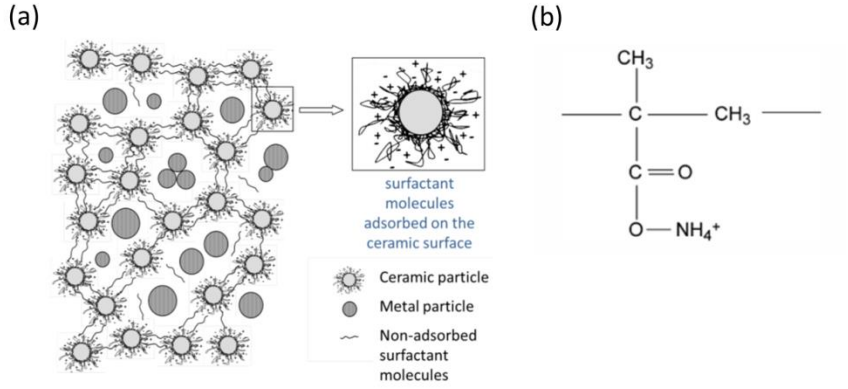

Fig 7.2-1. (a) Hypothetical diagram of a ceramic/metal network showing a ceramic particle in suspension and (b) chemical structure of Dolapix CE-64

In order to carry out sedimentation and rheology studies, suspensions with a solid content of 70 and 80 wt. % were prepared using distilled water as liquid media. The surfactant was added in a proportion of either 1 or 3 (wt. %). After milling with zirconia balls in polyethylene containers (150 rpm, 24 hours), the mixtures were placed into glass tubes for 24 hours to test the sedimentation behavior. In addition, viscosity was measured with a rotational rheometer (Haake Mars III, Thermo Fisher Scientific; Karlsruhe, Germany) including a Z40DIN cylinder sensor system (DIN53019/ISO3219) that also avoids the decantation of the mixture because it is a threaded cylinder. Each suspension is placed among two coaxial cylinders; the inner cylinder rotates while the outer containing the suspension remains immobile (Fig 7.2-2). When the rotor spins, the liquid flows over the grooves with a gradient of speed. The resistance of the liquid to flow is proportional to the torque and depends on viscosity. Between the drive motor and the rotor axis, a device measures the torque. Besides, the shear stress (τ) versus the shear rate (γ) is automatically calculated by the HAAKE RheoWin Software, version 4.30.0030 (Thermo Fisher Scientific; Karlsruhe, Germany). Typical graphics representing shear stress (τ) against shear rate (γ) are known as flow curves. The apparent viscosity (η) is also obtained by dividing the shear stress and the velocity gradient [2].

Fig 7.2-2. Haake Mars III rheometer with the Searle system.

The general flow behavior of the tested suspensions was obtained in a cycle of three steps performed at 20 °C. This cycle consisted in (1) increasing the shear stress, τ, continuously until a maximum of 100 Pa in 100 seconds, (2) maintenance of the maximum shear stress reached in step 1 for 60 seconds and (3) decreasing continuously from the maximum value to near zero in 100 seconds.

7.2.2 SPARK PLASMA SINTERING (SPS)

- Basics of sintering

Sintering is the densification of a material that takes place by a thermal treatment capable of initiating the diffusion of atoms from the grain boundaries in the particles of an initial powder. During sintering, the areas of the solid-vapor interface begin to decrease while the solid-solid interface is simultaneously formed; the motive force is the reduction of the free energy in the system [5]. The particle bonding occurs below the melting point of the material, at a temperature that is typically higher than the Taman temperature. This can be estimated as $T_m^{1/2}$; where T_m is the melting temperature in Kelvin.

Driving forces can be defined as those forces that act decreasing the free energy in the system during the sintering process. They correspond with: (1) the curvature of the surface of the particles, (2) the external pressure and (3) the chemical reaction. In the absence of external pressure and chemical reaction, the surface curvature provides the necessary motive force for sintering.

In polycrystalline materials, such as those involved in this work, the grain boundaries play a very important role because the reduction of the surface free energy is always accompanied by an increase in energy associated with the grain boundaries. Therefore, it should be considered for determining the magnitude of the motive force during sintering. There are two alternative ways of decreasing the energy in a system under sintering (Fig 7.2-3): densification that can be followed by grain growth or coarsening that implies an enlargement in the grains sizes by growing the bigger ones at the expense of the smaller ones.

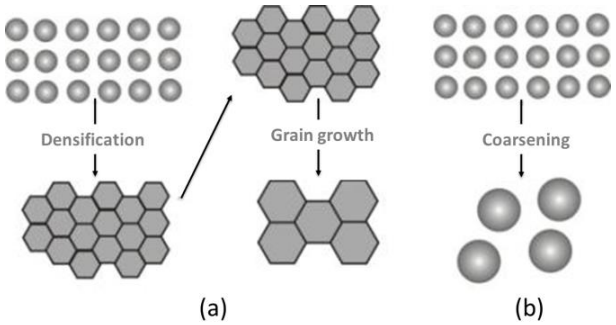

Fig 7.2-3. Densification followed by grain growth (a) and coarsening (b) as alternative ways of decreasing energy in the system.

The classical theories consider five mechanisms involved in the sintering process: (1) surface diffusion, (2) evaporation-condensation, (3) diffusion through the grain boundary, (4) volume diffusion and (5) flow diffusion. Surface diffusion and evaporation-condensation processes lead to the neck growth among particles, whilst the rest of mechanisms will produce a material contraction and hence its densification [6].

Three stages are involved in the sintering process [7]. In the initial stage, the motive force is the chemical gradient between the particle surface and the neck region. As explained by the *Two Spheres model,* Fig 7.2-4, the material is transported from areas of higher chemical potential to those of lower chemical potential by diverse mechanisms; some of them contribute to the grain growth while others favor densification [8]. In the intermediate stage, the grains begin to grow while the porosity is reduced to channels. At this step most of densification and microstructural change occur. It ends when grain boundaries form a continuous network, and the porosity is minimized. The final stage is the most important because it will determine the final properties in the materials. At the end of this step, it may remain isolated

pores in the grain boundaries, at the junction of three or four grains or trapped within the grains.

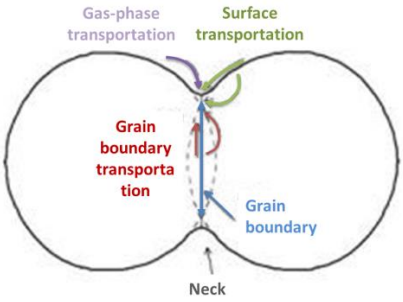

Fig 7.2-4. The two spheres model for the initial stage of sintering.

- Basics of Spark Plasma Sintering (SPS)

SPS is a fast sintering technique, which is assisted by pressure. It is also known as EFAS (*Electric Field Assisted Sintering*), PECS (*Pulsed Electric Current Sintering*), FAST (*Field Assisted Sintering technique*), PAS (*Plasma assisted technique*) or PPC (*Plasma pressure consolidation*). It is believed that by means of the pulsed electrical discharge, high temperature plasmas or *spark plasmas* are briefly generated between the voids in the compacted powder.

Sintering by SPS takes place in a wide range of temperature, which is controlled by the electric current [9, 10]. The pulsed discharge can produce *spark plasmas* and pressure due to its impact, heating by Joule effect, and also an effect of diffusion of electric field [10, 11].

SPS has evolved as a consolidation method for new materials that are difficult for manufacturing using conventional techniques, because this technology avoids the main drawbacks of conventional sintering: reactivity between starting materials and bigger grain sizes due to the application of high temperature during a longer cycle [10]. The simultaneous application of electrical pulses and uniaxial pressure increases the surface diffusion in the powders. This, along with a heating rate up to 800 °C/min, facilitates a rapid consolidation of the material, a density close to the theoretical value, and a similar grain size to that in the starting powders[12-16]. Thereby, SPS allows to reflect the attractive properties of the nanostructured powders in the dense materials [15, 17]. However, to achieve homogeneous sintered materials, it is necessary to avoid or minimize the temperature gradients that are generated as a result of the high heating rate. Among the factors that strongly

influence the temperature distribution during sintering are the size, shape, thickness, electrical and thermal conductivity of the mold and the pistons, the contact between the mold and the piston, the pressure, speed heating, as well as the electrical and thermal properties of the sample and its mass [18].

Fig 7.2-5 schematizes a typical SPS device (a) and a graphite mold filled with compacted powder and heated by passing electric current (b). In a typical assay, the powders are placed into the graphite mold, subjected to uniaxial pressing (10-30 MPa) and then introduced in the SPS-chamber.

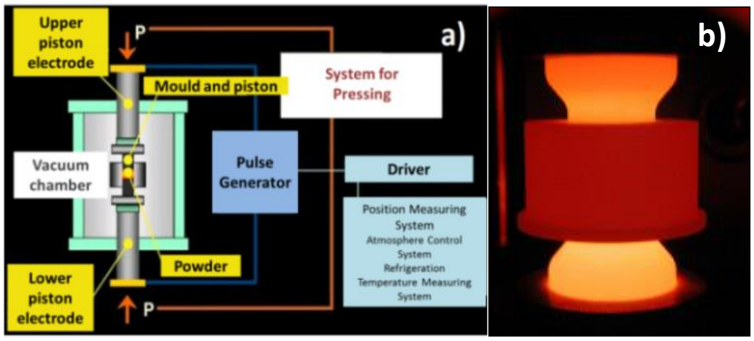

Fig 7.2-5. Diagram (a) of the SPS equipment and (b) of a graphite-mold.

Time, heating rate, duration and magnitude of pulses as well as voltage are parameters that can be modified in order to control the temperature along each cycle. Possible changes in the temperature, pulse power (voltage and/or current), piston displacement and sintering rate can be monitored during the process. A typical parameter set includes: (a) 50 and 100 MPa of pressure for a graphite-mold (pressure depends on the type of mold that is used), (b) heating rates up to 100 °C/min, (c) pulses of ≅ 10 ms with on-off cycles of 2-5 ms, and (d) a maximum current of 10^4 A and 10 V output voltage. Table 7.2-1 summarizes the technical data related to the FCT System GmbH (Frankenblick-Rauenstein, Germany) apparatus used in this work.

A characteristic cycle of SPS implies diverse stages [9] that are summarized in Fig 7.2-6. A vacuum is formed within the chamber and the suitable gas is then introduced, as long as sintering takes place within controlled-atmosphere. The beginning of the sintering will depend on the particle size because this is a limiting factor in the process. It is often difficult to determine when sintering has ended, although the rate of movement of the piston can help to deduce if the process has been completed.

When SPS is used to develop nanostructured materials, there is a range of temperatures, known as kinetic window, in which densification and grain growth can be separated [11]. The development of compacts with grain size similar to that in the starting powders implies to look for the kinetic window associated with each particular material [19].

Table 7.2-1: *Settings of FCT System GMBH (HPD 25).*

Force	5 - 250	kN	Pressing	0-1.100	mbar
Piston displacement	0 - 200	Mm	Output voltage (max)	10	V
Piston speed	0 – 4	$Mm{\cdot}s^{-1}$	Current (max)	10^4	A
Graphite mold diameter	20, 40, 80	Mm	Pulse duration	0-1000	ms
Temperature	RT 2200	°C	Pause duration	0-1000	ms
Heating rate	5 - 600	$°C{\cdot}min^{-1}$	Pulse number	0-1000	-
Final vacuum	$5x10^{-2}$	Mbar	Extra pause	0-1000	ms

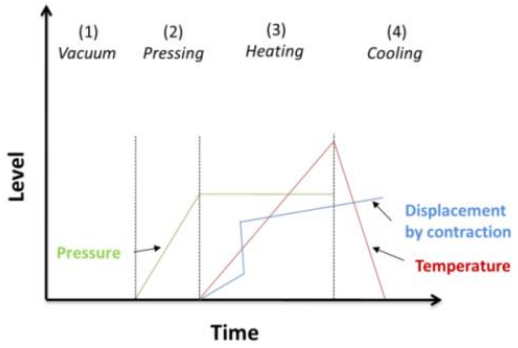

Fig 7.2-6. Main stages in a cycle of Spark Plasma Sintering.

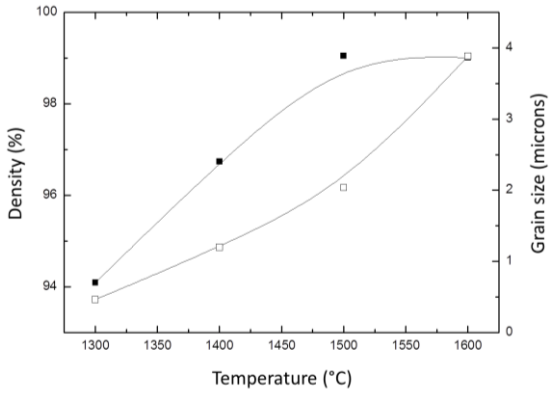

Fig 7.2-7. Main stages in a cycle of Spark Plasma Sintering.

7.3 PHYSICAL/CHEMICAL CHARACTERIZATION

7.3.1 DENSITY

The density or more precisely, the volumetric mass density of a substance is its mass per unit of volume. As shown in Equation 7.3-1, the density of each solid material is mathematically defined as the mass of the solid among the volume that it occupies.

$$\rho = \frac{m}{v} \qquad \text{Equation 7.3-1}$$

where ρ is the density, m is the mass, and V is the volume.

The density can be separated into the *theoretical density* that considers the solid volume excluding any type of porosity and the *bulk density* that considers the solid volume excluding the open porosity. The material porosity is formed by pores, which are cavities or channels of different types, as those schematized in Fig 7.3-1. Whilst open porosity is measured by immersion of the solid in a liquid (water, mercury, etc.), the closed porosity is determined by means of an analysis with helium, onto either the powder or the fired specimen.

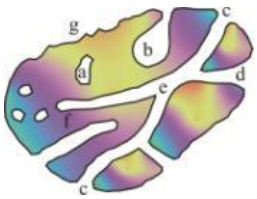

Fig 7.3-1. Types of pores: (a) closed or totally isolated; (b, c, d, e, f) open or communicated with the outer surface; (b, f) open at one end or (c) at both ends. Roughness (g) is understood as porosity when the depth of the irregularities is larger than their width.

Following instructions of ASTM C 373-88 [20], the *bulk density* of ten sintered solids was measured as per Archimedes method according to Equation 7.3-2:

$$D_{bulk} = \frac{M_1}{M_1 - M_2} D_L \qquad \text{Equation 7.3-2}$$

Where M_1 is the dry sample weight, M_2 is the immersed sample weight and D_L is the immersion liquid density at the assay temperature. The SARTORIUS VRD analytical balance (Sartorius Mechatronics SA, Spain), with ± 0.0001 g of precision, was used to calculate the different density values of all specimens.

7.3.2 X-RAY DIFFRACTION (XRD)

X-ray diffraction is a non-destructive technique for structural characterization of solid materials that presents high precision and versatility. X-rays are a form of electromagnetic radiation with high energy and wavelength in the interatomic level. When an X-ray beam impinges on a solid material, a part of this beam is scattered either by the electrons associated with the atoms or by the ions that are found in its path. Moreover, there is a remaining energy that may result in the phenomenon of X-ray diffraction as long as it exists an ordered arrangement of the atoms in the solid, as well as a relationship between the wavelength and the interatomic distance of the incidence angle in the diffracted beam [21].

Fig 7.3-2 shows a description of Bragg's model with the different types of atoms that are located on their respective parallel planes with $\Delta\phi$ spacing. The separation between blue and green planes creates interferences and differences of phases (between the reflected beams) giving rise to changes in intensity (depending on the direction). These changes of intensity allow to get information about the atoms forming the crystal [22].

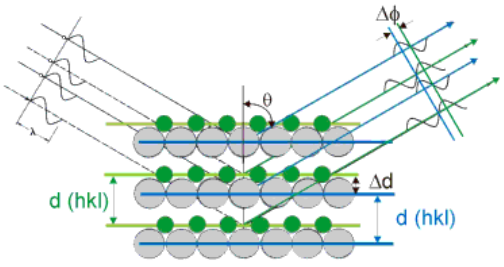

Fig 7.3-2. Interaction of X-rays with atoms [22].

Bragg diffraction, also referred to as the Bragg formulation of X-ray diffraction was first proposed by W. L. Bragg and W. H. Bragg in 1913 in response to their discovery that crystalline solids produced surprising patterns of reflected X-rays. They found that these crystals, at certain specific wavelengths and incident angles, produced intense peaks of reflected radiation (known as Bragg peaks) [23, 24]. The concept of Bragg diffraction applies equally to neutron diffraction and electron diffraction processes. Both neutron and X-ray wavelengths are comparable with inter-atomic distances (≈150 pm) and thus are an excellent probe for this length scale [24]. W. L. Bragg explained this result by modeling the crystal as a set of discrete parallel planes separated by a constant parameter, *d*. It was proposed that the incident X-ray radiation would produce a Bragg peak if their reflections of the various planes

interfered constructively [23]. The interference is constructive when the phase shift is a multiple of 2π; this condition can be expressed by Bragg's law according to Equation 7.3-3:

$$2d\text{sen}\theta = n\lambda \qquad \text{Equation 7.3-3}$$

where *n* is an integer, *λ* is the wavelength of incident wave, *d* is the spacing between the planes in the atomic lattice, and *Θ* is the angle between the incident ray and the scattering planes [21, 22]

The crystalline structure of the diverse materials involved in this work has been evaluated by means of several diffractometers depending on their availability. All of them exhibited the *Bragg-Brentano* or *reflection geometry* shown schematically in Fig 7.3-3, in which the source and detector are located toward the same side of the sample.

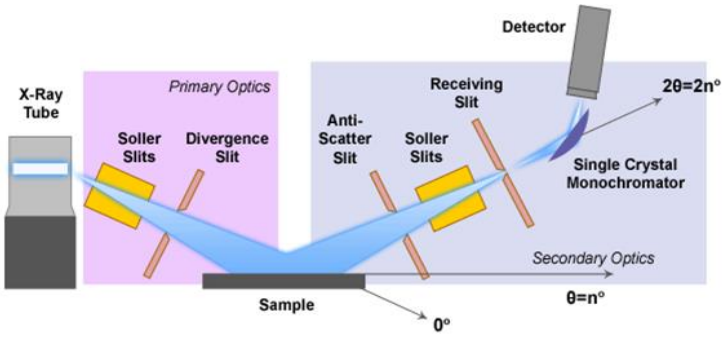

Fig 7.3-3. Typical scheme of a Bragg-Brentano type diffractometer [25].

A divergent beam broadens until it reaches the specimen and from there, it is focused onto the receiving slit, which is followed either by the detector or by some secondary monochromators. In the case of the secondary monochromators, the beam would be refocused onto the detector [25]. The diffracted rays from the crystal planes are collected by the detector to be converted into electric pulses, giving the characteristic diffractogram. For each assay, diffractograms were performed ranging from 5° to 80°. The step size was 0.02° and the time by step was 0.6 seconds. Every diffractometer used Cu Kα radiation (ʎ = 1.5418), working at 40 kV and with an intensity of 40 mA.

7.3.3 MECHANICAL PROPERTIES

All materials for biomedical applications ought to show a proper biomechanics to the aim sought. Thus, those materials intended for hard tissues replacement should ideally exhibit equivalent to bone mechanical properties. New cermets will be tested with regard to important mechanical properties such as strength, toughness and hardness, as well as regarding damage-tolerance and R-curve behaviour.

7.3.3.1 Bending strength

Due to the extreme fragility of ceramics, performing a tensile test is not easy because specimens usually break when they are grabbed with the jaws in the equipment. This leads to carry out alternative tests such as the bending test, a static test often used to analyze the mechanical properties of ceramic-based materials [26, 27]. The flexural strength, σ_f, is the ability that a material presents to withstand the forces applied to its longitudinal axis, in the area between the supporting points. As can be seen in Fig 7.3-4, a non-uniform stress state is imposed in the specimen under a flexural load; the bottom part is subjected to tensile while the top fiber is subjected to compression. Besides, there is a medium axis in which stress vanishes. A bending load produces therefore a combination of tensile, compression and shear stresses; the *maximum stress* or *fracture stress* in the flexural test is called either *flexural strength* or *modulus of rupture*. The flexural strength is also defined as the ratio between the bending moment, in the case of specimen fracture, and its moment of resistance.

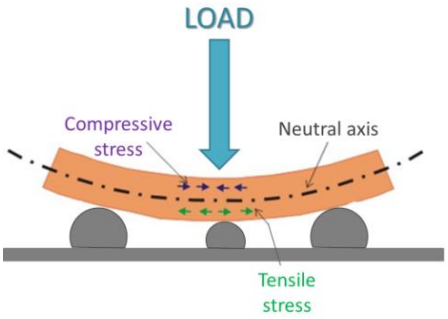

Fig 7.3-4. Set of strains in the sample under bending load in a biaxial flexure test.

Flexural tests were performed following the indications in ISO 6872:2008 that specifies the requirements and the corresponding test methods for dental

ceramic materials, for fixed all-ceramic and metal-ceramic restorations and prostheses [28]. The flexural strength was evaluated through a biaxial bending test. Each sample was placed onto a device with three balls of 6 mm in diameter that were made of hardened steel and disposed on a holder (12 mm of diameter) at 120° to each other. The load was applied with an ElectroPulse E10000 Test Instrument (Instron, Spain) by means of a plain head of 1.4 mm in diameter at a speed of 1 $mm \cdot min^{-1}$ [28] up the failure. The specimen thickness was measured at the breakage point. The bending strength is calculated according to Equation 7.3-4:

$$\sigma_f = -0.2387\ P\ (X - Y)\ /\ b^2 \qquad \text{Equation 7.3-4}$$

Where σ_f is the maximum tensile stress applied at the center of the sample (MPa), *P* is the total load that causes the rupture (N), *b* is the thickness (mm) and X and Y are factors that are calculated as following:

$$x = (1+\nu)Ln(\frac{r2}{r3})^2 + [(1-\nu)/2](\frac{r2}{r3})^2 \qquad \text{Equation 7.3-5}$$

$$y = (1+\nu)[1+\ln(\frac{r1}{r2})^2] + (1+\nu)(\frac{r1}{r2})^2 \qquad \text{Equation 7.3-6}$$

Where ν is the Poisson ratio, *r1* is the radius of the circle of support (6 mm), *r2* is the radius of the surface on which load is applied (1.5 mm) and *r3* is the radius of the sample.

7.3.3.2 Toughness

One of the macroscopic properties that characterize the fragility of a ceramic is the fracture toughness, K_{IC}, that describes the ease to crack propagation in a material [29]. In brittle materials, fracture begins from a single location, from a discontinuity such as a flaw or a defect, which acts as a localized stress concentrator. This may be developed mechanically, chemically or thermally. As a result of an applied stress, cracks from the flaw propagate, leading to catastrophic failure. Sub-critical, stable and unstable are the types of crack extension in a ceramic material. The progressive slow growth of crack (subcritical growth) in tension, particularly in the presence of water, is the reason for the well-known time-dependent strength decrease of ceramic materials [30, 31]. By increasing the load, the crack propagates until the component fails. The point of failure is characterized by the critical *stress intensity factor*, better-known as *fracture toughness,* K_{IC}. Whilst the material strength depends on the size of the initial crack in each particular sample, the fracture

toughness is an inherent property of the material to resist the rapid crack propagation and is independent of the size of preexisting cracks [29, 32].

Among the diverse techniques that exist to determine the fracture toughness [32-35], the single-edge-notch beam (SENB) technique that comprises conventional fracture mechanics has been selected. In this elementary fracture mechanics test, a starter notch is introduced using a diamond saw blade. The setup in the SENB test is performed as per instructions in [28] according to a three-points bending test. The specimen is placed with the notch face down. The specimens were loaded at a cross-head speed of 0.5 mm·min^{-1}. The values of fracture toughness, K_{IC}, were estimated by Equation 7.3-7 from the maximum load (P), as well as the dimensions of the specimen and the notch such as shown in Fig 7.3-5.

$$K_{IC} = \sigma\sqrt{aY} = \frac{P}{b\sqrt{w}} \times \frac{S}{w} \times \frac{3\sqrt{\alpha}}{2(1-\alpha)^{1.5}} Y \qquad \text{Equation 7.3-7}$$

Where K_{IC} is fracture toughness (MPa$\sqrt{m}$), σ is the fracture strength (MPa), P is the failure load (MN), b is the specimen thickness (mm), w is the sample width, S is the distance between supports and Y is the stress intensity factor that in the three-point test is calculated as below:

$$Y = 1.947 \cdot 2 - 5.047 \cdot 7 \propto +11.895 \cdot 4 \propto^2 - 18.063 \cdot 5 \propto^3 + 14.598 \cdot 6 \propto^4 - 4.689 \cdot 6 \propto^5$$

$\propto$ is the relative depth of the notch, which is measured by means of an optical microscope and has 0.4W depth.

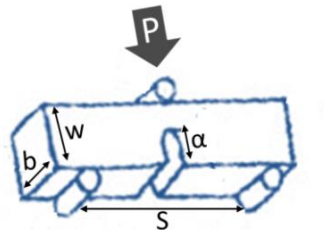

Fig 7.3-5. Illustration of a specimen in the single-edge notched-beam (SENB) method.

The SENB method avoids the main problem in the Indentation method, i.e. a scatter in the measured values up to 30-40%. The crack production and the subcritical crack growth associated with residual stresses, which remain in the indentations fields, make difficult an accurate measurement of the crack length [33, 35].

7.3.3.3 Vickers hardness

Another common value magnitude for characterizing the mechanical properties of ceramics and ceramic/metal composites is the Vickers hardness measurement. The assessment of hardness is particullary important in the dentistry field because it delimits the hardness of the material to which the natural dentition may be submitted [36].

Hardness is a measurement of a material resistance to permanent surface indentation or penetration. Indentation experiments have been used for over a hundred years to measure the hardness of solids. In such experiments a load is typically applied on the solid surface by an indenter and a hardness value is obtained by dividing the load by the residual projected area of the indentation. The residual area refers to the area of the indentation measured after the indenter has been completely unloaded from the sample [37].

The methodology used for the determination of Vickers hardness, H_V, was in accordance with ASTM C 1327-9925 specifications [38]. Thirty Vickers impressions were carried out in the surfaces of each one of the tested samples, which had previously been polished down 1 µm. The suitable load was applied during ten seconds by a Vickers diamond indenter (Leco 100-A, St. Joseph, MI, US) with a diamond-tip of pyramidal geometry and an apex of 136°, such as shown in Fig 7.3-6.

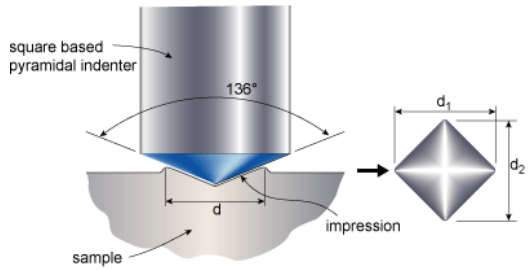

Fig 7.3-6. Diagram of the Vickers indenter (the penetration depth is 1/7 of the diagonal) and measurement of the impression diagonals [37].

After the diagonal length measurement, using an optical microscope (Leica DMR Model, Germany), the values of the Vickers hardness (GPa) were calculated by the Equation 7.3-8.

$$H_v = \frac{1853P}{d_1 d_2} \qquad \text{Equation 7.3-8}$$

Where P (N) is the applied load and d_1 and d_2 (m) are the length of the diagonals in the indentation.

A microdurometer (5100 Series-Version 2.10, Buehler Micromet, IL) was also used in Chapter 5 to investigate detrimental effects of the biofuctionalization treatments on the mechanical properties of the different materials. In this study, four samples per group were tested and 15 indentations per sample were evaluated and quantified (H_v). Load of 10^3 g·f for 10 seconds were applied on ZrO_2 and Z-75Ti surfaces and 10^2 g·f for 10 seconds on Ti surfaces as the latter is notably softer than the other two materials.

7.3.3.4 R-Curve behaviour and damage tolerance

A requirement for almost all structural materials is that they should be both strong and tough, i.e. damage tolerant. However, the properties of strength and toughness are often exclusive [39, 40] and, for safety-critical applications lower-strength and hence higher-toughness materials are used. Thus, the development of strong and tough (damage-tolerant) materials is still a challenge.

From a fracture-mechanics perspective, the ability of a microstructure to develop toughening mechanisms acting either ahead or behind the crack tip can result in a resistance-curve (R-curve) behavior where the fracture resistance increases with crack extension; the implication here is that toughness is often developed primarily during crack growth and not for crack initiation [39].

The interaction between the mechanisms that individually contribute to strength and toughness can originate from very different length-scales in a material's structural architecture [40]. All these reinforcement mechanisms involve an increase in the energy dissipation as the crack growth occurs [3].

The critical-stress-intensity factor, K_{IC}, depends on the intrinsic toughness of the material, K_0, as well as on the diverse reinforcement mechanisms, ΔK_c, that may exist; so that:

$$K_{IC} = K_0 + \Delta K_c \qquad \text{Equation 7.3-9}$$

Those mechanisms reduce the critical-stress-intensity factor at the crack tip, producing crack shielding to the applied load. If ΔK_C represents the effect of all the

toughening mechanisms, the necessary condition for the onset of fracture is the following:

$$K_{apl} = K_0 + \Delta K_c \qquad \text{Equation 7.3-10}$$

Where K_{apl} is the critical-stress-intensity factor that is applied.

Ceramic-based materials present different mechanisms that contribute to increase the toughness. In overall, the reinforcement mechanisms can be divided in two groups depending on the crack zone where they act: ahead or behind the crack tip. Each particular reinforcement mechanism has already been thoroughly explained in [3].

New ceramic/metal composite can defeat the conflict of strength versus toughness and achieve unprecedented levels of damage tolerance within their respective material classes.

R-curves were obtained using the indentation-strength method developed by Braun et al. in [41]. This method is based on the formation of a radial crack c produced by an indentation from a load P. After indentation, the crack is subjected to a tensile stress, σ_a, due to the applied stress load during the bending test. While this test is running, the crack undergoes to total stress intensity, K_t, which is the total contribution from the residual stress-intensity-factor acting on the indentation crack after unloading, K_r, and the stress intensity factor resulting from the applied stress, K_a.

$$K_t(c) = K_a(c) + K_r(c) = \psi\sigma_a\sqrt{c} + \xi\left(\frac{E}{H}\right)^{\frac{1}{2}}\frac{P}{c^{\frac{3}{2}}} = K_R(c) \qquad \text{Equation 7.3-11}$$

ψ is a material independent constant but dependent on the crack shape, ξ is a non-dimensional geometrical constant that is related with the indenter geometry and the Poisson's ratio of the indented material. E is the Young's modulus, H is the Vickers hardness and K_R is the material toughness that depends on the pertinent-toughening mechanism and the development of the process zone during crack growth.

In ceramics with R-curve behavior, crack propagates when the applied crack-driving force is equal to the crack-growth resistance. In terms of stress-intensity factors, this criterion for crack extension is given by the following Equation 7.3-12:

$$K_t(c) = K_R(c) \qquad \text{Equation 7.3-12}$$

Crack extension can be stable if the following condition is fulfilled:

$$\frac{K_t(c)}{dc} < \frac{K_R(c)}{dc} \qquad \text{Equation 7.3-13}$$

Or unstable crack extension when the following condition is met:

$$\frac{K_t(c)}{dc} > \frac{K_R(c)}{dc} \qquad \text{Equation 7.3-14}$$

The transition from stable to unstable crack propagation will occur for a specific crack extension value, c_f. In this point, the following equations are satisfied:

$$K_t(c_f) = K_R(c_f) \qquad \text{Equation 7.3-15}$$

$$\frac{K_t(c_f)}{dc} = \frac{K_R(c_f)}{dc} \qquad \text{Equation 7.3-16}$$

Ceramics R-curve behavior can be predicted by resolving simultaneously both equations. Therefore the R-curve is determined as the common envelope of the tangency points to the family of $K_t(c)$ curves obtained from the σ_f vs. P data sets.

The values of ψ and ξ parameters for the materials that have been involved in the study of R-curve behaviour and damage tolerance are summarized in Table 7.3-1. The ξ parameter values have been obtained from reference, for both pure alumina and alumina/titanium materials [42]. This parameter was found to be 0.016 for any type of material that undergoes volume-conserving deformation, such as in the present study. In the case of ψ parameter, the value for monolithic alumina has been obtained from previous works [43]. For the Al_2O_3/Ti (25 vol. %Ti) system, any reported of data have not been found in the literature. Calculating the shape factor (ψ) implies measuring the ratio of the crack depth (a), the crack half-length (c) and the surface crack, which surmises the evaluation of the ellipticity of the crack geometry. It is assumed that the shape of a crack induced by indentation, when subjected to bending, changes from semicircular to semi-elliptical as the crack size increases [44]. The estimation of the crack ellipticity was based on the assumption made by Li et al. [45] and the ψ is calculated from Newman and Raju's analysis [46].

Table 7.3-1: *Geometrical parameters of the monolithic alumina and alumina/titanium composite.*

MATERIAL	ψ	ξ
Al_2O_3	1.05	0.016
Al_2O_3/Ti	1.29	0.016

In the case of the indentation strength tests, they were performed using the 20 mm diameter disks, in which the centers of the tensile faces were indented with a Vickers diamond at contact loads, *P*, between 9.8 and 490 N. The mechanical test was performed immediately after indentation to avoid any subcritical crack growth due to stress corrosion effects. The strengths, σ_f, were calculated from the failure loads and the specimen dimensions. A special effort was made to examine all specimens after testing using reflected light optical microscopy (Leica, DMR model; Germany), to verify that the indentation contact site acted as the origin of failure.

7.4 SURFACE ANALYSIS

Surface properties have an enormous effect on the success or failure of a biomaterial device, thus the adequate characterization of the biomaterial surface has considerable importance. Such characterization is essential for correlating any surface modifications with changes in the biological performance.

7.4.1 CONTACT ANGLE (CA) GONIOMETRY

Wettability or wetting is the process when a liquid spreads (wets) on a solid substrate. The wettability of a solid with a liquid is usually determined from their contact angle, CA, or wetting angle. As schematized in Fig 7.4-1 (a), the shape of a liquid drop in contact with a solid substrate can be explained by the relative strength of the cohesive (Liquid/Liquid) and the adhesive (Solid/Liquid) forces. This is determined by the interfacial forces in those participating phases, which can be summarized in terms of the three states of matter as follows: vapor/liquid, vapor/solid, liquid/liquid, liquid/solid and solid/solid.

A strong adhesion with weak cohesion produces very low CAs with nearly complete wetting. As the solid/liquid interactions weaken and the liquid/liquid interactions strengthen, wetting diminishes and CA increases (Fig 7.4-1 (b)). Wetting

(hydrophilic) or non-wetting (hydrophobic) of a solid with water is a qualitative criterion from all surfaces of condensed-phase materials [47, 48].

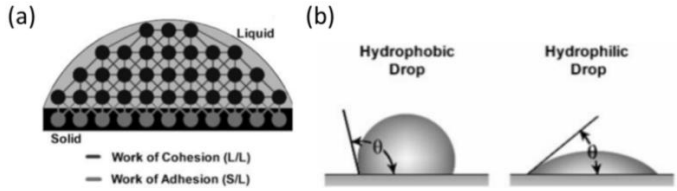

Fig 7.4-1. Distribution of adhesion and cohesion forces inside a drop (a), as well as hydrophobic and hydrophilic droplets with their characteristic contact angles (Θ) (b) [48].

The hydrophilicity of a surface is related to its affinity to water and by extension to its capability to form hydrogen bonds [49]. Furthermore, it has been suggested to define hydrophobicity as a repulsive force between non-polar molecules and water [50]. Hydrophobicity and hydrophilicity concepts can be simplified by grouping the different interactions between molecules into dispersion (Van der Waals) or polar (acid-base Lewis). From this standpoint, the interaction between a solid surface and a fluid molecule will be a particular case of intramolecular forces. In consequence, the overall interaction will depend on (1) the chemical groups on the surface that are mainly responsible for both polar and electrostatic interactions, (2) the surface typology (porosity, roughness and crystallography) and, (3) the structure and the functionality of the fluid components [48].

Thomas Young [51] proposed that the contact angle (Θ) of a liquid is derived from the condition of equilibrium of forces that represent surface tensions at the contact point of the three phases—solid, liquid and gas; such as shown in the equation below:

$$\sigma_{SV} = \sigma_{SL} + \sigma_{LV} \cos\theta \qquad \text{Equation 7.4-1}$$

where σ_{SV} is the surface tension on the solid–gas phase boundary, σ_{SL} is the surface tension on the solid–liquid phase boundary, σ_{LV} is the surface tension on the liquid–gas phase boundary and θ_v is the equilibrium contact angle.

As presented in Equation 7.4-2 the Young equation can also be derived from the energy balance for the triple point, so the equation will have the following form [52]:

$$\gamma_{SV} = \gamma_{SL} + \gamma_{LV} \cos\theta \qquad \text{Equation 7.4-2}$$

where γ denotes interphase energy and the other symbols have the same meaning as in Equation 7.4-1.

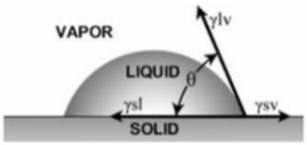

Fig 7.4-2. Contact angle and interphase-energy between the three phases: gas,liquid,solid

It is impossible to determine SFE directly from Fig 7.4-2 because there are two unknowns, γ_{SV} and γ_{SL}. Normally, the solid-vapor, γ_{SV}, and the liquid-vapor, γ_{LV}, interfacial free energy correspond to the intrinsic solid, γ_S, or liquid, γ_L, surface free energy, SFE. Thus, the following form of Equation 7.4-3 is commonly used to determine the SFE of solids [52-54]:

$$\gamma_S = \gamma_{SL} + \gamma_L \cos\theta \qquad \text{Equation 7.4-3}$$

where γ_S is the SFE of solids in a vacuum, γ_{SL} is the surface tension on the solid–liquid phase boundary, γ_L is the SFE of the measured liquid and θ is the contact angle measured on the examined surface.

Factors that have a substantial influence on the contact angle measurement are: Young's modulus (surface rigidity), surface roughness, surface physical and chemical homogeneity, surface impurities, type of measured liquid and humidity [52].

There are numerous methods for determining liquid SFE, such as the pendant drop method [55] but there are no direct methods for determining the SFE of solids. The calculation of the SFE of solids requires an equation that may link the interfacial free energy to other variables. Indirect methods to do that have been proposed [56] by Fowkes, Owens–Wendt and Wu [52]. Other methods are the Zisman method, the Neumann method and the Van Oss–Chaudhury–Good method [57, 58]. One of the most popular methods is the one proposed by Owens–Wendt, which has been used in this work.

SFE is one thermodynamic magnitude describing a state of equilibrium of atoms in the surface layer of materials, which is characteristic for each substance. It reflects the specific state of imbalance in the intermolecular interactions present at

the phase boundary of two mediums. It represents the work necessary for creating a new surface unit, while separating two phases in equilibrium, in a reversible isothermal process. It is measured in mJ/m^2 [52].

The Owens–Wendt method (also known as the Kaelble–Owens–Wendt method) consists in determining dispersion and polar components of SFE on the basis of the Bethelot hypothesis [52, 56], which claims that interactions between molecules of two substances present in their surface layer are equal to the geometric mean of intramolecular interactions within each substance (Equation 7.4-4).

$$\gamma_S = \gamma_S^d + \gamma_S^p \qquad \text{Equation 7.4-4}$$

Where γ_S is the SFE of the solid material, γ_S^d is the dispersive component of SFE and γ_S^p is the polar component of SFE. Components γ_S^d and γ_S^p can be calculated as explained in [52]

The SFE of a solid surface can be approached by using reference liquids, whose surface tension and polar and dispersion components of SFE are known. Following recommendations in [48], three different reference liquids were used to calculate the SFE of the studied solid surfaces: bipolar-water (ultrapure distilled water; MilliQ), non-polar diiodomethane and the strongly hydrogen-bonding liquid, formamide. Distilled water is a highly polar liquid with a total SFE of 72.8 mJ/m^2 and a polar component of 51 mJ/m^2. Diiodomethane has 1.3 mJ/m^2 of polar and 49.5 mJ/m^2 of dispersive components of SFE. Values of polar and dispersive components of SFE of formamide are respectively 19 mJ/m^2 and 39 mJ/m^2 [59, 60]. For every reference liquid, four measurements of contact angle were performed, at room temperature, in each of three specimens of each studied group.

The general procedure for measuring the contact angle is forming droplets under suitable conditions and make several measurements of the droplet's profile from a photograph obtained by a digital camera [48, 61]. Commercially available systems, often called goniometers, use the sessile drop method in order to measure the contact angle. This method involves the deposition of a liquid drop on the horizontal solid surface in order to subsequently observe it in cross-section. The angle formed between the liquid/solid interface and the liquid/vapor interface is the contact angle that is determined optically. The sessile drop method can accommodate varied surfaces and geometries, and its accuracy can be improved by increasing the number of observations through automated image processing techniques [61].

In Chapter 4, a video contact angle system OCA15+ (Dataphysics, Germany) was used to measure the apparent static contact angles (CA) of ultrapure distilled (DI) water on the diverse zirconia/titanium samples, with the sessile drop method through Young's equation. Four measurements were performed, at room temperature, in each of three specimen of each material. Complementarily, the surface free energy (SFE) with its dispersive and polar components was also studied in this system. These parameters were calculated with the SCA 20 software (Dataphysics, Germany) from the diverse CA values of DI-water, formamide and diiodomethane on the different substrates, by using the Owens-Wendt-Kaeble equation.

In Chapter 5, the wetability of modified substrates was assessed by the sessile drop method using a Dropmaster Series Contact Angle analyzer DM-CE1 (Kiowa Interfaces Co, Ltd., Japan) with Interface Measurements and Analysis System FAMAS V.3.0.0 (Kiowa Interfaces Co, Ltd., Japan) software. The volume of the DI-water dispensed droplets was 1.5 µl. Water contact angles (CA) were measured using the tangent method after drop stabilization on the surfaces for 10 seconds. Nine samples per group were tested on peptide-modified surfaces and 3 samples per group were tested on activated surfaces.

7.4.2 SCANNING ELECTRON MICROSCOPY (SEM)

A material surface can be characterized morphologically and chemically by means of a very thin electron-beam that scans the surface. As outlined in Fig 7.4-3, the electron beam goes across different lenses in the scanning electron microscope, crosses the copper coils and scans the sample while a secondary electrons detector collects those secondary electrons that are emitted from each surface point. Simultaneously, the focus of a cathode-ray-tube provides contrast at the image. The current through the coils generates a strong sweeping magnetic field, that acts as a convex lens deflecting the axial rays towards the focus [62, 63].

The diameter of the electron beam limits the image resolution, and the final current in the probe determines the intensity of secondary and backscattered electrons, and X-ray signals [64]. The angle of the conical beam impinging on the specimen governs the range of heights on the specimen that will simultaneously be in focus. The acceleration voltage (kV) determines the reliability degree on the image of the sample surface. The standard accelerating voltage of a scanning electron microscope ranges from 2 kV to 50 kV, whilst the resolution goes from 20 to 50 Angstroms [65, 66].

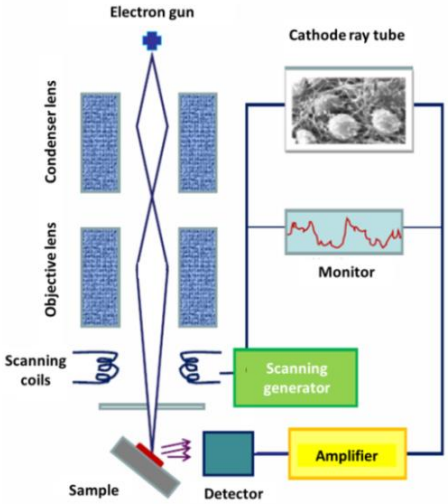

Fig 7.4-3. Diagram of a scanning electron microscope.

The SEM versatility for the study of solids is derived from the variety of interactions that the electron beam undergo within the specimen. As seen in Fig 7.4-4 (a), these interactions can be divided into two classes: (1) elastic events, which affect the trajectories of the beam electrons within the specimen without significantly altering the energy, and (2) inelastic events, which result in a transfer of energy to the solid that leads to the generation of secondary electrons, Auger electrons, characteristic X-rays, long-wavelength electromagnetic radiation in the visible, ultraviolet, and infrared regions, electron-hole pairs, lattice vibrations (phonons), and electron oscillations (plasmons) [67]. All these interactions derive information about the solid's nature, shape, composition, crystal and electronic structure, internal electric or magnetic fields, etc [68].

Due to the Coulomb force, the electrons are backscattered when they interact with the atomic core. Only a small amount of energy is lost in this interaction, so electrons may reach the surface of deep areas. The backscattered electrons vary with the type of core, providing information about elemental composition in the material. Furthermore, both incident electrons and backscattered electrons can interact with atomic electrons, ejecting secondary electrons of low-energy of outer layers. Because secondary electrons are released in all directions, they allow to study topography [69].

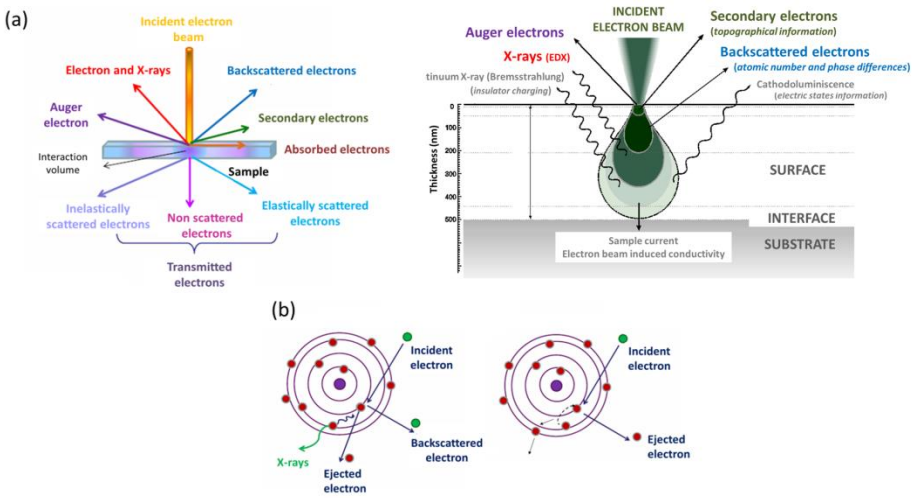

Fig 7.4-4. Interactions of an incident electron beam with the solid surface (a); electrons and X-rays (b)

An alternative interaction of electrons with matter involves a high energetic incident beam that ejects other electrons of inner atomic layers, resulting into ionized atoms (Fig 7.4-4 (b)). This unstable system will return to the minimum energy state; if taking place the emission process, and an electron of higher orbit occupies the vacant space, the excess of energy would be emitted as a photon of X-rays. Their detection is the base of the X-ray Analysis Energy Dispersive (EDS) or Wavelength (WDS) technique, a chemical analysis that takes place by measuring the energy and the intensity distribution of the X-ray signals associated with the focused electron beam. When the energy excess is yielded to a third electron into an upper layer, this may be released as an auger electron. Unlike photons of X-rays, the low-energetic auger electrons can only be detected near the surface [69, 70].

The topography and microstructure of the materials involved in this work were studied with a Hitachi analytical TableTop microscope TM3000 (Hitachi High Technologies, Nanotechnology Equipment Dep, Germany), which integrates an Energy Dispersive X-ray spectrometer (EDS) system (Bruker Quantax 70 Highlights; Hitachi High-Technologies corporation by Bruker AXS Microanalysis GmbH, Japan) for full-scale elemental analysis of samples. The working distances for observation and EDX analysis are the same (8.5mm) [71]. Complementarily, analyses at high magnification were carried out within high vacuum by a field emission scanning microscope (FE-SEM) with Quanta FEG 650 and S/TEM detector (FEI Company, The Netherlands). The FE-SEM uses electron source field emission cannon (Field Emission Gun, FEG) that provides electron beams with high and low energy that are more

focused; thereby improving the spatial resolution, minimizing charges on the specimens and causing less damage to sensitive samples. The S/TEM detector provides bright-field and dark-field sample imaging. Particularly, the microstructure of monolithic ceramics was assessed with FE-SEM in polished samples down to 1-µm, thermally treated (1000 °C, 1 h) within air-atmosphere and with an iridium coating. Because cermets could not be thermally treated, they microstructures are studied from fracture surfaces that are visualized by FE-SEM.

7.4.3 X-RAY PHOTOELECTRON SPECTROSCOPY (XPS)

Among the presently available techniques for surface analysis, XPS or ESCA (*Electron Spectroscopy for Chemical Analysis*) is the most quantitative, interpretable, and informative regarding chemical surface characterization. This is a non-destructive technique that provides a total elemental analysis (10-200 Å), except for hydrogen and helium, of any solid surface stable within vacuum [72]. XPS provides information about chemical bonding, local chemical environments, oxidation states of transition metals, the valence band electronic structure and the morphology of thin films [72, 73]. Although the detection limit depends on the element type, it may be established in 0.1 at % [74].

X-rays from a mono-energetic beam (Mg-K_α or Al-K_α) strike the tested surface inside an ultrahigh vacuum (UHV) environment that prevents the contamination and aids an accurate analysis of the sample. The X-ray beam penetrates about one micrometer in the sample surface and leads to the photoemission process (Fig 7.4-5).

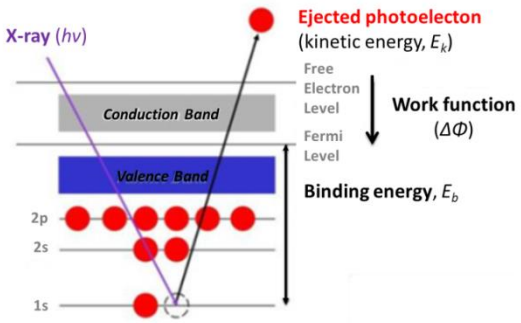

Fig 7.4-5. Schematic diagram of the photoemission process in XPS [74].

The incident photon energy, *hv,* is absorbed by a core level electron; if this *hv* is higher that the electron energy binding, E_b, the electron is emitted and a core hole is left behind. This core hole may be filled by an electron from a higher state, causing

emission of a secondary photon, or an Auger electron. The kinetic energies, E_k, of those emitted electrons are measured using an electrostatic charged-particle energy analyzer (the Cylindrical Mirror Analyzer, CMA), from which the electron binding energies can be calculated from the following Equation 7.4-5 [72-75]:

$$E_b = h\nu - E_k + \Delta\emptyset \qquad \text{Equation 7.4-5}$$

Where E_b is the electron binding energy, $h\nu$ is the photon energy from the X-Ray source, E_k is the electron kinetic energy measured in the XPS spectrometer, $\Delta\emptyset$ is the difference in the work function between the sample and the detector material, assuming that there is no charge in the sample surface.

As seen in Fig 7.4-6, a photoelectron spectrometer consists of a series of electrostatic lenses and steering voltages to selectively separate electrons of varying kinetic energies and bring them to the electron multiplier where they are detected [76]. Some electrons will be released without any problem giving the characteristic E_k of their elements. However, other electrons coming from inner layers will collide with other electrons of upper layers. The collisions cause a decrease in the electron energy and it no longer will contribute to the characteristic energy of the element, contributing to the noise signal in the spectrum. Moreover, the CMA does not only detect electrons from the irradiation of X-Rays; it can also detect electrons from irradiation by the electron gun located inside the CMA. The only electrons normally used in a spectrum from irradiation by the electron gun are Auger electrons, which can also be produced by X-ray irradiation [75].

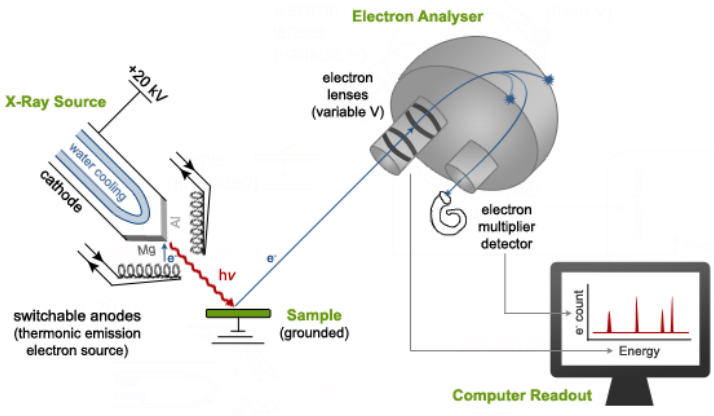

Fig 7.4-6. Diagram of an X-ray photoelectron spectrometer [76].

A typical XPS spectrum (XPS survey) is thus a plot of the number of photoelectron intensity as a function of binding energy [75]. The information content in a spectrum is enormous. There are various levels or hierarchies of spectral interpretation, including (1) simple elemental analysis, (2) detailed considerations of chemical shifts and chemical bonding nature in the surface region, and (3) various loss or relaxation structures, which provide further information on the chemical nature of the surface [72].

Different spectrophotometers were used according to the availability in the center in which the research was conducted. The model of each spectrophotometer is specified in the corresponding section. The radiation source was Mg X-ray at 1253.6 eV in all the cases. The pressure in the chamber was 10^{-10} mBar before the data were recorded and the current of the anode was 10 kV. The electron gun focused on an area close to 1 mm. Four survey-scans were recorded per sample (0-1100 eV) at 1eV step-size. Curve fitting of the spectra and elemental (atom %) semi-quantification from the surveys were performed with the corresponding software provided by each spectrophotometer's manufacturer.

In Chapter 3, the surface composition of modified titanium powder by attrition milling and yttria-coating and, in Chapter 4, the surface composition of ceramic/Ti specimens polished down to 1200 grit, which are intended to be used as substrates for cell culture were analysed by means of a spectrometer equipped with a Hemispherical Energy Analyzer PHOIBOS 150 (SPECS Surface Nano Analysis GmbH; Berlin, Germany). Curve fitting of the spectra and elemental (atom %) semi-quantification from the survey scans were conducted with the Casa XPS V 2.3.16 (Casa Software Ltd., 2005) software.

In Chapter 5, an EPS SSX 100 (Surface Science Instruments, USA) spectrometer (Al Kα X-ray, 1 mm^2 spot size, 200 W, 35° take-off angle) was used to characterize the surface chemistry of biofunctionalizated substrates. The neutralizer was used for analyzing the non-conductive ZrO_2 samples. Four survey-scans per sample were recorded (0-1100 eV) at 1eV step-size. Peak fitting and quantification were performed using ESCA 2005 (Surface Science Instruments, USA) software provided with the XPS system.

7.4.4 INTERFEROMETRIC MICROSCOPY

White light interferometry has been used for many years as a reliable non-contact optical profiling system for measuring step heights and surface roughness in many precision applications [48, 77, 78]. It has a great application to understand vertical features over a small lateral scale. The vertical (height) resolution reaches up to 0.01 nm, whilst lateral resolution is limited to around 0.35 µm [79]. White-light interferometry offers many advantages over profilometry and atomic force microscopy (AFM), because it presents high-speed and non-contact capabilities. 3D rendered surface can be acquired rapidly, making measurements immediately [80]. The interference microscopy technology combines an interferometer and microscope into one instrument. As seen in Fig 7.4-7, illumination from a white light beam passes through a filter and then by the microscope objective lens to the sample surface. The objective lens is coupled with a beam splitter, so some of the light is reflected from a reference mirror. The light reflecting back from the surface recombines with the reference beam. The recombined beams create bright and dark bands called *fringes*, which make up the interferogram. Fringes represent the object's topography [77].

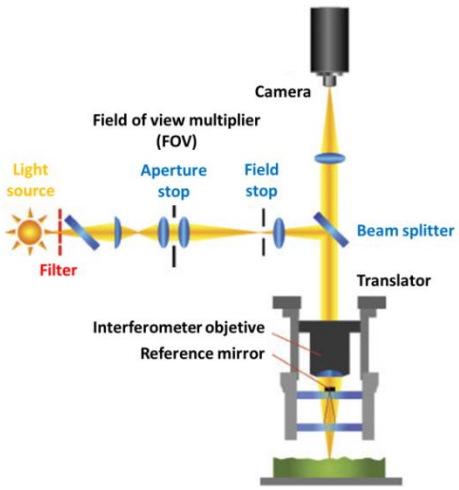

Fig 7.4-7. Schematic diagram of a white light interferometer [77]

White-light interferometry is used to evaluate the three-dimensional micro-roughness pattern in the surfaces that are cultured with cells (Chapter 4). On one hand, the three-dimensional surface micro-roughness of alumina/titanium composite and pure alumina was evaluated with a white light interferometer microscopy (MicroXAM™ Optical Profiler, KLA-Tencor Corporation; CA, US). Metrological data were acquired and analyzed using SPIP (Scanning probe image processor) software

(Nanoscience Instruments, Inc; IL, US). On the other hand, surface micro-roughness of zirconia/titanium composites and pure monolithics was examined using an optical Laser Interferometer (Wyko NT9300 optical profiling system, Veeco). The analysis area was 165.2x220.2 μm^2. Data analysis and filtering were performed with Wyko Vision 4.10^{TM} software (Veeco Instruments, NY, US).

All surfaces present irregularities or roughness of different wavelengths, which overlap with the sample shape. This defines topography that can be divided into three categories: roughness, waviness and shape error. Quantitative techniques for measuring roughness make use of phase correction filters, mostly Gaussian, which separate waviness and form error of roughness. A Gaussian filter was used to eliminate waviness and tilt from every surface analysis. Cut-off (λc) values of 0.08 mm were applied.

An isotropic surface presents identical characteristics, regardless of the direction of measurement; for example, surfaces with a random surface texture, which do not have any texture that stands out. However, a surface is said to be anisotropic if it has an oriented surface or a periodic structure (Fig 7.4-8) [81].

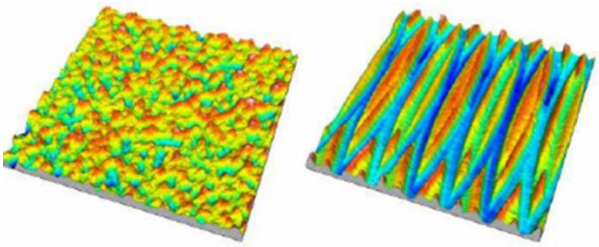

Fig 7.4-8. Surfaces with an isotropic (left) and anisotropic texture (right) [81].

The surface topography can be also described by several amplitude, spacing and hybrid roughness parameters [81-84]. Parameters are extracted from the interferograms obtained by testing the surfaces. A roughness value can either be calculated on a profile (line) or on a surface (area); the profile roughness parameters are more common but the area roughness parameters give more significant values in terms of international standards [82]. In order to distinguish 2D and 3D parameters, a capital letter *S* (for surface) is used to identify 3D parameters (as opposed to *R* for 2D parameters) [85, 86].

Surface roughness of alumina/titanium composites and their monolithics was evaluated from area parameters, which involve a statistical distribution of height values along the z axis [87].

- Average surface roughness (S_a) represents an overall roughness measurement, so it is insensitive to differentiate texture features. Thus, surfaces with vastly different spatial and height symmetry features may have the same S_a. The evaluation of this parameter may thus be misleading [87].
- Skewness of topography height distribution (S_{sk}) measures the asymmetry of surface deviations about the mean plane. S_{sk} is zero for a Gaussian surface with a symmetrical distribution of surface heights. For an asymmetric distribution of surface heights, S_{sk} will be negative when the distribution has a longer tail at the lower side of the mean plane or positive when the tail is longer at the upper side of the mean plane[87, 88]. The skewness parameter obtained from a 2D profile would be defined as above in Fig 7.4-9.

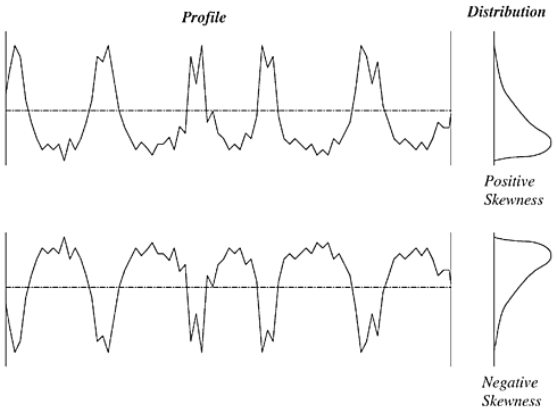

Fig 7.4-9. Skewness (R_{sk}) and the amplitude distribution curve [82]

The parameters used to quantify roughness in zirconia/titanium surfaces and their counterparts were the followings:

- Arithmetic average roughness (R_a) parameter gives a good overall description of height variations. As is collected in Fig 7.4-10, R_a is defined as the average absolute deviation of the roughness irregularities from the mean line over one sampling length [82].

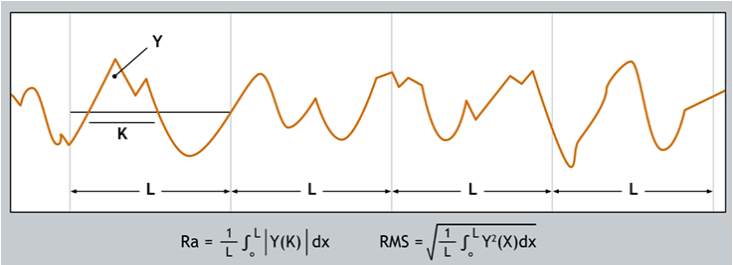

Fig 7.4-10 Definition of arithmetic average height, R_a

- Ten-point height (R_z) is more sensitive to occasional high peaks or deep valleys than R_a. This parameter is defined as the difference in height between the average of the five highest peaks and the five lowest valleys along the assessment length of the profile (Fig 7.4-11) [82].

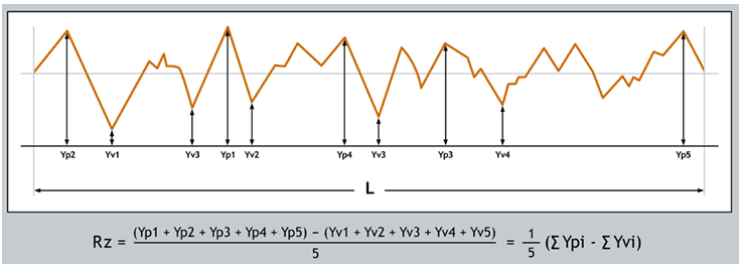

Fig 7.4-11. Definition of ten-point height, R_z [82]

- The index area (S_Al) is the real surface area/nominal surface area ratio. This indicates the increase in the real area compared to the nominal area of the sample due to roughness, so higher roughness leads to higher index area [85, 86].

7.5 BIOLOGICAL PROPERTIES

As animal cells are in a complex dynamic environment in the whole animal (*in vivo*), their regulatory processes are more readily examined in a more simplified external environment (*in vitro*). Animal cells that are removed from the body can be maintained (or cultured) for prolonged periods in an appropriate environment [89]. The cell culture approach treats mammalian cells virtually like bacterial cultures and this allows to study the cells' intrinsic functions like adhesion, migration, proliferation, differentiation, matrix synthesis, and death; as well as their interactions with each other and with their environment [90, 91].

7.5.1 PRIMARY CULTURE AND CELL LINES

Cell cultures are basically of two types: primary cultures and cell lines. Primary cultures are initiated from a tissue removed directly from the animal [89, 90]. This heterogeneous population of cells grows out to form a single layer completely filling the tissue culture vessel surface, which is called confluent monolayers. Confluent monolayers are treated with trypsin to detach individual cells to get a cell suspension that is transferred into other containers, obtaining more viable monolayer cultures. Following the initial subculturing of primary cultures, *first passage cultures* are obtained. *Second passage cultures* are obtained following the second subculturing and following multiple subculturing, *cell lines* in some cases are established.

Most normal cells isolated from the animal and put into culture are *short-term cultures* of *finite cell lines* that degenerate by undergoing a crisis of senescence after a set number of population doublings. However, some cells do not die, but instead they survive and divide indefinitely as *established or continuous cell lines*. They may be obtained from both normal and tumorigenic cells; and also by transformation with appropriate oncogenes or treating with carcinogenic chemicals, so that imply the mutation in the genes that regulate initiation or progression in the cell cycle [89, 91, 92]. Moreover, *cell strains* are cell lines that are selected, either by cloning or by physical cell sorting, to produce a purified line with defined characteristics [91]. They have a finite division potential, stopping of dividing after 40 to 60 population doublings.

As can be observed in Fig 7.5-1, each mammalian tissue type is derived from the embryonic germ layer consisting of ectoderm, endoderm and mesoderm, which differentiate into the many cell types that organize into tertiary structures such as skin, muscle, internal organs, bone and cartilage, the nervous system, blood and blood vessels [93]. The cell types most frequently found in primary cell culture are epithelial cells, fibroblasts, osteoblasts, keratinocytes, melanocytes, endothelial cells, muscle cells, hematopoietic and mesenchymal stem cells or MSCs.

Primary cell cultures more closely mimic the physiological state of cells *in vivo* and generate more relevant data representing living systems, but they reach senescence after a limited number of doublings and the necessity of reestablishing fresh cultures from the explanted tissues is a tedious process. Using immortalized cell lines is handy and more suitable to get a consistent material throughout an extensive research project.

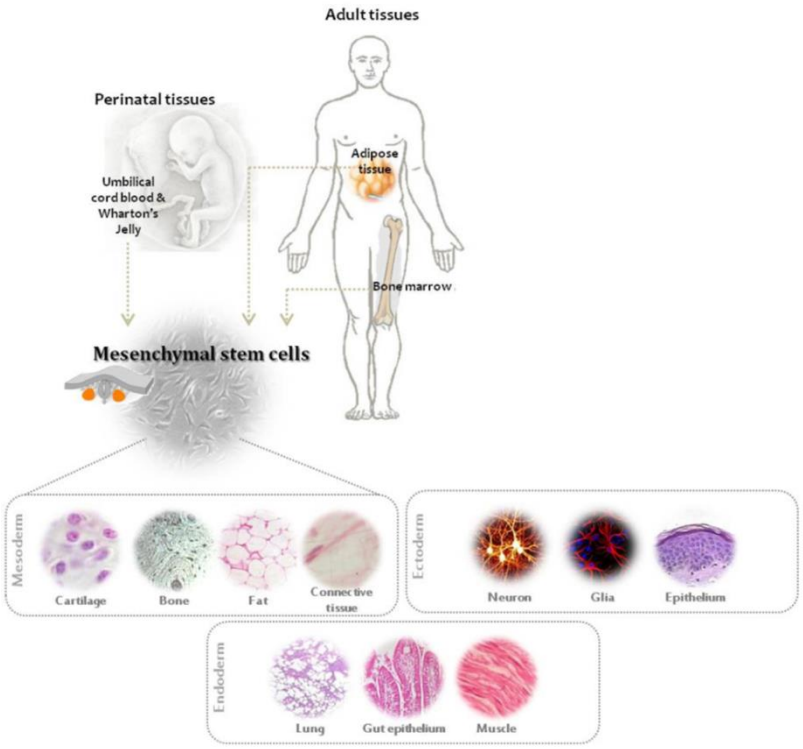

Fig 7.5-1. Mesenchymal stem cells (MSC) from different perinatal and adult tissues and the cell fate regarding the mesodermic, endodermic or ectodermic cell lineage (adapted from [94]).

7.5.2 BONE TISSUE CULTURES

Bone cell culture systems have extensively been exploited in order to design biomaterials that enhance bone formation. The knowledge of which materials are biocompatible with human hosts has mainly come from the co-cultures of cells and implantable materials. These studies have been invaluable for assessing toxicity to osteoblasts, adhesion characteristics, osteoblast phenotypic expression, and mineralization. Cells with an *osteoblast-like* phenotype (Fig 7.5-2) have probably been the most intensively investigated of all the bone-derived cell types. They are isolated from human bone and from all commonly used experimental species, as well as from bone tumors. Their phenotype is established in a functional sense, by their ability to produce matrix-rich multicellular *nodules* that mineralize, usually in the presence of organic phosphate donors. Patterns of gene expression and morphologic changes in cultured osteoblast-like cells correlate well with those that take place during bone formation *in vivo* [90].

Phenotype	Species	Cell line	References	Comments
Osteoblast-like	Rat	ROS	Majeska *et al.*, 1980	
	Osteosarcoma	UMR	Martin *et al.*, 1979	
	Human	SaOS-2	Rodan *et al.*, 1987	
	Osteosarcoma	Mg-63	Franceschi *et al.*, 1988	
Osteoblast-like	Rat	RCJ	Grigoriadis *et al.*, 1988	Spontaneous
	Mouse	MC3T3	Sudo *et al.*, 1983	Immortalization
Osteoblast-like	Rat	RCT-3	Heath *et al.*, 1989	SV-40 T *in vitro*
(Pre-osteoblastic)		(RCT-1)	Keeting *et al.*, 1992	immortalization
Osteoblast-like	Human	HOBIT	Harris *et al.*, 1995	
	Human		Ghosh-Choudhury *et al.*, 1997	SV-40 T *in vitro* (Conditional)
	Mouse			BMP-driven SV40T-antigen-expressing mice
Marrow Stroma	Mouse	MBA-15	Benayahu *et al.*, 1989	
	Mouse		Diduch *et al.*, 1993	Phenotype variants
			Matsumoto *et al.*, 1995	Support hematopoiesis
	Mouse		Chambers *et al.*, 1993	T-ag-transgenic
Osteocyte-like	Mouse	MLO-Y4	Kato *et al.*, 1997	T-ag-transgenic?
Pre-osteoclast	Human	FLG29.1	Gattei *et al.*, 1992	
Pre-osteoclast	Mouse		Hentunen *et al.*, 1998	

Fig 7.5-2 Examples of permanent bone-derived cell lines [90].

Co-cultives of newly-developed materials and bone-derived cell lines were performed with two different osteablastic cell lines: SaOS-2 and MC3T3. The methodology of each type of cell culture has been developed in accordance with the standards in the lab in which the *in vitro* assays were performed. Using Saos-2 cell line offers the following advantages: well-documented characterization data, the possibility to obtain large amounts of cells in short time, and the fact that they can fully differentiate as osteoblastic cells naturally do [95, 96]. MC3T3-E1 pre-osteoblastics are an established mouse calvarial cell line at the early stages of differentiation to a full osteoblast cell. This cell line is commonly used for studies of osteoblast differentiation due to its ability to form extracellular matrix and collagen *in vitro* under suitable conditions [97]. Thus, both types of osteblastic cell lines constitute a valuable model for studying events associated with the late-stage differentiation of the cells that are in contact with the studied materials.

7.5.3 COLORIMETRIC ASSAYS

Colorimetric assays are sensitive, reliable, precise, and imply the absence of radioisotopes. They can be used to quantify viability, adhesion, proliferation and differentiation of cells previously seeded onto the interest materials. These quantitative assays detect indirectly certain enzymatic activity by means of measuring the amount of the generated signal, which is dependent on the degree of cell activation. Furthermore, by using this type of tests, results are immediately obtained with a multi-well scanning spectrophotometer [98-100].

7.5.3.1 Water-soluble Tetrazolium Salt (WST-1) and MTS cell viability assays

The *Cell Proliferation Reagent WST-1* (Cell Proliferation Reagent; Roche Applied Science, Penzberg, Germany) is a sterile, ready-to-use solution that contains WST-1 and an electron coupling reagent diluted in phosphate buffered saline. As seen in Fig 7.5-3, WST-1 (4-[3-(4-Iodophenyl)-2-(4-nitro-phenyl)-2H-5-tetrazolio]-1, 3-benzene disulfonate) is a tetrazolium salt that in contact with metabolically active cells gets cleaved to formazan by mitochondrial dehydrogenases. The darker the formazan dye, the greater the number of metabolically active cells on the materials [88]. This reagent can be used for a variety of experiments, including the evaluation of possible cytotoxicity associated to new biomaterials.

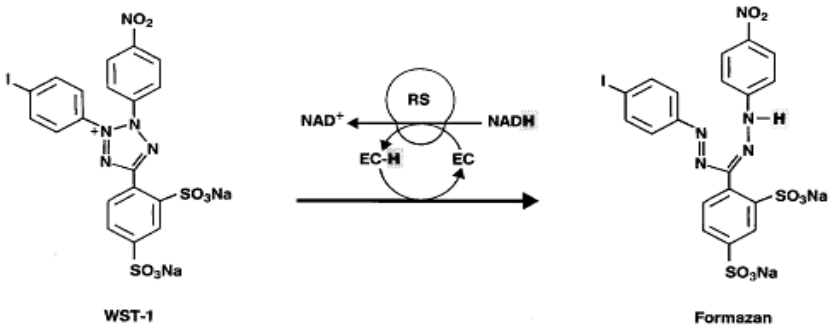

Fig 7.5-3. Cleavage of the tetrazolium salt WST-1 to formazan (EC = electron coupling reagent; RS = mitochondrial succinate-tetrazolium-reductase)[88].

In fact, potential cytotoxicity of zirconia/titanim cermet was assessed using this reactive following indication in ISO 10993-5 [101]. Briefly, three samples of each group were incubated in supplemented phenol red-free McCoy's 5A culture medium (Promocell; Labclinics SA, Spain) for 72 h at 37°C. SaOS-2 cells ($5x10^3$) were grown for 24 hours, and then incubated in presence of the complete extracts (named as extraction vol.) and their diluted extracts (ranging from 1:1 to 1:1000). After the exposure period, WST-1 (diluted 1:10 in serum free McCoy's 5A without phenol red) was used for cell quantification. The reagent was added to the cells for 2 h. Mitochondrial dehydrogenases in metabolically active cells cleaved the slightly yellow tetrazolium salt to dark yellow formazan salt, which was assessed at 440 nm using the PowerWaveX spectrophotometer with the Gen5 Data Analysis software (Bio-Tek Instruments, Inc.; Winooski, VT, US).

The potential cytotoxicity associated with the alumina/titanium materials was evaluated using the *CellTiter 96® AQueous One Solution Cell Proliferation Assay, MTS* (Promega Corporation, Promega Biotech Ibérica, Spain). The kit was used as per

manufacturer's instructions. It has the same basis that the Cell Proliferation Reagent, WST, with the only difference that this contains the tetrazolium salt, MTS [3-(4,5-dimethylthiazol-2-yl)-5-(3-carboxymethoxyphenyl)-2-(4 sulfophenyl)-2H-tetrazolium] and the electron coupling reagent phenazine ethosulfate, PES. Mitochondrial dehydrogenases in metabolically active cells cleaved this slightly yellow tetrazolium salt to brown formazan salt, which was assessed at 490 nm using a microplate reader (BIO-RAD, model 680) with Microplate Manager™ Software Version 5.2.

7.5.3.2 LDH Cytotoxicity Detection Kit (LDH) - cell proliferation

Cell proliferation tests are crucial because they allow to monitor cellular health as well as the division capability. The markers for measuring cell proliferation include average DNA content and/or cellular metabolism in a population [102]. In this work, the lactate dehydrogenase (LDH) activity was assessed along the time to quantify the osteoblasts capability to proliferate onto the ceramic/titanium materials and the corresponding monolithics. As seen in Fig 7.5-4, this enzyme is an oxidoreductase that catalyses the conversion of pyruvate to lactate in anaerobic glycolysis, which is accompanied by the reduction of NAD^+. The reverse reaction occurs in liver when the lactate concentration is high (Cori cycle) due to feedback inhibition. LDH is not specific to any single tissue; it is found in heart, liver, kidney, skeletal muscle, brain, blood cells, and lungs. The enzyme resides inside cells and is released into the bloodstream after tissue damage or red-blood-cell hemolysis. Since LDH is a fairly stable enzyme, it has a broad range of applications as evaluating the presence of cell damage and toxicity, evaluating the cell number along a proliferation assay or diagnosis of pathological conditions, in which LDH results elevated such as in cancer [103].

In order to study the cell proliferation capability onto ceramic/titanium composites and onto zirconia, alumina and titanium pure materials, osteoblasts were seeded onto each sample. The cytoplasmic LDH activity was measured at different times by using the Cytotoxicity Detection Kit^{PLUS} LDH (Roche Applied Science; Penzberg, Germany). After each assay time, the samples were rinsed with PBS, the cells lysed with the reagent M-PER® (Mammalian Protein Extraction Reagent; Thermo Scientific, Waltham, MA, US) and the plates were kept at -80 °C until the assay moment. This was carried out following the manufacturer's instructions [104]. The reduction of tetrazolium salts to red-formazan is coupled to the LDH activity existing in the cell lysates. Thus, the formazan dye was measured at 492 nm using either the PowerWaveX spectrophotometer with the Gen5 Data Analysis software (Bio-Tek Instruments, Inc.; Winooski, VT, US) for studying the zirconia/titanium system or using

a BIO-RAD microplate reader (model 680, Bio-Rad Laboratories;US) with Microplate Manager™ Software Version 5.2. for studying the alumina/titanium system.

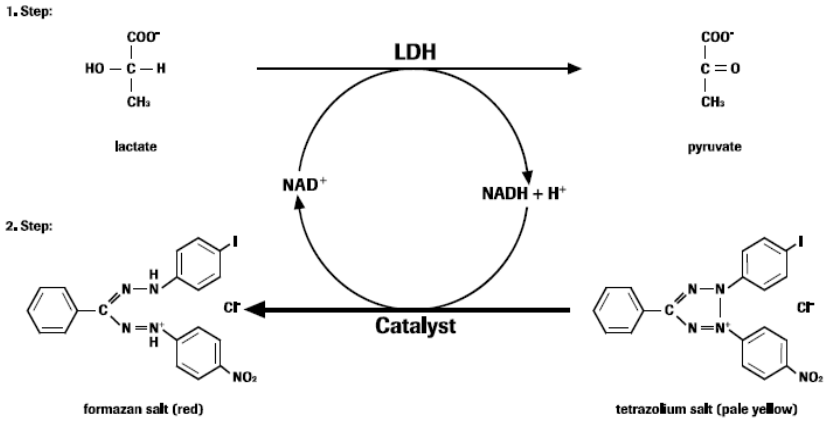

Fig 7.5-4. LDH reduces NAD^+ to $NADH^+/H^+$ by oxidizing lactate to pyruvate. In the second enzymatic reaction, 2 hydrogens are transferred from $NADH^+/H^+$ to the red tetrazolium salt by catalysis.

7.5.3.3 Alarmar blue assay

Cell proliferation on the Al_2O_3/Ti (25% vol. Ti) system was further evaluated using the alamarBlue assay kit (Invitrogen; Life Technologies, Thermo Fisher Scientific Inc, Spain). This is a nontoxic, cell permeable compound, that acts as indicator of cell viability because it uses the ability of living cells to reduce resazurin (blue; non-fluorescent) to resorufin (red; highly fluorescent) (Fig 7.5-5) [105, 106]. The assay was performed following the manufacturer instructions in [107]. Briefly, AlamarBlue reagent (120 µL) was added to the culture medium for 90 minutes at 37 ºC. The fluorescence was then measured (λ_{ex}=530 nm; λ_{em}=590 nm) by a Bio-Tek FL600 fluorescence microplate reader (Bio-Tec® Instruments, Inc; US) subtracting blank readouts.

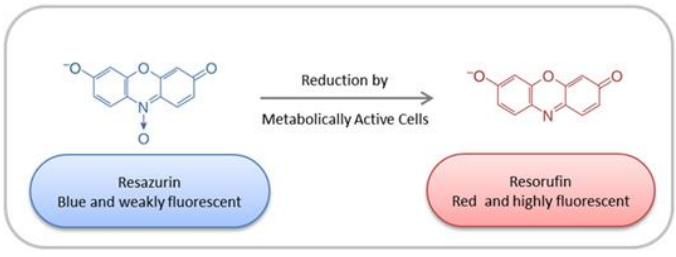

Fig 7.5-5. Reduction of non-fluorescent resazurin to resorufin with a strong red-flourescence by metabolically active cells

For this assay, cells were seeded onto the diverse samples previously placed into a non-treated 24-well plate. Thirty minutes after plating, pre-warmed complete culture medium was carefully added onto each sample. Cell proliferation was evaluated at five time points (1, 3, 7, 14 and 21 days). In order to ensure that the measured fluorescence was exclusively originated from attached cells at the materials, the studied substrates were moved into new wells with fresh medium before the tests. In parallel and for comparative purposes, a cell proliferation assay was carried out with osteoblasts directly seeded onto tissue culture-treated plates for cell attachment.

7.5.3.4 Alkaline phosphatase assay kit (ALP) – cell differentiation

Differentiation is a developmental process in which cells change their genetic programs to become more restricted in their potential to mature into functional cells of diverse tissues and organs [108, 109]. Changes in the ALP level and activity are also involved in a variety of physiological and pathological events, such as bone development or bone-related diseases [110]. Matrix maturation and mineralization are usually enhanced *in vitro,* by growing the cells to complete confluence and by adding specific osteogenic factors [109]. Thus, once osteoblasts were in confluence, the medium was supplemented with osteogenic factors (ascorbic acid, 50 μg/mlm; β-glycerophosphate, 10 mM; dexamethasone, 100 mM; Sigma-Aldrich; St. Louis, MO, US). Ascorbic acid is an essential element in the formation and maintenance of tissues that make up the human body, because of its key role in the synthesis of collagen. β-glycerol phosphate acts as phosphate donor, which is essential in bone formation. Dexamethasone stimulates osteogenesis in bMSC cultures, and cells constitutively express this glucocorticoid receptor. The continuous presence of dexamethasone in cell cultures stimulates ALP mRNA but also the mRNA level of ostecalcin and osteopontin [111]. The capability of differentiation of osteoblasts cultured onto the new substrates was evaluated by quantification of the alkaline phosphatase (ALP) activity with the *SensoLyte pNPP Alkaline Phosphatese Assay Kit* (AnaSpec Inc.; Fremont, CA, US). This assay kit provides a convenient colorimetric assay for detecting alkaline phosphatase by using colorimetric pNPP (p-Nitrophenyl phosphate), phosphatase substrate. Upon dephosphorylation, pNPP turns yellow so can be detected at an absorbance of 405 nm. By means of this colorimetric assay concentrations of active ALP, up to 0.2 ng/ml, can be detected.

After each time point studied, cells were PBS -rinsed and then lysed time with M-PER® extraction reagent (Thermo Scientific, Thermo Fisher Scientific, Inc.; Waltham, MA, US). Cellular extracts were incubated at room temperature with the

colorimetric ALP substrate, pNPP. After measuring the absorbance, optical density (DO) values were extrapolated to a calibration curve of ALP standard from calf intestine provided by the kit (serial dilutions from 1000 to 0 ng/ml).

7.5.4 IMMUNOCYTOCHEMISTRY

Immunocytochemistry is an immunological technique used to visualize the presence of a specific antigen in cells [112]. This is a highly productive method in biomedical research to identify proteins and other macromolecules [113, 114]. Blood smears, cultured cells, cell suspensions are types of samples that can be investigated. Fig 7.5-6 shows a fundamental procedure of immunocytochemistry, which implies primary antibody, secondary antibody and colour disclosure.

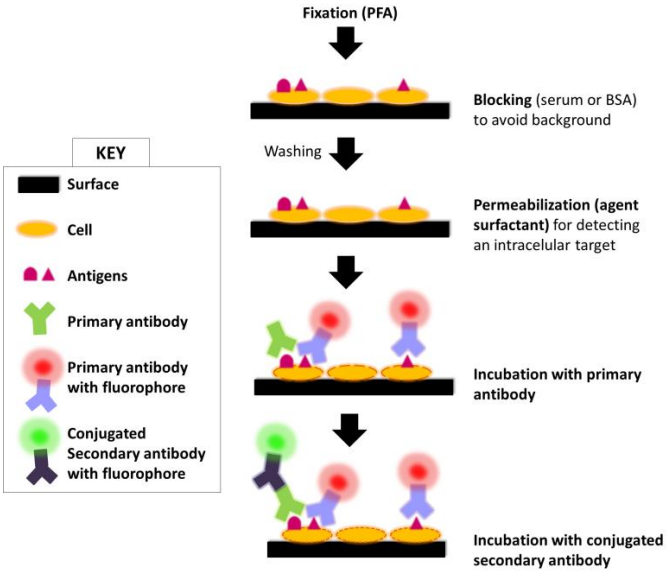

Fig 7.5-6. Basic steps in an immunolabeling process.

Sample preparation involves fixing the target cells. Ideally, fixation would immobilize the antigens while retaining native cellular architecture and permitting unhindered access of antibodies to subcellular compartments. Fixation methods include organic solvents and cross-linking reagents. Organic solvents like alcohols or acetone remove lipids and dehydrate the cells, while precipitating the proteins on the cellular architecture. Cross-linking reagents (paraformaldehyde) form intermolecular bridges through free amino groups creating a network of linked antigens. In overall, cross-linkers preserve the cellular structure better than organic solvents [112, 114, 115]. They require a permeabilization step to allow the access of the antibody to the

specimen; organic solvents and mild surfactants are used for this purpose. Saponin, Triton X-100, Tween-20, etc., are the most common surfactants used because they present ability to disrupt membranes [112, 114, 115]. The third step of cell staining involves an incubation of cell preparations with antibodies. Unbound antibody is removed by washing, and the bound antibody is detected either directly (if the primary antibody is labeled) or, indirectly by enzyme-labeled or fluorochrome-labeled secondary reagents through a fluorescence or confocal microscope [114-116].

In order to assess the capability of osteoblasts to adhere at ceramic/titanium substrates and the monolithic materials, immunocytochemistry technique is used. Different fluorescent-probes were used in order to disclose various sub-cellular structures (nucleus, f-actin cytoskeleton and/or vinculin, protein that constitutes focal adhesions). The variability among fluorescent-probes and protocols are related to the availability in the center in which the assays were performed. Both the types of molecular probes that were used and each specific immunolabeling procedure are explained in the corresponding section. For disclosing the fluorescence in the probes, either fluorescence or confocal microscopies were used, depending on the image resolution that was needed. Every microscope model is also specified in the corresponding section.

7.5.5 FLUORESCENCE AND CONFOCAL MICROSCOPY

7.5.5.1 Fluorescence basis

Fluorescence is the optical phenomenon where absorption of light of a given wavelength by a molecule is followed by the emission of light at longer (visible) wavelengths. Fluorescence imaging uses high intensity illumination to excite fluorescent molecules in the sample. As illustrated in Fig 7.5-7, when a molecule absorbs photons, electrons are excited to a higher energy level. As electrons *relax* back to the ground-state, vibrational energy is lost and, as a result, the emission spectrum is shifted to longer wavelengths [117, 118].

Most fluorophores or fluorochromes are organic molecules containing double, triple bonds or aromatic systems. In order to label specific environments these fluorophores are coupled to other molecules such as lipids, proteins, antibodies, etc. These different fluorescent probes tend to accumulate in the environment for which they were designed. The availability of flourescently-labeled antibodies for protein localization allows to probe details of cellular organization and function with a high precision [119, 120].

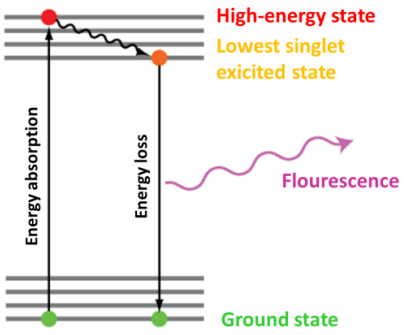

Fig 7.5-7. Jablonski diagram showing fluorescence phenomenon.

7.5.5.2 Fluorescent microscopy

Fluorescence microscopy adds to the fundamental power of light microscopy the ability to examine the spatial distribution of specific cellular components. Fluorescent molecules can absorb only at specific wavelengths, so the fluorescence microscope must have a light source that produce various wavelengths for excitation. Either a xenon-arc lamp or a mercury-vapour lamp can generate white light that is a mixture of all visible wavelengths. An excitation filter removes any other wavelength of light that the wavelength used to excite the fluorescent probe. In the fluorescence microscopes (Fig 7.5-8), the objective focuses the excitation light and collects the light returning to the eyepiece or detector. Fluorescence is separated from excitation by means of a dichroic mirror and appropriate filters. Whilst the excitation light is reflected back into the objective, fluorescence is transmitted. Filters, excluding and/or transmitting selected wavelengths, optimize fluorescence and reduce unwanted *background noise* [121, 122].

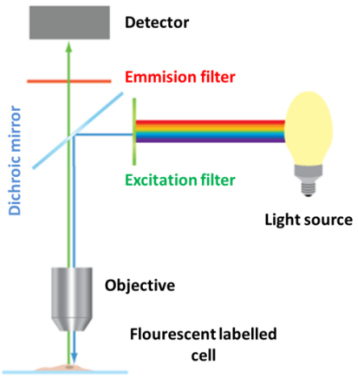

Fig 7.5-8. Main components of a fluorescent microscope [121].

7.5.5.3 Confocal microscopy

Confocal microscopy solves one of the problems of fluorescence microscopy: the sample is completely illuminated by the excitation light, so the entire sample is fluorescing at the same time. The highest intensity of the excitation light is at the focal point of the lens, but also there is additional light from other parts that contributes to a background haze in the resulting image. In the confocal microscope, this problem is solved by adding a pinhole/screen combination [123, 124]. By having a confocal pinhole, the microscope is really efficient at rejecting out of focus fluorescent light. The practical effect is that the image comes from a thin section. By scanning many thin sections through the sample, a very clean 3-D image can be built up. Also, a similar effect happens with points of light in the focal plane, but not at the focal point - emitted light from these areas is blocked by the pinhole screen [124]. Thus, a confocal microscope has slightly better resolution horizontally, as well as vertically than the fluorescent microscope. In practice, the best horizontal resolution of a confocal microscope is about 0.2 microns, and the best vertical resolution is about 0.5 microns [125].In the confocal microscope (Fig 7.5-9), a laser provides the excitation light in order to get very high intensities. The laser light reflects off a dichroic mirror. From there, the laser hits the mirrors, which are mounted on motors, and the mirrors scan the laser across the sample. Probe in the sample fluoresces, and this emitted light gets descanned by the same mirrors that are used to scan the excitation light from the laser. The emitted light passes through the dichroic and is focused onto the pinhole. The light passes through the pinhole and is finally measured by a detector, i.e. a photomultiplier tube. Therefore, there is never a complete image of the sample at any given instant; only one point of the sample is observed. The detector is attached to a computer that builds up the image, one pixel at a time [126, 127].

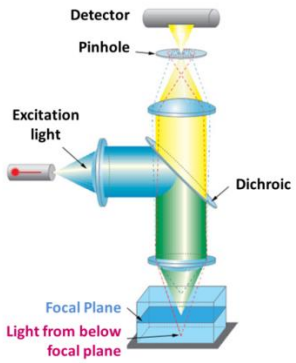

Fig 7.5-9. Schematic diagram of a confocal microscope.

7.5.5.4 Triple immunostainig of osteoblastic-cells

In Chapter 4, the actin cytoskeleton of cells cultured on the alumina/Ti system was immonstained to indirectly study cell adhesion. Osteoblasts were PBS-rinsed twice and fixed with 4% paraformaldehyde (Sigma-Aldrich Co. LLC., St. Louis, MO; US) for 40 minutes. Then, cellular membranes were permeabilized with 0.1% Triton X-100 and, after a PBS-wash step, cells were incubated with Texas Red Phalloidin reagent (Invitrogen, Life Technologies Corp.) for 20 minutes avoiding light exposure. Subsequently, samples were turned upside down in the plate and images were taken in an inverted fluorescence microscope (Olympus IX51, Olympus Corporation of the Americas, US) at 10x magnification adjusting the FITC filter to detect F-actin. The images were processed using the CellD analysis software (Olympus Corp. of the Americas, US).

On the other hand, the triple immunostaining of adhered osteoblasts at the zirconia/titanium surfaces was performed following the manufacturer's instructions in the Actin Cytoskeleton and Focal Adhesion Staining Kit, FAK 100 (Millipore; Billerica, MA, US). Briefly, cells were fixed for 20 min in 4% PFA and permeabilized for 15 min in 0.1% Triton X-100. Cells were blocked using 1% BSA (in 1xDPBS) for 1 hour and, incubated for 2 hours with 1:200 mouse anti-vinculin. Alexa Fluor® 488 Goat anti-mouse IgG (1:1000; Invitrogen, Life Technologies Corp.) and TRITC-conjugated Phalloidin (1:300) were simultaneously applied for 1 hour in dark. Nuclei were stained using DAPI (1:1000) for 2 minutes. At least five images were randomly acquired from each assay condition by an E600 fluorescence microscope (Nikon, Japan) at 20x and treated with Cell F software (Olympus, Japan) in order to visualize the F-actin cytosquleton. In addition, the green-immunofluorescence of vinculin was visualized using a confocal laser scanning microscopy TCS-SP5 (Leica Microsystems; Wetzlar, Germany).

In Chapter 5, a triple imminostaning was performed to study cell adhesion. After each experimental time cells were fixed in 4% PFA-PBS solution (20 minutes), permeabilized in 0.25% Triton X-100 (5 minutes) and blocked in 6% BSA-FBS (1 hour). The staining was developed by dark incubation with Anti-vinculin (1:2000) and Alexa Fluor 488 secondary antibody (1:500) for vinculin labeling (focal adhesions), rodhamine phalloidin (1:500) for F-actin labeling (cytoskeleton) and DAPI (1:1000) for cell nucleus labeling. At least 3 images per sample on 5 different samples per group were taken on randomly-selected locations using a fluorescence microscope (E600, Nikon, Japan) and processed with Cell F (Olympus, Japan) software. The number of adhered cells per image field (10x) was counted using appropriate image analysis

software (ImageJ, http://rsbweb.nih.gov/ij/, NIH, USA). This was also used to qualitatively analyze (20x) the spreading of cells and focal adhesion points on the studied surfaces.

7.5.5.5 Fluorescent-labeling of RGD oligopeptides

In Chapter 5, peptides were conjugated with a green-fluorescent probe to directly visualize the organic coatings. EDC/NHS crosslinking of carboxylates with primary amines in the peptides was performed with the NHS and Sulfo-NHS kit (Thermo scientific) following manufacturer's instructions. Briefly, RGD-containing peptides (1 mg) were dissolved in activation buffer (0.1 MES, 0.5 M NaCl; pH 6.0). 2 mM EDC and 5.0 mM NHS were subsequently added to the peptide solution to allow the reaction for 15 min (room temperature). Fluorescent 5-FAM cadaverine (1.5 mM) was added to the solution for conjugating with oligopeptides (2 h; pH 7.2-7.5). Fluorescent probes and EDC were added in excess (1.5 and 10-fold molar, respectively) to ensure full labeling of KKKGGGGRGDS peptides. The non-reacted reagents were removed by dialysis through a cellulose acetate membrane (MWCO: 500–1000 Da) in PBS buffer overnight. The product collected after dialysis was firstly frozen (-80 ºC, 48 h) and then lyophilized for 24 h using a Freeze Dryer 4.5 (Labconco, US). The fluorescent oligopeptides were immobilized on the studied surfaces following the aforementioned procedures. Micrographs of the labeled surfaces were taken using a fluorescence microscope (Eclipse E800; Nikon, Japan) with b-2E/C FITC fluorescence filter.

7.6 STATISTICAL ANALYSIS

Data were presented as the mean value with the corresponding error of the average. In every test, the number of independent experiments (*n*) is stated. In every experiment, we look for ensuring consistency. For *in vitro* experiments, significant differences between groups were analyzed by ANOVA tests followed by *post hoc* pairwise comparisons using Tukey-HDS or Dunnet-C depending on the homogeneity of the variance. Differences were also analyzed using Kruskal-Wallis non-parametric test followed by Mann-Whitney test with Bonferroni correction with very similar results. All statistical analyses were performed with SPSS statistics v20 (IBM, Armonk, NY, US) at two different levels of significance ($p<0.05$, $p<0.01$). In overall, two symbols/letters denoted $p<0.05$ and 1 symbol/letter indicated $p<0.01$.

7.7 REFERENCES

[1] Diaz M, Bartolomé J, Requena J, Moya J. Wet processing of mullite/molybdenum composites. Journal of the European Ceramic Society 2000;20:1907-14.

[2] Muñoz MD. Procesamiento por vía húmeda de sistemas particulados disimilares mullita-molibdeno: Universidad Autónoma de Madrid; 2001.

[3] Gutiérrez González C. Nuevos Materiales: Cerámica–Niobio con Aplicaciones Biomédicas. Instituto de Ciencia de Materiales Madrid: Tesis Doctoral 2009: 1-258; 2009.

[4] BAST R. Organic additives for ceramics - An overview. British Ceramic Transactions 1993;92(5):217-8.

[5] Kang S-JL. Sintering: densification, grain growth and microstructure: Butterworth-Heinemann; 2004.

[6] Ikegami T, Kitami Y, Tsutsumi M. Reduction in specific surface area of an alumina powder at a relatively low temperature. Ceramics international 1999;25:183-90.

[7] Blendell JE. Encyclopedia of Materials: Science and Technology. Solid-state sintering. Ed Elsevier online 8745-50.

[8] He Z, Ma J. Grain-growth law during Stage 1 sintering of materials. Journal of Physics D: Applied Physics 2002;35:2217.

[9] Kim H-C, Shon I-J, Garay J, Munir ZA. Consolidation and properties of binderless sub-micron tungsten carbide by field-activated sintering. International Journal of Refractory Metals and Hard Materials 2004;22:257-64.

[10] Anselmi-Tamburini U, Garay J, Munir Z. Fundamental investigations on the spark plasma sintering/synthesis process: III. Current effect on reactivity. Materials Science and Engineering: A 2005;407:24-30.

[11] Chen I-W, Wang X-H. Sintering dense nanocrystalline ceramics without final-stage grain growth. Nature 2000;404:168-71.

[12] Gao L, Shen Z, Miyamoto H, Nygren M. Superfast densification of oxide/oxide ceramic composites. Journal of the American Ceramic Society 1999;82:1061-3.

[13] Kumar R, Cheang P, Khor K. Spark plasma sintering and in vitro study of ultra-fine HA and ZrO< sub> 2</sub>–HA powders. Journal of Materials Processing Technology 2003;140:420-5.

[14] Saji S. Spark plasma sintering of niobium aluminide powders. Metal Powder Report 1998;53:36-.

[15] Wan J, Duan R-G, Mukherjee AK. Spark plasma sintering of silicon nitride/silicon carbide nanocomposites with reduced additive amounts. Scripta materialia 2005;53:663-7.

[16] Zheng Y, Wang S, You M, Tan H, Xiong W. Fabrication of nanocomposite Ti (C, N)-based cermet by spark plasma sintering. Materials chemistry and physics 2005;92:64-70.

[17] Zhan G-D, Kuntz JD, Garay JE, Mukherjee AK. Electrical properties of nanoceramics reinforced with ropes of single-walled carbon nanotubes. Applied Physics Letters 2003;83:1228-30.

[18] Sairam K, Sonber J, Murthy T, Subramanian C, Fotedar R, Nanekar P, et al. Influence of spark plasma sintering parameters on densification and mechanical properties of boron carbide. International Journal of Refractory Metals and Hard Materials 2014;42:185-92.

[19] Liu J, Shen Z, Nygren M, Su B, Button TW. Spark Plasma Sintering Behavior of Nano-Sized (Ba, Sr) TiO3 Powders: Determination of Sintering Parameters Yielding Nanostructured Ceramics. Journal of the American Ceramic Society 2006;89:2689-94.

[20] ASTM International WC, PA. ASTM Standard C373 - 88. Standard Test Method for Water Absorption, Bulk Density, Apparent Porosity, and Apparent Specific Gravity of Fired Whiteware Products

www.astm.org.2006.

[21] Guinier A. X-Ray Diffraction: In Crystals, Imperfect Crystals, and Amorphous Bodies. Dover Books on Physics 2013.

[22] CSIC. DoCSB. Learn Crystallography with us! http://www.xtal.iqfr.csic.es/Cristalografia/index-en.html.

[23] Warren BE. X-ray Diffraction: DoverPublications. com; 1969.

[24] Zachariasen W. A general theory of X-ray diffraction in crystals. Acta Crystallographica 1967;23:558-64.

[25] Council ALT. My Scope: training for advanced research. http://li155-94.members.linode.com/myscope/xrd/introduction/2011.

[26] Wachtman JB, Cannon WR, Matthewson MJ. Mechanical properties of ceramics: Wiley. com; 2009.

[27] Callister WD, Rethwisch DG. Materials science and engineering: an introduction. 2007.

[28] International Organization for Standardization I. ISO 6872:2008. Dentistry -- Ceramic materials2008.

[29] Rocha-Rangel R. Fracture Toughness Determinations by Means of Indentation Fracture: InTech; 2011.

[30] Dowling NE, Prasad KS, Narayanasamy R. Mechanical behavior of materials: engineering methods for deformation, fracture, and fatigue: prentice Hall Upper Saddle River^ eNJ NJ; 1999.

[31] Wessel JK. The handbook of advanced materials: enabling new designs: John Wiley & Sons; 2004.

[32] Scherrer SS, Denry IL, Wiskott H. Comparison of three fracture toughness testing techniques using a dental glass and a dental ceramic. Dental Materials 1998;14:246-55.

[33] Wang H, Pallav P, Isgrò G, Feilzer AJ. Fracture toughness comparison of three test methods with four dental porcelains. Dental Materials 2007;23:905-10.

[34] Soderholm K-J. Review of the fracture toughness approach. Dental Materials 2010;26:e63-e77.

[35] Fischer H, Marx R. Fracture toughness of dental ceramics: comparison of bending and indentation method. Dental Materials 2002;18:12-9.

[36] Albakry M, Guazzato M, Swain MV. Fracture toughness and hardness evaluation of three pressable all-ceramic dental materials. Journal of Dentistry 2003;31:181-8.

[37] TWI. Hardness Testing Part 1. http://www.twi-global.com/technical-knowledge/job-knowledge/hardness-testing-part-1-074/2014.

[38] ASTM International WC, PA. Standard Test Method for Vickers Indentation Hardness of Advanced Ceramics. ASTM C1327 - 082008.

[39] Launey ME, Ritchie RO. On the Fracture Toughness of Advanced Materials. Advanced Materials 2009;21:2103-10.

[40] Ritchie RO. The conflicts between strength and toughness. Nature materials 2011;10:817-22.

[41] Braun LM, Bennison SJ, Lawn BR. Objective Evaluation of Short-Crack Toughness Curves Using Indentation Flaws - Case-Study on Alumina-Based Ceramics. Journal of the American Ceramic Society 1992;75:3049-57.

[42] Kaliszewski MS, Behrens G, Heuer AH, Shaw MC, Marshall DB, Dransmann GW, et al. Indentation Studies on Y_2O_3-Stabilized ZrO_2 .1. Development of Indentation-Induced Cracks. Journal of the American Ceramic Society 1994;77:1185-93.

[43] Gutierrez-Gonzalez CF, Bartolome JF. Damage tolerance and R-curve behavior of Al_2O_3-ZrO_2-Nb multiphase composites with synergistic toughening mechanism. Journal of Materials Research 2008;23:570-8.

[44] Smith SM, Scattergood RO. Crack-Shape Effects for Indentation Fracture-Toughness Measurements. Journal of the American Ceramic Society 1992;75:305-15.

[45] Li CW, Lee DJ, Lui SC. R-Curve Behavior And Strength For Insitu Reinforced Silicon Nitrides With Different Microstructures. Journal of the American Ceramic Society 1992;75:1777-85.

[46] Newman JC, Raju IS. An empirical stress-intensity factor equation for the surface crack. Engineering Fracture Mechanics 1981;15:185-92.

[47] Kaplan WD, Chatain D, Wynblatt P, Carter WC. A review of wetting versus adsorption, complexions, and related phenomena: the rosetta stone of wetting. Journal of Materials Science 2013;48:5681-717.

[48] Pegueroles Neyra M. Interactions between titanium surfaces and biological components http://hdl.handle.net/10803/6066: Universitat Politècnica de Catalunya 2009.

[49] Adamson AW, Gast AP. Physical chemistry of surfaces: Wiley New York; 1990.

[50] Southall NT, Dill KA, Haymet A. A view of the hydrophobic effect. The Journal of Physical Chemistry B 2002;106:521-33.

[51] Young T. An essay on the cohesion of fluids. Philosophical Transactions of the Royal Society of London 1805;95:65-87.

[52] Rudawska A, Jacniacka E. Analysis for determining surface free energy uncertainty by the Owen–Wendt method. International Journal of Adhesion and Adhesives 2009;29:451-7.

[53] Sharma P, Hanumantha Rao K. Analysis of different approaches for evaluation of surface energy of microbial cells by contact angle goniometry. Advances in colloid and interface science 2002;98:341-463.

[54] Chibowski E. Surface free energy of a solid from contact angle hysteresis. Advances in colloid and interface science 2003;103:149-72.

[55] Kwok D, Neumann A. Contact angle measurement and contact angle interpretation. Advances in Colloid and Interface Science 1999;81:167-249.

[56] Żenkiewicz M. Methods for the calculation of surface free energy of solids. Journal of Achievements in Materials and Manufacturing Engineering 2007;24:137-45.

[57] Bormashenko E. Young, Boruvka–Neumann, Wenzel and Cassie–Baxter equations as the transversality conditions for the variational problem of wetting. Colloids and Surfaces A: Physicochemical and Engineering Aspects 2009;345:163-5.

[58] Shen Q. On the Choice of the Acid/Base Ratio of Water for Application to the van Oss–Chaudhury–Good Combining Rules. Langmuir 2000;16:4394-7.

[59] Owens DK, Wendt R. Estimation of the surface free energy of polymers. Journal of Applied Polymer Science 1969;13:1741-7.

[60] Gindl M, Sinn G, Gindl W, Reiterer A, Tschegg S. A comparison of different methods to calculate the surface free energy of wood using contact angle measurements. Colloids and Surfaces A: Physicochemical and Engineering Aspects 2001;181:279-87.

[61] Aparicio C, Maazouz Y, Yang D. Measuring Wettability of Biosurfaces at the Microscale. Nanotechnology in Regenerative Medicine: Springer; 2012. p. 163-77.

[62] Seiler H. Secondary electron emission in the scanning electron microscope. Journal of Applied Physics 1983;54:R1-R18.

[63] Todokoro H, Ezumi M. Scanning electron microscope. Google Patents; 1999.

[64] Goldstein J, Newbury D, Echlin P, Joy D, Lyman C, Lifshin E, et al. Image Formation and Interpretation. Scanning Electron Microscopy and X-ray Microanalysis: Springer US; 2003. p. 99-193.

[65] Goldstein J, Newbury D, Echlin P, Joy D, Lyman C, Lifshin E, et al. The SEM and Its Modes of Operation. Scanning Electron Microscopy and X-ray Microanalysis: Springer US; 2003. p. 21-60.

[66] AMMRF. Australian Microscopy & Microanalysis Reserch Family. http://www.ammrf.org.au/myscope/xrd/background/machine/.

[67] Goldstein J, Newbury D, Echlin P, Joy D, Fiori C, Lifshin E. Electron-Beam-Specimen Interactions. Scanning Electron Microscopy and X-Ray Microanalysis: Springer US; 1981. p. 53-122.

[68] Goldstein J, Newbury DE, Joy DC, Lyman CE, Echlin P, Lifshin E, et al. Scanning electron microscopy and X-ray microanalysis: Springer; 2003.

[69] Goldstein J, Newbury D, Echlin P, Joy D, Lyman C, Lifshin E, et al. X-Ray Spectral Measurement: EDS and WDS. Scanning Electron Microscopy and X-ray Microanalysis: Springer US; 2003. p. 297-353.

[70] Hayat MA. Principles and techniques of scanning electron microscopy. Biological applications. Volume 1: Van Nostrand Reinhold Company.; 1974.

[71] GmbH HH-TE. http://www.hht-eu.com/cms/19823.html. 2010.

[72] Andrade J. X-ray Photoelectron Spectroscopy (XPS). In: Andrade J, editor. Surface and Interfacial Aspects of Biomedical Polymers: Springer US; 1985. p. 105-95.

[73] Watts JF, Wolstenholme J. An introduction to surface analysis by XPS and AES. An Introduction to Surface Analysis by XPS and AES, by John F Watts, John Wolstenholme, pp 224 ISBN 0-470-84713-1 Wiley-VCH, May 2003 2003;1.

[74] Crist BV. Handbook of monochromatic XPS spectra, The elements of native Oxides. Handbook of Monochromatic XPS Spectra, The Elements of Native Oxides, by B Vincent Crist, pp 548 ISBN 0-471-49265-5 Wiley-VCH, October 2000 2000;1.

[75] Troć R. US: X-ray Photoelectron Spectroscopy (XPS) and Photoelectron Spectroscopy (PES). In: Wijn HPJ, editor. Actinide Monochalcogenides: Springer Berlin Heidelberg; 2009. p. 392-9.

[76] Queen's University CD, Dr. J. Hugh Horton. X-ray photoelectron spectroscopy. http://www.chem.queensu.ca/people/faculty/horton/research.html2009.

[77] Woods S. Understanding scanning white light interferometry. MICROmanufacturing: http://www.micromanufacturing.com/; 2009.

[78] Wyant JC. White light interferometry. AeroSense 2002: International Society for Optics and Photonics; 2002. p. 98-107.

[79] Blunt RT. White Light Interferometry–a production worthy technique for measuring surface roughness on semiconductor wafers. Proceedings of the CS MANTECH Conference2006.

[80] Schnell U, Zimmermann E, Dandliker R. Absolute distance measurement with synchronously sampled white-light channelled spectrum interferometry. Pure and Applied Optics: Journal of the European Optical Society Part A 1995;4:643.

[81] Blateyron F. New 3D parameters and filtration techniques for surface metrology. Quality Magazine 2006:1-7.

[82] Gadelmawla ES, Koura MM, Maksoud TMA, Elewa IM, Soliman HH. Roughness parameters. Journal of Materials Processing Technology 2002;123:133-45.

[83] Blunt L, Jiang X. Advanced techniques for assessment surface topography: Development of a Basis for 3D Surface Texture Standards" Surfstand": Elsevier; 2003.

[84] Hansson S. Surface roughness parameters as predictors of anchorage strength in bone: a critical analysis. Journal of biomechanics 2000;33:1297-303.

[85] Pegueroles M, Aparicio C, Bosio M, Engel E, Gil FJ, Planell JA, et al. Spatial organization of osteoblast fibronectin matrix on titanium surfaces: Effects of roughness, chemical heterogeneity and surface energy. Acta Biomaterialia 2010;6:291-301.

[86] De Oliveira RRL, Albuquerque DAC, Cruz TGS, Yamaji FM, Leite FL. Measurement of the Nanoscale Roughness by Atomic Force Microscopy: Basic Principles and Applications2012.

[87] Dong WP, Sullivan PJ, Stout KJ. Comprehensive study of parameters for characterising three- dimensional surface topography: III: Parameters for characterising amplitude and some functional properties. Wear 1994;178:29-43.

[88] Blunt L, Jiang X. 2 - Numerical Parameters for Characterisation of Topography. In: Blunt L, Jiang X, editors. Advanced Techniques for Assessment Surface Topography. Oxford: Kogan Page Science; 2003. p. 17-41.

[89] Taub ML. Chapter 14 Cell culture. In: Bittar EE, Neville B, editors. Principles of Medical Biology: Elsevier; 1996. p. 463-83.

[90] Majeska RJ, Gronowicz GA. Chapter 89 - Current Methodologic Issues in Cell and Tissue Culture. In: Bilezikian JP, Raisz LG, Rodan GA, editors. Principles of Bone Biology (Second Edition). San Diego: Academic Press; 2002. p. 1529-41.

[91] Freshney RI, Obradovic B, Grayson W, Cannizzaro C, Vunjak-Novakovic G. Chapter Twelve - Principles of tissue culture and bioreactor design. In: Lanza R, Langer R, Vacanti J, editors. Principles of Tissue Engineering (Third Edition). Burlington: Academic Press; 2007. p. 155-83.

[92] Meleady P, O'Connor R. Chapter 2 - General Procedures for Cell Culture. In: Celis JE, editor. Cell Biology (Third Edition). Burlington: Academic Press; 2006. p. 13-20.

[93] Stein GS, Borowski M, Luong MX, Shi M-J, Smith KP, Vazquez P. Human Stem Cell Technology and Biology: A Research Guide and Laboratory Manual: John Wiley & Sons; 2011.

[94] Virginie N, Cécile C, Bernard R, Sabine W-G. Neural Fate of Mesenchymal Stem Cells and Neural Crest Stem Cells: Which Ways to Get Neurons for Cell Therapy Purpose? 2013.

[95] McQuillan DJ, Richardson MD, Bateman JF. Matrix deposition by a calcifying human osteogenic sarcoma cell line (SAOS-2). Bone 1995;16:415-26.

[96] Hausser HJ, Brenner RE. Phenotypic instability of Saos-2 cells in long-term culture. Biochemical and Biophysical Research Communications 2005;333:216-22.

[97] Brakefield AC, Prieto EM, Guelcher SA. A Characterization of Three Groups of MC3T3-E1 Pre-Osteoblastic Cells to Aid in Testing of Polyurethane-Bone Scaffolds for Wound Healing.

[98] Mosmann T. Rapid colorimetric assay for cellular growth and survival: application to proliferation and cytotoxicity assays. Journal of immunological methods 1983;65:55-63.

[99] Ng KW, Leong DTW, Hutmacher DW. The challenge to measure cell proliferation in two and three dimensions. Tissue engineering 2005;11:182-91.

[100] Denizot F, Lang R. Rapid colorimetric assay for cell growth and survival: modifications to the tetrazolium dye procedure giving improved sensitivity and reliability. Journal of immunological methods 1986;89:271-7.

[101] 10993-5:2009 I. Biological evaluation of medical devices. . Part 5: Tests for in vitro citotoxicity2009.

[102] Ng KW, Leong DT, Hutmacher DW. The challenge to measure cell proliferation in two and three dimensions. Tissue engineering 2005;11:182-91.

[103] Grice HC, Carlson RG. The changing role of pathology in modern safety evaluation. CRC Critical Reviews in Toxicology 1972;1:119-52.

[104] https://cssportal.roche.com/LFR_PublicDocs/ras/11644793001_en_08.pdf.

[105] Al-Nasiry S, Geusens N, Hanssens M, Luyten C, Pijnenborg R. The use of Alamar Blue assay for quantitative analysis of viability, migration and invasion of choriocarcinoma cells. Human reproduction 2007;22:1304-9.

[106] Nakayama GR, Caton MC, Nova MP, Parandoosh Z. Assessment of the Alamar Blue assay for cellular growth and viability in vitro. Journal of immunological methods 1997;204:205-8.

[107] Inc TFS. alamarBlue®—Rapid & Accurate Cell Health Indicator. http://www.lifetechnologies.com/es/en/home/brands/molecular-probes/key-

molecular-probes-products/alamarblue-rapid-and-accurate-cell-health-indicator.html2014.

[108] Levenberg S, Khademhosseini A, Langer R. Chapter 63 - Embryonic Stem Cells in Tissue Engineering. In: Lanza R, Gearhart J, Hogan B, Melton D, Pedersen R, Thomas ED, et al., editors. Essentials of Stem Cell Biology (Second Edition). San Diego: Academic Press; 2009. p. 571-81.

[109] Coelho M, Fernandes M. Human bone cell cultures in biocompatibility testing. Part II: effect of ascorbic acid,< i> β</i>-glycerophosphate and dexamethasone on osteoblastic differentiation. Biomaterials 2000;21:1095-102.

[110] Walsh MC, Kim N, Kadono Y, Rho J, Lee SY, Lorenzo J, et al. Osteoimmunology: interplay between the immune system and bone metabolism. Annu Rev Immunol 2006;24:33-63.

[111] Hoemann C, El-Gabalawy H, McKee M. In vitro osteogenesis assays: influence of the primary cell source on alkaline phosphatase activity and mineralization. Pathologie Biologie 2009;57:318-23.

[112] Biological US. https://www.usbio.net/misc/Immunocytochemistry.

[113] Burry RW. Controls for Immunocytochemistry An Update. Journal of Histochemistry & Cytochemistry 2011;59:6-12.

[114] Burry RW. Immunocytochemistry: a practical guide for biomedical research: Springer; 2010.

[115] Polak JM, Van Noorden S. Introduction to immunocytochemistry: Bios Scientific Publishers Oxford; 1997.

[116] IHC WORLD LSPS. http://www.ihcworld.com/_protocols/general_ICC/staining.htm. 2003-2011.

[117] Elson EL, Magde D. Fluorescence correlation spectroscopy. I. Conceptual basis and theory. Biopolymers 1974;13:1-27.

[118] Valeur B. Molecular fluorescence: principles and applications: John Wiley & Sons; 2013.

[119] Lakowicz JR. Principles of fluorescence spectroscopy: Springer; 2009.

[120] Tsien RY, Waggoner A. Fluorophores for confocal microscopy. Handbook of biological confocal microscopy: Springer; 1995. p. 267-79.

[121] Axelrod D. Total internal reflection fluorescence microscopy in cell biology. Traffic 2001;2:764-74.

[122] Mathies RA, Peck K. Laser excited confocal microscope fluorescence scanner and method. Google Patents; 1992.

[123] Diaspro A. Confocal and two-photon microscopy: foundations, applications, and advances: Wiley-Liss New York; 2002.

[124] Pawley JB. Handbook of biological confocal microscopy: Springer; 1995.

[125] Inc OA. Microscopy resource centre. Introduction to Confocal Microscopy. http://www.olympusmicro.com/primer/techniques/confocal/2012.

[126] Smith CL. Basic confocal microscopy. Current Protocols in Neuroscience 2001:2.. 1-2.. 18.

[127] Carlsson K, Åslund N. Confocal imaging for 3-D digital microscopy. Applied optics 1987;26:3232-8.